

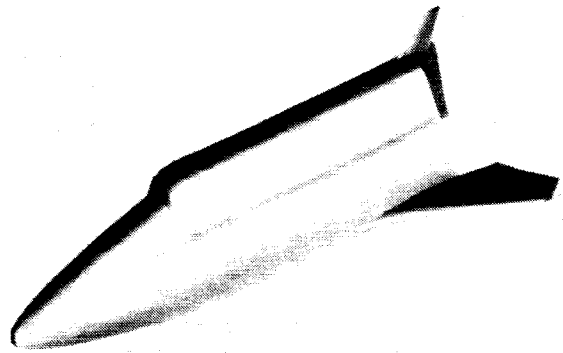
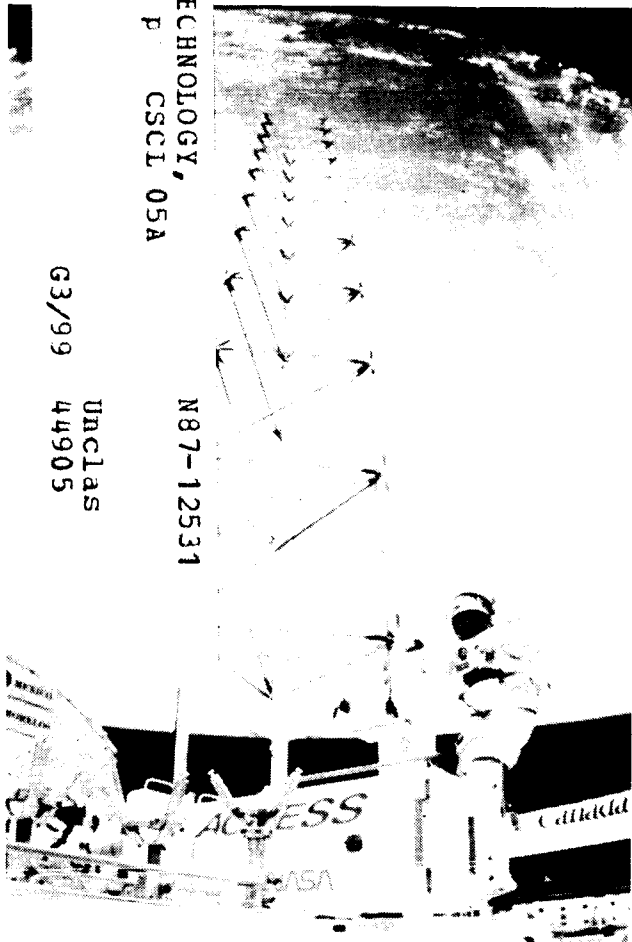
# Research and Technology 1986

*Annual Report of the  
Langley Research Center*

(NASA-TM-89037) RESEARCH AND TECHNOLOGY,  
1986 Annual Report (NASA) 113 p CSCI 05A

N87-12531

G3/99  
Unclas  
44905



**NASA**

National Aeronautics and  
Space Administration

# Research and Technology 1986

*Annual Report of the  
Langley Research Center*



National Aeronautics and  
Space Administration


**Langley Research Center**  
Hampton, Virginia 23665-5225

1986



## Foreword

The mission of the NASA Langley Research Center is to increase the knowledge and capability of the United States in a full range of aeronautics disciplines and in selected space disciplines. This mission will be accomplished by: performing innovative research relevant to national needs and Agency goals; transferring technology to users in a timely manner; and providing development support to other United States Government agencies, industry, and other NASA centers. This report contains highlights of the major accomplishments and applications that have been made during the past year. The highlights illustrate both the broad range of the research and technology activities at the NASA Langley Research Center and the contributions of this work toward maintaining United States leadership in aeronautics and space research. For further information about the report, contact Jerry C. South, Chief Scientist, Mail Stop 103, NASA Langley Research Center, Hampton, Virginia 23665, (804) 865-3316.



Richard H. Petersen  
Director

**PRECEDING PAGE BLANK NOT FILMED**

## **Availability Information**

The NASA program office and the corresponding Agency-wide Research and Technology Objectives and Plans (RTOP) work breakdown structure are listed in the Contents for each research and technology accomplishment. OAST designates the Office of Aeronautics and Space Technology; OSSA designates the Office of Space Science and Applications; AA designates the Associate Administrator; OCE designates the Office of the Chief Engineer; OCP designates the Office of Commercial Programs; OSF designates the Office of Space Flight, and OSS designates the Office of the Space Station.

For additional information on any summary, contact the individual identified with the highlight. This individual is generally either a member or a leader of the research group submitting the highlight. Commercial telephone users may dial the listed extension preceded by (804) 865. Telephone users with access to the Federal Telecommunications System (FTS) may dial the extension preceded by 928.

# Contents

|                                    |     |
|------------------------------------|-----|
| Foreword . . . . .                 | iii |
| Availability Information . . . . . | iv  |

## Aeronautics Directorate

|  |    |
|--|----|
| Aeronautics Directorate . . . . .  | 1  |
| Implicit Upwind-Biased Algorithm for Navier-Stokes Equations . . . . .   | 1  |
| OAST (505-60-01)   |    |
| Application of Spectral Multigrid Methods to Engineering Calculations . . . . .  | 2  |
| OAST (505-60-01)   |    |
| Three-Dimensional Transonic Viscous-Inviscid Interaction Program . . . . .   | 3  |
| OAST (505-60-01)   |    |
| Multiple-Domain Extension to Spectral Collocation Methods . . . . .  | 3  |
| OAST (505-60-11)   |    |
| Experimental Validation of Stability Theory for Airfoils . . . . .   | 4  |
| OAST (505-60-21)   |    |
| Euler Code With Interacted Viscous Effects . . . . .   | 4  |
| OAST (505-60-21)   |    |
| EA-6B Maneuver Improvement Design . . . . .  | 5  |
| OAST (505-60-21)   |    |
| Aerodynamic Loads for Slender-Wing/Body Configurations . . . . .   | 6  |
| OAST (505-60-21)   |    |
| Aircraft Wake Decay in the Atmosphere . . . . .  | 6  |
| OAST (505-60-21)   |    |
| F-16XL Vortex Flap Development . . . . .   | 7  |
| OAST (505-60-21)   |    |
| Vortex Flap Hinge Moments . . . . .  | 8  |
| OAST (505-60-21)   |    |
| Flow Visualization Study of Juncture Flow Control . . . . .  | 8  |
| OAST (505-60-21)   |    |
| Holocinematographic Velocimeter for Studying Complex Flows . . . . .   | 9  |
| OAST (505-60-31)   |    |
| Transition Detection System for Cryogenic Wind Tunnels . . . . .   | 9  |
| OAST (505-61-01)   |    |
| Transonic Wind Tunnel Wall Interference Assessment/Correction (WIAC) Procedure . . . . .                                   | 10 |
| OAST (505-61-01)   |    |
| Development of Spin Resistance Criteria for Light General-Aviation Airplanes . . . . .                                     | 11 |
| OAST (505-61-41)   |    |
| Rotor Inflow . . . . .   | 11 |
| OAST (505-61-51)   |    |
| Extension and Evaluation of Supersonic Wing Design-Space Concept . . . . .   | 12 |
| OAST (505-61-71)   |    |
| Pitot Pressure Surveys Over 75° Swept Delta Wing . . . . .   | 13 |
| OAST (505-61-71)   |    |
| Deflectable Forebody Strakes for Increased High Angle-of-Attack Yaw Control<br>of Generic Research Configuration . . . . . | 13 |
| OAST (505-61-71)   |    |
| Thrust Reverser Investigation on Jet Transport Model in Ground Effect . . . . .  | 14 |
| OAST (505-61-71)   |    |

|   |    |
|---|----|
| Three-Dimensional Computation and Validation of Transverse Jet Mixing<br>in Scramjet Combustor Models . . . . . | 14 |
| OAST (505-62-81)  |    |
| Numerical Simulation of Supersonic Chemically Reacting Mixing Layer . . . . .                                   | 15 |
| OAST (505-62-81)  |    |
| Cavity Door Effects on Aerodynamic Loads of Stores Separating From Cavities at Supersonic Speeds . .            | 16 |
| OAST (505-68-91)  |    |
| Nonaxisymmetric Afterbody Three-Dimensional Flow Analysis . . . . .   | 16 |
| OAST (505-68-91)  |    |
| Thrust Vectoring Control From Canted Nozzles . . . . .  | 17 |
| OAST (505-68-91)  |    |
| Transonic Airfoil Design Procedure . . . . .  | 18 |
| OAST (505-68-91)  |    |
| F-14 Yaw Vane Investigation . . . . .   | 18 |
| OAST (505-68-91)  |    |

### Electronics Directorate

|   |    |
|---|----|
| Electronics Directorate . . . . .   | 20 |
| In Situ Laser Absorption Measurements of Carbon Monoxide Over Amazon Forest . . . . .               | 20 |
| OSSA (176-40-05)  |    |
| Amplitude-Modulated Laser System for Distance and Displacement Measurement . . . . .                | 21 |
| AA (307-05)   |    |
| Nondestructive Evaluation/Fracture Mechanics Prediction of Filament Wound Casing Strength . . . . . | 21 |
| OCE (323-51-66)   |    |
| Analytic Function and Signal Processing Techniques to Image Thin Composite Plate Damage . . . . .   | 22 |
| OCE (323-51-66)   |    |
| Flight Balance for Skin Friction Measurements . . . . .   | 23 |
| OAST (505-61-01)  |    |
| Laminar-Separation Bubble Detection With Thermal Film Sensors . . . . .                             | 23 |
| OAST (505-61-01)  |    |
| OH Absorption Technique for Measurement of Combustor Temperature . . . . .                          | 24 |
| OAST (505-62-81)  |    |
| Metal Ion Effects on Polymer Properties by Positron Annihilation Spectroscopy . . . . .             | 24 |
| OAST (505-63-91)  |    |
| Dual-Block Grid Generation Around an Aircraft . . . . .   | 24 |
| OAST (505-90-21)  |    |
| High-Temperature Acoustic Transducer . . . . .  | 25 |
| OAST (506-43-11)  |    |
| Nondestructive Evaluation Detection of Temper Embrittlement in HY-80 Steels . . . . .               | 25 |
| OAST (506-43-11)  |    |
| Acoustic Characterization of Glass Transition Temperature . . . . .                                 | 26 |
| OAST (506-43-11)  |    |
| Optical and Thermal Properties of Titanium-Doped Sapphire Laser Materials . . . . .                 | 26 |
| OAST (506-45-31)  |    |
| Narrowband Ti:Al <sub>2</sub> O <sub>3</sub> Self-Injection Locking Feasibility . . . . .           | 28 |
| OAST (506-45-31)  |    |
| Injection-Controlled Titanium-Doped Sapphire Laser Using Pulsed Dye Laser . . . . .                 | 28 |
| OAST (506-45-31)  |    |

|   |    |
|---|----|
| Continuous, Multielement, Hot-Film Transition Gauge . . . . . | 29 |
| OAST (506-61-43)  |    |
| Event Thermometer for Cosmic Ray Detectors . . . . .          | 29 |
| OSSA (871-00-00)  |    |

### Flight Systems Directorate

|   |    |
|---|----|
| Flight Systems Directorate . . . . .  | 31 |
| Dielectric Resonator Band-Pass Filter Technology for Future Aerospace Applications . . . . .            | 31 |
| AA (307-51-06)  |    |
| Space Station Antenna Obscuration . . . . .   | 32 |
| OSS (482-59-23)   |    |
| Dynamic Remapping of Parallel Computations . . . . .  | 32 |
| OAST (505-65-01)  |    |
| Time Delay and Pitch Control Sensitivity Effects in Flared-Landing Task . . . . .                       | 33 |
| OAST (505-66-01)  |    |
| Lateral/Directional Control System Design Using Thrust Vectoring . . . . .                              | 34 |
| OAST (505-66-01)  |    |
| Flight Data Analysis From Highly Augmented Aircraft . . . . .   | 34 |
| OAST (505-66-01)  |    |
| First Practical Multicolor Thin-Film Electroluminescent Flat-Panel Display . . . . .                    | 35 |
| OAST (505-66-11)  |    |
| Characterization of Fault Recovery Behavior of Fault-Tolerant Systems . . . . .                         | 36 |
| OAST (505-66-21)  |    |
| Flight Test Design Considerations for Fault-Tolerant Integrated Avionics Sensor Configuration . . . . . | 36 |
| OAST (505-66-21)  |    |
| Algorithm for Computing Near-Optimum Flight Plans . . . . .   | 37 |
| OAST (505-66-41)  |    |
| Impact of Advanced Technologies on Terminal Area Capacity . . . . .                                     | 38 |
| OAST (505-67-01)  |    |
| Characterized Microburst Severity Via Weibull Probability Distributions . . . . .                       | 38 |
| OAST (505-67-01)  |    |
| Application of Heart Rate Measures to Assessment of Pilot Workload . . . . .                            | 38 |
| OAST (505-67-11)  |    |
| Very-High-Speed Integrated-Circuit Processor Development . . . . .                                      | 39 |
| OAST (506-44-11)  |    |
| Very-High-Speed Integrated-Circuit Multiprocessor Simulation . . . . .                                  | 39 |
| OAST (506-44-11)  |    |
| Information Network Architecture . . . . .  | 40 |
| OAST (506-44-11)  |    |
| Real-Time Video Processing . . . . .  | 41 |
| OAST (506-44-11)  |    |
| Linear Laser Diode Array for High-Speed Optical Disk Recorder . . . . .                                 | 41 |
| OAST (506-44-11)  |    |
| Regional Pattern Calculations for Large Reflector Antennas . . . . .                                    | 42 |
| OAST (506-44-21)  |    |
| Spacecraft Control Laboratory Experiment . . . . .  | 42 |
| OAST (506-46-11)  |    |
| Near-Field Testing of 5-Meter Tetrahedral Truss Reflector . . . . .                                     | 43 |
| OAST (506-62-43)  |    |

|   |    |
|---|----|
| Improved Image Gathering and Processing . . . . .               | 44 |
| OAST (549-01-31)  |    |
| Multifunction Recognition Operator for Robotic Vision . . . . . | 44 |
| OAST (549-01-51)  |    |

### Space Directorate

|  |    |
|--|----|
| Space Directorate . . . . .  | 46 |
| Study of Tropospheric Trace Gases From Satellites . . . . .  | 46 |
| OSSA (176-10-05)   |    |
| Increasing Atmospheric Levels of Ethane . . . . .  | 47 |
| OSSA (176-20-02)   |    |
| Airborne Lidar Measurements of Ozone and Aerosols Over Amazon Rain Forest of Brazil . . . . .  | 48 |
| OSSA (176-40-04)   |    |
| Modeling Space Radiation Effects . . . . .   | 48 |
| OSSA (199-22-76)   |    |
| Atomic Oxygen Beam Generator . . . . .   | 49 |
| AA (307-51-06)   |    |
| Calculation of Heating on Aeroassist Flight Experiment Vehicle . . . . .   | 49 |
| OAST (506-40-11)   |    |
| Factors Affecting Crew Escape Trajectories From Shuttle Orbiter at Subsonic Speeds . . . . .   | 50 |
| OAST (506-40-11)   |    |
| Hypersonic Aerodynamic Characteristics of Maneuvering Reentry Research Vehicle . . . . .   | 50 |
| OAST (506-40-11)   |    |
| Measured and Predicted Vortex-Induced Leeward Heating on Biconic<br>Planetary Entry Vehicle at Mach 6 and 10 . . . . .                     | 51 |
| OAST (506-40-11)   |    |
| Experimental Investigation of Circular-Body Earth-to-Orbit Transport Vehicle . . . . .   | 52 |
| OAST (506-40-11)   |    |
| Navier-Stokes Simulations for Hypersonic Low-Density Flows . . . . .   | 52 |
| OAST (506-40-11)   |    |
| 10-Watt Continuous-Wave Solar-Pumped Laser . . . . .   | 53 |
| OAST (506-41-41)   |    |
| Shuttle Entry Air Data System (SEADS) Experiment . . . . .   | 54 |
| OAST (506-48-11)   |    |
| Shuttle II Study . . . . .   | 54 |
| OAST (506-49-11)   |    |
| Geometry Modeller for AVID . . . . .   | 55 |
| OAST (506-49-11)   |    |
| Uniform Damping Control of Vibrating Truss Structures . . . . .  | 55 |
| OAST (506-49-21)   |    |
| Analysis for Flexible Spacecraft Sensor and Actuator Placement . . . . .   | 56 |
| OAST (506-49-21)   |    |
| Aeroassist Flight Experiment Vehicle Aerodynamics . . . . .  | 57 |
| OAST (506-51-13)   |    |
| First Spectroscopic Measurements of Stratospheric Peroxynitric Acid,<br>Chlorine Nitrate, Carbonyl Fluoride, and Methyl Chloride . . . . . | 58 |
| OSSA (618-21-00)   |    |
| Simultaneous Dual-Polarization Airborne Lidar Measurements of Polar Stratospheric Clouds . . . . .   | 58 |
| OSSA (665-10-40)   |    |

|  |    |
|--|----|
| ERBE Measurements of Cloud Forcing . . . . .   | 59 |
| OSSA (665-45-30)   |    |
| Springtime Antarctic Ozone Depletion Observed by SAGE II . . . . .                                   | 60 |
| OSSA (665-45-30)   |    |
| Lidar Studies of Stratospheric Aerosols . . . . .  | 60 |
| OSSA (672-21-14)   |    |
| Ground-Based Lidar Measurements of Cirrus Clouds for Project FIRE . . . . .                          | 61 |
| OSSA (672-22-11)   |    |
| Improving Cloud Measurement From Space . . . . .   | 61 |
| OSSA (672-22-12)   |    |
| Sun-Synchronous Satellite Estimates of Solar Radiation at Earth's Surface . . . . .                  | 62 |
| OSSA (672-40-06)   |    |
| Validation and Calibration Studies for Satellite Instruments . . . . .                               | 63 |
| OSSA (672-40-04-70)  |    |
| Detection of Stratospheric HNO <sub>3</sub> Response to Solar UV Variability . . . . .               | 63 |
| OSSA (673-41-07)   |    |
| Response of Stratospheric Ozone to Short-Term Solar UV Variability . . . . .                         | 64 |
| OSSA (673-41-07)   |    |
| Nonlocal Thermodynamic Equilibrium Effects in Mesospheric Ozone . . . . .                            | 65 |
| OSSA (673-41-10)   |    |
| Area Diagnostics of Seasonal Trends in Stratospheric Circulation . . . . .                           | 65 |
| OSSA (673-41-10)   |    |
| Three-Dimensional Model Simulations of Ozone Transport During Sudden Stratospheric Warming . . . . . | 66 |
| OSSA (673-64-02)   |    |
| Transient Medium-Scale Wave Activity in Summer Stratosphere . . . . .                                | 67 |
| OSSA (673-64-02)   |    |
| Explanation for Antarctic "Ozone Hole" . . . . .   | 67 |
| OSSA (673-62-02)   |    |
| Improved Measurement Capability for Spectral Filter Characterization . . . . .                       | 68 |
| OSSA (678-12-04)   |    |

#### Structures Directorate

|   |    |
|---|----|
| Structures Directorate . . . . .  | 69 |
| Role of IMAT Study in Selection of Space Station Truss Bay Size . . . . .   | 69 |
| OSS (483-32-33)   |    |
| Use of Equivalent Plate Representation to Expedite Analysis of Aircraft Wing Box Structures . . . . .                 | 70 |
| OAST (505-33-53)  |    |
| Load Reduction Associated With Twin-Supersonic-Plume Resonance . . . . .  | 71 |
| OAST (505-61-11)  |    |
| Sidewall Treatment for Aircraft Cabin Noise Control . . . . .   | 71 |
| OAST (505-61-11)  |    |
| Low-Frequency Downwind Sound Propagation . . . . .  | 72 |
| OAST (505-61-11)  |    |
| Improved Interlaminar Fracture Toughness of Graphite/Epoxy Composites<br>by Through-the-Thickness Stitching . . . . . | 72 |
| OAST (505-63-01)  |    |
| Method for Analyzing Complex Cracked Configurations to Minimize Modeling . . . . .                                    | 73 |
| OAST (505-63-01)  |    |
| Improved, Elevated Temperature Strengths Through Use of New Aluminum-Lithium Alloys . . . . .                         | 74 |
| OAST (505-63-01)  |    |

|  |    |
|--|----|
| Improvement of Aluminum Matrix Composite Properties Through Microstructural Refinement . . . . .       | 74 |
| OAST (505-63-01)   |    |
| Approximate Analysis for Buckling of Plates With Cutouts . . . . .                                     | 75 |
| OAST (505-63-11)   |    |
| Computational Transonic Flutter Boundary Tracking Procedure Development . . . . .                      | 75 |
| OAST (505-63-21)   |    |
| New Method for Approximating Unsteady Aerodynamics of Aeroservoelasticity Computations . . . . .       | 76 |
| OAST (505-63-21)   |    |
| New Algorithm Development for Efficient Transonic Unsteady Aerodynamic Analyses . . . . .              | 77 |
| OAST (505-63-21)   |    |
| Automated Transonic Aeroelasticity Analysis Program Development . . . . .                              | 78 |
| OAST (505-63-21)   |    |
| Identification of Unusual Instability Boundary for ARW-2 as Narrow Transonic Response Region . . . .   | 78 |
| OAST (505-63-21)   |    |
| Structural Analysis of Jet Transport Controlled Impact Demonstration . . . . .                         | 79 |
| OAST (505-63-41)   |    |
| FAA Test Data Comparisons Using NASA ANOPP Propeller Analysis System . . . . .                         | 80 |
| OAST (505-61-51)   |    |
| Visualization of the Interaction Between Rotor Blades and Tip Vortices . . . . .                       | 80 |
| OAST (505-61-51)   |    |
| Mathematical Method to Control Vibrations by Node Point Placement . . . . .                            | 81 |
| OAST (505-61-51)   |    |
| Euler Code for Blade-Vortex Interaction Noise . . . . .  | 82 |
| OAST (505-61-51)   |    |
| Resin Use Amount in Test for Composite Matrix Toughness . . . . .                                      | 82 |
| OAST (506-43-01)   |    |
| High Mechanical Properties of Semicrystalline Polyimides . . . . .                                     | 83 |
| OAST (506-43-11)   |    |
| Fatigue Performance of Toughened Matrices for Composites . . . . .                                     | 83 |
| OAST (506-43-11)   |    |
| Integrated Fluid-Thermal-Structural Algorithm for Nonlinear Thermal and Stress-Strain Analysis . . . . | 84 |
| OAST (506-43-21 and 506-43-31)   |    |
| High-Strength Aluminum Alloys for Graphite-Reinforced Metal-Matrix Composites . . . . .                | 85 |
| OAST (506-43-21)   |    |
| Reusable High-Temperature Cryogenic Foam Insulation System . . . . .                                   | 85 |
| OAST (506-43-31)   |    |
| Inviscid Finite-Element Flow Analysis Applied to Experimental Model . . . . .                          | 86 |
| OAST (506-43-31 and 506-40-21)   |    |
| ACCESS Flight Experiment Results . . . . .   | 86 |
| OAST (506-43-41 and 928-50-06)   |    |
| Integrated Interdisciplinary Optimization Procedure for Large Space Antenna Design . . . . .           | 87 |
| OAST (506-43-41)   |    |
| Effects of Atmosphere on Slewing Control of Flexible Structure . . . . .                               | 88 |
| OAST (506-43-51)   |    |
| Vibration Testing and Analysis of Large Space Antenna . . . . .  | 88 |
| OAST (506-43-51)   |    |
| Lifting Surface Theory Using Acoustic Approach . . . . .   | 89 |
| OAST (535-03-11)   |    |



|  |    |
|--|----|
| Propeller-Induced Structureborne Noise . . . . .   | 90 |
| OAST (535-03-11)   |    |
| Comparison of Advanced Turboprop and Conventional Aircraft Community Noise Annoyance . . . . . | 90 |
| OAST (535-03-11)   |    |

### Systems Engineering and Operations Directorate

|  |     |
|--|-----|
| Systems Engineering and Operations Directorate . . . . .   | 92  |
| Automatic Control for Particulate Pollution Reduction . . . . .                                  | 92  |
| AA (307-45-71)   |     |
| Seeding System for In-Flight Flow Visualization of F-106B Leading-Edge Vortex Systems . . . . .  | 93  |
| AA (307-05-01)   |     |
| Composite Wings for Cryogenic Wind Tunnel Models . . . . .                                       | 93  |
| AA (307-06-01)   |     |
| Thermal Control of Tubular Composites in Space . . . . .   | 93  |
| OSS (481-33-13)  |     |
| Pultrusion Development for High-Performance Thermoplastic, Polyetherimide/Graphite Composite . . | 94  |
| OSS (482-53-23)  |     |
| Ammonia Flow Test Facility . . . . .   | 94  |
| OSS (482-31-23)  |     |
| Use of Closed-Cell Polyurethane Foam for Molds . . . . .   | 95  |
| OAST (505-60)  |     |
| Gaseous Nitrogen Flow Blocker Seal for NTF Nacelle . . . . .                                     | 96  |
| OAST (505-61-01)   |     |
| Brazing Research Results . . . . .   | 96  |
| OAST (505-61-01)   |     |
| Composite Lightning Rods for Aircraft . . . . .  | 97  |
| OAST (505-68-01)   |     |
| Telescope Door Release Device for HALOE Flight Instrument . . . . .                              | 97  |
| OSSA (678-12-04)   |     |
| Calibration of HALOE Broadband Sun Sensor . . . . .  | 98  |
| OSSA (678-12-04)   |     |
| HALOE Portable Radiation Stimulus Test Set . . . . .   | 98  |
| (678-12-04)  |     |
| Miniature High-Stability High-Temperature Space-Rated Blackbody Radiance Source . . . . .        | 99  |
| OSSA (678-12-04)   |     |
| HALOE Photovoltaic Detector Response Uniformity Mapping Program . . . . .                        | 100 |
| OSSA (678-12-04)   |     |

### Technology Utilization Program

|  |     |
|--|-----|
| Technology Utilization Program . . . . .   | 101 |
| Water Quality Monitoring System . . . . .  | 101 |
| OCP (141-20-10)                            |     |
| Low-Energy Electron Magnetometer . . . . . | 102 |
| OCP (141-20-10)                            |     |
| Intracranial Pressure Dynamics . . . . .   | 102 |
| OCP (141-20-40)                            |     |

# Aeronautics Directorate

The Aeronautics Directorate is composed of approximately 300 scientists and engineers engaged in basic and applied research in the various aeronautics disciplines. The directorate is organized into three research divisions, which conduct aeronautical research to advance the state of the art throughout the complete aerodynamic speed range.

The Low-Speed Aerodynamics Division conducts research in the areas of basic fluid mechanics, low-speed aerodynamics, flight dynamics and flight management, aircraft operations, aviation safety, laminar-flow control, and improved test methods. The division develops and validates theoretical aerodynamic methods for subsonic conditions and design methodology required to improve subsonic aerodynamic performance, stall/spin behavior, handling qualities, and takeoff and landing performance.

The Transonic Aerodynamics Division conducts research to advance the state of the art of transonic aircraft technology in the areas of fundamental aerodynamics, with particular emphasis on Reynolds number effects, laminar-flow concepts, stability and control, performance analysis, configuration concepts, and related aerodynamic phenomena. Particular areas of emphasis include improving the efficiency and reducing the fuel consumption of conventional jet transports, developing the technology for advanced military combat aircraft, developing theoretical and analytical methods for predicting aerodynamic characteristics in separated and transonic flows, developing advanced airfoils for low-speed and transonic aircraft and helicopters, and developing advanced experimental techniques, including advanced wall concepts, for transonic wind tunnels, cryogenic wind tunnel technology, and magnetic suspension and balance systems.

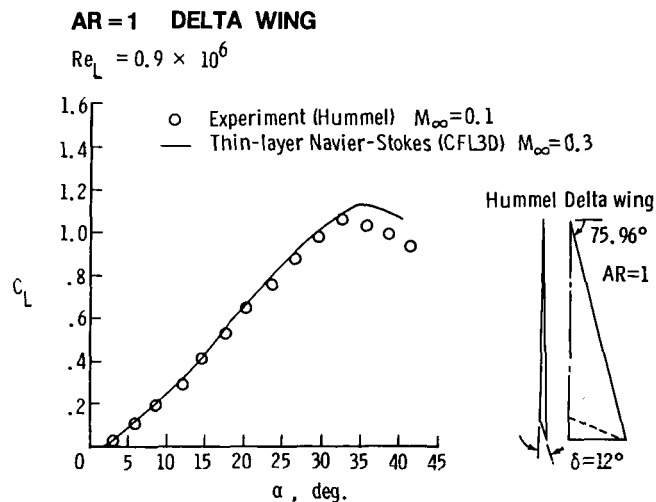
The High-Speed Aerodynamics Division conducts research to advance the state of the art for supersonic aircraft, hypersonic aircraft, and missiles and to support the development of high-performance military aircraft, advanced cruise and tactical missiles, the Space Shuttle, and follow-on advanced space transportation systems. New analytical methods for design and analysis are derived and applied to advanced high-speed aircraft and missile concepts. Key experiments are conducted to validate the analytical methods, explore the potential of advanced concepts, and provide a data base for use by industry design teams. Conceptual designs for advanced high-speed vehicles are conceived and analyzed in order to determine the performance payoff from the application of advanced research results.

## Implicit Upwind-Biased Algorithm for Navier-Stokes Equations

An efficient computational algorithm for the compressible Navier-Stokes equations has been developed. The spatial differencing reflects the predominant nature of the equations in the limit of Reynolds number  $Re \rightarrow \infty$  (hyperbolic) and  $Re \rightarrow 0$  (parabolic) through upwind differencing of the convective and pressure terms and central differencing of the viscous shear stress and heat flux terms. The method is naturally dissipative so that no additional smoothing terms are required and is particularly well-suited for transonic and supersonic flows where strong shock waves are prevalent.

The algorithm is advanced implicitly in time by applying the backward-time Euler integration scheme to the governing equations, linearizing the equations in time, and using the delta form so that the steady-state solution is independent of the time step. Efficient solutions to the systems of equations are obtained at subsonic and transonic speeds through spatially split approximate factorization and at supersonic speeds through a hybrid relaxation/approximate-factorization technique. Extremely efficient solutions to the steady-state equations are obtained with multigrid acceleration.

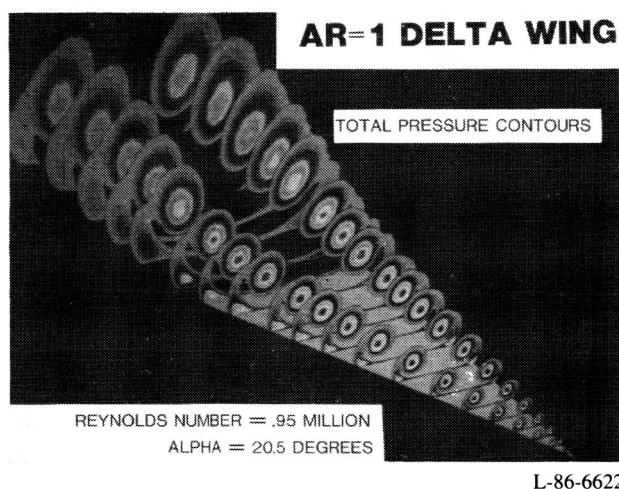
Results from an example computation for the subsonic flow over an aspect ratio  $AR$  equal to one delta wing at an angle of attack  $\alpha$  of  $20.5^\circ$  are shown in the first figure. In this figure, Reynolds number based on length is represented by  $Re_L$ , free-stream Mach number by  $M_\infty$ , lift coefficient by  $C_L$ , and trailing-edge



Lift versus angle of attack of highly swept delta wing.

flap angle by  $\delta$ . The total pressure contours (shown in the second figure) indicate the primary vortex, which is shed from the leading edge, and the secondary vortices (underneath the primary) which are induced by boundary-layer crossflow separation. The computation of lift versus angle of attack shows good agreement with experimental data and includes the prediction of maximum lift associated with the onset of vortex breakdown.

(J. L. Thomas, 4646)



Total pressure contours for highly swept delta wing.

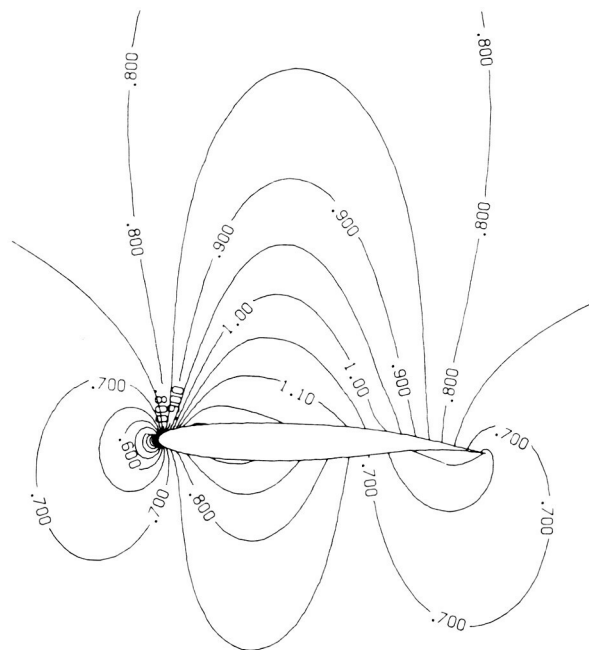
## Application of Spectral Multigrid Methods to Engineering Calculations

The high-order error decay rate that is associated with spectral methods can be used to an advantage in multidimensional engineering calculations by reducing the rapid growth in the number of points required by even modest increases in accuracy. To realize this advantage, however, efficient solution techniques must be devised to solve the equations that result from spectral discretization; these equations tend to be far more difficult to solve than the corresponding finite-difference equations. A number of techniques have been applied to spectral methods with considerable success. One such method involves preconditioning the spectral equations with a solution to the corresponding finite-difference equations and computing, at each step, the iteration parameters that yield fastest convergence. Preconditioning is a classical technique in which an algebraic system,

which is to be solved iteratively, is modified by the inverse matrix of a related system which is easier to solve. This preconditioning clusters the eigenvalues of the system and results in faster convergence. Another powerful technique that has been employed is the well-known multigrid method. In this method, convergence is accelerated by taking advantage of the characteristic that is inherent in most relaxation schemes: convergence is rapid for short-wavelength error components, but it is slow for long-wavelength components. Relaxation solutions of related equations (written on a sequence of progressively coarser grids) are used to remove the entire error spectrum because a long-wavelength error on a fine grid appears as a short-wavelength error on a coarse grid.

An example of a solution that is produced by a spectral multigrid technique is shown in the figure, which illustrates the Mach number contours about a transonic shock-free airfoil. Simulation of shock-free transonic flow presents a severe test of the accuracy of a method. Low-accuracy flow field solutions often bear little resemblance to the true solution because nearly sonic flow is extremely sensitive to small area changes in the stream tubes. The equations produced by the spectral discretization of the potential equation could not be solved for this example by any other iterative method than the multigrid method.

(C. L. Streett, 2627)



Mach contours about a shock-free transonic airfoil.

## Three-Dimensional Transonic Viscous-Inviscid Interaction Program

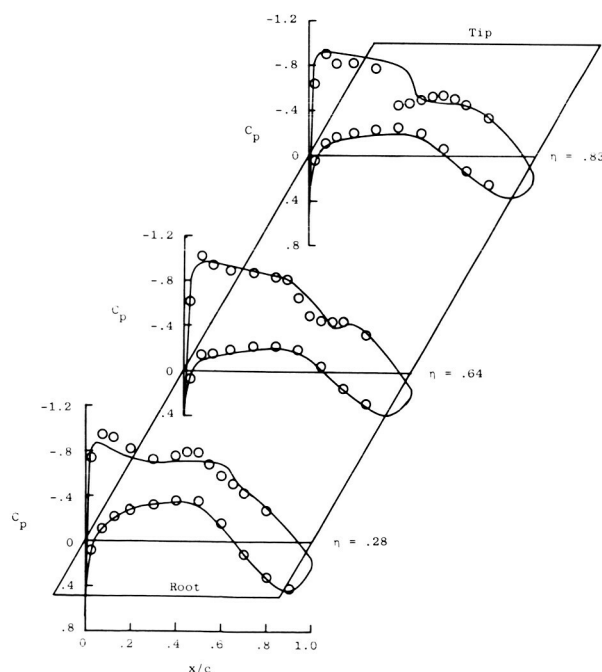
Over the past 5 years, the computer code TAWFIVE (Transonic Analysis of a Wing and Fuselage with Interacted Viscous Effects) has been under development at NASA Langley. The program was developed to accurately predict the transonic flow about wing-body configurations. In TAWFIVE, the conservative full-potential equation is used to model the outer inviscid portion of the flow field on a boundary-fitted grid. A three-dimensional integral boundary-layer method is used to model the inner viscous region of the flow field. Wake curvature and displacement thickness effects are also included.

The TAWFIVE code has recently been modified in an effort to significantly decrease its computation time and to add several new capabilities. Originally, TAWFIVE used a relaxation scheme to solve the outer inviscid portion of the flow. To accelerate convergence, the multigrid method has been incorporated. This method reduces total run times by at least 50 percent. Some improvements in the grid have also been made, and user input to the program has been reduced. Also, the capabilities to allow the wing lift level to be specified

and the angle of attack to be a result of the calculation have been added.

As a sample of the capability of TAWFIVE, results from a TAWFIVE calculation for the *Pathfinder I* configuration are compared with experimental data from the National Transonic Facility. The flow conditions are  $M_\infty = 0.82$ ,  $\alpha = 1.93^\circ$ , and a Reynolds number  $R_e$  of  $17 \times 10^6$  based on mean chord. The figure shows good agreement for pressure coefficient  $C_p$  versus chord fraction  $x/c$  at three span function  $\eta$  locations.

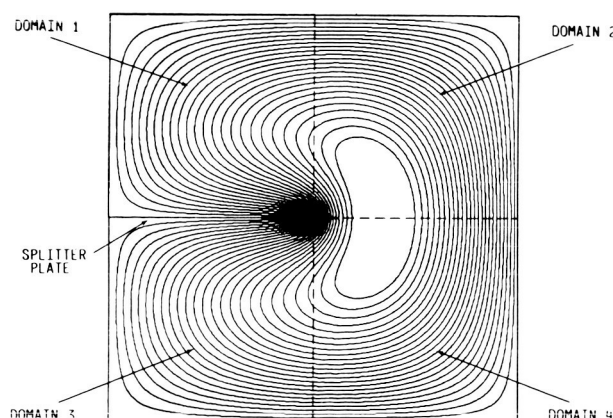
(N. D. Melson, 2627)



Comparison of computational and experimental pressures for the *Pathfinder I* at  $M_\infty = 0.82$ ,  $\alpha = 1.93^\circ$ ,  $R_e = 17 \times 10^6$ .

## Multiple-Domain Extension to Spectral Collocation Methods

Spectral collocation methods have proved to be efficient discretization schemes for many aerodynamic and fluid mechanic problems. The high-order accuracy shown by these methods allows either engineering-accuracy solutions on coarse meshes or, alternatively, very accurate solutions that are essential for fluid mechanic simulations. One drawback to spectral collocation has been the requirement that a complicated physical domain must be mapped onto a simple computational domain via a high-order mapping if the spectral advantages are to be preserved. Additionally, problems with discontinuous boundary conditions cannot be treated with conventional spectral methods. Such restrictions are over-



Solution to Laplace's equation on splitter plate geometry.

come by splitting the domain into regions; adjoining regions are interfaced by enforcing a global flux balance that preserves the high-order continuity of the solution.

This multidomain method has proved to be effective on a wide range of test problems, which include resolution of a singular perturbation problem with spatial scales different by 5 orders of magnitude, and an elliptic equation in generalized nonorthogonal curvilinear coordinates. The figure shows the solution isolines for Laplace's equation in a region that contains a line of fixed conditions within the domain. This discretization will be used in the simulation of transition in the shear layer behind the trailing edge of a splitter plate.

(C. L. Streett, 2627)

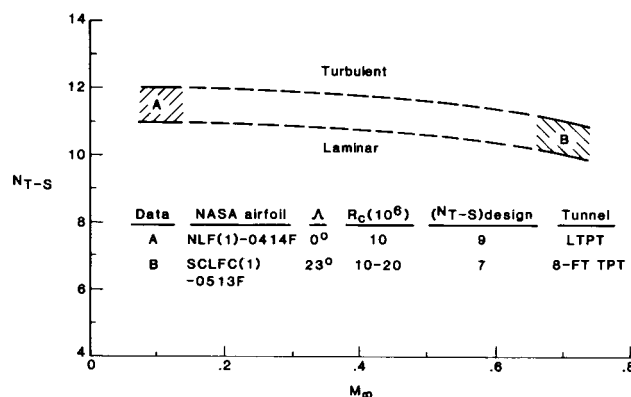
## Experimental Validation of Stability Theory for Airfoils

Recent natural laminar-flow (NLF) and laminar-flow control (LFC) airfoil design concepts have included the application of linear, incompressible stability theory for determining the growth of disturbance amplitudes (A) in laminar boundary layers relative to their values at the neutral stability point ( $A_0$ ). The natural logarithm of this ratio ( $\ln A/A_0$ ) is termed the amplification, or *N*-factor. When this quantity reaches a value on the order of 10, the consensus of opinion is that transition can be expected to occur. Thus, a goal is to validate the use of linear stability theory for airfoil designs, whose performance has been measured in wind tunnels with known excellent flow quality over a chord Reynolds number ( $R_c$ ) range.

The figure is a summary of *N*-factors at transition for two airfoils based on a Tollmien-Schlichting (T-S) type disturbance that dominates the transition process. Both airfoils were originally designed using the incompressible SALLY and MARIA linear stability codes and design *N*-factor limit. The measured surface pressure distribution for the unswept NLF(1)-0414F airfoil and the pressure and suction distributions on the upper surface for the SC LFC(1)-0513F airfoil with sweep ( $\Lambda$ ) were input into the codes to calculate local disturbance growth rates and integrated amplification ratios (*N*-factors). Transition locations, obtained from flush-mounted surface thin-film gauges, were compared with the calculated T-S disturbance amplification ratios to arrive at transition *N*-factors. The results show that T-S transition *N*-factors consistently fall within the range of 10 to 12

in agreement with or exceeding previous studies in wind tunnels. This is the first opportunity in which all pertinent experimental data were available for advanced theory correlation on modern swept and unswept airfoils with and without suction over the indicated speed range. The consistency of the correlation validates the use of incompressible linear stability theory as a conservative design tool. Analysis of these data bases will continue (using a compressible version of the linear stability code called COSAL) in order to extend the correlation to include transonic speeds and the effects of compressibility.

(W. D. Harvey, 2631)



Experimental disturbance amplification ratios.

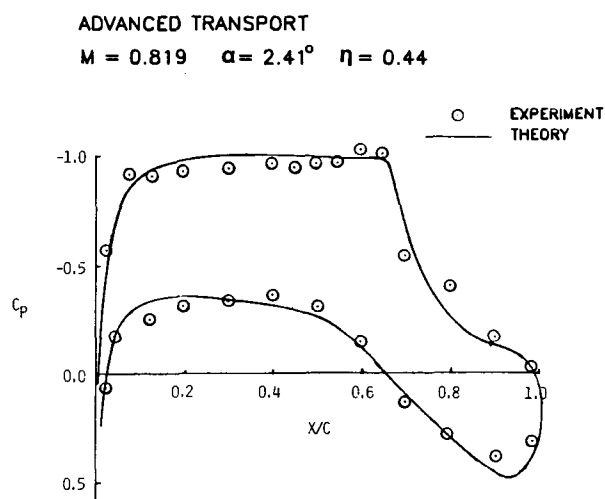
## Euler Code With Interacted Viscous Effects

An Euler code coupled with a boundary-layer solver has been developed by Keith Koenig, Mississippi State University, under contract to NASA. The code solves for the viscous flow field around a wing/fuselage combination. The finite-volume Euler solver uses flux-vector splitting of the governing equations and solves the discretized split equations with an implicit, upwind, second-order predictor-corrector scheme. The viscous solver is an inverse integral technique that has analytical expressions for the velocity profiles which are valid for attached and separated turbulent boundary layers. The code is structured such that results can be obtained to

engineering accuracy on the Control Data Corporation's VPS-32 computer in a DEBUG category run.

Results are presented for an advanced transport configuration at  $\alpha = 2.41^\circ$ ,  $M = 0.819$ , and  $R_e = 5.9 \times 10^6$  and compared with experimental pressure coefficients at a midspan location on the wing. The computations were performed on a medium density C-H-shaped mesh ( $97 \times 17 \times 17$ ). Comparisons of computed and experimental results on other configurations (including *Pathfinder I*) have also been made and are good. Plans are under way to apply the code to lower-aspect-ratio fighter-type configurations to further validate its capability.

(E. G. Waggoner, 2601)



*Euler calculation with interacted viscous effects.*

## EA-6B Maneuver Improvement Design

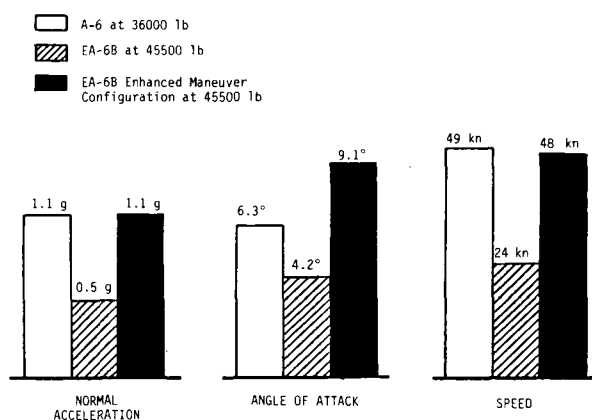
Aircraft modifications have been identified and developed which are projected to significantly improve the EA-6B defensive maneuvering capability and improve the basic airplane stall margins. The EA-6B has basically the same wing planform and contour as the A-6 airplane; however, the EA-6B weighs nominally 9000 lb more than the A-6. This results in significant reductions in maneuver margins, as shown in the figure.

One objective of the joint Navy/Grumman ADCAP (Advanced Capability) Program for the EA-6B is to

increase maneuver performance, particularly at low speeds, while maintaining high-speed cruise performance. This objective has been addressed in a complementary computational/experimental design and validation study. State-of-the-art low-speed and transonic two- and three-dimensional techniques were used to design modifications to the wing leading-edge slat and trailing-edge flap. Modifications were defined which yielded a predicted 14-percent increase in low-speed maximum lift coefficient with only a minimum increase in computed wave drag at high-speed conditions. The modified airfoils were characterized by a blunter, slightly drooped, leading-edge slat and trailing-edge flap with a relatively thick trailing edge.

Experimental testing verified the predictions. Test results showed maximum usable lift coefficients were improved nominally 15 percent across the aircraft's operational speed regime. Drag data at  $M = 0.80$  showed a decrease in drag at lift coefficients above 0.30 with a maximum drag increment of 10 counts at 0.10 lift coefficient (sea-level high-speed dash). These improvements in terms of cruise maneuver margins are included with baseline A-6 and EA-6B data in the figure. The data show the experimental/computational study provided required performance improvements to significantly expand the operational capability of the EA-6B aircraft.

(E. G. Waggoner, 2601)

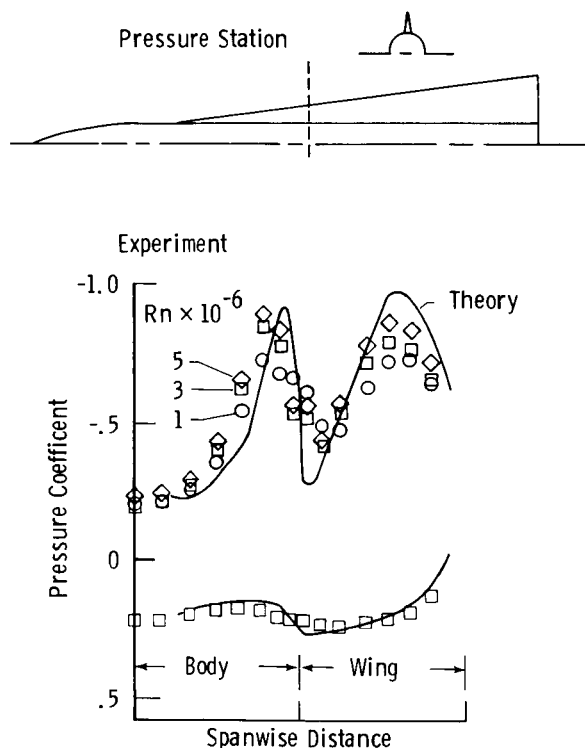


*Margin to stall for a 60° banked-turn maneuver at 250 kn.*

## Aerodynamic Loads for Slender-Wing/Body Configurations

Low-aspect-ratio wings are desirable for vehicles that require supersonic or hypersonic capability, such as advanced fighter configurations, missiles, or the proposed Aero-Space Plane. Due to their slender nature, these configurations exhibit substantial wing/body interference. In addition, separation-induced vortex flows naturally occur at moderate-to-high angles of attack and are dominant at conditions required for takeoff, landing, and maneuver. One theory that accounts for this flow, the free-vortex-sheet, has recently provided successful estimates, which include vortex-induced effects, of the surface load distributions for a slender configuration. Results from this theory are fully three dimensional and represent an inviscid "upper bound," which data tend to approach but not surpass as Reynolds number is increased.

A typical solution from the free-vortex-sheet theory is compared with experimental results in the figure for a slender-wing/body configuration at an angle of attack of  $20^\circ$  and a free-stream Mach number of 0.5. The results are presented at a longitudinal station in which



Surface pressure correlation.

the body radius is approximately one-half of the configuration semispan. Both theory and experiment show a double suction peak on the upper surface. The maximum pressure coefficient between these two peaks occurs at the wing/body juncture. The outboard suction peak occurs on the wing and is typical of leading-edge vortex flow; the inboard peak occurs on the fuselage and, for the theory, is solely due to induced effects of the wing primary vortex on the body.

The data, which are shown on the upper surface for three Reynolds numbers, approach the (inviscid) theory as the Reynolds number is increased. The correlation between theory and experiment is good on both the upper and lower surfaces. Similar correlations were achieved at other longitudinal stations. The experimental Reynolds number effects shown are significant, and, in this sense, the inviscid free-vortex-sheet theory may provide useful estimates of the full-scale flow that occurs at significantly higher Reynolds numbers than those shown.

(J. M. Luckring, 2601)

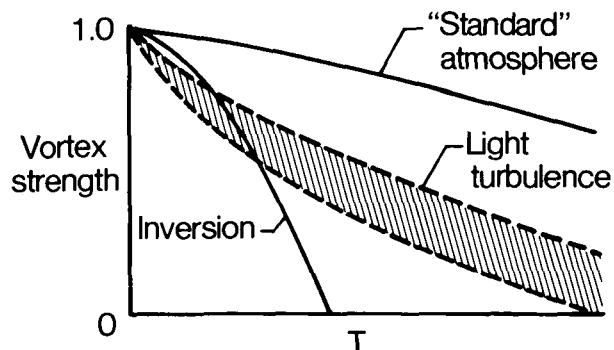
## Aircraft Wake Decay in the Atmosphere

The aircraft trailing-wake hazard is currently the limiting factor in safely reducing aircraft spacing in the terminal area and may limit the application of new technologies for increasing airport capacity. Although wake decay in the atmosphere is observed to be highly variable, current aircraft spacing is based on maximum wake lifetimes and therefore may be conservative most of the time. A research effort has been initiated to determine if the observed variability could be modeled to identify atmospheric conditions in which aircraft spacing could be safely reduced.

An approximate wake decay model, which includes the effects of stable density stratification (resulting from nonadiabatic vertical temperature profiles) and atmospheric turbulence, has been developed at NASA Langley. The effects of stable stratification and turbulence on wake decay are shown in the figure. The solid lines correspond to vortex decay in the absence of atmospheric turbulence for vertical density variation corresponding to the standard atmosphere and stably stratified conditions associated with a typical temperature inversion. The shaded region represents the standard atmosphere with the addition of light atmospheric turbulence. Since atmospheric conditions may change rapidly during the day, wake lifetimes will vary considerably. By

monitoring the atmosphere, one can predict when the wake hazard will be especially persistent or decay rapidly.

(G. C. Greene, 2961)



*Vortex decay characteristics.*

## F-16XL Vortex Flap Development

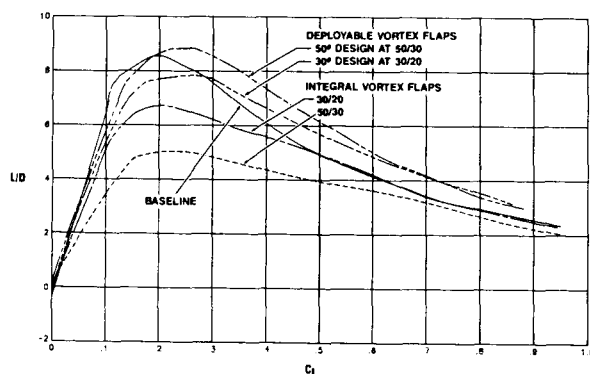
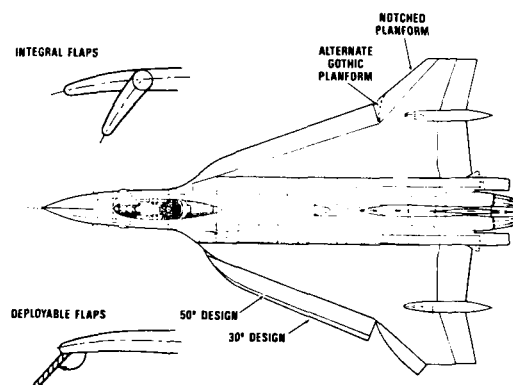
Vortex flaps are deflectable leading-edge devices designed to reduce the drag of maneuvering highly swept wings by recovering the leading-edge suction normally lost under those conditions (because of leading-edge flow separation) in the form of a vortex "trapped" above the flap itself. Both deployable and integral vortex flaps have been designed for the cranked and highly cambered wing of the F-16XL fighter aircraft (as shown in the figure). The deployable flap had a sharp leading edge and added planform area to the configuration. The integral flap maintained the baseline F-16XL planform and leading-edge radius when undeflected. The design conditions were a lift coefficient  $C_L = 0.5$  and a Mach number  $M = 0.9$ .

Integral flap deflection caused a nose-down pitching moment, which reduced the flap-derived drag benefit when the configuration was trimmed. Conversely, the nose-up moment generated by the deployable flap improved the flap-derived drag benefit at trimmed conditions. The trimmed performance results for various inboard/outboard flap deflections  $\delta_i/\delta_o$  (measured in

a plane normal to the flap hinge) at a Mach number of 0.9 are shown in the figure. Planform area effects have been removed from these data. While the deployable flaps provided a large performance improvement relative to the baseline, the improvements provided by the integral flaps at  $M = 0.6$  (not shown) degraded the performance at transonic speeds.

Upper-surface pressure and oil-flow data suggest that the compromised performance of the integral vortex flaps was largely due to upper-surface flow separation that occurred at the vortex flap hingeline. Possible causes of separation include hingeline surface curvature and the flap camber and leading-edge radii. Further wind tunnel testing will be required to develop improved integral flap geometries.

(W. E. Schoonover, Jr., 2601)



*Effects of deployable and integral vortex flaps.*

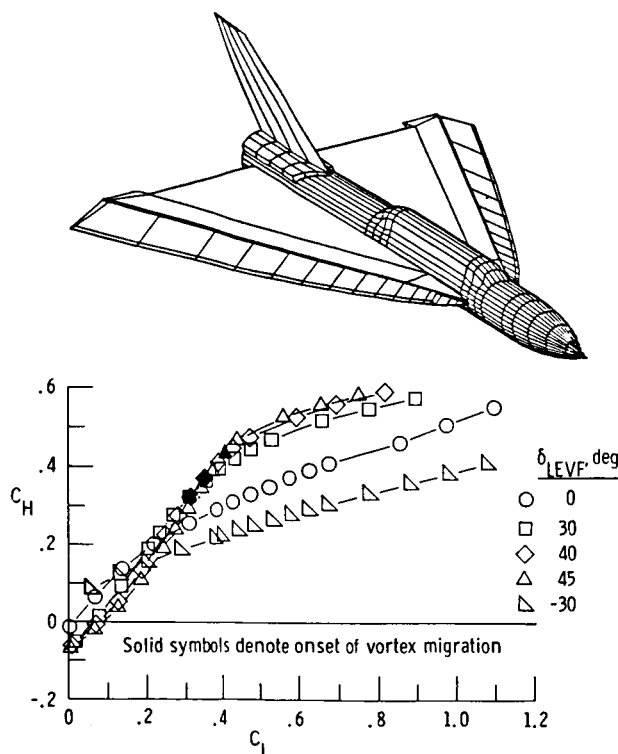


## Vortex Flap Hinge Moments

Vortex flap technology has matured to the point that aircraft companies are conducting system studies to consider how these flaps might be activated. There has been, however, a serious lack of experimental hinge-moment measurements from which to base load estimates for support and actuation. A wind tunnel experiment was conducted with the purpose of generating a triadic data base that consists of longitudinal aerodynamics, surface pressures, and vortex flap hinge moments on a common model. The model, illustrated by a wire-frame sketch in the figure, represents a slender-wing/body configuration with a curved leading-edge vortex flap, which is deflectable about a  $74^\circ$  swept hinge line. The test was conducted at a Mach number of 0.4 and Reynolds number of 5.41 million.

Total vortex flap hinge moments were measured directly by instrumenting two of the ten fixed mounting brackets with strain-gauge bridges. Installation was such that the flap was metrically isolated from the wing and

connected only by the fixed brackets. The figure illustrates the level of strain-gauge-measured hinge moments developed at the five flap deflections tested. The break in the slope of the curves for deflections of  $30^\circ$ ,  $40^\circ$ , and  $45^\circ$  is caused by a reduction in flap loads over the aft region. This feature results from a natural tendency for the leading-edge vortex to migrate inboard away from the flap and over the wing as angle of attack or lift coefficient increases. Comparisons of total hinge moment have been made between strain-gauge measured data and selected pressure-integrated values where upper- and lower-surface measurements were available. The two methods are in good qualitative agreement, but hinge moments measured from strain-gauge brackets were generally 18- to 20-percent lower than those determined from integrated surface pressures.  
(N. T. Frink, 2601)



*Strain-gauge-measured vortex flap hinge moments at five flap deflections.*

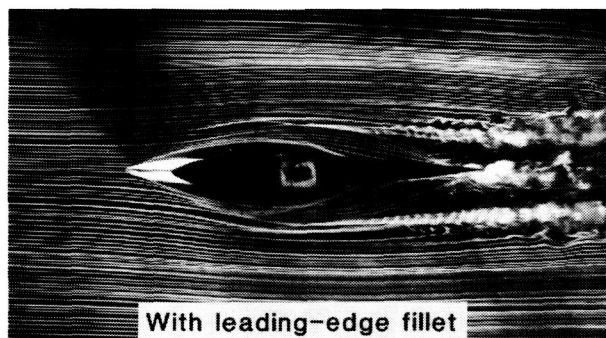
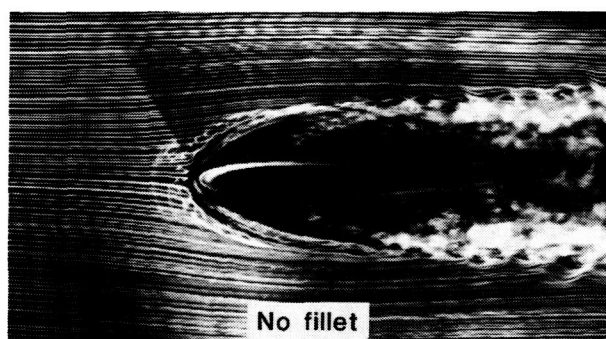
## Flow Visualization Study of Juncture Flow Control

An experiment to evaluate the effectiveness of leading-edge fillets in improving the flow around a wing/fuselage-type juncture was conducted in the 12-Inch by 18-Inch Low-Speed Wind Tunnel at the Langley 8-Foot Transonic Pressure Tunnel complex. The wing/fuselage juncture was simulated by mounting an unswept wing (NACA 0012 cross section) normal to a vertical splitter plate (fuselage). A nominal flow speed of 18 ft/sec (corresponding to a chord Reynolds number of 60,000) was used. The smoke-wire technique was used for visualizing the juncture flow field.

Sample pictures of flow around the basic juncture and the filleted juncture are presented in the figure. In both cases, the flow visualization plane is located near the plate at a distance that corresponds to six-tenths of the plate boundary-layer thickness. In the no-fillet case, the streamwise flow on the plate separates ahead of the wing leading edge, and this results in a horseshoe-type vortex system around the juncture. In the case of the filleted juncture, there is considerable reduction in the juncture vortical flow, and the juncture wake near the wing trailing edge is narrower. In this configuration, the flow in the juncture has remained mostly laminar. Other results indicate that, even at farther distances from the plate, the flow in the filleted juncture is better behaved and that longer fillets (more slender leading edge near the root) result in better performance.

At an angle of attack of  $0^\circ$ , the use of a leading-edge fillet considerably improves the flow around the wing juncture and in the wake. This improvement is significant because the use of these fillets can result in better cruise performance where relatively low incidence is encountered. The results are also applicable to wind tunnel testing of two-dimensional airfoils at low angles of attack.

(W. D. Harvey, 2631)



*Effect of fillets on juncture flow.*

## Holocinematographic Velocimeter for Studying Complex Flows

A technique has been developed to examine complex three-dimensional turbulent flows. This approach, which is called holocinematographic velocimetry (HCV), uses dual-view holographic movies to track the movement of small tracer particles in a flow. This is the first technique to be developed which is capable of

obtaining the full three-dimensional and time information needed to completely examine complex turbulent flows and to check numerical turbulent simulations.

The present HCV system is a small-scale, low-speed version of a future, larger scale facility. A new type of water tunnel, which provides several seconds of high-quality steady flow, was developed and built to be used in conjunction with the HCV. This prototype system was used to examine a well-known flow: the Kármán vortex street behind a circular cylinder. Holographic movies of the flow field were made at a flow speed of 0.1 ft per second and a movie rate of 15 frames per second. The reconstructed holograms produced high-quality images of the tracer particles, and the data reduction system developed the time histories of the particle coordinates. The prototype system was used to verify the laser and film components in an actual flow situation. This successful proof-of-concept test has demonstrated that the technique can provide complete three-dimensional turbulence data in complex flow fields. A full-scale version of this technique is currently under design.

(L. Weinstein, 4546)

## Transition Detection System for Cryogenic Wind Tunnels

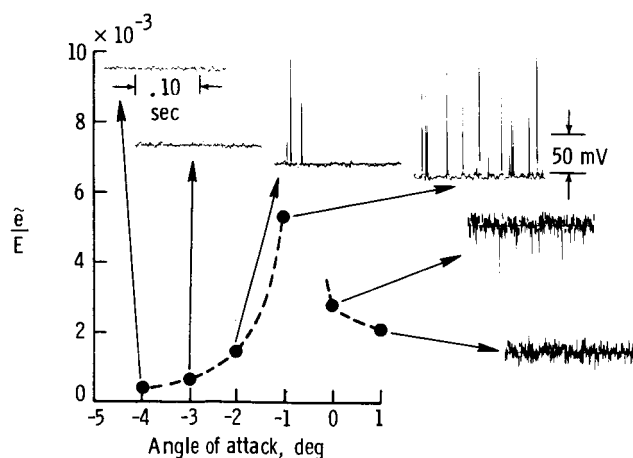
The ability to detect boundary-layer transition on models in the National Transonic Facility (NTF) has been a prime user requirement since the inception of this unique facility. In the past, hot-film gauges (hot films) have proved to be one of the best devices to obtain the beginning and end of boundary-layer transition on models in conventional wind tunnels. Because of the wide range of temperatures and the high Reynolds numbers encountered in the NTF, however, the conventional hot films would be unsuitable for use in the NTF and, in fact, would induce boundary-layer transition. A new hot-film system, which uses a vapor deposition process, was developed by the Douglas Aircraft Company as a potential method to obtain boundary-layer transition in high-Reynolds-number cryogenic tunnels.

The Douglas Aircraft Company hot-film technique was used to instrument the upper surface of a supercritical airfoil (NASA SC(3)-0712) with 38 hot films. This model was used in a transition detection study in the Langley 0.3-Meter Transonic Cryogenic Tunnel (0.3-m

TCT) at Mach numbers from 0.3 to 0.6 and chord Reynolds numbers from 3.0 to 10.5 million. The hot films were successfully operated at 360°R and at a cryogenic temperature of 169°R. The figure shows the normalized root mean square (rms) voltage ( $\bar{e}$  is rms voltage and  $E$  is mean voltage from the hot-film anemometer) output from a hot film at 48 percent of chord versus angle of attack for a Mach number of 0.3 and a chord Reynolds number of 3.0 million. Each normalized rms voltage data point has the corresponding voltage-versus-time trace. Voltages indicated that the boundary layers were (1) laminar at angles of attack of  $-4^\circ$  and  $-3^\circ$ , (2) transitional at an angle of attack of  $-1.0^\circ$ , and (3) fully turbulent at an angle of attack of  $+1.0^\circ$ . The transition data obtained from these tests are the first data of this type to be obtained in a cryogenic tunnel.

Since these tests, NASA Langley has been developing the capability to install a similar-but-improved type of hot-film system for transition detection on large wings (about a 4-ft span) for models to be tested in the NTF. Significant technology improvements have been made in the hot-film application process, and components of the hot films have been successfully tested in the NTF at ambient and cryogenic conditions. In addition, two types of data acquisition systems are being developed for an on-line boundary-layer transition detection capability in the NTF.

(C. B. Johnson, 4380)



Variation in hot-film fluctuating voltage output with angle of attack.

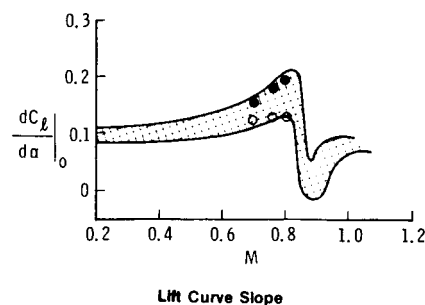
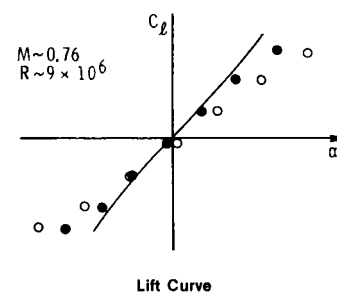
## Transonic Wind Tunnel Wall Interference Assessment/Correction (WIAC) Procedure

For transonic flow conditions in ventilated-wall tunnels, classical linear-theory wall interference predictions are known to be unsatisfactory. Using concepts and capabilities from both adaptive-wall and computational transonic technologies, posttest WIAC procedures have been formulated which circumvent many shortcomings of the classical theory. Both two- and three-dimensional codes have been developed and tested using computer-simulated wind tunnel flow data and limited experimental data.

The WIAC procedure developed for the Langley 0.3-Meter Transonic Cryogenic Tunnel (0.3-m TCT) uses Kemp's TWINTN4 code, which takes into account sidewall boundary-layer effects using the Barnwell-Sewall concept and customary top and bottom wall effects. The TWINTN4 code uses measured pressure data

NACA 0012

Published Experimental Data  
 ○ Uncorrected Data  
 ● WIAC Corrected  
 — Free-Air Calculation  
 } 0.3m TCT



Transonic four-wall correction of airfoil lift data.

along top and bottom tunnel walls and on the model; thus, classical homogeneous-wall boundary conditions are not used. Corrections are obtained as shifts in the tunnel (measured) Mach number and angle of attack; validation of this procedure has been accomplished using data from five airfoil tests in the 0.3-m TCT.

Since many transonic airfoil tunnels are designed at near-minimum blockage using classical theory, the corrections may be relatively small for Mach number but not for angle of attack. The figure shows the influence of this latter correction on the lift curve and lift curve slope (at zero lift) for an NACA 0012 airfoil. The band of published experimental data for the lift curve slope is from numerous facilities; the data spread is about 40 percent at  $M = 0.8$ . It appears that much of this spread may be due to improperly accounting for wind tunnel wall interference.

(C. R. Gumbert, 2627)

increase in spin resistance beyond that of current configurations; and (3) incorporation of a wing leading-edge modification can provide sufficient spin resistance to meet the criteria.

(H. P. Stough, III, 3274)



L-83-6,174

## Development of Spin Resistance Criteria for Light General-Aviation Airplanes

Research conducted during the last several years has identified promising means to improve the spin resistance of light airplanes. In order to manufacture and certify such airplanes, a standard is needed to describe the desirable traits of a spin-resistant airplane and to provide a measure by which the airplane can be evaluated. Using results from the NASA Stall-Spin Research Program, researchers at NASA Langley have assisted the General-Aviation Manufacturers Association (GAMA) in the development of criteria for spin-resistant airplanes. GAMA has proposed these criteria to the FAA as an alternative to existing standards for light-airplane certification.

To provide additional data for evaluation of the criteria during the rule-making process, NASA Langley tested a representative four-place, single-engine light airplane against the criteria. Both a baseline wing configuration and a modified wing leading-edge configuration for enhanced spin resistance were tested. The baseline configuration failed 22 percent of the criteria stall tests and 67 percent of the spin tests. The modified leading-edge configuration passed all of the tests.

These tests showed: (1) the criteria are not overly restrictive, i.e., a practical airplane can be designed to meet the criteria; (2) the criteria require a significant

*Spin resistance research aircraft with modified leading edge.*

## Rotor Inflow

The first phase of an experimental program to conduct detailed measurements of the inflow and wake velocities of a rotor in forward flight has been completed in the Langley 4- by 7-Meter Tunnel. The program is aimed at providing a complete data base of rotor flow field velocities for use in evaluating current and developing computational methods for rotor performance computation. New, emerging, higher order computational methods for predicting rotor aerodynamics, acoustics, and vibration characteristics require high-fidelity loads information that is not provided by existing simplified inflow models. More comprehensive information is needed on the details of the precise nature of rotor inflow in order that better mathematical models of the flow may be constructed.

The 5.42-ft-diameter model rotor used for the tests was fully articulated, had four tapered blades, and was mounted on a representative advanced-configuration fuselage. The figure shows the model mounted for testing in the tunnel. Velocity measurements perpendicular and parallel to the free stream were acquired with a two-component laser velocimeter (LV) system, which is also shown in the figure. For this phase, measurements were made in a plane that was one blade-chord above the rotor tip path plane over the entire rotor disc. The velocity measurements were synchronized with rotor azimuthal position and were taken at selected radial stations from 40 percent to 110 percent of the rotor radius in 30° increments around the rotor. A preliminary comparison of the measured wake velocities with predictions based on an existing free-wake analysis shows generally good correlation for the condition tested, and analysis of the data is continuing.

This is believed to be the first comprehensive measurement designed specifically to examine the inflow for the complete rotor disc. The real payoff of a detailed data base of rotor inflow and wake measurements will be the ability to evaluate predictions of the helicopter total flow field environment during vehicle design. Confidence in advanced computational tools will reduce the risk of new and innovative designs.

(J. W. Elliott, 3611)



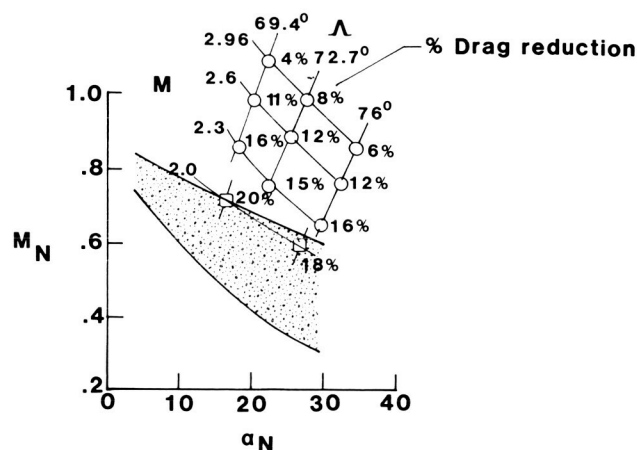
L-86-2666

*Test setup for laser velocimeter measurements above a rotor tip plane.*

## Extension and Evaluation of Supersonic Wing Design-Space Concept

A NASA Langley technique to select a design space for efficient supersonic wings has been expanded to include wings with thickness and camber and has been substantiated with experimental data. The original design-space formulation was based on experimental upper-surface and lower-surface normal-force characteristics for flat, uncambered delta wings. It has since been shown that these general characteristics, and thus the design-space concept, are valid for various thickness distributions and for various amounts of leading-edge camber.

The original design-space formulation was also based on the assumption that the combination of Mach number and leading-edge-sweep angle, which would produce an equal division of flat-wing normal force between the upper and lower surface, would be the proper combination to give the best cambered-wing performance. This assumption has now been substantiated with experimental data, as illustrated by the correlation between wing performance data and the design space shown in the figure. For a lift coefficient of 0.2, the



*Drag reduction related to design space.*

design space is shown as the shaded region in terms of conditions normal to the wing leading edge, specifically normal Mach number ( $M_N$ ) and normal angle of attack ( $\alpha_N$ ). Cambered-wing performance at Mach numbers from 2.0 to 2.96 is shown for two sets of wings having leading-edge-sweep angles that range from 69.4° to 76°.



Wing performance is presented as a percent drag reduction with respect to an uncambered wing of the same planform and thickness distribution. It is clearly shown that the data closest to the design space have the best performance.

(D. S. Miller, 4004)

## Pitot Pressure Surveys Over 75° Swept Delta Wing

The validation of computational fluid dynamic methods requires a large amount of detailed flow field data. Investigations are being conducted in the new Basic Aerodynamics Research Tunnel to obtain these flow field quantities. Recently the first phase of an investigation of the flow field about a 75° swept delta wing at  $\alpha = 20.5^\circ$  was completed. This initial phase obtained surface and flow field visualization for Reynolds numbers  $R_N$  from 500,000 to 2,000,000 in increments of 250,000, and detailed pitot pressure surveys were made at five longitudinal stations at Reynolds numbers of 500,000; 1,000,000; and 1,500,000, in both the primary and secondary vortices.

The results indicate that Reynolds number has only a minor effect on the global structure of the flow field in the Reynolds number range that was investigated. The boundary-layer transitions from laminar to turbulent

at the trailing edge of the wing at  $R_N = 1.0 \times 10^6$ , and the transition moves forward to  $x/L = 0.4$  at  $R_N = 2.0 \times 10^6$ . The position of the primary vortex cores is insensitive to Reynolds number in this range; however, the lateral position of the secondary vortex core moves outboard aft of the region where the boundary-layer transitions from laminar to turbulent.

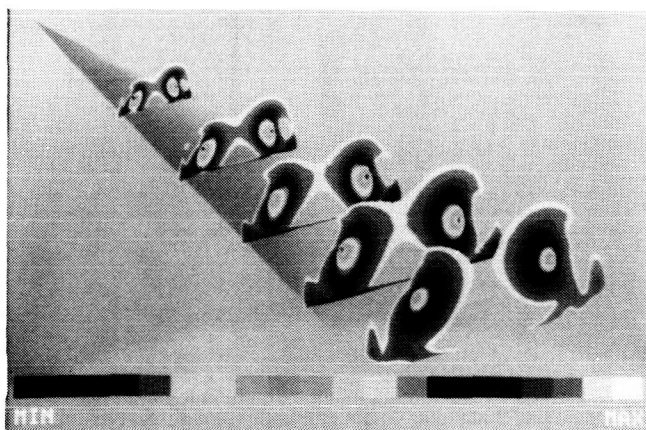
Presented in the figure are the pitot pressure surveys for a Reynolds number of 1,000,000 superimposed with a geometrical representation of the 75° swept delta wing. Each pitot pressure survey contains approximately 3,000 data points. Surveys made in the secondary vortex contain approximately 1,800 data points. The next phase of testing will use a three-component laser velocimeter to obtain detailed velocity information in the flow field.

(S. O. Kjelgaard, 4646)

## Deflectable Forebody Strakes for Increased High-Angle-of-Attack Yaw Control of Generic Research Configuration

A primary factor that limits the high-angle-of-attack maneuverability of current fighter aircraft is the degradation of rudder yaw control as wing stall develops. One promising means to improve high-angle-of-attack yaw control is designed to take advantage of the strong vortex flow field and the favorable moment arm provided by a fighter aircraft forebody. Conformally stored strakes, when deployed, force asymmetric vortex shedding from the forebody, thereby generating a controlled yawing moment. As part of an ongoing investigation of this concept, tests were conducted in the Langley 12-Foot Low-Speed Tunnel using the generic fighter model shown in the figure.

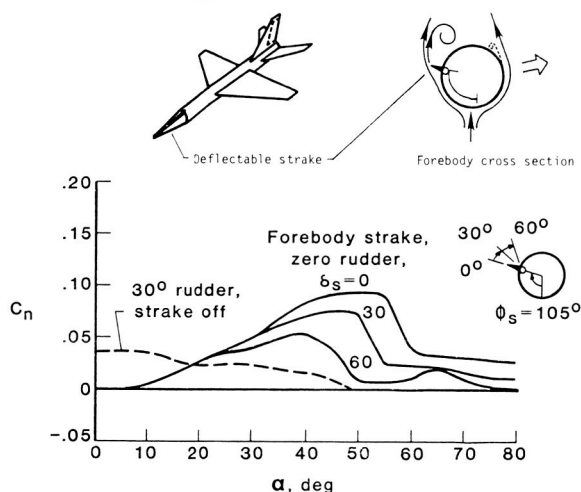
The model included a conically shaped forebody, in which thin tapered aluminum strakes (chord = 0.3 local forebody radius) were tested at a variety of radial locations and strake deflection angles. The data shown in the figure were measured with a single strake located at a radial location ( $\phi$ ) of  $105^\circ$  from the bottom of the forebody. This concept allowed conformal strakes, which could be deployed singly to produce the direction and level of yaw control desired, to be used on each side of the forebody. The data show that while the conventional rudder begins to lose effectiveness above  $\alpha = 10^\circ$ , the forebody strake increases in effectiveness and provides very large increments in yaw control to



Computer-generated figure showing pitot pressure surveys superimposed on 75° delta wing at angle of attack of  $20.5^\circ$ .

much higher angles of attack. Also, above  $\alpha = 30^\circ$ , the data indicate a controllable variation of yawing moment with strake deflection. In addition to these results, this strake concept was found to be effective over a wide sideslip range and was responsible for only minor control coupling in the pitch and roll axes.

(D. G. Murri, 2184)



*Comparison of yawing moment generated by deflectable forebody strake and conventional rudder.*

## Thrust Reverser Investigation on Jet Transport Model in Ground Effect

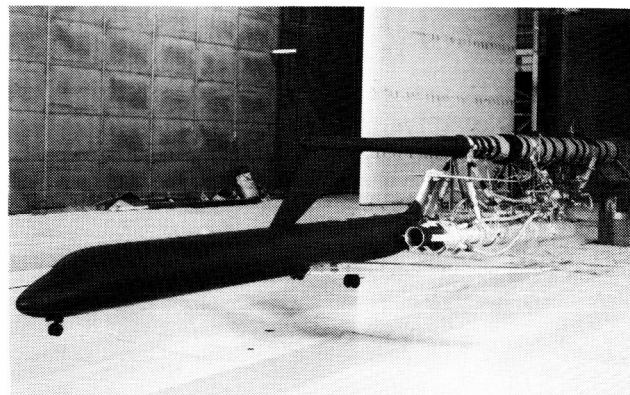
A wind tunnel investigation has been conducted in the Langley 4- by 7-Meter Tunnel to determine the sensitivity of thrust reverser performance to variations in inlet-to-exit mass flow ratio and to obtain a better understanding of the reversed engine flow field through velocity measurements and flow visualization.

A model of a modern jet transport was used in the tests, and three different thrust-reverser designs that represented cascade, target, and four-door configurations were studied. A high-pressure air system was used to simulate the engine exhaust flow and to power an ejector for engine inlet flow. The engine simulators were mounted on a separate support system alongside the airplane model. Separate controls were used for inlet and exhaust flows so that mass-flow ratios could be varied. Force-and-moment data and ground-board pressure data were obtained on the aircraft model. Flow

visualization was performed by using smoke in the wind tunnel free stream, water spray in the reversed engine flow, and a sheet of laser light for illumination.

The ratio of inlet-to-exit mass flow was varied over a wide range of forward speeds, and in all cases the effects of mass-flow ratio on configuration aerodynamics were minor. This result is significant because it shows that effective thrust-reverser research can be conducted on simplified models without the additional expense and complexity of providing for both inlet and exhaust flow simulation. With respect to the effects of forward speed, the cascade configuration was least sensitive to changes in free-stream velocity, while the four-door configuration was the most sensitive. All reverser plumes propagated farther upstream on a fixed ground plane than on a moving-belt ground plane as was expected. Overall aerodynamic characteristics of the airplane, with reversers operating, were highly configuration dependent and were different for each reverser arrangement.

(G. M. Gatlin, 3611)



L-86-5370

*Thrust reverser test apparatus.*

## Three-Dimensional Computation and Validation of Transverse Jet Mixing in Scramjet Combustor Models

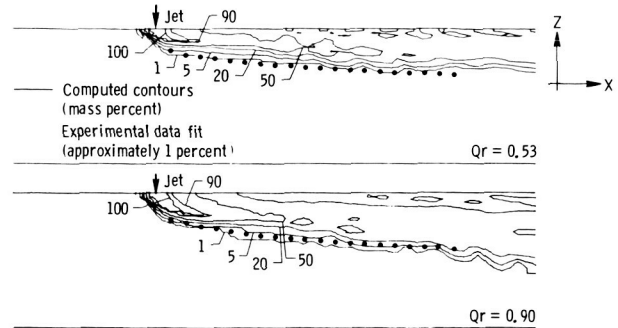
A three-dimensional full-elliptic computer code, which predicts nonreacting binary gas mixing between

a transversely injected gas through orifice injectors and a supersonic airstream in typical scramjet combustor configurations, has been developed and experimentally validated. This is the first such code that can analyze fuel mixing in the near field of orifice injectors of realistic three-dimensional combustor configurations. The accurate prediction of fuel mixing in the near field of fuel injectors is critical in the design of efficient scramjet combustors.

The code was developed by Kenji Uenishi of Vignyan Research based on the fully elliptic Navier-Stokes solver developed by Ajay Kumar at NASA Langley. The laser-induced fluorescence data obtained by J. McDaniel at the University of Virginia were used to validate the code. The first figure shows one of the experimental combustor models and the experimental conditions utilized for the validation study. The second figure is an example of the comparison between the numerical prediction and the experimental data in terms of injected gas penetration in the jet centerline plane for dynamic pressure ratios  $Qr$  of 0.53 and 0.90. In the second figure, the numerical prediction obtained by the code is shown as mass contours for 1, 5, 20, 50, 90, and 100 percent, and the experimental data are for one-percent mass fraction. The comparison of the one-percent mass fraction between the numerical and experimental results is excellent.

This code has been modified to include hydrogen-air combustion for analysis of chemically reacting flow fields in scramjet combustors.

(G. B. Northam, 2803)



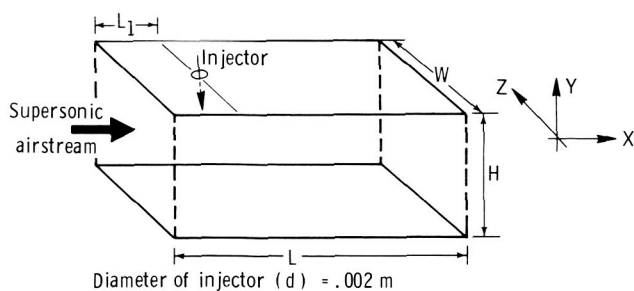
Comparison of jet penetration for constant area duct in jet centerline plane.

## Numerical Simulation of Supersonic Chemically Reacting Mixing Layer

Work is currently under way to achieve a detailed understanding of important phenomena present when a supersonic flow undergoes chemical reaction. To achieve this understanding, detailed physical models of fuel/air mixing and reaction have been developed at NASA Langley, and numerical algorithms have been constructed to solve the governing equations that arise from these models. A computer program employing these physical models and algorithms was then written to consider the multicomponent diffusion and convection of important chemical species, the finite-rate reaction of these species, and the resulting interaction of the chemistry and fluid mechanics.



Water mass fraction in a chemically reacting shear layer.



Diameter of injector ( $d$ ) = .002 m

$H/d = 9$ ,  $L/d = 35$ ,  $L_1/d = 10$ ,  $W/d = 14$

|                        | Injected gas | Main airstream |
|------------------------|--------------|----------------|
| Mach number            | 1.0          | 2.06           |
| Static temperature (K) | 240.0        | 170.0          |
| Static pressure (KPa)  | 81.0 & 137.0 | 36.0           |

Schematic of experimental configuration and data.



The code integrates the governing equations using a partial-implicit finite-difference time-stepping scheme, and either a finite-difference or a hybrid finite-difference Chebyshev spectral discretion to integrate the equations in space. Using this program, the chemically reacting flow field in a nonpremixed supersonic, spatially developing hydrogen/air mixing layer has been calculated. An example of the resulting flow field, given as a picture of the flow at an instant in time, is shown in the figure. The figure shows the distribution of the water mass fraction that results from the chemical reaction of hydrogen and air in the mixing layer. These studies yield an improved understanding of basic combustion phenomena that will ultimately lead to the design of more efficient aircraft propulsion systems. (J. P. Drummond, 3171)

## Cavity Door Effects on Aerodynamic Loads of Stores Separating From Cavities at Supersonic Speeds

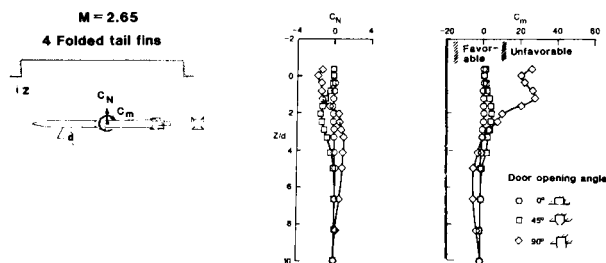
An experimental study has been conducted to investigate the effects of cavity doors on the aerodynamic loads of compact-carriage store configurations that separate from a shallow cavity (closed cavity flow) in a generic parent aircraft at supersonic speeds. Information from this study will help identify internal carriage configurations that facilitate safe launch of stores from supersonic aircraft.

The generic parent aircraft for this study was simulated with a two-dimensional splitter plate that extended from the floor to the ceiling of the low Mach number test section of the Langley Unitary Plan Wind Tunnel. A rectangular box cavity that has a length-to-depth ratio of 14 and a width to accommodate three missiles was located in the plate. The store model consisted of a 1/6-scale model of an advanced compressed carriage missile configuration and was instrumented with a six-component force-and-moment balance. The tunnel model support system was used to remotely vary the model position relative to the cavity. Aerodynamic loads for store configurations (with folded and unfolded tail fins) were measured during separation for a variety of cavity door configurations and door-opening angles at Mach numbers from 1.70 to 2.65. The cavity opening was large enough for the store to pass through for all door-opening angles.

Preliminary results presented in the figure show typical effects of door-opening angle on folded tail-fin

store aerodynamic characteristics (normal force coefficient  $C_N$  and pitching-moment coefficient  $C_M$ ) during separation. These data indicate acceptable store separation characteristics for door-opening angles of 0° and 45° and unfavorable separation characteristics for an opening angle of 90°.

(A. B. Blair, Jr., 4010)



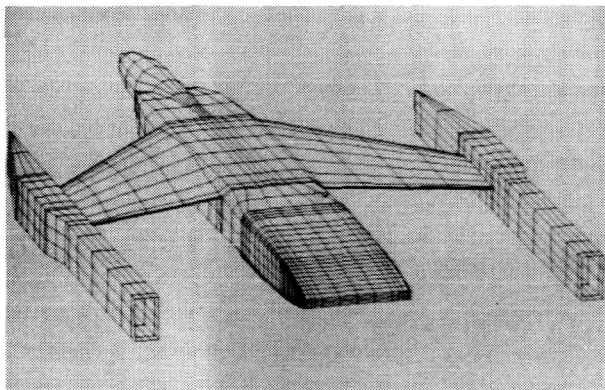
*Effect of door opening angle on store aerodynamic characteristics during separation.*

## Nonaxisymmetric Afterbody Three-Dimensional Flow Analysis

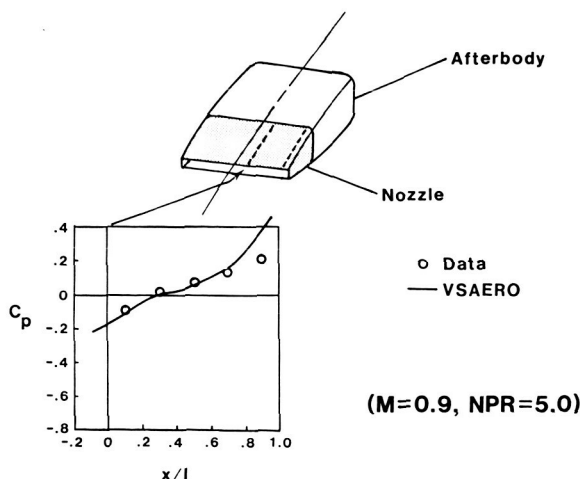
A computer code (VSAERO) was used to analyze the flow about the external surface of a generic twin-engine fighter model with two-dimensional convergent-divergent nozzles installed on the afterbody. The experimental data were obtained from a program that studied the effects of nozzle boattail angle on nozzle/afterbody drag. The experiment was conducted in the Langley 16-Foot Transonic Tunnel. Developed by Analytical Methods, Inc., the code is a surface singularity method that uses quadrilateral panels to represent arbitrary three-dimensional bodies. The method is designed to handle vortex flows and includes the modeling of wing wakes and jet-exhaust wakes. The wake shapes can be fully relaxed from solutions calculated by the code.

Predictions of the flow have been made on the various nozzle geometries studied on this configuration. The calculations were performed using symmetry conditions about the vertical plane. A representative paneling of the wing-tip-supported afterbody model is shown in the figure. A calculation that represents a flat cross-section boattail with a terminal angle of 10° is shown.

Pressure distributions from the near-centerline region on the nozzle-boattail show good agreement with the experimental data. The lack of an accurate exhaust plume model would account for some of the mismatch of the pressure coefficients in the trailing-edge region of the boattail. The ability to predict effects of changing configuration geometries is needed to understand the aerodynamic interactions in modern aircraft nozzle installations. The code is currently being used for further parametric studies of the effects of boattail shaping. (J. R. Carlson, 2673)



Representative paneling of wing-tip-supported afterbody model

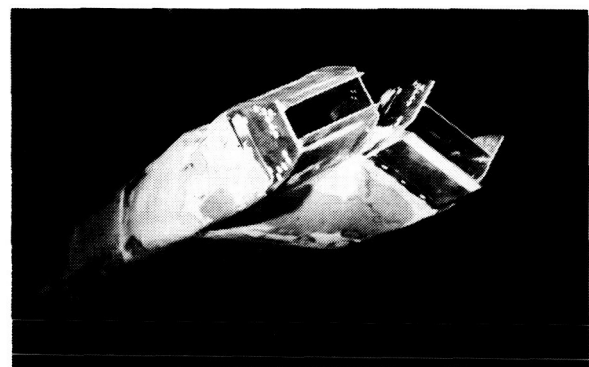


VSAERO pressure coefficient predictions on nozzle boattail compared with experimental data (where  $C_p$  is static pressure coefficient and  $x/l$  is nondimensional length along boattail).

## Thrust Vectoring Control From Canted Nozzles

Modern air combat requires the aircraft to maneuver effectively at high-angle-of-attack conditions. However, the angle-of-attack envelope of current fighters is limited by a combination of degraded stability characteristics and inadequate control effectiveness. One promising means of providing large control moments that are not dependent on angle of attack and dynamic pressures, as are aerodynamic controls, is vectoring the engine exhaust. One concept that can provide control moments in both the pitch and yaw planes is canting the nozzles. With the nozzles canted, pitching moment is obtained by symmetric nozzle pitch vectoring, whereas yawing moment is produced from asymmetric pitch vectoring. To explore the potential of this concept, tests were recently conducted in the Langley 16-Foot Transonic Tunnel on a twin-engine general-research model with two-dimensional convergent-divergent (2-D C-D) nozzles at Mach numbers from 0.20 to 1.20, angles of attack up to  $27^\circ$ , and nozzle pressure ratios up to 7.0. Nozzle cant angle and pitch vector angle were also varied.

The results of this investigation indicate that significant levels of combined pitch and yaw control moments were generated with the canted nozzles. The increment in control moment that resulted from pitch or yaw vectoring remained essentially constant over the entire angle-of-attack range for all Mach numbers tested. Longitudinal and directional control power from thrust vectoring was greater than that provided by aerodynamic control effectors at low speeds or high angles of attack. (F. J. Capone, 2674)



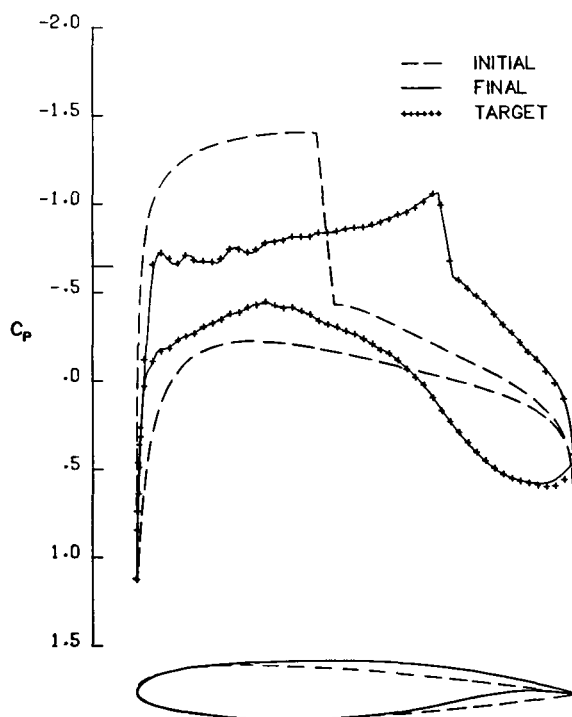
$$\delta_{v,p} = 0^\circ/20^\circ$$

Configuration with nozzles canted  $30^\circ$ .

## Transonic Airfoil Design Procedure

Transonic computational methods have matured to the point that they are being extensively used in the design of new configurations and the modification of existing aircraft. Their role in the design process has generally been to predict the flow field about a given configuration and to give the designer information about how changes affect the aerodynamic characteristics of the aircraft. More recently, automated design methods have been incorporated into some of the codes in an effort to expedite the design process.

A new algorithm at NASA Langley has been developed for use in the design of airfoils or wings that have a specified pressure distribution. This algorithm relates differences between the calculated and target pressure distributions to changes in airfoil surface curvature, then iteratively modifies the initial airfoil to achieve the desired pressures. This method works well for subsonic or transonic conditions because it accurately locates shocks when they are present, allows only a portion of the airfoil to be modified (if desired), and guarantees trailing-edge closure.



Airfoil design code pressure distributions  $C_p$ .

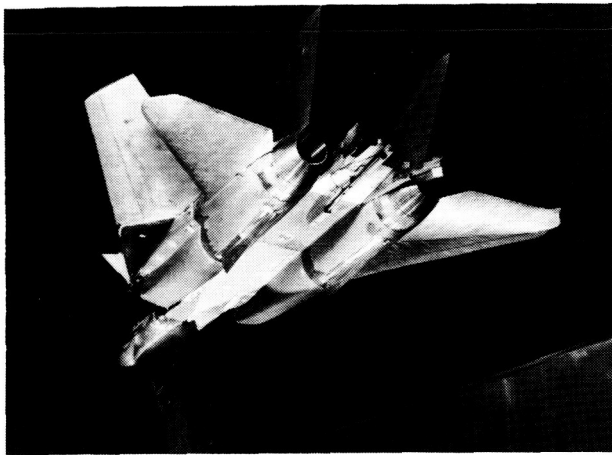
The Garabedian and Korn two-dimensional airfoil code has been modified to include this design procedure, and a number of test cases have been run at subsonic and transonic conditions. Results thus far indicate that the procedure is robust and accurate. An example of these results is shown in the figure. The target pressure coefficients were generated from an analysis run of the code for an existing supercritical-type airfoil at a Mach number of 0.734 and a lift coefficient of 0.60. The code was then run in the design mode using an NACA 0012 as the initial airfoil. At these conditions, both the initial and final pressure distributions show a considerable amount of supercritical flow on the upper surface terminating in a shock. The final pressure distribution for the modified airfoil was very close to the target pressure distribution.

(R. L. Campbell, 2601)

## F-14 Yaw Vane Investigation

Most of today's high-performance fighter aircraft are limited in high-angle-of-attack maneuvering capability because the lateral stability of the configuration deteriorates as a result of the vertical-tail surfaces being washed with low-energy flow from massive areas of separation on the lee side of the body and wings. One of the methods proposed to give these configurations a high-angle-of-attack maneuvering capability is to utilize the propulsion system and to vector the exhaust for powered controls. A proposed vectoring system for an existing aircraft, the Navy-Grumman F-14, is to mount vanes that can be rotated into the exhaust flow on the aircraft afterbody (as shown in the first figure). These vanes not only vector the exhaust but also produce yawing moment and side force.

The yaw vane concept was investigated on a 1/12-scale propulsion model of the F-14 in the Langley 16-Foot Transonic Tunnel at Mach numbers from 0.7 to 1.25. Presented in the second figure are lateral results for the basic F-14 afterbody and afterbody with yaw vanes that were installed at deflections of  $0^\circ$ ,  $10^\circ$ , and  $20^\circ$  at  $M = 0.7$  and at an angle of attack equal to  $4.3^\circ$  with the F110-GE400 maximum afterburning nozzles installed. The yaw vane deflection has only a small (but desirable) effect on rolling moment ( $C_l$ ), but significant effects (as desired) on both yawing moment ( $C_n$ ) and side force ( $C_y$ ). Both the yawing moments and side forces produced by the vane at  $10^\circ$  and  $20^\circ$  yaw angle



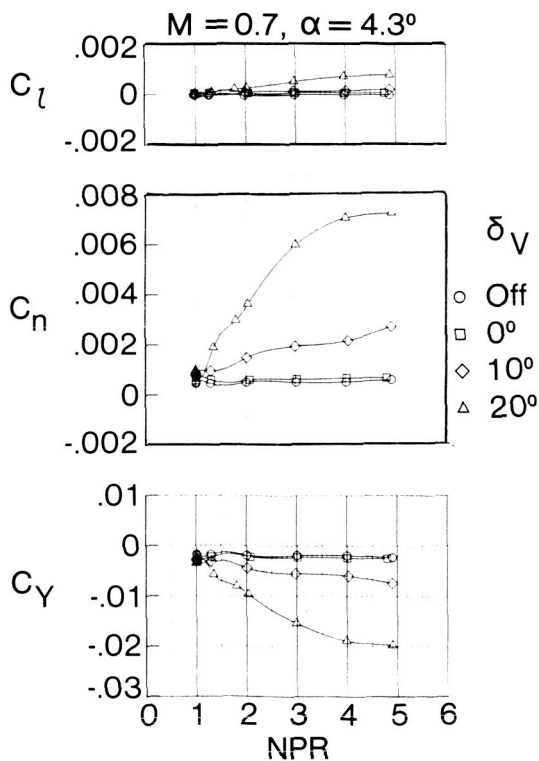
L-85-4243

at a nozzle pressure ratio (NPR) of 4 are roughly equivalent to that produced by the rudder when deflected about  $1^\circ$  and  $4^\circ$ , respectively. While the equivalent rudder deflections may seem small, it must be noted that at this Mach number and associated high dynamic pressure, a small rudder deflection will yield significant yawing moments and side forces on the configuration. At the typical high-angle-of-attack maneuvering conditions of low Mach number and resulting low dynamic pressure, the same forces and moments are equivalent to higher rudder deflection angles.

Because this concept has shown promise, the Navy is preparing to flight-test the yaw vanes on an F-14 aircraft.

(D. E. Reubush, 2673)

F-14 model with yaw vanes in Langley 16-Foot Transonic Tunnel.



F-14 afterbody lateral characteristics with and without yaw vane installation (F110 afterburning nozzles).

# Electronics Directorate

The Electronics Directorate is responsible for the planning, direction, and evaluation of research and applications programs in the areas of measurements and computer science which will potentially benefit the Center's aerospace research activities, and for the management of the Center's instrumentation, data acquisition, and data processing resources. The directorate is organized into three divisions with specific support functions.

The Analysis and Computation Division is responsible for the development and application of mathematical and computer theory to the solution of computational problems arising from theoretical and experimental aerospace research activities performed at NASA Langley. Additional responsibilities include conception, design, implementation, and management of advanced centralized data processing systems, flight software systems, and flight simulators, as well as providing consultation on NASA Langley application of computer technology.

The Instrument Research Division provides instrumentation and measurement support for experimental aerospace research activities performed at NASA Langley, with primary responsibility for the instrumentation of ground-based facilities. The division conducts research and development programs in instrument areas where present measurement capabilities are deficient or nonexistent to satisfy both current and future aerospace test program requirements. Additional responsibilities include providing engineering and application expertise to support computer-based data acquisition and control requirements, developing and maintaining measurement standards, calibrating and repairing instruments, and managing an instrument pool.

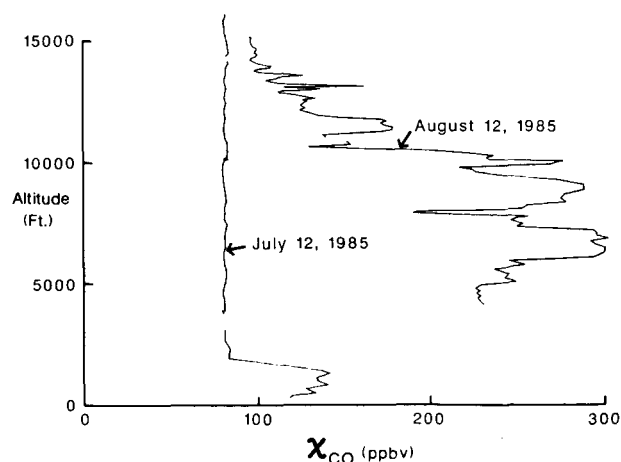
The Flight Electronics Division is responsible for the development and application of electronic and electro-optical systems for aerospace flight and flight-related projects. The division conducts research and development programs in electronics, optics, lasers, and related disciplines to provide measurement, communication, and data processing systems. Additional responsibilities include design, fabrication, testing, and operation of ground and flight electronic and instrumentation equipment for approved flight projects and applications.

The Electronics Directorate is also responsible for the implementation and management of the following projects or functions: The Earth Radiation Budget Experiment/Stratospheric Aerosol and Gas Experiment (ERBE/SAGE II) Project, the Long Duration Exposure

Facility (LDEF) Project, the Control of Flexible Structures (COFS) Project, the Space Technology Flight Experiments Office (STFEO), and the Scout Project.

## In Situ Laser Absorption Measurements of Carbon Monoxide Over Amazon Forest

Tropical forests contain a substantial portion of the global living biomass. Through biogenic emission and biomass burning, these regions can therefore represent important sources of key tropospheric gases. Carbon monoxide is particularly important since it may contribute to global climate change because of the "greenhouse effect." Evidence of CO emission from the Amazon region has been obtained by the MAPS (Measurement of Air Pollution from Satellites) instrument which, from the Space Shuttle, remotely measured enhanced CO levels off the Brazilian coast. A joint USA/Brazil field expedition named the Amazon Boundary Layer Experiment (ABLE) took place in July and August 1985 to study (1) the emission of CO and other important gases from the Amazon forest; (2) the transport of these gases into the free troposphere; and (3) the photochemistry taking place in this high ultraviolet (UV) flux environment.



*Carbon monoxide profiles taken over Manaus, Brazil, during ABLE expedition.*

A laser-based in situ instrument named the Differential Absorption CO Measurement instrument participated in ABLE by taking 100 hours of flight data on-board the NASA Wallops Electra aircraft. The high-sensitivity ( $<1$  ppbv) and fast-response (1 sec) capabilities of this instrument proved invaluable in attaining a better understanding of the contribution of this region to the global CO budget. Because the expedition occurred during the transition from a wet to a dry season, the timing of the expedition offered an opportunity to observe the atmosphere not only during the wet season when biogenic emission predominated but also during the dry season when biomass burning had an important impact. The figure shows the dramatic seasonal change in the CO distribution over the Amazon region which occurred between the day of arrival and the day of departure. (G. W. Sachse, 2818)

## Amplitude-Modulated Laser System for Distance and Displacement Measurement

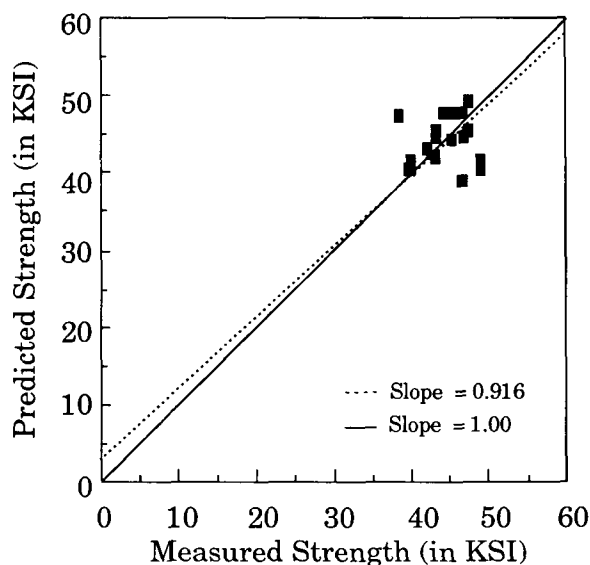
A laser distance and displacement measurement system is being developed at NASA Langley to monitor small displacements in large space structures for strain analysis and structural control. The laser is amplitude modulated at a variable frequency by a voltage controlled oscillator that also serves as a reference oscillator in a mixer. The reflected laser beam is focused on a detector, and the detected signal is mixed with the reference. The d.c. error voltage from the mixer is maintained at null by shifting the modulating frequency. Small displacements are indicated by a change in modulation frequency which is adjusted to maintain quadrature between the received signal and the reference signal from the voltage-controlled oscillator in a phase-locked loop. Measurement of absolute distance is accomplished by sweeping the modulation frequency from a quadrature lock point to an adjacent lock point.

The laser system has been tested under laboratory conditions, and a resolution of one part per million has been demonstrated with an AlGaAs diode laser modulated at frequencies near 20 MHz. This corresponds to a displacement measurement of 0.1 mm at a range of 100 m, which is an order of magnitude better resolution than can be obtained with pulsed laser systems. (R. S. Rogowski, 3036)

## Nondestructive Evaluation/Fracture Mechanics Prediction of Filament Wound Casing Strength

Thick composites, such as filament wound casings, can sustain significant internal damage from impact with no outward appearance of damage. Researchers in fracture mechanics have developed models for predicting the failure strength of thick composites that have been impacted. These models require specific information about the damage which is difficult to obtain, especially when the damage is internal.

In order to obtain this information, an algorithm was developed which estimated the characteristics of the damage from quantitative ultrasonic attenuation and velocity measurements made in transmission. The ultrasonic response of the samples was modelled depending on the attenuation and velocity of an effective damaged composite material and good composite material. If the ultrasonic attenuation and velocity values of both the good and the effective damaged composite are known, then values for the dimensions of the damaged region can be calculated. This information can then be supplied to the fracture strength prediction equation to predict the ultimate load of a composite sample under tension.



*Predicted versus measured strength from NDE data.*

To test the nondestructive evaluation (NDE) model and the fracture mechanics model, a set of filament wound casing samples was subjected to low-velocity impact, ultrasonically tested, and then stressed in tension until failure. The predicted results showed relatively good correlation with the measured, remaining strength after impact, which left no visible surface mark. As shown in the figure, all the data scatter around the unity correlation line. Eighty percent of the data are within a few percent of the line and have a variance typical of material variability. (E. Madaras, 3036)

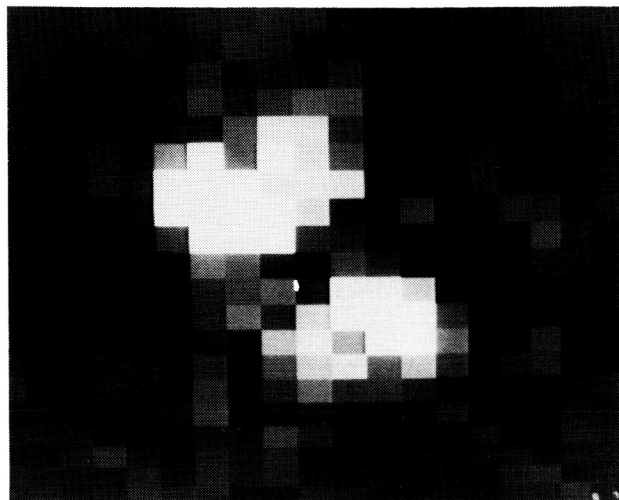
### Analytic Function and Signal Processing Techniques to Image Thin Composite Plate Damage

The nondestructive evaluation of impact damage in thin composite material is an important problem. Usually, these materials exhibit little indication of the degree or state of internal damage. The ability to more accurately and quantitatively describe such damage is a primary goal of this research.

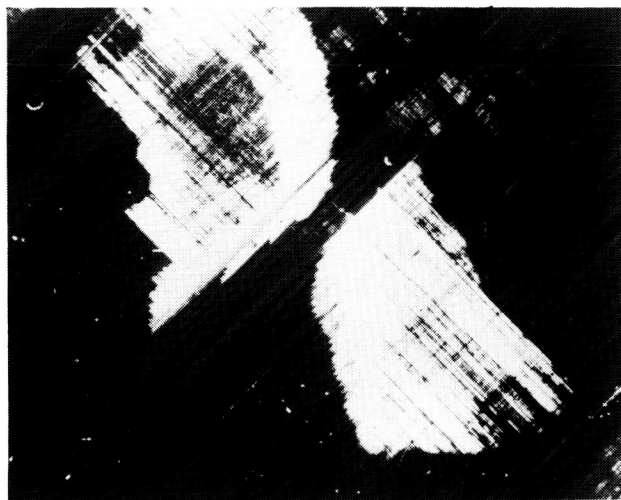
An ultrasonic system with a fast waveform digitizer has been set up to record the signals ultrasonically back-scattered from samples. A region of interest is scanned by moving the transducer over the surface in two dimensions. At each scan site, a digitized ultrasonic response is recorded for postprocessing. This postprocessing involves filtering, deconvolution of the system response, and, finally, generation of the analytic function of the waveform. These procedures result in a more accurate image of the internal damage. A movie can be generated which shows a layer-by-layer ultrasonic reconstruction of the inside of a composite independent of the measurement systems.

To test this technique, a set of 2-mm-thick composite plates was impacted and ultrasonically scanned at 15 MHz with our system. The samples were then destructively evaluated by a pyrolytic deply technique in collaboration with the Lockheed-Georgia Company. The results indicate that our technique can quantitatively detect the size of the delaminations within the sample. Delamination between two layers is shown in the first figure, and an ultrasonic image of the same delamination region is shown in the second figure. Qualitatively,

these images are similar. Quantitative measurements of the delamination areas indicate an 0.82 correlation coefficient comparing the delamination size measured ultrasonically with the destructive deply technique. (E. Madaras, 3036)



*Gold-chloride-enhanced area of a deply section.*



*Ultrasonic image from same deply region.*

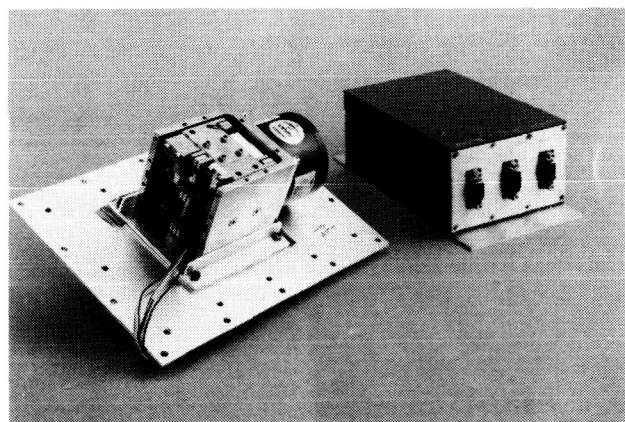


## Flight Balance for Skin Friction Measurements

A balance designed to measure the skin friction force on an aircraft fuselage has been developed at NASA Langley. This instrument incorporates a 5-cm-diameter floating sensing element, which is servo controlled to make a direct skin-friction force measurement. The balance is insensitive to background rectilinear vibrations due to a unique mechanical design. This special feature and its ability to sustain large transient loads make it most attractive for flight testing. The full-scale range of the balance is adjustable from 0.1 gm/cm<sup>2</sup> to 1.0 gm/cm<sup>2</sup>, and the overall size is 20 cm by 13 cm by 13 cm deep. A rear view of a fully assembled balance and the external electronics controller box are shown in the figure.

Two identical units were fabricated, calibrated, and installed on a Lear jet aircraft to take skin friction measurements in a flight test program. Both balances functioned satisfactorily, and balance data repeated within 5 percent for similar test profiles conducted on different days.

(P. Tcheng, 3483)



L-85-13,003

*Sensor rear view and supporting electronics package.*

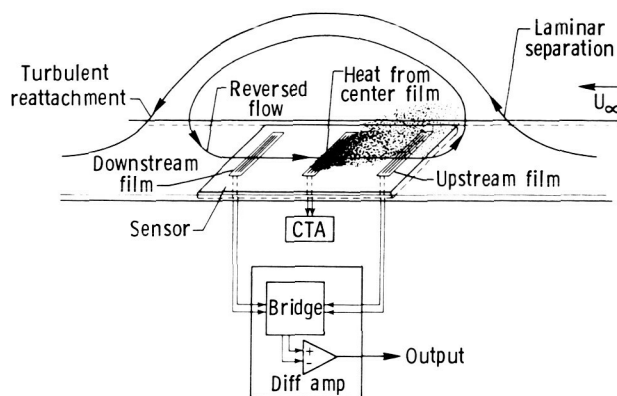
## Laminar-Separation Bubble Detection With Thermal Film Sensors

Flight and wind tunnel experiments have been conducted and have successfully validated a thermal film,

laminar-separation sensor. The very-thin surface-mounted sensor detects a laminar-separation bubble with a flush array of three parallel films oriented perpendicular to the local free stream. The center film is electronically heated by means of a constant temperature anemometer (which makes this element useful as a hot-film transition sensor as well). The outer films are incorporated into two legs of a bridge circuit and operate as resistance thermometers. When the sensor is exposed to air flow, heat is transferred from the center film to either the upstream or downstream film, depending on the direction of the flow in the boundary layer. The difference in resistance between the upstream and downstream films (corresponding to a change in film temperatures) is measured by the bridge and a high-gain differential amplifier. The direction of the flow is then determined by the polarity of the output signal from the amplifier. If the flow over the sensor is reversed from the free-stream direction, a laminar-separation bubble (characterized by this phenomenon) exists.

The sensor was evaluated in flight on a NASA Lear 28/29 jet and in a wind tunnel on a 12-in. chord natural-laminar-flow airfoil. The experimental procedure in both the wind tunnel and flight tests consisted of first locating and characterizing a laminar-separation bubble using flow visualization techniques. Laminar-separation sensors were then strategically placed so that the bubble would not exist on the sensor at low angles of attack, but would exist on the sensor at high angles of attack when transition moved forward.

(D. Carraway, 3446)



*Conceptual operating principle of a thermal film laminar-separation sensor.*

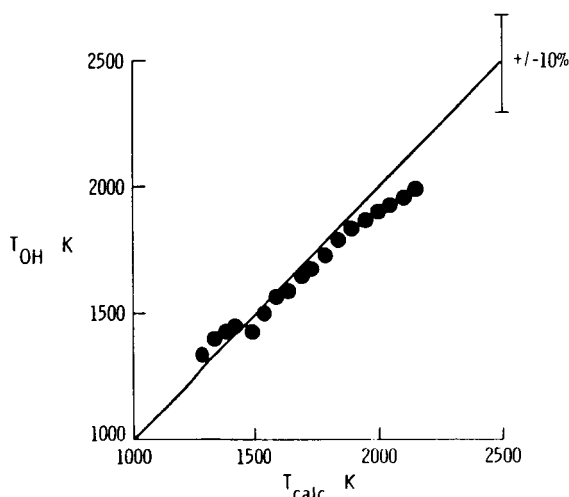


## OH Absorption Technique for Measurement of Combustor Temperature

A simple, rugged, ultraviolet absorption technique was developed to perform temperature measurements in hypersonic combustors and other harsh test facilities. Ultraviolet light at over 100 discrete wavelengths in the 300-nm region is piped to and collimated through a combustor with an optical fiber/lense arrangement. The transmitted light is picked up with a second fiber/lense and analyzed with a custom modified quarter-meter spectrometer. The differential absorption of different wavelengths by the naturally occurring flame species OH (hydroxyl radical) forms the basis of the temperature determination.

A series of measurements were performed on a well-characterized hydrogen/air premixed flat flame burner. The figure compares the OH temperature to that calculated from thermodynamic heat balance between reactants and products and illustrates the potential of the technique. Each displayed data point requires 5 sec to obtain and is the result of averaging 50 individual measurements, taken at 0.1 sec intervals. Using 20 m of fiber optics, preliminary measurements were performed in a test cell and indicated similar promise under extremely harsh operating conditions. The optical fiber coupling should allow access to a variety of difficult engine-combustion environments in the future.

(W. Lempert, 2791)



OH temperature plotted against calculation.

## Metal Ion Effects on Polymer Properties by Positron Annihilation Spectroscopy

Organic matrix composites are promising materials for diverse aerospace and industrial applications because of their high strength, low mass, and low cost. However, their use in aerospace applications has been rather limited because of lightning hazard to electronic equipment onboard the aircraft and because of their inability to dissipate space charge effects due to their nonconducting nature. Both these limitations may be overcome if the polymers can be made to conduct by the addition of small amounts of appropriate organometallic complexes without significantly affecting their thermomechanical properties. However, the effects of various metal ions on polymer properties cannot be easily predicted because of strong stereochemical effects of material curing procedures.

The Positron Annihilation Spectroscopic techniques have been developed to measure free-electron densities and associated cross-link densities. These techniques have been applied to investigate the effects of transition metal ions on polymeric properties. These studies have shown that chromium atoms coexist as divalent ions (Cr II) and trivalent ions (Cr III) in the chromium-polymer system. Similarly, triply ionized iron atoms (Fe III) exhibit hybridized octahedral and tetrapyramidal symmetries. Triply ionized cobalt atoms (Co III), contrary to expectations, have four spin-unpaired electrons resulting from weak ligand fields in the cobalt-epoxy systems. Doubly ionized cobalt atoms (Co II) and nickel atoms (Ni II) behave uniquely because their coordination symmetries remain unaffected by the resin-curing procedures.

(J. J. Singh, 3907)

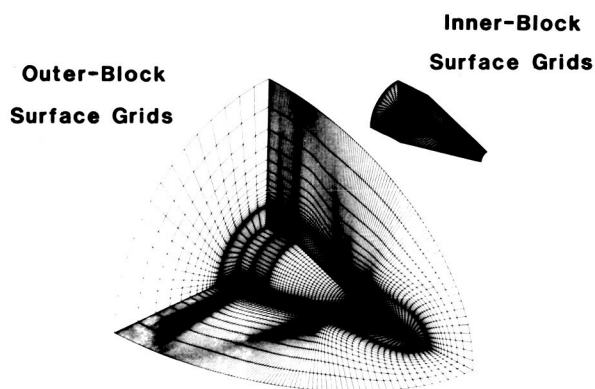
## Dual-Block Grid Generation Around an Aircraft

A major task in the simulation of inviscid compressible fluid flow is the generation of structured grids in flow domains. Single-block grids have been used with great success on a large class of problems with relatively simple boundary geometries, but for more complex boundaries, it is recognized that multiblock grids are more effective.

A dual-block grid topology and associated computer software to generate grids about fighter-type aircraft configurations have been developed at NASA Langley. A patched dual-block grid is used because the conservation of mass, momentum, and energy is easily maintained across patched grid interfaces and because a dual-block grid offers high overall resolution for this type of aircraft geometry.

The figure shows several grid surfaces for a fuselage/cocked-wing/canard configuration. The inner grid discretizes the region around the inner part of the wing and has a natural concentration of grid points at the wing apex; this is important for accurate simulation of the leading-edge vortex generated at sharp leading edges at high angle of attack. The outer grid matches the inner grid with first derivative continuity and discretizes the region around the nose, canard, and outer part of the wing. The entire grid is computed with transfinite interpolation, which is an algebraic method based on the Boolean sum of various univariate interpolations.

(R. E. Smith, Jr., 3978)



*Dual-block grid for fighter configurations.*

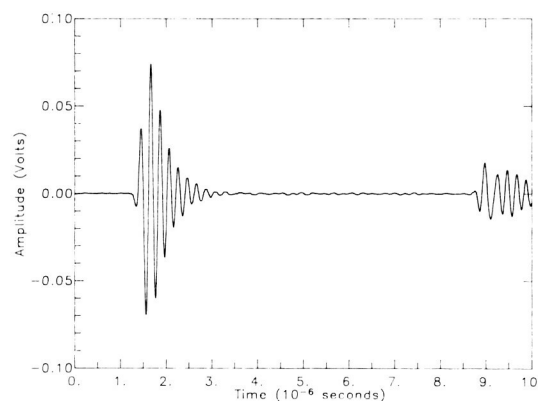
## High-Temperature Acoustic Transducer

Continuous characterization of polymer composites during cure at high temperatures is important for controlling the process of the polymer to yield a composite with increasing integrity. A new acoustic transducer has been developed at NASA Langley which allows for continuous measurements up to 350°C. The acoustic

transducer consists of a lithium niobate acoustic transducer bonded to a high-density graphite buffer rod with LARC-TPI (a high-temperature polyimide also developed at NASA Langley). The acoustic properties of the graphite buffer rod have a closer match to the acoustic properties of a composite and increase the dynamic range of the measurement system. In addition, tests have shown the transducer to be stable for several hundred hours of operation at high temperatures.

Currently, this sensor is being used to characterize the composite cure in a laboratory press to establish a scientific base for cure control. The sensor is also being incorporated into a fixture for testing in an autoclave.

(F. R. Parker, 3036)



*Response of high-temperature transducer at 320°C.*

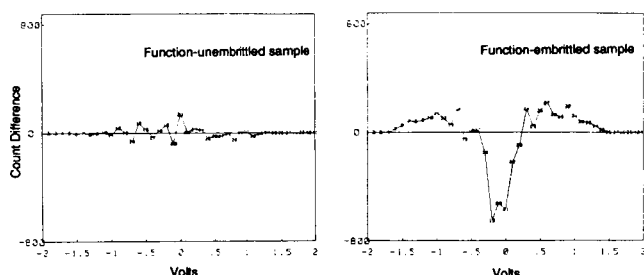
## Nondestructive Evaluation Detection of Temper Embrittlement in HY-80 Steels

A magneto-ultrasonic technique has been developed to detect the effects of temper embrittlement in HY-80 steel alloy castings. The technique works in the following way: The material under test is subjected to a low-frequency (60 Hz) a.c. magnetizing field. An ultrasonic transducer (with a frequency range of 100 kHz to 300 kHz) "listens" to the noise generated by the domain wall motion within the sample. When the rate-change of the magnetic field in the sample reaches its maximum value, the noise pulse height from the transducer is measured. After a large number of such measurements have been taken, a distribution of the pulse

heights is determined for each sample. A function was made by subtracting each distribution from the (reference) distribution of a sample that was not embrittled. It was found that the functions vary in a way that correlates with the state of embrittlement of the HY-80 steel casting, as measured by the Charpy V-notch test.

A typical set of results is shown in the figure. The x-axis represents the recorded pulse heights and the y-axis represents the function, which is the difference between the number of counts in corresponding pulse height intervals between a sample under test and the reference sample. The diagram on the left shows the function of an unembrittled sample. The diagram on the right shows the function of an embrittled sample. We see that the function of the embrittled sample shows a substantial difference in its noise pulse height distribution than does the unembrittled sample, especially among the low-voltage pulse heights. This technique leads to a definite evaluation of the state of embrittlement.

(S. G. Allison, 3036)



*Function-unembrittled and function-embrittled samples.*

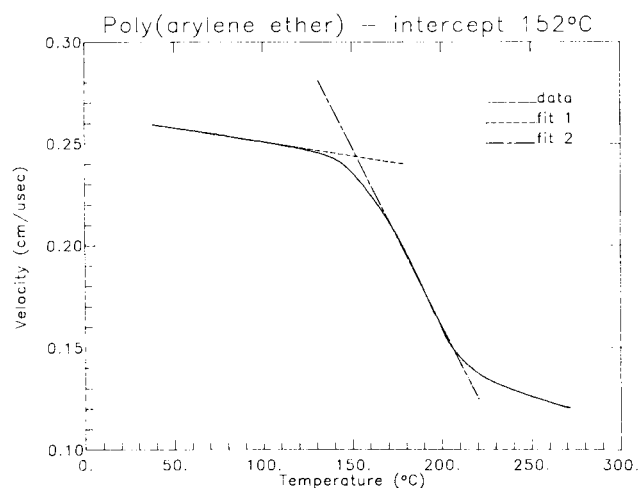
## Acoustic Characterization of Glass Transition Temperature

The development of tough high-temperature thermoplastics for composites has led to stricter constraints on the manufacturing process. Obtaining a viable product with conventional techniques requires a reproducibility in materials which is difficult to obtain with current manufacturing operations. To achieve materials that have predictable properties, the manufacturing process

needs to be based on a sensor technology to characterize the materials as they evolve during the cure. A real-time characterization of the materials during processing provides information for a process controller which can tailor a process to manufacture a part with the highest quality.

A technique has been developed to determine the glass transition temperature of a thermoplastic from the temperature dependence of its acoustic velocity. The temperature dependence of the acoustic velocity has a linear portion both below and above the glass transition temperature. An extrapolation of these two linear regions intercepts at the glass transition temperature. The glass transition temperature is an important processing parameter to determine the temperature and pressure required to fabricate a composite. The acoustic glass transition temperature agrees with values found from traditional techniques to within 1°C. The measurement technique, however, differs from these traditional techniques in that it can implement in an autoclave environment and perform the characterization during materials processing.

(W. P. Winfree, 4928)



*Acoustic response of poly(arylene ether) around glass transition temperature.*

## Optical and Thermal Properties of Titanium-Doped Sapphire Laser Materials

Remote sensing of atmospheric species from aircraft or from space-based systems requires efficient and

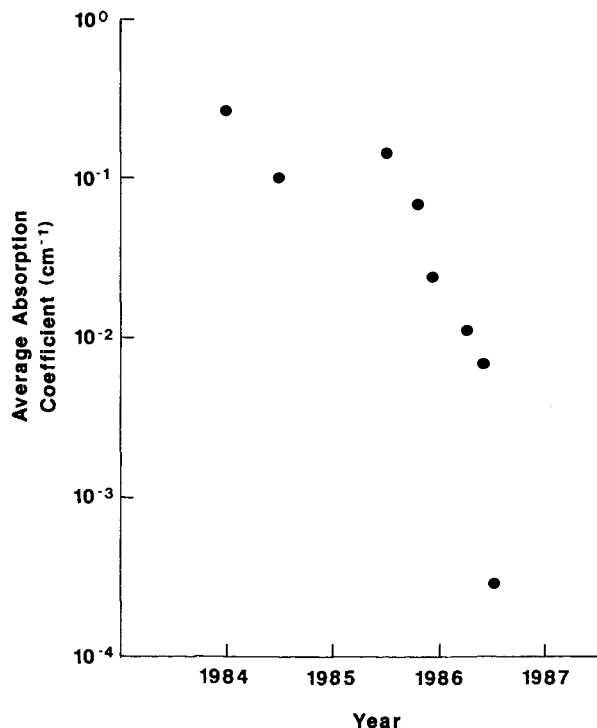
reliable tunable lasers. A primary candidate for the next generation of such lasers is centered on titanium-doped sapphire, which has been shown to be an efficient room temperature tunable solid-state laser material. This material is a leading candidate for atmospheric remote sensing using Differential Absorption Lidar (DIAL) from spacecraft platforms. However, early growths of this material indicated anomalously high absorption in the lasing region resulting in significant reductions in efficiency and laser damage thresholds.

A coordinated effort between Union Carbide Corporation, which was responsible for the growth and postgrowth treatment, and NASA Langley, which performed the materials characterization, has led to the successful reduction of this anomalous absorption by 3 orders of magnitude, i.e., from 27 percent/cm losses in the initial growths down to 0.025 percent/cm losses in the latest growth (as shown in the first figure). This reduction was achieved by carefully controlling the growth conditions, altering the postgrowth annealing temperature and gaseous environment, and increasing the requirements for the quality of the starting materials.

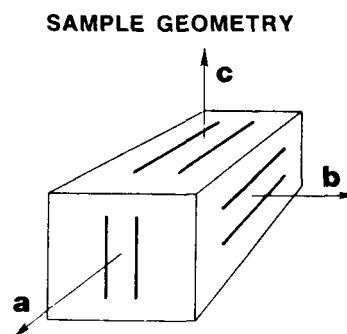
In a continuing effort to characterize this material for use in all solid-state laser transmitters, its thermal

properties were measured and incorporated in a model for heat transport in a laser rod. Using a dynamic measurement technique, the specific heat capacity of titanium-doped sapphire and its thermal conductivity were determined along principal optical axes. The principal optical axes are shown in the top part of the second figure. Values for these measurements are shown in the lower part of the second figure. Two parallel nickel strips (each  $\approx 10 \mu\text{m}$  by 3 mm) are evaporated onto an oriented surface of the sample. One strip acts as a linear periodic heat source; the other strip is used as a resistance thermometer. Heat conducted through the sample from the heater strip causes a periodic variation in temperature in the sensor strip. This results in a modulated resistance across the sensor which is detected synchronously with a lock-in amplifier. The measured values of the resistance as a function of heater frequency are fit to the predictions of a detailed calculation for the heat transport between the strips. This fitting yields the values of the specific heat capacity and the thermal conductivity shown.

(C. E. Byvik, 2818)



Reduced anomalous absorption.



RESULTS FOR TI:SAPPHIRE (T=23C)

|                                   | Pure Sapphire | Ti:Sapphire |
|-----------------------------------|---------------|-------------|
| Specific Heat Capacity (cal/gm-K) | 0.188         | 0.219       |
| Thermal Conductivity (W/cm-K)     |               |             |
| ⊥ c                               | 0.340         | 0.358       |
| c                                 | 0.377         | 0.386       |

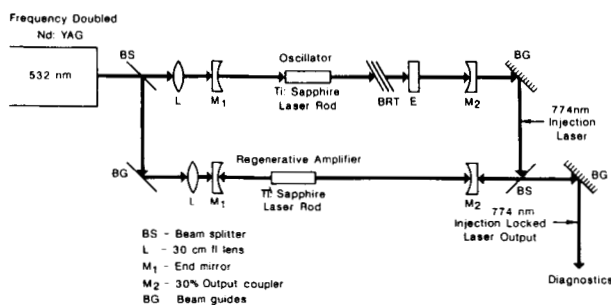
Measured thermal properties of titanium-doped sapphire.

## Narrowband Ti:Al<sub>2</sub>O<sub>3</sub> Self-Injection Locking Feasibility

Future space- and air-based lidar systems require efficient, reliable, compact laser transmitters with narrow linewidth outputs at specific wavelengths. Self-injection-locked laser cavity designs promise benefits in weight and size and in efficient wavelength and linewidth control. A low-power, line-narrowed Ti:Al<sub>2</sub>O<sub>3</sub> (titanium-doped sapphire) laser oscillator has been used at NASA Langley to injection lock a relatively high-power regenerative amplifier. This demonstrates for the first time the feasibility of engineering a self-injection locked Ti:Al<sub>2</sub>O<sub>3</sub> laser, in which a single cavity serves as both the oscillator and regenerative amplifier and thus reduces size and weight. Another advantage of this technique is that all of the controllable power losses are confined to the low-power oscillator portion of the system where the effect on efficiency is minimum.

The output of a frequency-doubled Nd:YAG laser is split into two beams to serve as optical pumps for the Ti:Al<sub>2</sub>O<sub>3</sub> laser system (as shown in the figure). Nominally 10 mJ of 532 nm pump energy is absorbed by the oscillator and 20 mJ by the amplifier. If allowed to operate freely, the Ti:Al<sub>2</sub>O<sub>3</sub> laser system linewidth is more than 100 nm; therefore, a three-plate birefringent tuner and a thin and a thick etalon were inserted into the oscillator cavity to give an 0.25-nm linewidth output at 774 nm with pulse energies  $\approx 0.2$  mJ. The narrowband output (injection pulse) is coupled into the regenerative amplifier cavity through a 30-percent transmissive mirror. When proper timing between the injected pulse and the amplifier pump pulse is achieved, the amplifier lases at a linewidth and wavelength identical to the injected pulse but with amplified energy ( $>3.5$  mJ).

(J. C. Barnes, 3761)

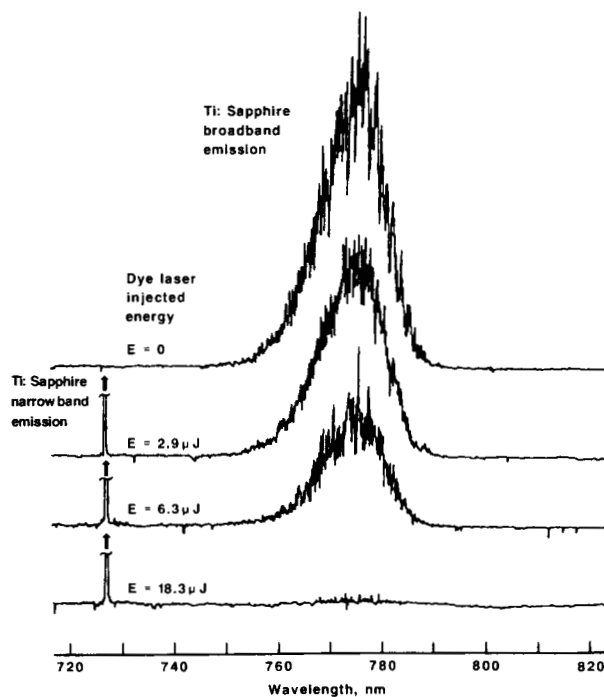


*Laser injection locking titanium-doped sapphire configuration.*

## Injection-Controlled Titanium-Doped Sapphire Laser Using Pulsed Dye Laser

Because of their wide tuning ranges ( $\approx 700$  to  $1000$  nm), titanium-doped sapphire lasers are candidates for remote lidar measurements of H<sub>2</sub>O vapor at wavelengths of  $\approx 720$  and  $940$  nm and of pressure and temperature using O<sub>2</sub> lines at  $\approx 760$  nm. These measurements require efficient, narrow bandwidth operation and accurate wavelength control. One method to achieve efficient narrow bandwidth operation is by injection control.

In this experiment, a dye laser system developed for flight measurement of H<sub>2</sub>O vapor at  $727$  nm was used to injection control a titanium-doped sapphire laser. Spectral content of the titanium-doped sapphire laser is shown in the figure. The top curve shows the spectral output when no injection signal was introduced into the titanium-doped sapphire cavity and indicates that the free-running laser has broadband laser emission from  $760$  to  $790$  nm. Note that the injected wavelength,  $727$  nm, was well removed from the free-running laser wavelength range. The next three curves show the change in spectral character with injected energy at



*Spectral scans of titanium-doped sapphire output.*

727 nm as a parameter. The bottom curve shows that, with approximately 18  $\mu\text{J}$  of dye-laser-injected intracavity energy, almost all of the broadband emission was suppressed and almost all the laser energy was extracted in a narrow band at the injection wavelength of 727 nm. A Fabry-Perot etalon was used to measure the bandwidth of the injection-controlled titanium-doped sapphire laser. The bandwidth was 2.5 pm (picometer), which matched the bandwidth of the dye laser.

Measurements of the laser output energy for the injection-controlled and free-running laser conditions indicated that nearly identical energy extraction was being obtained; this indicates that titanium-doped sapphire is homogeneously broadened and that injection control can be used to obtain efficient narrow linewidth operation.

(P. Brockman, 2818)

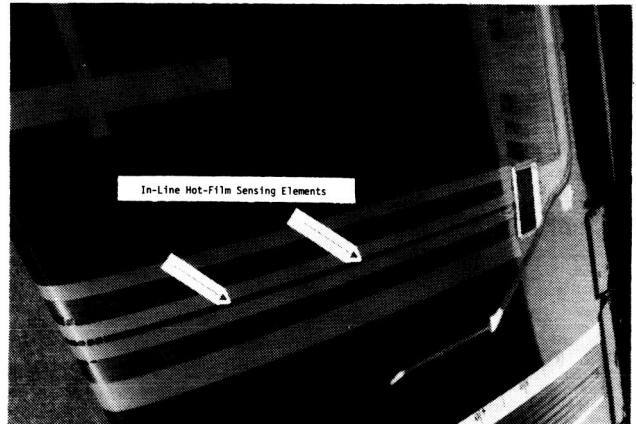
## Continuous, Multielement, Hot-Film Transition Gauge

Accurate measurement of the location where a laminar boundary-layer undergoes transition to a turbulent one serves many purposes in basic aerodynamic research and development testing. A complete understanding of performance, stability, and control of a laminar-flow airplane requires knowledge of transition locations on the wing surfaces, empennage surfaces, fuselage, and nacelles. A useful device for wind tunnel and flight applications is the thin, miniature, surface-mounted, hot-film gauge. Hot films indicate transition by responding to the differences in heat transfer between laminar and turbulent flows. Conventional hot-film gauges are typically applied by strain-gauge mounting techniques. However, the external wiring at the downstream end of each gauge causes a boundary-layer disturbance that prevents chordwise measurements. The need to stagger the hot-film gauges is the most significant disadvantage of these gauges.

The continuous, multielement, hot-film transition gauge concept, which was developed at NASA Langley, overcomes the disadvantages of the individual, hot-film gauges by integrating the required number and distribution of hot-film sensing elements and associated signal wiring leads into a long, continuous, thin sheet. The length of the sheet, which begins at the leading edge and continues downstream of the transition region as

shown in the figure, covers the area of interest for transition measurements. The gauge is attached using double-backed adhesive tape and incorporates appropriately spaced hot-film sensing elements as needed to determine stagnation line and transition location. The width of the sheet provides space for the thin signal leads to be carried to the downstream end of the sheet where external wiring arrangements are made. The multielement gauge uses an improved electronic (MOSFET) switch that permits an experimenter to select critical gauges for simultaneous real-time monitoring. Its very-high switching speed allows sensor elements to be switched into the servo loop at very-high rates without damage to the sensors.

(F. K. Harris, 3585)



*Wing-mounted multielement hot-film gauge.*

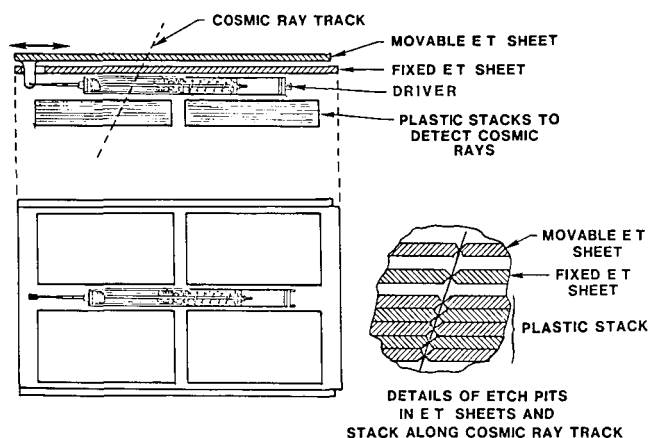
## Event Thermometer for Cosmic Ray Detectors

Knowledge of the abundance of the rare actinide group elements in cosmic rays can provide vital clues to the origin and evolution of such high-energy radiation. Actinide abundances can be established by analyzing the tracks they produce in stacks of thin plastic sheets that have been exposed for a number of years on satellites. To analyze the tracks, the exact temperature of the plastic at the time each track is produced must be known. A flight data system to measure and precisely

record the stack temperature at the time each track is produced or a system to control the stack temperature during the space exposure would be complex and costly. A simple, inexpensive, passive event thermometer (ET) has now been developed at NASA Langley which eliminates the need for either system. This ET is planned for future use on the NASA Heavy Nuclei Collector (HNC) experiment.

The ET concept is functionally illustrated in the figure. Two plastic sheets (identical to the stack sheets) are mounted above the stacks. The upper sheet is movable, and its position is controlled, as a function of the stack temperature, by a thermally activated driver. During the postflight analysis of tracks, the temperature of the stack at the time a selected track was produced can be determined by aligning the track in the movable sheet with the track in the fixed sheet and noting the stack temperature that is required for the driver to position the sheet. The driver employs the thermal expansion and contraction of silicon oil to move a spring-loaded piston that is connected to the movable ET sheet. The stacks and the oil in the driver are thermally coupled together to ensure temperature uniformity. Calibrations of the ET have shown that it has a precision of  $\pm 1^\circ\text{C}$ .

(R. L. O'Neal, 3704)



*Schematic of ET for cosmic ray experiment to fly on an LDEF mission.*

# Flight Systems Directorate

The Flight Systems Directorate conducts basic research and development in the broad, multidisciplinary area associated with aerospace flight systems. This includes systems hardware and software architecture concepts and design guidelines, validation and verification methods for reliable flight control systems, advanced cockpit interfaces, advanced airborne systems technology, aircraft operating procedures, fundamental electronics research, automation and robotics technology, and aircraft and spacecraft guidance and control system design methods, guidelines, and criteria.

The Advanced Transport Operating Systems Program Office coordinates a wide-scale focused technology research and development effort aimed at developing and improving the technology base for transport aircraft operating systems and the integration of these systems with the current and future air traffic control environments. The office also provides a focus for research and development of improved airborne operations and procedures and operates the NASA Boeing 737 aircraft and associated simulator.

The Information Systems Division conducts research to provide an advanced technology base for future spacecraft and aircraft systems. Specifically, the division performs research in the areas of robotics and automation, fault-tolerant systems validation, reliable software, system architectures, electronic/optical subsystem technology, and software engineering. The scope of activities is broad and encompasses both the highest level systems considerations and the investigation of solid-state physics phenomena.

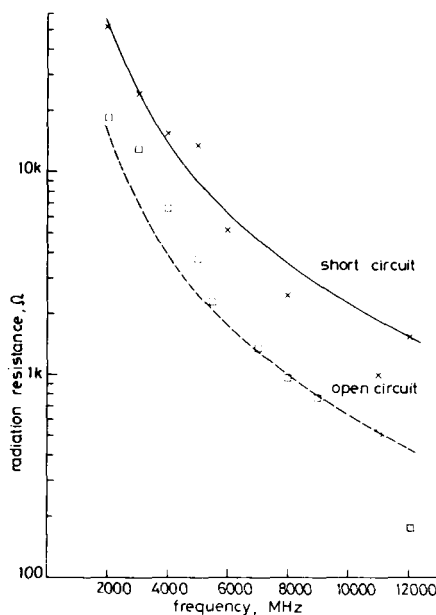
The Guidance and Control Division conducts generic and applied research on aircraft and spacecraft guidance, control, and antenna systems. The research is directed toward the development of a technology base for advanced aircraft and spacecraft systems analysis and design methods, including validation and verification demonstrations of advanced concepts. The division also develops multidisciplinary computer-based tools and techniques which allow appropriate guidance, control, and antenna design issues to be considered through all stages of aircraft and spacecraft design.

The Flight Management Division conducts research to provide a viable technology base for future aircraft and spacecraft flight management systems. Specifically, the division provides technologies required by designers of crew station systems; defines and evaluates improved guidance and control procedures;

and studies advanced airborne systems technology, traffic control strategies, and operating procedures for improving the efficiency of air traffic control operations. In addition, the division provides methodologies and criteria for measuring crew workload and stress.

## Dielectric Resonator Band-Pass Filter Technology for Future Aerospace Applications

The objective of this research task was to develop the technology for the design of ultra-low-loss (high-Q) dielectric resonator band-pass filters that are required for future communications and remote-sensing missions involving microwave and low-millimeter wave frequencies. Due to the limitations of current theoretical analyses of multipole dielectric resonator (DR) filters, an empirical approach was developed to obtain the necessary engineering data. Measurements were made in test configurations in which the variables were: input/output coupling, wall-to-puck and top-to-puck separation, and puck-to-puck coupling versus spacing. Extensive data have been generated using network analyzer measurements for the purpose of designing a three-pole filter.



*Theoretical and experimental values of radiation resistance for open- and short-circuit microstrip lines.*



An experimental filter was designed (using the empirical data base), constructed, and evaluated. The three-pole, 5-percent bandwidth filter exhibited an insertion loss of 0.15 dB at 4.3 GHz. It has been demonstrated that short-circuit coupling lines are superior to the widely used open-circuit lines, as shown in the figure. Various coupling configurations have been evaluated in an effort to minimize resonator Q degradation. Finally, considerable research has been devoted to improving the efficiency of coax-to-microstrip transitions and thereby reducing filter insertion loss. (C. P. Hearn, 3631)

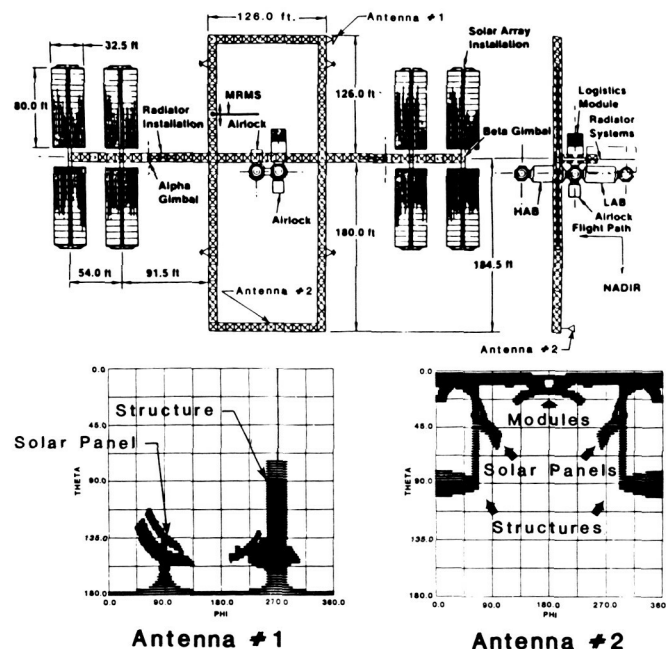
## Space Station Antenna Obscuration

Analytical computer codes have been developed which can accurately predict not only the performance of the Space Station communications and tracking system antennas but also the effects of the complex Space Station structure. These codes are easily transportable, have relatively rapid running times, and provide trade-off analysis capability so that optimum performing antenna designs and sitings can be found.

The basic scattering code (BSC), which uses the uniform geometrical theory of diffraction (UTD), combined with a numerical electromagnetic code (NEC) can be very useful to accurately predict the performance of antennas on the Space Station. For very large structures such as the Space Station, however, these codes require long computer running times that limit the number of antenna design cases that can be analyzed for determining suitable antenna locations. An obscuration program, which can rapidly compute the antenna's clear line-of-sight path and blockage contours, provides good information on suitable antenna locations on the Space Station. Once candidate locations are established, then the NEC/BSC computer codes can be used to analyze the antenna pattern performance for candidate antenna designs. The obscuration program, called SHADOW, has been developed and documented (Ohio State Technical Report 716199-7) under a NASA Langley grant. This report gives a description of the code, a user's manual, and examples of its use on sample Space Station antenna locations.

An example of an obscuration calculation for two antenna locations on the Space Station reference configurations is shown in the figure. A preliminary version of the NEC/BSC codes, which are being developed to

analyze antenna performance on the Space Station, is presently being run on a NASA Langley VAX computer. (E. M. Bracalente, 3631)



Computed obscuration-shadowing solar panels rotated 45°.

## Dynamic Remapping of Parallel Computations

A large class of numerical problems can be partitioned for parallel computation. These partitions must be carefully mapped onto individual processors of a multiprocessing system to balance the computational load. Following an initial mapping, system performance often deteriorates with time as the computational load shifts and some of the processors become overloaded while others become idle. In order to maintain high performance, it may be necessary to remap the problem in order to redistribute the computational load.

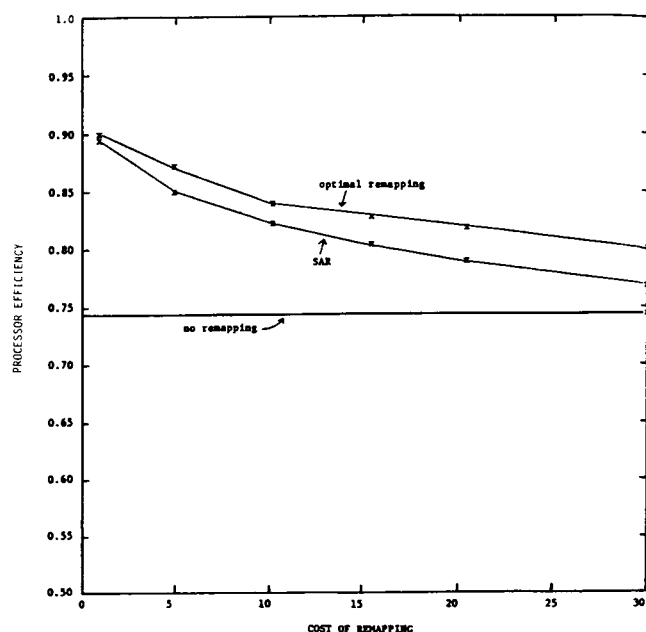
A remapping decision policy must balance the overhead cost of remapping with the expected performance gain. Researchers, working under a NASA Langley contract at the Institute for Computer Applications in Science and Engineering (ICASE), have evaluated several policies for two qualitatively different problems. One problem assumes that performance de-

teriorates gradually (multiple Markov chain [MUM] model); the other problem assumes that performance deteriorates suddenly.

These analytical model problems have been used to study remapping policies and also to express the relationship between performance and remapping cost, number of processors, and stochastic activity of the computation. For example, for a problem with the MUM model of computational behavior, a comparison between the performance of the optimal remapping decision policy and the performance of SAR (a sub-optimal heuristic called the Stop-at-Rise policy) is shown in the figure. This comparison indicates that the SAR policy is close to the optimal remapping strategy. For both policies, as the cost of remapping increases, the processor efficiency drops to approach the no-remapping strategy.

Simple policies for deciding when a problem should be remapped (such as SAR) have been shown through simulation to be effective and robust, for both classes of problems, compared with computationally expensive optimal decision policies.

(S. J. Voigt, 3535)

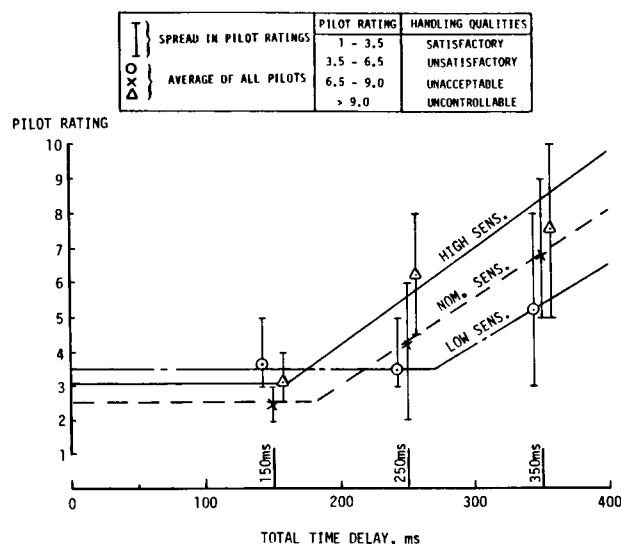


Performance of optimal remapping decision policy compared with performance of SAR for MUM model of computational behavior.

## Time Delay and Pitch Control Sensitivity Effects in Flared-Landing Task

In the past, attempts have been made to specify whether various levels of total effective time delay are acceptable or not acceptable for given flight tasks. Attempting to specify these levels has resulted in some confusion because examples have appeared that seem to be exceptions to the rule, e.g., large aircraft in general and, more recently, the X-29. In both of these cases, Level I (satisfactory) performance has been achieved with time delays that were considered by most of the literature to be excessive. Recent experience has indicated that pilot opinion and performance are not only affected by a given amount of time delay but also can be dependent on a number of additional parameters such as command gain (pitch control sensitivity), open-loop frequency and damping, and feel system dynamics. Command gain is the most dominant of these parameters. During fiscal year 1986, a flared-landing generic flight-control research program was conducted by NASA Langley and utilized the USAF Total In-Flight Simulator (TIFS) airplane. One of the major objectives of this program was to examine time delay and command gain effects in a real-world environment.

The data in the figure indicate that: (1) an upper limit of 220 milliseconds (ms) for Level I performance



Effects of time delay and pitch sensitivity for wheel controllers.

(pilot rating is  $\leq 3.5$ ) and an upper limit of 350 ms for Level II performance (pilot rating is  $\leq 6.5$ ) for nominal, well-designed command gain magnitudes can be achieved; (2) increased command gains are less tolerant of time delays; and (3) reduced command gains are more tolerant of time delays. The data are consistent with past piloting experience in which high pilot gain has contributed to aircraft stability and pilot workload problems.

The time delay data from this program will be used to develop parameters that correlate time delay and pitch-rate sensitivity. These parameters should provide the designer information concerning acceptable time delays, pitch sensitivity, and range of pitch sensitivities for the flared-landing task. These types of data have been needed by handling qualities/flight control system design specialists to design advanced aircraft with good flying capabilities. The results of this in-flight research study are a major step in filling the present voids in flying qualities criteria and requirements.

(W. D. Grantham, 2132)

## Lateral/Directional Control System Design Using Thrust Vectoring

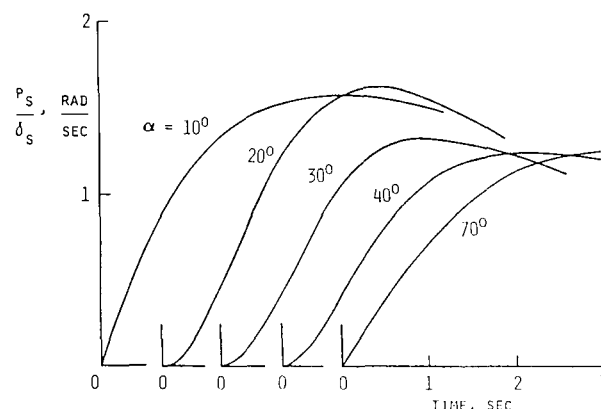
A design study of a lateral-directional control system for a two-engine fighter airplane capable of controlled operation at extreme angles of attack has been conducted. Aerodynamic control surfaces and thrust-vectoring controls are scheduled so that they are driven by separate lateral and directional pseudocontrols. This scheduling is accomplished by calculating combinations of the controls which affect the roll and spiral modes for the lateral pseudocontrol and the Dutch roll mode for the directional pseudocontrol. During flight at low angles of attack and high airspeeds, aileron and differential tail movements are used for lateral control, and rudder movements are used for directional control. During flight at high angles of attack (near or beyond stall) and low airspeeds, yawing moments produced by thrust vectoring are used for lateral control, and rolling moments produced by thrust vectoring are used for directional control.

State variable feedback gains are obtained from the solution of a linear quadratic regulator (LQR) problem which minimizes the difference between the response of the airplane and an idealized model. The gains are used to calculate feedback gains which are scheduled as functions of flight condition.

The directional control channel uses a measure of turn coordination error, an estimate of the time rate of change of sideslip angle, and yaw rate to improve the damping of the Dutch roll mode. The lateral control channel uses lateral acceleration and yaw rate feedbacks to improve the rolling response of the airplane and eliminate the coupling of the roll and spiral modes.

Thrust vectoring provides moments necessary for airplane control at extremely high angles of attack. The formation of pseudocontrol variables provides optimal scheduling of the aerodynamic and thrust-vectoring controls and forms a control system structure that is divided into lateral and directional components. Application of multivariable controls design methodology produces feedback control loops that modify the airplane dynamic modes to make piloted control possible. Simulated responses to step pilot control inputs are stable and well behaved. For hard-over lateral stick deflections, stability-axis roll rates consistently reach 1.25 to 1.60 rad/sec in about 2 sec over an angle-of-attack range of  $10^\circ$  to  $70^\circ$  (as shown in the figure). For rudder pedal inputs, steady-state sideslips are reached in about 2 sec over the same range.

(F. J. Lallman, 3801)



*Normalized stability-axis roll rate response to lateral stick input.*

## Flight Data Analysis From Highly Augmented Aircraft

Highly augmented, statically unstable aircraft present new problems in the area of system identification.

Correlation among the increased number of control surfaces and between input and output variables due to the flight control system (FCS) computer can lead to severely degraded accuracy in estimated stability and control derivatives. As a step toward understanding identification procedures for such aircraft, a project was undertaken to determine the mathematical model structure and to estimate the associated stability and control derivatives of the highly augmented AFTI/F-16 airplane.

Existing flight test data from an AFTI/F-16 were obtained on magnetic tape from the Air Force Flight Test Center, Edwards, California. System identification methodology developed at NASA Langley was applied to that data, and the results were compared with published wind tunnel and F-16A flight test models.

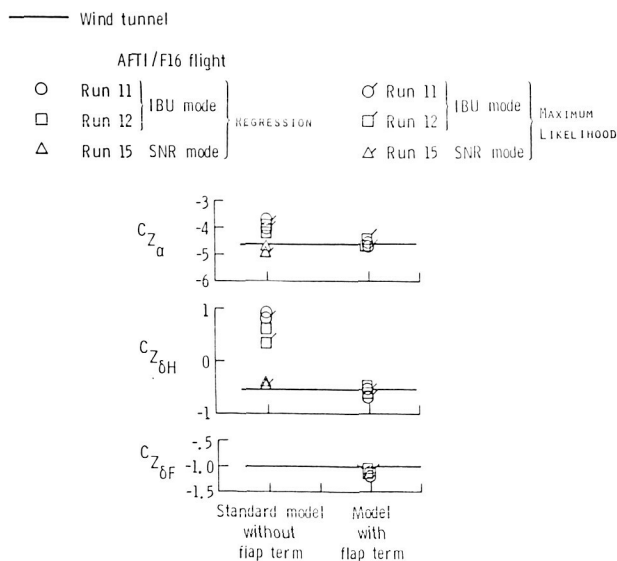
The main results of the study are that (1) a linear aerodynamic model is adequate for all maneuvers analyzed; (2) longitudinal parameter estimates are very sensitive to assumed model structure; (3) in FCS modes with low augmentation (independent backup unit [IBU]), all primary stability and control derivatives are identifiable; and (4) correlations between control surface motion and suppression of airplane response by the FCS severely degrade parameter estimates in highly augmented FCS modes (standard normal [SNR] and decoupled air-to-air gunnery [DAAG]). Model structure sensitivity is illustrated in the figure in which the vertical force stability and control derivatives with respect to angle of attack ( $C_{Z\alpha}$ ), stabilator deflection ( $C_{Z\delta H}$ ),

wing trailing-edge and flap deflection ( $C_{Z\delta F}$ ) are presented. It is seen that for a highly augmented mode, a model that does include flap effects will confidently generate biased estimates of all derivatives including the ones with the wrong signs.

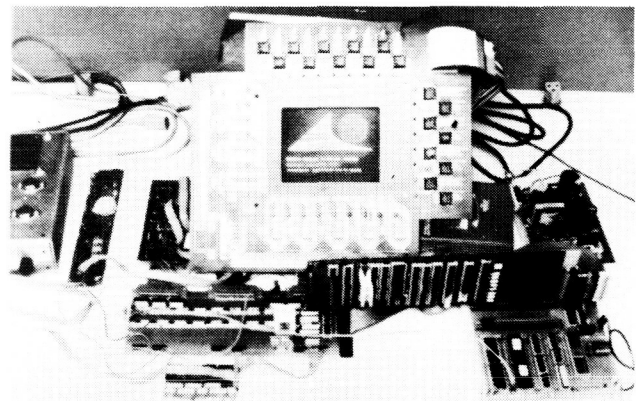
This enhancement and application of system identification methodology and the discovery of severe problems that may be induced by the nature of the FCS represent a step toward understanding the successful mathematical modeling of modern fighter aircraft in all flight regimes. This capability is highly important for safe operation of aircraft near flight envelope limits. (J. G. Batterson, 4887)

## First Practical Multicolor Thin-Film Electroluminescent Flat-Panel Display

Thin-film electroluminescent (TFEL) flat-panel display technology is needed to replace color CRT (Cathode ray tube) technology in future transport aircraft because of its potential to improve flexibility and reliability, reduce weight, space, and power consumption, and have graceful degradation characteristics. The TFEL display technology, however, is an emerging technology that has several technical challenges to overcome. Among these challenges is the need to increase screen size, improve resolution, and add color capability. The goal of this research is to significantly advance all of these capabilities.



Effect of adding flap term to standard linear model.



L-86-683

Multicolor TFEL display and brass board addressing electronics.

Because of the pioneering nature of our goal to achieve a new color display technology, the research plan has required the development of a series of complex materials and devices, each of which has been progressively more difficult to achieve. All research activity has been conducted under a NASA/Army/Navy contract. In the latest experimental TFEL flat-panel display, the screen size has been increased to 3.5 in. by 4.7 in., and the resolution has been increased to 68 lines per inch. These improvements have yielded a display with 240 by 320 picture elements. This new multicolor TFEL display provides a more realistic model to test phosphor systems and multilayer construction/addressing techniques. This display is the world's first TFEL color display that has a practical size and resolution.

(J. B. Robertson, 3917)

## Characterization of Fault Recovery Behavior of Fault-Tolerant Systems

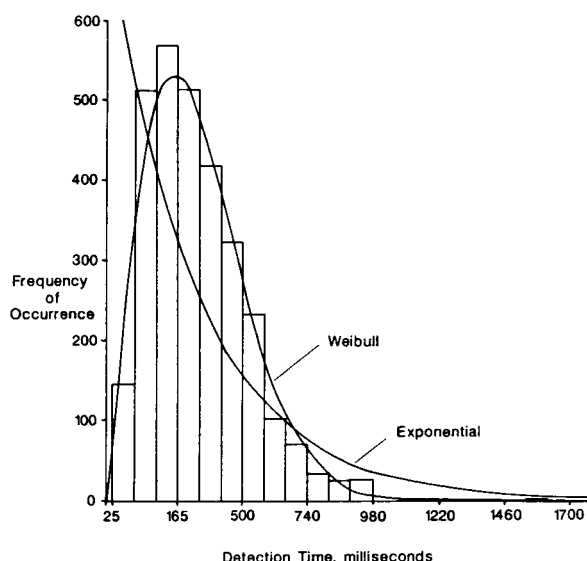
Reliability modeling and estimation are essential steps in designing and validating fault-tolerant systems. Architectures achieve fault tolerance and consequently high reliability by incorporating fault recovery mechanisms which enable them to continue functioning properly in the presence of faults. To produce credible reliability models and parameter estimates, it is necessary to characterize fault recovery behavior. This can be done by repeatedly injecting a fault into a test specimen and recording the times to detect the fault, to identify the faulty unit, and to reconfigure that unit out of the active configuration.

To provide the basis for the development of sampling methods and parameter estimation techniques, fault injection experimentation was conducted in AIR-LAB on the fault-tolerant multiprocessor (FTMP) system. "Stuck-at" type faults were injected at the pins of integrated-circuit chips in FTMP. The resultant fault detection times were analyzed to discover and identify the sources of variation in detection times and to establish the statistical distribution of the detection phenomenon. Detection time was chosen for analysis because it accounted for most of the variation in total recovery time. Multiple comparisons among the data sets showed that there were distinct groupings of detection time behavior; however, none of the factors varied in the experiment for the groupings. Distribution fitting revealed

that none of the distributions tested (exponential, normal, lognormal, Weibull, or gamma) could be shown to be the overall best.

Of particular importance is the result that the exponential distribution was the worst fit over all data sets investigated, thus refuting the common assumption of reliability modeling that detection times are exponentially distributed. These results suggest that stratified random-sampling methods and statistically robust parameter estimation techniques are required to characterize fault detect behavior.

(G. B. Finelli, 3681)



*Typical histogram of detection times with Weibull and exponential distributions superimposed.*

## Flight Test Design Considerations for Fault-Tolerant Integrated Avionics Sensor Configuration

A fault-inferring nonlinear detection system (FINDS) has been developed under a NASA Langley contract to ensure the integrity of flight data from integrated avionics sensors. The algorithm utilizes an extended Kalman filter to provide fault-tolerant aircraft state estimates required by guidance and control laws.

A bank of filters is used to estimate sensor failure levels. Isolation of failures is determined from likelihood ratios based on the failure estimator outputs.

The FINDS algorithm was developed by Charles River Analytics with the use of a digital simulation and flight-recorded data from a commercial transport aircraft. For flight test purposes, FINDS has been modified at NASA Langley to fit the size and execution speed constraints of the Center's simulator and aircraft flight computers. The table lists the program size and execution speed improvements of this effort. Near-real-time flight computer operation has been realized from these changes.

| FINDS Modifications                             | Program Size Kb | Execution Speed (x real time) |
|---|-----------------|-------------------------------|
| Double Precision                                | 340             | 120                           |
| Single Precision                                | 240             | 60                            |
| Reduced Array Sizes                             |                 |                               |
| Delete Interactive I/O                          | 126             | 50                            |
| Special Matrix Routines                         |                 |                               |
| Constant State                                  |                 |                               |
| Transition Matrix                               | 115             | 30                            |
| New Detection Strategy (without isolation test) | 115             | 11                            |
| Piecewise Constant-Gain                         |                 |                               |
| Update Frequency 4 Hz                           | 115             | 3.5                           |
| Update Frequency 1 Hz                           | 115             | 1.4                           |

*FINDS program size and execution speed modification summary.*

Improvements in sensor models and a new detection strategy have resulted in improved FINDS performance; however, failure detection performance as a function of piecewise constant-gain update frequency deteriorates below 4 Hz. Currently, the decoupled translational and rotational dynamics are being implemented on a dual-flight-computer configuration. This will allow real-time operation of FINDS at higher update frequencies as determined by bias estimation performance.

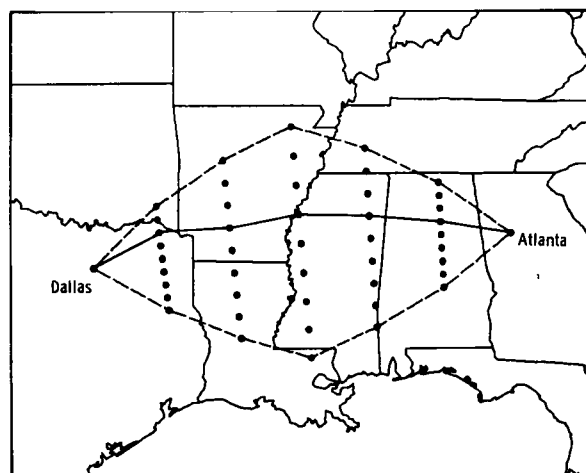
(F. R. Morrell, 3404)

## Algorithm for Computing Near-Optimum Flight Plans

Flight planning is a preflight, ground-based process that defines the horizontal and vertical path, fuel load, and speed schedule for flying between a given pair of cities. The method currently used by most airlines for flight planning is a direct search of a predefined set of routes to select the one that is most efficient to handle the forecasted weather conditions. NASA Langley contracted with Analytical Mechanics Associates (AMA) to develop an algorithm to compare various methods of flight planning which optimize direct operating costs. The algorithm was to include performance models for a variety of airplane types and a weather model to account for wind and temperature effects.

The characteristic constraints that must be considered in the flight planning process, such as reserve fuel requirements, route structure, and weather modeling, were defined in the initial phase of the study. Various optimization techniques were then investigated to determine those best suited for horizontal path optimization. The computer program developed through this study can serve as a useful tool to conduct sensitivity studies of various methods of flight planning and to evaluate the impact of weather and airplane type on that process. The flight planning algorithm is currently being documented for public release.

(D. D. Vicroy, 3621)



*Route grid structure for dynamic programming.*

## Impact of Advanced Technologies on Terminal Area Capacity

The Massachusetts Institute of Technology (MIT), under a grant funded by NASA Langley, performed a study to determine the potential improvements in terminal area capacity that could be achieved with various advanced technologies and procedures. A critical examination was made of current aircraft separation criteria, and variable, risk-based separation criteria were proposed. In the analysis, primary consideration was also given to a proposed approach concept that employed split, angled approaches to closely spaced parallel runways or to a single runway. By using capacity coverage curves, estimates were made of the annual capacity increase achievable at the Boston and Denver terminals.

The study indicated that the current 5-mile separation criterion contains adequate buffer space to be used as an acceptable performance criterion. In this case, it is expected that the 5-mile separation will be violated to a small degree about 50 percent of the time. The present practice of regarding less than a 5-mile separation as a safety violation causes controllers to use a larger working separation goal, thereby reducing airspace capacity. The separation criterion proposed by MIT was not a constant radius about the aircraft but varied with the conflict geometry. Analysis showed that the split approaches proposed by MIT produced an annual capacity increase of only 4.7 percent (e.g., at Denver) due to the high occurrence of weather that permitted visual approaches. At Boston, however, the technique produced a 37-percent capacity increase. Several research issues related to variable separation criteria and split approaches were identified. The results of this study show that the capacity improvements that can be realized from advanced procedures may be heavily dependent on the specific terminal area considered.

(D. A. Hinton, 3621)

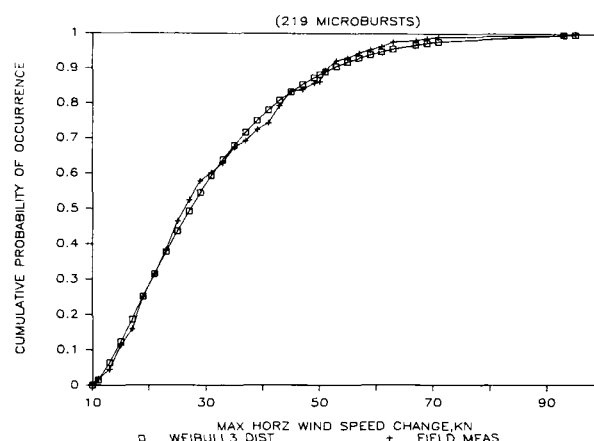
## Characterized Microburst Severity Via Weibull Probability Distributions

The importance of microbursts as a factor causing airplane accidents has been established. An important part of the NASA Langley effort, which encompasses airborne detection, avionics, and flight management, is the characterization of microbursts in terms of their wind shear severity. Specifically, the objective of this

effort is to define the probability distribution of wind shear severity in microbursts in order to predict exceedance probabilities and other statistical characteristics. This research effort provides an empirically based foundation for estimating the statistical properties of wind shear phenomena and is thus a vital step toward establishing alert/warning criteria for airborne systems.

An estimate of the probability distribution of wind shear magnitudes by the three-parameter Weibull distribution was completed. The microbursts data derived from field measurements used in the data fit and the estimated Weibull distribution are shown in the figure. The data are highly skewed, which is typical of wind speed data. Estimation of the empirical distribution and density by the Weibull method is considered good because the root mean square (rms) of the residuals is low (0.0187). A visual comparison of the two data sets also appears similar. These results suggest that the Weibull distribution provides an excellent characterization of the microburst phenomenon.

(B. T. McKissick, 3621)



*Comparison of Weibull and field measurements.*

## Application of Heart Rate Measures to Assessment of Pilot Workload

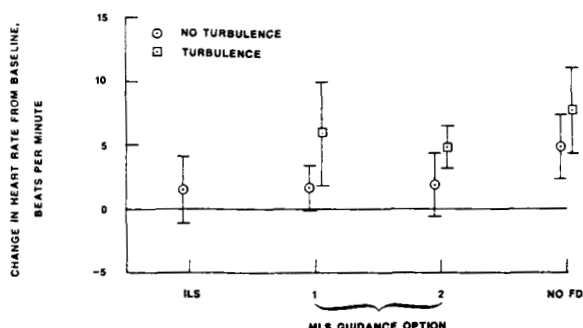
NASA Langley has been evaluating human physiological responses to quantify pilot workload.



Heart rate measurement has been shown by some researchers to be indicative of workload changes during aircraft flights; however, other researchers have not been able to obtain similar results in laboratory tests of mental tasks. Therefore, this effort was designed to evaluate whether heart rate measurement would be useful in simulated aircraft operations and to develop the appropriate experimental protocols and analysis techniques that would maximize the effectiveness of the measurement technique. Heart rate data were collected during a simulation project in the Langley Visual Motion Simulator (VMS), and these data were used to evaluate various Microwave Landing System (MLS) guidance schemes.

The analysis of the data showed that the difference in heart rate obtained during the period prior to the flight test (baseline), as compared to the period of the actual test landing approach, was a significant measurement parameter that was sensitive to some of the parameter changes imposed on the pilots. The incorporation of turbulence in the simulation produced an increase in the heart rate over the baseline. The removal of flight director information also resulted in an increase of the heart rate over the baseline. The use of heart rate measurements, when taken in consort with other physiological measures, will provide simulation-based researchers with a measure of the level of anxiety experienced by pilots during test runs.

(R. L. Harris, Sr., 3917)



*Heart rate measure adapted and applied to measurements of pilot workload.*

## Very-High-Speed Integrated-Circuit Processor Development

High-speed microprocessors will be needed to control system functions in future space transportation vehicles. Software and hardware models for very-high-speed integrated-circuit-based microprocessors, using the MIL-STD-1750A Instruction Architecture Set (ISA), have been developed and tested. These software and hardware simulation models were created using the Research Triangle Institute's Architectural Design and Analysis System (ADAS) software tool set to support empirical system requirements. The methodology for algorithm modeling and hardware mapping was generated from processor block diagrams, processor instruction cycle times, and MIL-STD-1750A ISA specifications. A general matrix multiplication algorithm was chosen for the initial testing since many engineering applications use this function. Comparative analysis and testing of the simulation model and actual algorithm performance on several 1750A processor implementations were conducted.

Comparative analysis of the algorithm simulation and the actual hardware performance revealed that the congruency of the software model is strongly dependent on the architecture of the hardware. The architectural considerations that had the most impact on the design of the software model were the level of pipelining within the microprocessor and the data flow parallelism for arithmetic operations. Incorporation of the architectural considerations into the software model was best achieved by adding subgraphs at the register transfer level (RTL) to preserve the integrity of the model for use in the comparative analysis of a variety of hardware implementations.

(K. T. Looney, 3777)

## Very-High-Speed Integrated-Circuit Multiprocessor Simulation

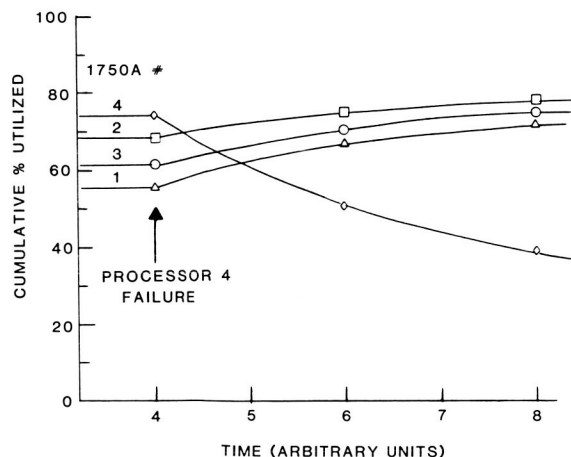
A NASA-Langley-funded simulation was made to evaluate the mapping of a triple modular redundant (TMR) flight control algorithm onto a very-high-speed integrated-circuit (VHSIC) modular multiprocessor architecture. This simulation, which was performed by Westinghouse Electric Corporation, was an initial effort toward the development of a design methodology that



afforded both simplex parallel processing and TMR processing. The method used self-testing, general-purpose, VHSIC multiprocessors and enabled flexible application of various degrees of fault tolerance. The computer system hardware used in the simulation consisted of four MIL-STD-1750A processors (each with 256 K local memory) and a global bulk-memory module for program storage and fault logging.

The flight algorithm was arranged in a directed graph representation with logically related functions grouped into similarly sized software nodes. The operating system for the TMR simulation incorporated software-implemented fault-detection and reconfiguration scenarios. The occurrence of a failed processor, as shown in the figure, resulted in the autonomous reconfiguration of the processor system to exclude the faulty processor. Although no processing bottlenecks were detected, the operating system required an excessive 89-percent processor utilization. This result identifies the need to optimize both the operating system and the application algorithm to reduce the number of queues. With such optimization, it appears that the processor utilization due to the operating system can be reduced by more than 50 percent.

(P. J. Hayes, 3777)



*Dynamic reconfiguration simulation.*

## Information Network Architecture

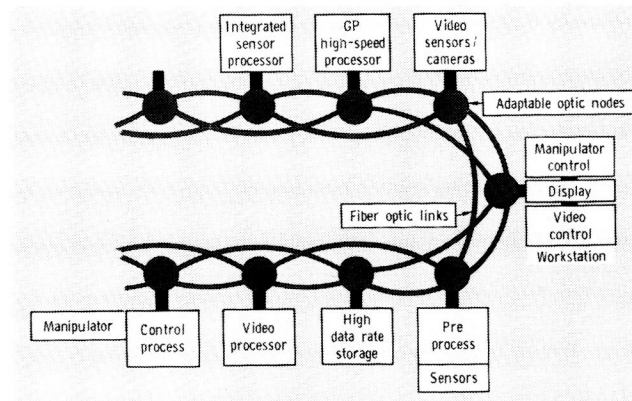
A major problem in the creation of future information systems for applications such as NASA's Space

Station or Aero-Space Plane is the design of adaptable, high-performance, fault-tolerant data networks that can evolve as mission requirements change. Because these networks will carry real-time data, both delays and delay variability must be minimized.

As part of its data systems research program, NASA Langley is identifying and developing network technologies for future information systems. This effort has determined that the bandwidth and delay characteristics are bimodally distributed for an integrated digital video-image and data network. Most control and process-to-process communications require data rates of less than 100 Mbps and can tolerate low transmission delays. Digital video-speed requirements are 2 to 3 orders of magnitude more stringent but can better tolerate delays provided delay variability is minimized and sufficient short-term storage is provided.

The analysis has identified key architectural elements capable of meeting the diverse traffic requirements. These elements include data transfer/control strategy, network topology, and protocols to employ on the network. One study conclusion has been that the multiconnected braided mesh topology (shown in the figure) is a good compromise among availability, performance, modularity, complexity, layout, and ease of implementation in optics. Of the three fundamental switching classes (circuit, message, and packet), it has been determined that a fast-circuit-switched approach is the most appropriate method to handle both video-image and interprocessor data. This approach can be easily implemented in optics.

(N. D. Murray, 3535)



*High-performance, fault-tolerant network.*

## Real-Time Video Processing

A key challenge to the success of man working in the Space Station environment is efficient use of available crew time. Initially, a crew member will interactively control (either directly or remotely) most activities. During this man-in-the-loop phase, it is important to provide the operator the best available information. As the Space Station matures, many operations will become autonomous (with human supervision), thus freeing man for higher level decision making and creative thinking.

An important technology central to automation and robotics is that of image processing. During the man-in-the-loop phase, video images will be presented to operators from cameras located near an activity. As more automation is incorporated, video processing will assist many activities that initially required human intervention.

Potential functions for video-image processing were investigated. For real-time video, these functions (and their complex image analysis tasks) result in enormous data volumes that are well beyond the performance capabilities of conventional computer architectures. This is illustrated by the figure, which shows the type of processing operations required, the rates, and the most suitable type of parallel architecture.

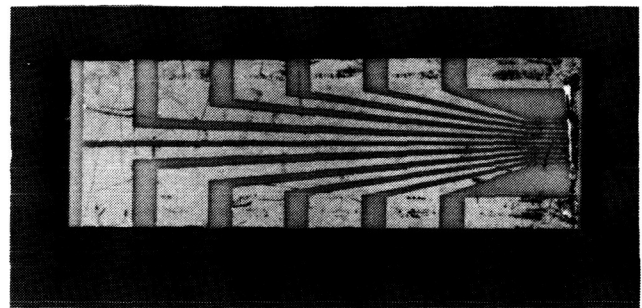
The figure shows that as video information proceeds from processing raw sensor data (low level) to the presentation of symbolic information (high level) there is a need for several computer architectures. A single optimal architecture for all does not presently exist. A given architecture degrades significantly and rapidly when applied to problems outside of its domain. It was found that low-level functions are best executed

by an array processor, and higher level processing is best done by a multiprocessor architecture.

(N. D. Murray, 3535)

## Linear Laser Diode Array for High-Speed Optical Disk Recorder

Future long-term space missions will require the storage of large quantities of data for long periods of time. Optical disks meet this need by providing a means by which large quantities of data ( $10^{12}$  bits) can be stored. Effective use of the optical disk recorders requires data recording/readout rates of  $10^9$  bits/sec. These high rates can be achieved through the use of multiple diodes in a linear array. As part of its electronics and data systems research program, NASA Langley has been developing AlGaAs channelled substrate planar linear array semiconductor lasers for optical disk recording.

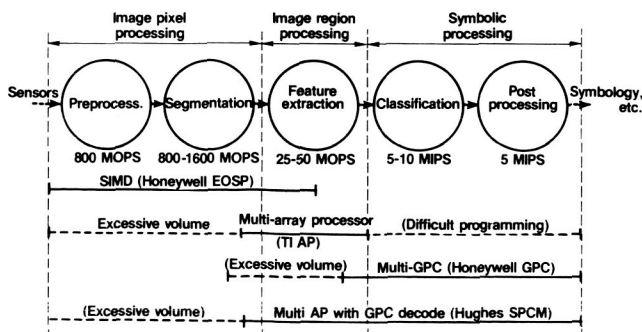


L-84-10,174

10-element linear laser diode array.

Target performance parameters of a 10-element linear array have recently been obtained for the first time in United States industry at RCA's David Sarnoff Research Laboratory and have been confirmed in tests at NASA Langley. This parameter research was funded by NASA Langley. Multiple arrays, which consist of 10 individually addressable lasers, have been demonstrated. Each laser is capable of 30 mW of power output with almost identical far-field patterns for each of the 10 lasers. Power-versus-current characteristics for each laser in the array were within  $\pm 10$  percent of the average value. This technology provides at least an order-of-magnitude increase in speed over current methods and thus allows full recording speed to be achieved in the high-speed optical disk buffer.

(H. D. Hendricks, 3777)



Real-time image-processing architecture.

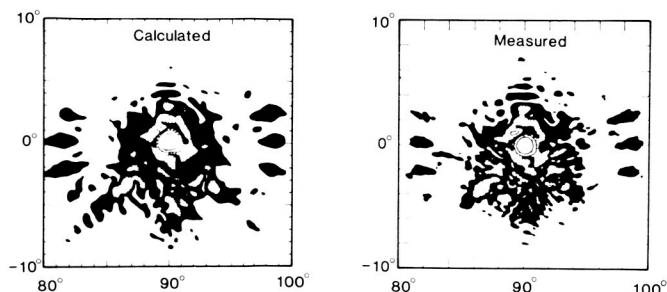
## Regional Pattern Calculations for Large Reflector Antennas

Research to develop analytical methods and computer codes has been completed which will enable the designer of future large space deployable antennas to calculate the radio frequency (RF) performance of mesh reflectors whose surface contains thermal, structural, and design configurations.

The use of geometrical optics combined with aperture integration techniques gives good results for reflector antennas in which the surfaces slowly vary. The calculation of the antenna radiation pattern for an antenna over an angular ( $\theta$ ,  $\phi$ ) region (as opposed to a constant  $\theta$  or constant  $\phi$  plane) requires the double numerical integration of electromagnetic fields over the projected aperture of the antenna for each  $\theta$ ,  $\phi$  direction. A technique, which is documented in NASA TM-87644, has recently been developed which models the aperture as an overlapped array of subapertures and thereby reduces the numerical integration problem to a summation with a small number of terms. This approach enables the calculation over an angular region to be performed in an efficient and accurate manner.

The overlapping subaperture approach has been applied to the 15-meter hoop/column antenna to calculate the contour radiation patterns and to compare with measurements. The figure shows these results for a cluster feed design (NASA TM-85666) and includes the effect of distortions as well as the feed spillover onto adjacent reflecting paraboloidal surfaces.

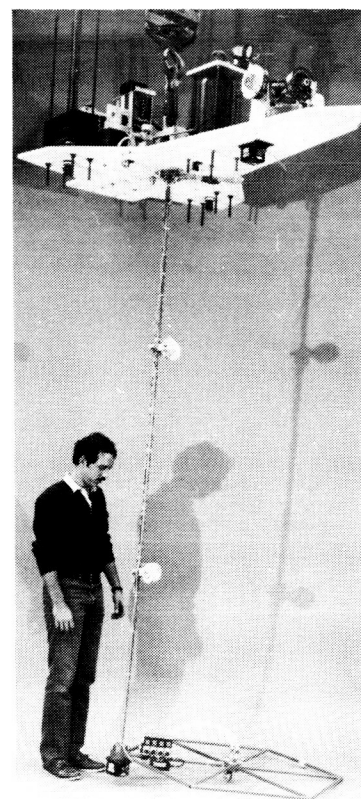
(M. C. Bailey, 3631)



15-m hoop/column antenna, 4.26-GHz contour radiation patterns (10 dB increments).

## Spacecraft Control Laboratory Experiment

Analytical investigations into the identification and control of large space structures have received much attention from the research community for many years; however, few laboratory validations of these developments have been conducted because of the lack of available testing facilities. The Spacecraft Control Laboratory Experiment (SCOLE) has been conceived to provide an accessible physical test bed to evaluate control techniques for large flexible spacecraft (as shown in the first figure).



L-85-12,278

SCOLE test facility.

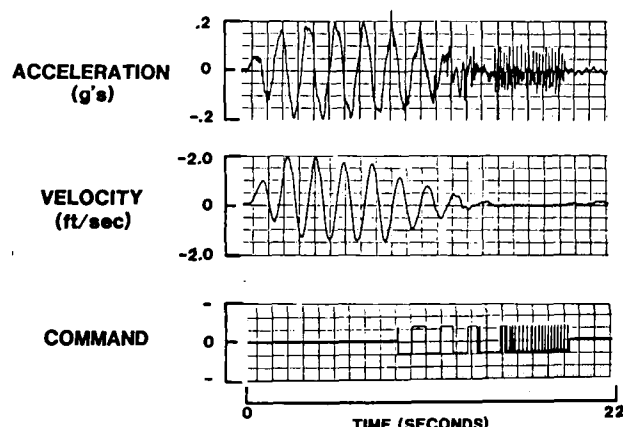
The facility consists of a planform representation of the Space Shuttle with an attached flexible beam that supports a generic rigid reflector. The Space Shuttle representation is equipped with a set of double-gimbal control moment gyros (CMGs) to provide system control for maneuvering and reorientation. Twin reaction wheel

assemblies are attached to the flexible beam for control of the flexible modes. The reflector is also equipped with a reaction jet package for maneuver load alleviation, vibration suppression, and control. Appropriate sensors, such as accelerometers, rate gyros, and remote optical position sensors, are also provided with this facility and are used in system performance evaluation and loop closures. This test bed development has been complemented with a series of thorough mathematical representations to permit early validation of any proposed algorithm. Access to the test bed can be achieved from remote user sites through telephone hookups, thus minimizing costs associated with experimental validation programs.

Test results from this facility are shown in the second figure. Suppression of the first vibrational mode of the cantilevered beam of the SCOLE configuration was effected using the reaction jet system located at the hub of the reflector. The control method utilized in this test was highly effective in damping out the encountered disturbance.

(J. P. Williams, 4591)

Cantilevered Mast – First Mode



*SCOLE vibration suppression using on-off thrusters.*

## Near-Field Testing of 5-Meter Tetrahedral Truss Reflector

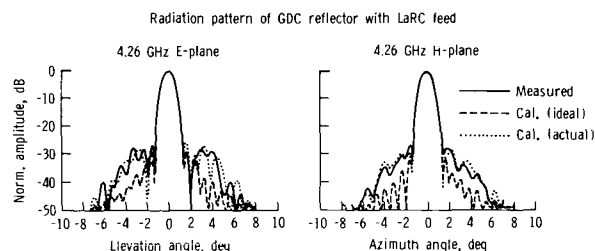
NASA Langley has sponsored a near-field test of a 5-m tetrahedral truss reflector, which was manufactured by the General Dynamics Convair (GDC) Corporation, to determine its radio frequency (RF) performance characteristics and to study deployable reflector

concepts for large space antenna applications. These tests were conducted in the Martin Marietta Near-Field Facility in Denver, Colorado.

The NASA Langley feeds used for earlier hoop/column tests were adapted to the GDC feed structure and to a subset of patterns that were run identically to those for the hoop/column antenna. The reflector surface was mapped using the same photogrammetry and near-field phase mapping techniques as those used for the NASA Langley hoop/column reflector. A NASA-Langley-developed code was used to calculate the far-field patterns expected from this antenna surface as well as antenna feed type, frequency, polarization, and orientation. Analyses of these data consist of calculated versus measured far-field patterns and photogrammetric versus near-field phase surface measurements. A set of 10 measurement tests was conducted at frequencies of 2.27 GHz, 4.26 GHz, 7.73 GHz, and 11.6 GHz using both co- and cross-polarization. One test was conducted using a scanned beam. A complete set of photogrammetric data was obtained and reduced by Geodetic Sciences, Incorporated and NASA Langley.

The following results were obtained: (1) The surface measurements made by the near-field phase method and by the photogrammetric methods were in good agreement; (2) Unexpected surface anomalies of 33 mil rms (with peak values of 180 mil) were detected by both the photogrammetry and the near-field phase measurements; and (3) Far-field pattern measurements, including the higher sidelobe levels due to 33 mil rms surface distortions, were shown to be in very good agreement (as shown in the figure) with calculated patterns using the actual surface as an input. These analyses will be added to the growing body of knowledge of RF performance of large-scale mesh antennas. The data will be utilized to further the development of large-scale antenna systems.

(L. C. Schroeder, 3631)



L-86-6819

*NASA-Langley-sponsored tests and electromagnetic analysis of tetrahedral truss reflector.*

## Improved Image Gathering and Processing

An improved mathematical foundation has been developed for the design of image-gathering systems and for the formulation of data processing algorithms, both for restoring clear and sharp images and for improving machine vision systems.

This advance consists of (1) extending Shannon's formulation of communication theory and Wiener's formulation of optimal filtering, both for time-varying signals, to image gathering and digital processing for spatially varying radiance fields, and (2) relating the information density of the acquired image data to the fidelity of images that are optimally restored. The extension of Shannon's communication theory to image gathering and processing has not been attempted before, and the previous extension of Wiener's optimal filter to image restoration has not been generally valid. This failure of previous Wiener and other image-restoration filters to correctly account for the image-gathering degradations has pervaded throughout published papers and books on image restoration and has led to many erroneous conclusions about the design of image-gathering systems and the performance of data processing algorithms.

Analyses and computer simulations show that (1) informationally optimized image-gathering systems tend to maximize the fidelity of optimally restored images, (2) the properly formulated Wiener-restoration filter significantly improves upon the performance of the conventional Wiener-restoration filter, and (3) an intuitively satisfying relationship exists among the informationally optimized design of image-gathering systems, the response and sensitivity of natural vision, and the reliable detection of radiance-field changes (e.g., edges) for pattern recognition and machine vision.

(F. O. Huck, 3777)

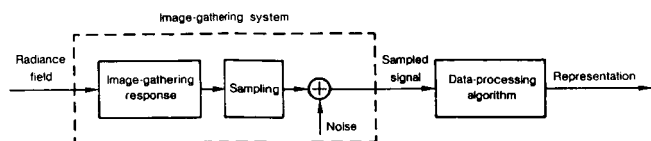


*Image-gathering and processing system.*

## Multifunction Recognition Operator for Robotic Vision

The primary task of a vision sensor in a robotic system is to provide information about the position of the system's effector relative to objects of interest in its environment. The task is accomplished by performing functions that allow the recognition and location of the targeted objects by analyzing their images as recorded by the sensor. The functions include segmentation of the image to isolate each of the objects, decomposition of each complexly shaped object into simple shapes, recognition of the simple shapes, and determination of the orientation and location of the object in the axis system of the robot's effector. An operator has been developed which performs the functions of simple shape recognition and object location in human real time (approximately 0.25 sec) and can be extended to accomplish the other functions.

The operator is based on the elastic template matching approach to pattern recognition in which the model of an object is distorted to approximate the image of the object. The template is a system of equation pairs in which each pair represents a linear combination of patterns that a point on the model can describe in moving to a point on the image. The amount of displacement that each pattern contributes to the distortion is determined by identifying the values of the parameters  $A_i, B_i$  associated with each of the distortion patterns. The parameter values are derived by minimizing the difference between corresponding model and image points without violating the pattern constraints. The computational tool used to identify the parameters is the simplex algorithm.

$A_0, B_0$  : Displacement

$A_1, B_1$  : Gain

$A_2, B_2$  : Rotation in X-Y plane

$A_3, B_3$  : Perspective of triangular shape information

$A_4, B_4$  : Semicircular shape information

$A_5, B_5$  : Elliptical shape information

$f(X, Y)$  : Model function

$f(X', Y')$  : Image function

$$X + A_0 + A_1X + A_2Y + A_3XY + A_4(X^2 - Y^2) + A_5XY^2 = X'$$

$$Y + B_0 + B_1Y + B_2X + B_3XY + B_4(Y^2 - X^2) + B_5YX^2 = Y'$$

| Distortion pattern | Distortion term |
|--------------------|-----------------|
|                    | XY              |
|                    | $XY^2$          |
|                    | Y               |
|                    | $Y^2 - X^2$     |
|                    | $YX^2$          |
|                    | X               |
|                    | $X^2 - Y^2$     |

*Elastic matching algorithm.*

A single prototype shape (e.g., a rectangle) can be used to identify several simple shapes by distorting it to match the image of some unknown shape. The values of parameters  $A_3$  through  $A_5$  and  $B_3$  through  $B_5$  yield information that allows recognition of triangles, rectangles, and ellipses regardless of orientation. Once an object is identified, either as a simple shape or a combination of simple shapes, an exact model of its normal view is distorted to match the known image, and information regarding its location and orientation can be derived from the parameters  $A_0$  through  $A_3$  and  $B_0$  through  $B_3$ .

(P. W. Goode, 3871)

# Space Directorate

The Space Directorate conducts research in atmospheric and Earth sciences, identifies and develops technology for advanced transportation systems, conducts research in energy conversion techniques for space applications, and provides the focal point for conceptual design activities for both large space systems technology and Space Station activities.

The Atmospheric Sciences Division is a leader in the area of atmospheric sciences. Its researchers are involved in seeking a more detailed understanding of the origins, distributions, chemistry, and transport mechanisms that govern the regional and global distributions of tropospheric and stratospheric gases and aerosols, and in the study of the Earth radiation budget and its effect on climate processes. The research seeks to better understand both natural and anthropogenic processes and covers a wide spectrum of activities, including the development of theoretical and empirical models; collection of experimental data from in situ and remote sensing instruments designed, developed, and fabricated at NASA Langley; organization of extended field experiments; and development of data management systems for the efficient processing and interpretation of data derived from airborne and satellite instruments.

The Space Systems Division conducts research on and systems analysis of advanced transportation systems, large space systems, and space station concepts, as well as basic research on energy conversion techniques for potential space application. The division is a leader in the development of highly interactive and user-friendly computer-aided design (CAD) tools that enable the rapid evaluation of system concepts and the identification of technologies necessary for the development of space transportation systems, large space systems, and the Space Station. The evaluation of advanced space transportation systems covers a wide range of capability, including Earth-to-orbit vehicles, Shuttle II, orbit-on-demand launches, service vehicles, and orbital transfer vehicles.

The development of orbiter experiments that utilize the Shuttle as a reentry research vehicle to study aerothermodynamic and aerodynamic characteristics has been a key activity and one which will provide the data base required for the development of advanced vehicle systems.

The Space Station Office is the focal point for NASA Langley involvement in the Agency-wide Space Station Program and is responsible for the implementation and/or coordination of NASA Langley's direct support of this program. The Space Station Office is the

NASA lead for the identification, definition, and evaluation of the Evolutionary Space Station capabilities and for the identification of technology and advanced development required for long-term evolutionary development. The office represents the engineering community as technology users of the Space Station. It also advocates flight experiments on future Space Shuttle flights which contribute to Space Station technology use as well as flight experiments from technology programs which can contribute to both the initial operational capability and the evolutionary station. The office provides NASA Langley support to the NASA-wide in-house Space Station systems engineering and integration in areas consistent with demonstrated NASA Langley capabilities and expertise.

## Study of Tropospheric Trace Gases From Satellites

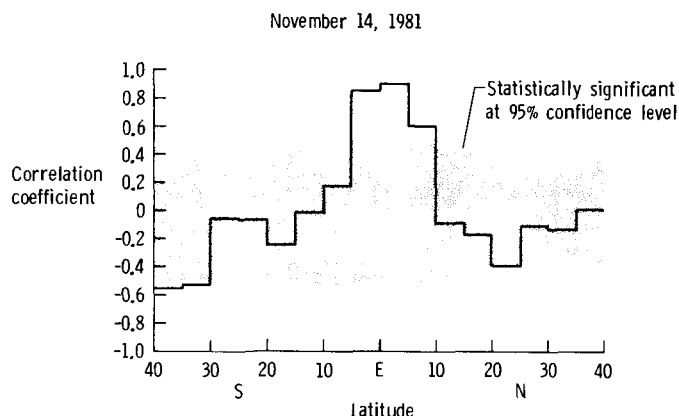
Although approximately 90 percent of the ozone in the atmosphere is located in the stratosphere, a recent study at NASA Langley suggests that the variability of the tropospheric component of total ozone (i.e., the remaining 10 percent) may be primarily responsible for the variability of the total column at tropical latitudes. The correlation coefficients depicted in the figure compare total ozone measurements on November 14, 1981, from the TOMS (Total Ozone Mapping Spectrometer) instrument on Nimbus 7 with carbon monoxide measurements on the same day taken with MAPS (Measurement of Air Pollution from Satellites), which is a NASA-Langley-developed instrument that was flown aboard the Space Shuttle on that date. To examine the relationship between TOMS and MAPS data, a linear regression coefficient has been computed for the two variables for every 5° latitude band.

As can be seen from the figure, a very strong positive correlation between these two quantities is present between 5°S and 10°N (at statistically significant values well above the 95-percent confidence level). Since all carbon monoxide sources are located in the troposphere, the strong co-variability of these two quantities suggests that total ozone variability at low latitudes is highly influenced by a tropospheric source that is probably biomass burning. The relatively high anticorrelation between TOMS and MAPS at southern mid-



latitudes is probably a result of large-scale atmospheric circulation processes.

(J. Fishman, 2294)



*Correlation between TOMS total ozone and MAPS carbon monoxide measurements.*

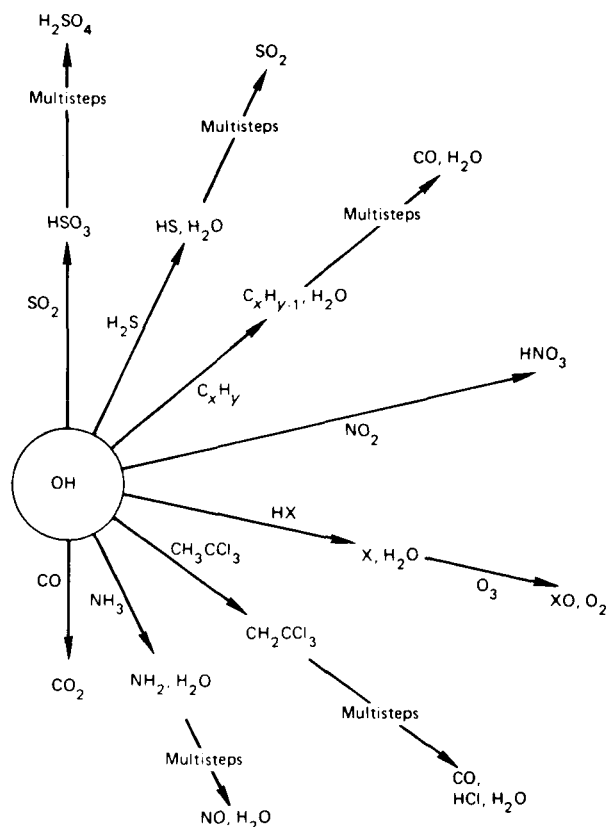
## Increasing Atmospheric Levels of Ethane

Nonmethane hydrocarbons (NMHC) are compounds that contain atoms of hydrogen and carbon in various combinations and are an important family of chemically active atmospheric trace gases. Ethane ( $C_2H_6$ ) is the most abundant atmospheric NMHC. Ethane is produced by the burning of biomass (e.g., forests, grasslands, and agricultural fields) and gasoline (in internal combustion engines) and is also released into the atmosphere during the collection of natural gas. Ethane and the other NMHCs react with the hydroxyl radical (OH) which initiates a series of chemical reactions that lead to the chemical production of carbon monoxide (CO) (as shown in the figure). In fact, the reactions between OH and methane ( $CH_4$ ) and the NMHCs are the major sources of CO on the global scale. This is particularly important because CO not only controls the global destruction of OH (by far the most chemically active gas in the lower atmosphere) but also controls the chemical lifetime of almost every atmospheric gas (also shown in the figure).

Ground-based solar infrared spectra obtained in 1951 at the Jungfraujoch Scientific Station in the Swiss Alps and analyzed at NASA Langley indicated that northern hemispheric mid-latitude atmospheric levels

of  $C_2H_6$  may have increased by about 70 percent over the last 3 decades. This discovery represents one of the largest increases in the concentration of an atmospheric gas. Calculations performed at NASA Langley with a one-dimensional photochemical model of the troposphere indicate that the 70-percent increase in atmospheric  $C_2H_6$  may be explained by a 33-percent increase in the production of  $C_2H_6$  by its surface sources (the only significant sources of  $C_2H_6$ ). This new evidence of increasing atmospheric concentration of  $C_2H_6$ , along with the recent discovery that atmospheric concentrations of CO may have increased by about 70 percent and  $CH_4$  by 40 percent since 1951, clearly suggests that the trace gas composition of the atmosphere is not static but varies, which is probably due to anthropogenic activities.

(J. S. Levine, 2187)



*Key role of the hydroxyl radical (OH) in the chemical transformation of trace gases in the lower atmosphere. OH transforms nonmethane hydrocarbons, such as ethane, to carbon monoxide, which in turn controls the global destruction of OH itself.*



## Airborne Lidar Measurements of Ozone and Aerosols Over Amazon Rain Forest of Brazil

The NASA Ultraviolet Differential Absorption Lidar (UV DIAL) system was flown during July and August 1985, as part of the NASA Global Tropospheric Experiment (GTE) Amazon Boundary Layer Experiment (ABLE-2A). Investigations of aerosol and ozone distributions were conducted in undisturbed and disturbed atmospheric conditions over the tropical rain forest near Manaus, Brazil. The UV DIAL system was operated from the NASA Wallops Electra aircraft to remotely obtain profiles of aerosols and ozone below the aircraft and profiles of aerosols above the aircraft.

The airborne lidar system provided detailed information on the structure and dynamics of the planetary boundary layer (PBL) and free troposphere in undisturbed and disturbed atmospheric conditions. The PBL depth was found to be typically less than 50 m at night, and by 10:00 l.s.t. (local standard time), the PBL depth was about 500 m with an average growth rate during the late morning of 10 cm/sec. The depth of the PBL from the previous day ranged from 2.2 to 3.2 km. Undisturbed daytime ozone mixing ratios were found to be about 17 ppbv (parts per billion by volume) in the PBL and 25 to 30 ppbv in the lower free troposphere. Regions of high- and low-ozone mixing ratios were seen in outflow regions of deep convective storms due to downward and upward transport processes, respectively. Large-scale variations in the vertical and horizontal distributions of ozone and aerosols were observed on all flights with ozone exceeding 50 ppbv in localized regions of haze related to biomass burning. A significant increase in ozone and aerosol concentrations across the Amazon Basin was observed over the period of ABLE-2A. These results are being interpreted in relation to the chemistry and dynamics of the atmosphere over the tropical rain forest of Brazil.

(E. V. Browell, 2576)

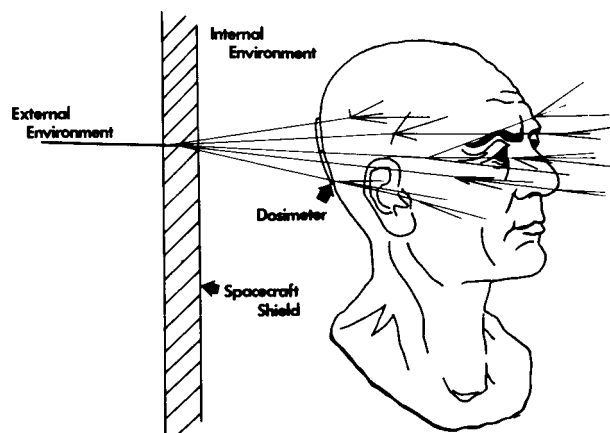
## Modeling Space Radiation Effects

In the approaching era of career astronauts and space workers who may spend significant periods of time in space, knowledge of galactic cosmic ray interaction and transport in bulk matter is required to accurately analyze requirements for shielding astronauts and

spacecraft components from these radiations. Of particular interest is the high-energy heavy ion (HZE) component of the incident space radiation spectrum. As these high-velocity nuclei strike the spacecraft, they undergo nuclear fragmentation (breakup) interactions within the vehicle structure and components and also within the bodies of the astronauts. Accurate methods to describe the transport of these HZE particles through bulk matter are under development at NASA Langley; however, efforts are hampered by an inadequate experimental data base and a lack of knowledge of the underlying physics involved in the fragmentation process. Recently, a simple calculational method for estimating fragmentation cross sections for use as input into HZE transport computer codes was developed.

This semiempirical HZE fragmentation model is a modification of an earlier two-stage (abrasion/ablation) model proposed by researchers at the Lawrence Berkeley Laboratory (LBL). As originally formulated, the LBL model reproduced general trends observed in the experimental fragmentation data, but its predictions were often inaccurate. By incorporating a second-order correction to the nuclear surface energy term used to estimate the excitation energy following the abrasion step, improved estimates of the fragmentation cross sections were obtained. Further improvements in the accuracy of the predictions were obtained by incorporating a frictional interaction term that treats these fluctuations explicitly. The full development of the model awaits the resolution of disagreements among various existing experimental data sets and an expansion of the data base to a wider range of projectile-target combinations.

(L. W. Townsend, 3781)



*Space radiation transport and effects.*

## Atomic Oxygen Beam Generator

The composition of the atmosphere at a spacecraft's orbital altitude (200 to 1000 km) combined with the spacecraft orbital velocity results in hyperthermal atomic oxygen (O) impinging on spacecraft surfaces with a flux of  $10^{15} \text{ cm}^{-2}\text{-sec}^{-1}$  and a kinetic energy (E) of approximately 5 eV. The high chemical reactivity of this O-atom flux has caused substantial degradation of organic materials aboard the Space Shuttle and suggests that materials on the proposed Space Station, composites used in large space structures, exterior coatings on the optics of the Hubble Space Telescope, proposed ultraviolet telescopes, and future laser communications systems may have substantially reduced lifetimes. It is therefore essential to study the reactivity of these materials toward atomic oxygen in ground-based laboratories.

A promising approach to develop a laboratory atomic oxygen gun that simulates the orbital condition involves the use of two unique phenomena: the unusually high permeability of oxygen through silver and the utilization of electron stimulated desorption (ESD). Normally, when the O atoms arrive at the vacuum interface, surface diffusion occurs and results in O-atom collisions and subsequent desorption of  $\text{O}_2$  molecules. By using an incident flux of low-energy electrons (100 to 500 eV) upon this surface, the O atoms are excited to antibonding states before they can recombine and desorb

as hyperthermal O neutrals and  $\text{O}^+$  ions with an energy of  $1 > E > 10 \text{ eV}$ .

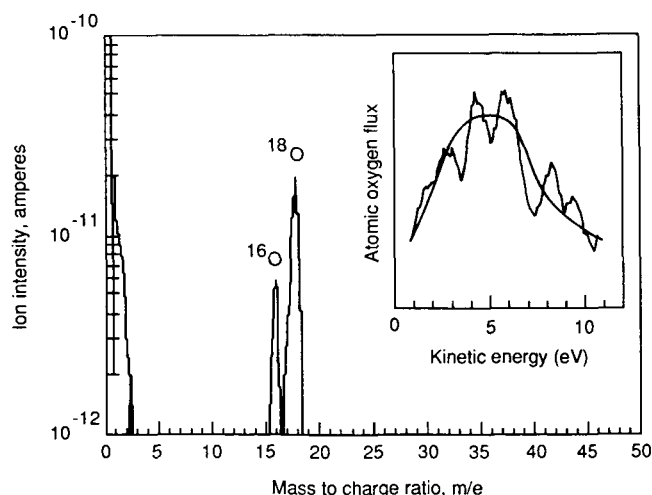
Results of laboratory experiments have demonstrated proof of this concept. High-purity atomic oxygen signals with flux levels greater than  $1 \times 10^{12} \text{ cm}^{-2}\text{-sec}^{-1}$  and kinetic energies between 2 and 6 eV have been measured and provide a basis for the development of a laboratory instrument.

(R. A. Outlaw, 3781)

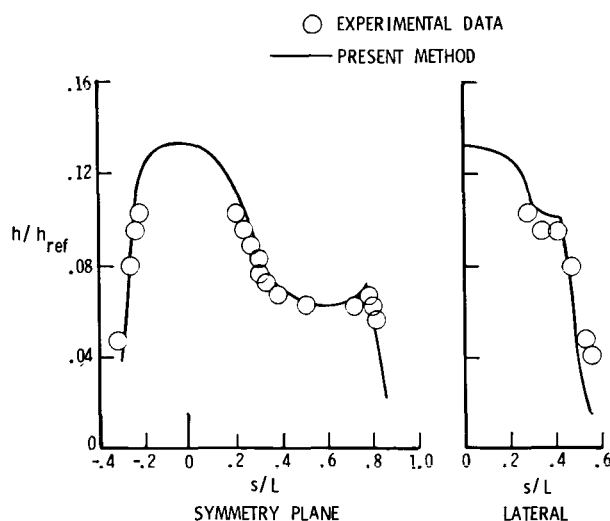
## Calculation of Heating on Aeroassist Flight Experiment Vehicle

A method developed for calculating heating on general three-dimensional vehicles has been used to predict the heating rates on the Aeroassist Flight Experiment (AFE) vehicle. The method is based on an approximate three-dimensional boundary-layer code (AA3DBL) and uses the results from an inviscid flow field solution (HALIS) to determine edge conditions for the boundary-layer calculation.

The AFE vehicle is composed of a blunted, raked, elliptic cone with a skirt attached near the base. The skirt reduces the heat at the end of the cone where the flow expands rapidly into the base region. Nondimensional heat-transfer coefficients ( $h/h_{\text{ref}}$ ) calculated using



Atomic oxygen signal intensity desorbed by ESD from silver surface. Insert shows kinetic energy distribution of the flux.



Heating distribution on AFE vehicle.

the present code are shown in the figure along with experimental wind tunnel data measured at Mach 9.86. The distributions with nondimensional surface distance ( $s/L$ ) are shown in both the symmetry plane and in a lateral direction away from the symmetry plane. The angle of attack for this case is  $0^\circ$ , which is approximately the angle of attack at which the vehicle has been shown to trim in flight. The agreement between the present calculations and the experimental data is excellent. (H. H. Hamilton, 3271)

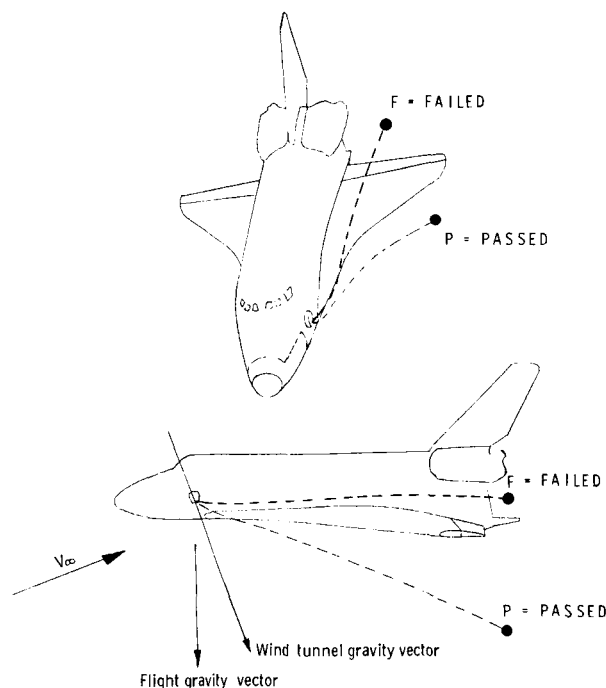
## Factors Affecting Crew Escape Trajectories From Shuttle Orbiter at Subsonic Speeds

Several factors that affect the bailout characteristics from the Space Shuttle orbiter at low-subsonic speeds were examined in the Langley 12-Foot Low-Speed Tunnel and the Langley 4- by 7-Meter Tunnel with 0.03-scale crew models. Tunnel conditions corresponded to

full-scale values of an altitude of 15,000 ft and velocities of 316 to 365 ft/sec depending on vehicle angle of attack. Exits from the main side hatch were investigated in the wind tunnel for ranges of angle of attack and sideslip with the orbiter model upright and from the upper cabin hatch with the orbiter model inverted. The effects of crew model weight (scaled values of 150, 200, and 250 lb), model configuration (standing, seated, and tucked), and model exit velocity were studied.

The escape trajectories of the crew models exiting from the side hatch were most affected by body configuration. The tucked, low-drag position produced the highest percentage of successful escape trajectories. (An escape was considered to be successful when the crew model passed below the wing without striking any part of the vehicle.) Also, the heavier crew models had a higher success rate than the lighter models. In general, the higher exit velocities produced a higher number of successful drops for all crew-model configurations. The 250-lb scaled model was successfully dropped in the seated and tucked positions at full-scale exit velocities equal to or greater than 8 ft/sec, but the lightest model (scaled to 150 lb) was successful only at full-scale exit velocities of 20 ft/sec or greater. With the orbiter model inverted, all crew-model exits from the upper hatch were successful.

(G. M. Ware, 3984)



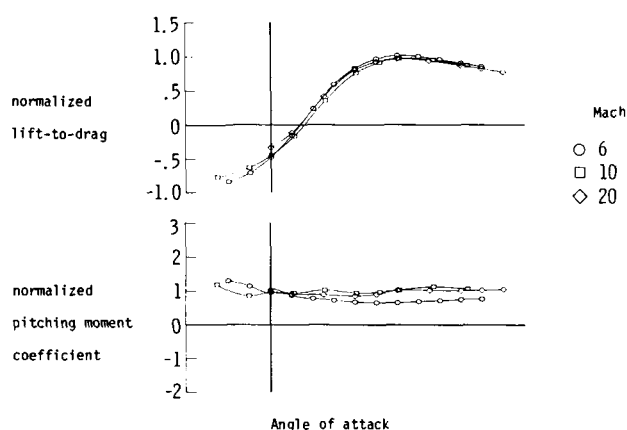
*Pass-fail examples for typical escape trajectories from main side hatch of orbiter model.*

## Hypersonic Aerodynamic Characteristics of Maneuvering Reentry Research Vehicle

Aerodynamic coefficients for a lifting configuration proposed by the Air Force as a maneuvering reentry research vehicle (MRRV) were measured in several NASA Langley hypersonic wind tunnels. The MRRV was conceived to provide flight data along trajectories representative of advanced reentry vehicles but not possible with the Space Shuttle orbiter because of aerodynamic limitations and safety concerns. Static longitudinal and lateral-directional characteristics on a 3.5-percent scale model were examined over Mach numbers from 6 to 20 and a range of Reynolds numbers. The effect of body flap deflections, elevon deflections, and nose bluntness on longitudinal characteristics and the effect of rudder and aileron deflections on the lateral-directional characteristics were determined at angles of attack from  $0^\circ$  to  $18^\circ$  and sideslip angles of  $0^\circ$ ,  $2.5^\circ$ , and  $5^\circ$ .

Control effectiveness was adequate to provide longitudinal trim from the maximum lift-drag ratio  $(L/D)_{\max}$  to the maximum angle of attack tested. The MRRV was stable in rolling moment and side force due to variation in sideslip angle but unstable in yawing moment at angles of attack below  $(L/D)_{\max}$ ; however, this instability was small at  $(L/D)_{\max}$ . The rudder had negligible effect on lateral-directional stability at angles of attack in excess of  $8^\circ$ , corresponding to the shielding of the vertical fin by the body. Blunting the nose decreased the trimmed  $(L/D)_{\max}$  about 20 percent. A decrease in Reynolds number resulted in a decrease in  $(L/D)_{\max}$  for the baseline configuration with controls set at zero.

(G. J. Brauckmann, 2483)



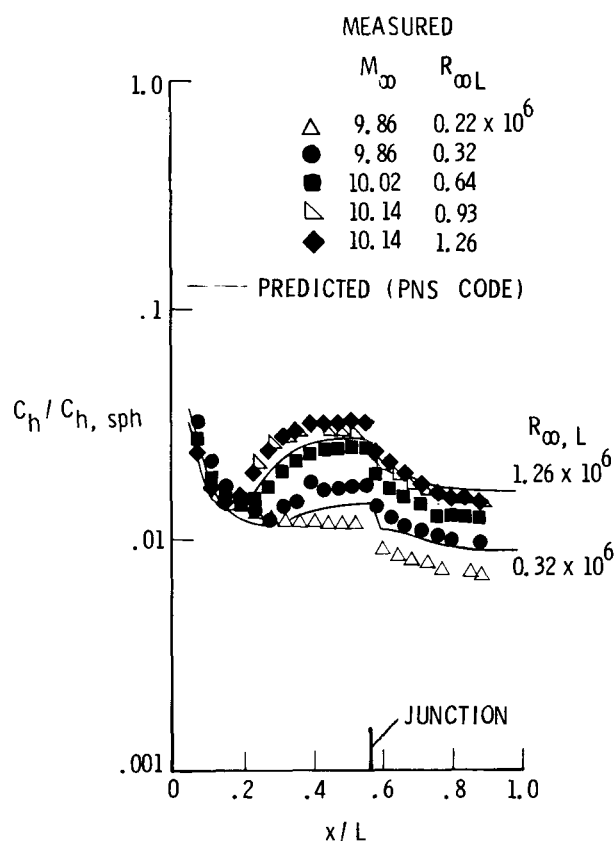
Effect of Mach number on longitudinal characteristics.

## Measured and Predicted Vortex-Induced Leeward Heating on Biconic Planetary Entry Vehicle at Mach 6 and 10

Detailed longitudinal and circumferential heating distributions were measured on the leeward side of a proposed planetary aerobrake/aerocapture vehicle. This vehicle, a spherically blunted,  $13^\circ/7^\circ$  biconic, was tested over a range of angles of attack from  $0^\circ$  to  $27^\circ$ . The effect of Mach number was examined by testing in the Langley 20-Inch Mach 6 and 31-Inch Mach 10 Tunnels,

and the free-stream Reynolds number based on the model length was varied from  $0.4 \times 10^6$  to  $4.8 \times 10^6$  at Mach 6 and from  $0.3 \times 10^6$  to  $1.3 \times 10^6$  at Mach 10. Heating distributions predicted with a parabolized Navier-Stokes (PNS) code for laminar flow were compared with measurements.

Leeward heating distributions and levels exhibited a strong dependence on both Mach number and Reynolds number as shown in the figure. In this figure, free-stream Mach number is represented by  $M_\infty$ , free-stream Reynolds number based on model length by  $R_\infty$ , free-stream Reynolds number based on model length by  $R_{\infty L}$ , heat transfer coefficient by  $C_h$ , stagnation point heat transfer for a sphere by  $C_{h,sph}$ , distance from nose tip by  $x$ , and model length by  $L$ . An increase in the Reynolds number or a decrease in the Mach number caused cross-flow separation on the leeward side at a lower angle of attack. Heating along the most leeward ray decreased with decreasing Mach number and increasing Reynolds number at low angles of attack as



Effect of Reynolds number on heating distribution along most leeward ray at angle of attack equal to  $20^\circ$ .

long as the flow remained attached; however, the opposite was true at angles of attack for which the flow was separated. The PNS code qualitatively predicted the longitudinal and circumferential heating distributions for the present flow conditions and angles of attack. Although quantitative agreement between measurement and prediction was good in some cases, the PNS code generally underpredicted the leeward heating. (C. G. Miller, 3984)

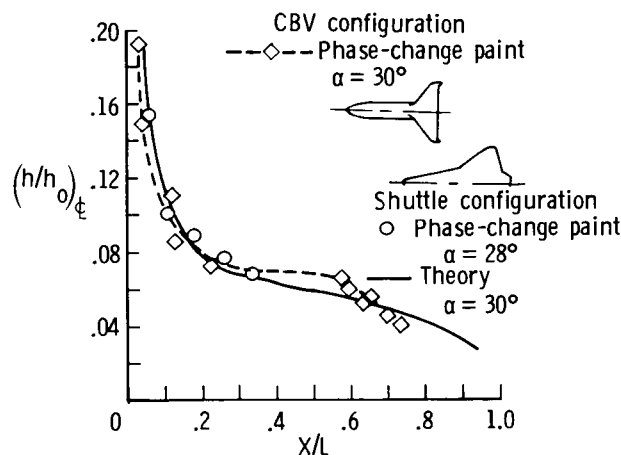
## Experimental Investigation of Circular-Body Earth-to-Orbit Transport Vehicle

Among the concepts being considered for future Earth-to-orbit transportation vehicles are fully reusable single-stage systems that take off vertically and land horizontally. Because these vehicles carry their propellant internally, they are much larger than the Space Shuttle orbiter. One such vehicle under study is a circular-body configuration (CBV), which has the advantages of simple structural design and large volume-weight ratio. As part of an overall evaluation of this configuration, a series of force-and-moment tests at subsonic and supersonic speeds and heat-transfer tests at Mach 10 were performed.

The effects of various control surfaces were examined. Elevons and ailerons were examined for pitch and roll; wing-tip fins, a nose-mounted dorsal fin, and conventional vertical tail with split rudder were examined for yaw; and body flaps were examined for trimming at hypersonic speeds. All configurations tested at subsonic speeds were longitudinally stable. The dorsal was the most effective directional control device; however, it required active controls both laterally and directionally. The tip fin was directionally unstable and also required active controls. When scaled to flight, the magnitude and distribution of the heat-transfer coefficient along the windward centerline of the CBV were similar to those obtained on the Space Shuttle orbiter (as shown in the figure). In this figure, angle of attack is represented by  $\alpha$ , distance from nose tip by  $x$ , model length by  $L$ , heat transfer coefficient by  $h$ , and stagnation point heat transfer coefficient for sphere by  $h_o$ . Wing windward heating distributions were also similar. (The chordwise streaks of higher heating occurred at angles of attack less than  $25^\circ$ , but they were not evident at high angles of attack.) Oil-flow studies revealed a complicated leeside flow field due to cross-flow separation

and reattachment that resulted in localized hot spots on the upper fuselage. Overall, the heating was sufficiently similar to the Space Shuttle orbiter to suggest that existing thermal protection systems may be adequate for the proposed CBV.

(W. L. Wells, 3984)



Comparison of windward centerline heating distribution of CBV and Space Shuttle orbiter.

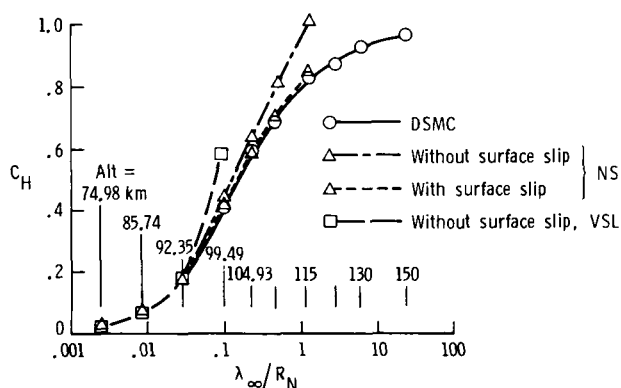
## Navier-Stokes Simulations for Hypersonic Low-Density Flows

For an accurate prediction of the aerothermal environment of a space vehicle entering the Earth's atmosphere in the high-altitude (low-density) flight regime, the multicomponent nonequilibrium gas chemistry, as well as the surface slip effects, must be included in modeling the flow field. Such rarefied and highly energetic flows are of particular interest for current and future space transportation systems. Recent numerical simulation studies have been performed in which the Navier-Stokes (N-S) equations were used to model chemical nonequilibrium flows with multicomponent surface slip boundary conditions. These solutions are applicable along the stagnation streamline of a blunt nose tip at low-density hypersonic flow conditions. The

governing equations are highly nonlinear and are solved by a numerical finite-difference method known as Successive Accelerated Replacement (SAR).

The comparison of the N-S stagnation-point heat-transfer results with those obtained with the direct simulation Monte Carlo (DSMC) method (a particle approach) provides an indication of the applicability of continuum methods to low-density hypersonic flows. Also shown are the continuum viscous shock-layer (VSL) results without either surface or shock slip boundary conditions. The VSL data begin to depart from the DSMC results for free-stream Knudsen numbers ( $\lambda_\infty/R_N$  where  $\lambda_\infty$  is the undisturbed mean free path length and  $R_N$  is the nose radius, which is 1.3 m) of about 0.03. The departure is rapid for the VSL results. The departure of the N-S results without surface slip is less rapid because the N-S simulation included the shock wave structure by integrating all the way to free-stream conditions and also because it contains higher order terms than the VSL equations. Finally, the N-S solution with surface slip provides good agreement with the DSMC heat-transfer calculations for free-stream Knudsen numbers as large as unity. The three methods are in good agreement at an altitude of 92.35 km. For altitudes less than 92.35 km, the results from the N-S and VSL methods compare well.

(E. V. Zoby, 2707)

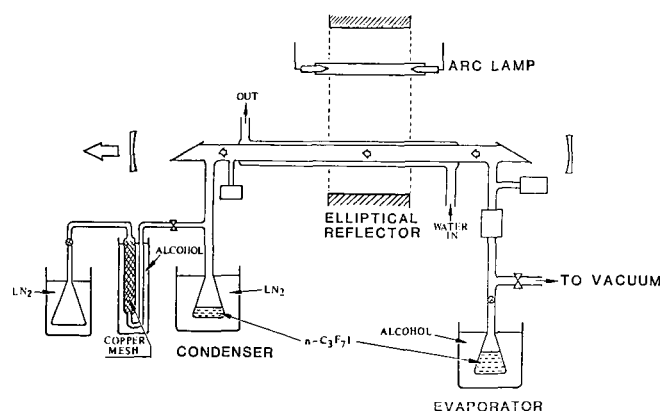


Heat transfer coefficient versus Knudsen number.

high-power satellites, such as space factories, is being evaluated. One pivotal technology receiving detailed study involves the use of sunlight to directly pump a gas laser. Significant progress has been achieved over several years with an organic-iodide photodissociation lasant. The first solar-pumped lasing was achieved with the lasant sealed in a laser cavity at low pressure and pumped at 10,000 solar constants over 5 cm of length by a solar simulator. Lasing occurred at  $1.3 \mu\text{m}$  from excited iodine atoms at an initial power level of 1 mW for 10  $\mu\text{sec}$ . Later, lasing was increased to approximately 1 W for up to 50 msec. When continuous lasant recirculation was added, lasing time was extended from a fraction of a second to 1 hr.

With the activation this year of a new high-power solar simulator, a new experiment was developed. To maximize the transfer of light from the 20-cm-long arc lamp to the laser, an elliptical silvered concentrator with plane silvered end plates was constructed with the simulator at one focus and the laser at the other. Water cooling of the laser was required because of the high reflectivity concentrator. The optical power not absorbed by the lasant circulates repeatedly through the foci, and very weak absorption in the laser-envelope produces temperatures sufficient to soften quartz. During operation at 1274 solar constants, a continuous-wave lasing emission of more than 10 W was achieved for approximately one-half min. Power was limited by incomplete absorption in the lasant, and lasing time was limited by the transfer of all lasant from the evaporator.

(J. Lee, 3781)



High-power solar simulator/elliptical reflector/iodine laser.

## 10-Watt Continuous-Wave Solar-Pumped Laser

The concept of laser power transmission from a high-altitude orbiting power station to low-altitude,

## Shuttle Entry Air Data System (SEADS) Experiment

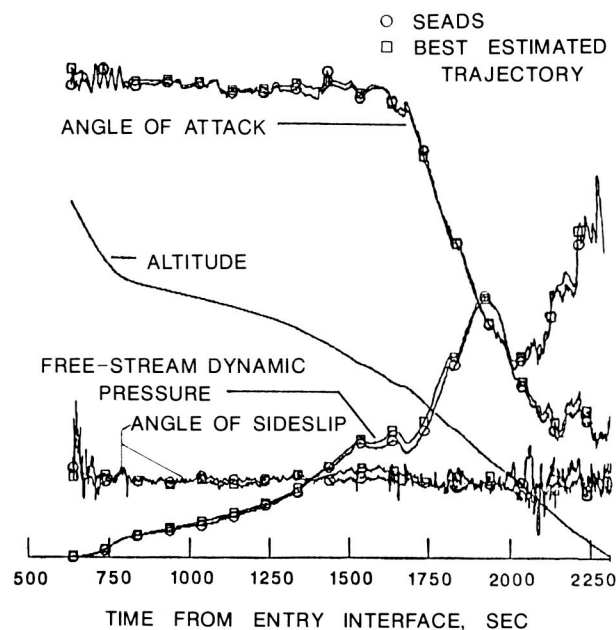
Determination of air data (i.e., angles of attack, sideslip, and free-stream dynamic pressure) is critical to real-time flight control and/or postflight performance analysis of flight vehicles. During atmospheric entry, the Space Shuttle orbiter operates without an in situ source of air data down to about Mach 3.5, at which point the orbiter's air data system is activated. The lack of measured air data in the hypersonic regime has compromised the orbiter's postflight aerodynamic performance analyses, and, from a research perspective, accurate air data and flight aerodynamics determination are critical to the development and evaluation of ground-to-flight extrapolation and analytical prediction techniques.

The SEADS experiment, incorporated in the orbiter *Columbia*, allows postflight determination of across-the-speed-range air data from an altitude of about 300,000 ft to landing. The SEADS is a replacement reinforced carbon-carbon nose cap containing 14 silicide-coated columbium penetration assemblies distributed about the nose cap in a cruciform pattern. A small hole through each penetration assembly is connected through internal plumbing to pressure sensors and data recording equipment for postflight processing.

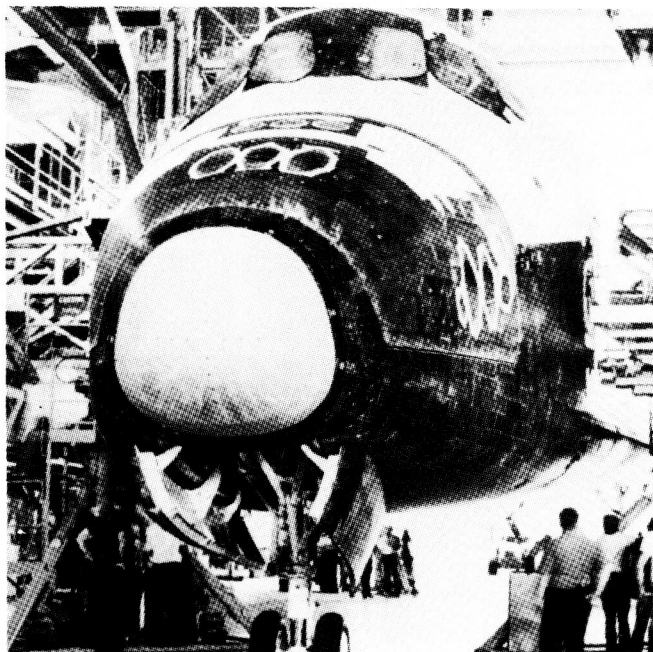
The first SEADS flight on mission STS 61-C in January 1986 was fully successful. Results that were

compared with the orbiter's postflight-constructed performance data show that angles of attack and sideslip were measured to an accuracy of  $0.3^\circ$  and free-stream dynamic pressures to 3 percent in the hypersonic and supersonic flight regimes. Corresponding values were  $0.8^\circ$  and 4 percent for the transonic and subsonic regimes.

(P. M. Siemers, 3031)



*SEADS comparison with orbiter performance data.*



L-85-12,051

*SEADS nose cap on Space Shuttle orbiter Columbia.*

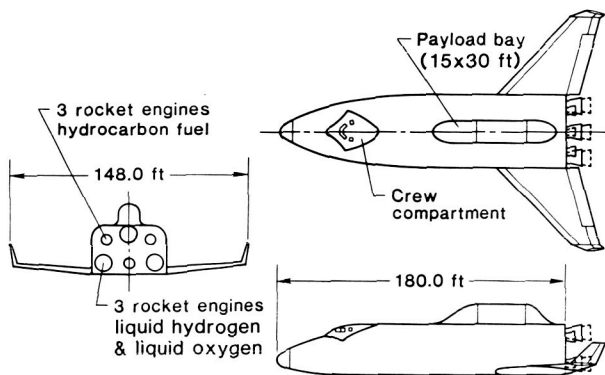
## Shuttle II Study

Possible expansions of man's activities in space over the next several decades, as exemplified by the Report of the National Commission on Space, will require routine and low-cost space transportation. In the NASA Langley Shuttle II Study, desired system and operational characteristics and several vehicle concepts have been defined to fulfill these goals. Concepts studied include single- and two-stage fully reusable winged rocket systems designed for vertical takeoff and horizontal landing. With only moderate technology advancements over the Space Shuttle, these concepts not only

weigh less but also offer improved operational simplicity in meeting cost and mission goals.

The study has identified several key technologies in need of development; these include reusable cryogenic tankage, hydrocarbon-fueled rocket engines, and durable thermal protection systems. Both single- and two-stage vehicles use a detachable payload container to simplify operations and an aeroshell structure to allow for pullout periodic inspection of propellant tankage. The single-stage-to-orbit concept is well-suited for small payload deliveries but involves higher technical risks. The payload performance can be augmented by the use of small auxiliary rocket units. The two-stage vehicle concept, while having greater operational complexity, is less demanding in terms of degree of technology development. Both concepts satisfy the goals of routine, low-cost access to space.

(T. A. Talay, 2768)

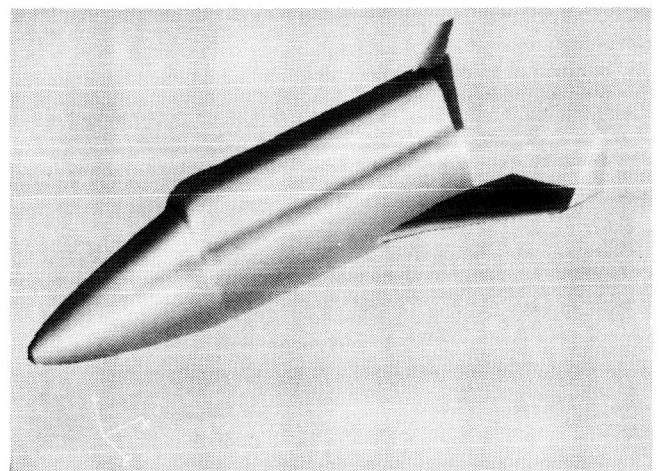


*Single-stage-to-orbit Space Shuttle II concept.*

weights and assess clearances as well as to provide the designer with the essential visualization of the object being designed. For aerospace vehicles, the geometry is used in aerodynamic and heating analyses to design the shape, structural concept, and thermal protection system.

A 3-D interactive geometry modeller has been developed for AVID at NASA Langley using state-of-the-art software techniques and computer graphics hardware. The modeller, based on bicubic Bizer surface patches, allows a designer to describe complex vehicle shapes in a natural way. The designer is able to create 3-D objects by modifying primitive objects such as spheres, cylinders, and cubes; by extending 2-D shapes by revolving or lofting; and by merging two objects to form one. Many of these techniques are performed dynamically, in real time, by the designer. Vehicle shapes are generated and can be rotated to be viewed from any angle. Full-color shaded images can be generated to provide a realistic picture of the vehicle. The figure shows a Shuttle II concept that was generated using the AVID geometry modeller.

(J. Rehder, 4967)



*Computer-generated Shuttle II concept.*

## Geometry Modeller for AVID

Computer-aided design (CAD) is used extensively in the conceptual and preliminary design of advanced space transportation concepts. A second-generation version of NASA Langley's AVID (Aerospace Vehicle Interactive Design) system is being developed. A key element of AVID is a description of the geometry of the objective being designed. A three-dimensional (3-D) geometrical description can be used to determine

## Uniform Damping Control of Vibrating Truss Structures

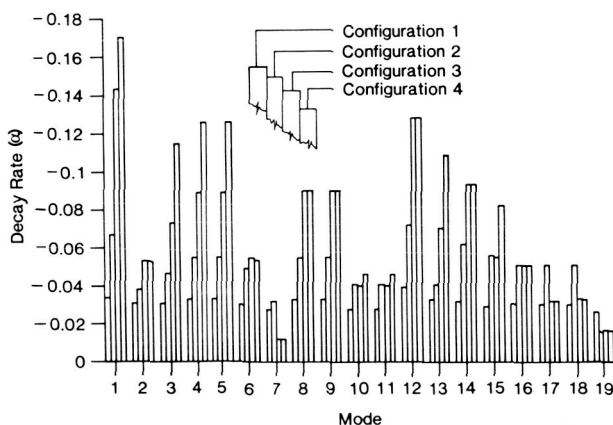
Because flexible body motion plays a significant role in the distortion errors of large truss structures,



such as antennas, a study was conducted concerning vibration suppression of a planar truss structure using uniform damping control. This form of control dampens every vibrational mode at the same desirable exponential decay rate. The control law is not explicitly dependent on an accurate knowledge of the structure; it is decentralized and robust. The control forces are directly proportional to the distribution of the structural mass.

A generic truss structure (4 bay by 4 bay box cube with diagonals), which had four different actuator/sensor configurations, was analyzed to determine the effects of decreasing controller number on controllability, controller total power requirement, and controller peak-power requirement. Each subsequent controller configuration used fewer controllers (80, 32, 16, and 8 for configurations 1 through 4, respectively). The figure illustrates configuration effects on the real part of the closed-loop poles (exponential decay rate), which is a measure of mode controllability in terms of the deviation of the closed-loop exponential decay rate from the design decay rate of  $-0.04$ . Based on the number of controllers, power needs, and closed-loop pole locations, the use of 16 controllers was optimum. The results of the study demonstrated that flexible-body control of a large truss structure could be obtained using only a limited number of actuators and sensors with a minimal reduction in control system performance, compared to the completely distributed control system.

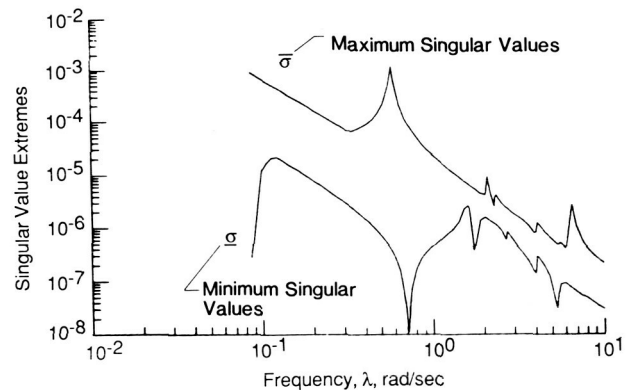
(G. C. Andersen, 1982)



Controller configuration effects on closed-loop exponential decay rates.

## Analysis for Flexible Spacecraft Sensor and Actuator Placement

Large space structures, which have been proposed for a variety of applications (such as communications and power generation), present especially difficult problems for control system designers. Some of these difficulties may be reduced early in the conceptual design phase by structural designers if there is not only an adequate understanding of the control issues but also a useful set of analysis tools with which to evaluate the concepts. To this end, tools employed in modern, multivariable control system synthesis and evaluation have been investigated to identify analyses that might be appropriate for conceptual design. Measures of controllability and observability and calculation of transmission zeros were determined to be of use in evaluating the structures/controls interactions and in providing insight into effects that are produced by changes in the spacecraft configuration or in actuator and sensor selection or placement. Also, as shown in the figure, plots of

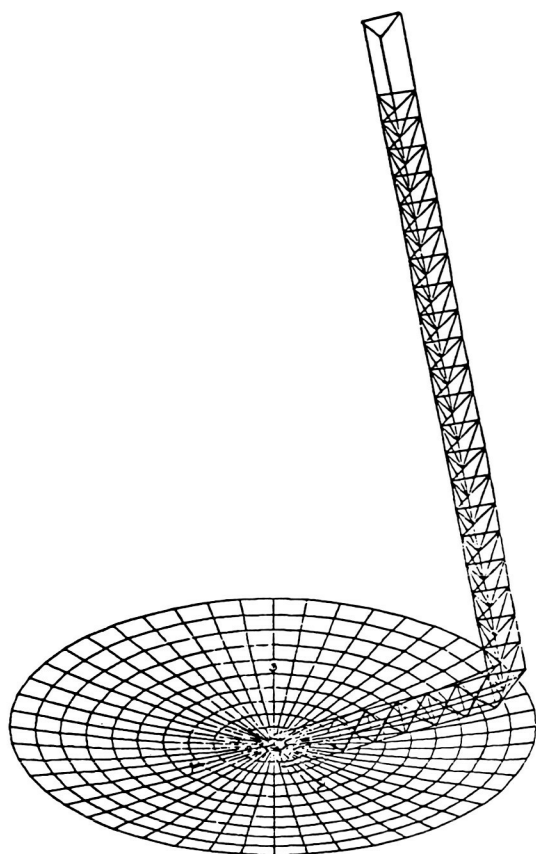


Singular value extremes for torquer/sensor configuration located on wrap-rib antenna central hub.

singular value extremes give some indication of difficulties that may be encountered in trying to meet desired controller bandwidth.

An analysis program has been developed so that, given the structure's modal matrix, natural frequencies, and other physical properties, the user may specify a proposed sensor/actuator configuration and then generate the information described previously. This program has been applied to the wrap-rib antenna concept and has provided insight into the effectiveness of proposed

sensor/actuator locations and types for detecting and controlling individual modes.  
(L. F. Rowell, 4983)



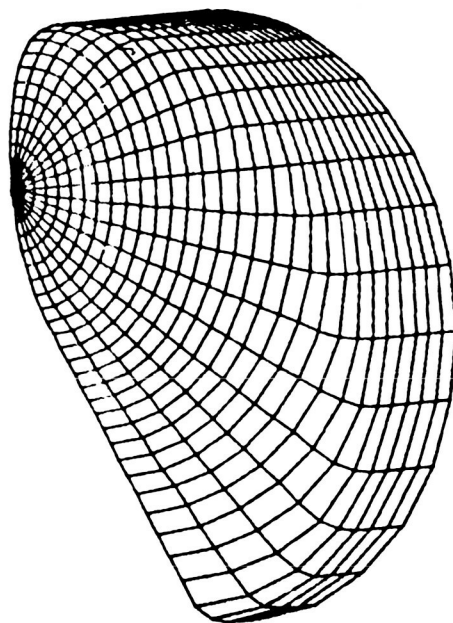
*Finite-element model of 55-m offset wrap-rib antenna.*

## Aeroassist Flight Experiment Vehicle Aerodynamics

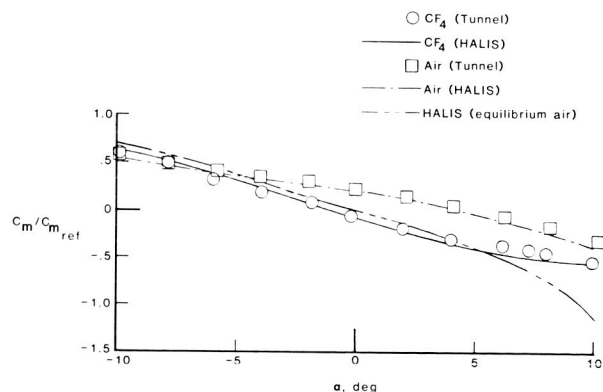
The Aeroassisted Orbital Transfer Vehicle (AOTV) will use aerobraking rather than all-propulsive braking during its return from geosynchronous orbit to low-Earth orbit. The use of aerobraking will result in a substantial increase in payload size and weight. To better understand this flight environment, several NASA Centers have proposed a flight experiment called AFE (Aeroassist Flight Experiment), which uses an aeroshell configuration as illustrated. This asymmetric body is generated

by raking an elliptically blunted  $60^\circ$  cone at  $73^\circ$  relative to the body axis.

The AFE mission success will depend on accurate assessment of the aeroshell aerodynamics. Thus, parallel efforts in CFD (computational fluid dynamics) and ground-based facility testing were undertaken at NASA Langley. The CFD results were obtained with the NASA-Langley-developed HALIS (High Alpha Inviscid Solution) code, which was designed to compute the flow field about vehicles in a supersonic/hypersonic stream



*Representation of AFE aeroshell in computational grid.*



*Comparison of computed and measured longitudinal pitching moments for AFE aeroshell as function of angle of attack.*

with large regions of embedded subsonic flow. Also, the HALIS code can treat the gas flow either as calorically perfect or in chemical equilibrium. Ground-based tests were conducted in facilities over a Mach number range of 6 to 20. Real-gas effects were simulated by testing at Mach 6 in tetrafluoromethane ( $\text{CF}_4$ ) and in air. Pitching-moment coefficient comparisons of CFD results show that the agreement is excellent. The HALIS-generated results using the equilibrium air chemistry option are shown in the second figure. The  $\text{CF}_4$  tunnel data are in good agreement with the HALIS computations for this case, also.

(K. J. Weilmuenster, 3272)

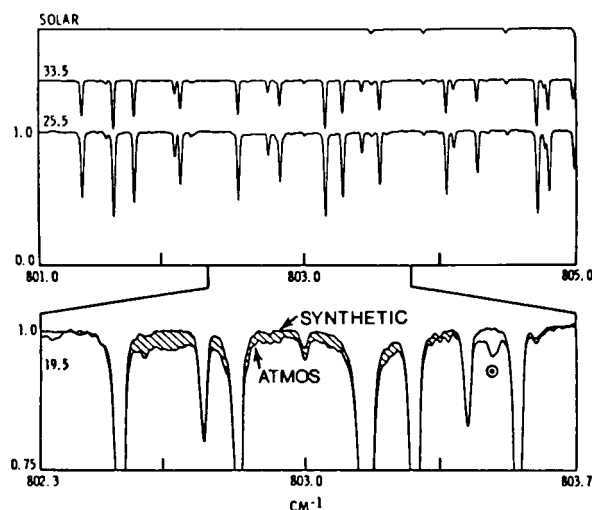
## First Spectroscopic Measurements of Stratospheric Peroxynitric Acid, Chlorine Nitrate, Carbonyl Fluoride, and Methyl Chloride

During its first mission onboard Spacelab 3, April 30 to May 6, 1985, the ATMOS (Atmospheric Trace Molecule Spectroscopy) Fourier transform spectrometer recorded more than 1000 high-resolution infrared solar absorption spectra of the Earth's upper atmosphere. Initial analysis of the stratospheric spectra has revealed the presence of absorption arising from three previously unobserved trace constituents: peroxynitric acid ( $\text{HO}_2\text{NO}_2$ ), chlorine nitrate ( $\text{ClONO}_2$ ), and carbonyl fluoride ( $\text{COF}_2$ ). Both  $\text{HO}_2\text{NO}_2$  and  $\text{ClONO}_2$  are predicted by models to be important temporary reservoirs involved in the trace gas photochemistry of the stratosphere, whereas  $\text{COF}_2$  is predicted to be an important intermediate photodissociation product of chlorofluorocarbons (CFCs) in the stratosphere. Also, methyl chloride ( $\text{CH}_3\text{Cl}$ ), an important chlorine source gas for the stratosphere, was detected for the first time in infrared stratospheric spectra.

As an example, the figure shows a portion of four ATMOS spectra in a region containing absorption by  $\text{HO}_2\text{NO}_2$ . The lowest scan, on an expanded scale, shows a weak, broad absorption centered around  $802.7\text{ cm}^{-1}$  (shaded area). This feature is not reproduced in the synthetic spectrum, which was calculated for all gases except  $\text{HO}_2\text{NO}_2$ . Based on the agreement between the position and shape of this feature and absorption by  $\text{HO}_2\text{NO}_2$  measured in laboratory spectra, this feature in the ATMOS spectra has been identified as resulting

from  $\text{HO}_2\text{NO}_2$ . Peroxynitric acid is important in the lower stratosphere, where it couples the chemistry of the odd hydrogen and odd nitrogen families. In collaboration with other ATMOS science team investigators, the observed features have been analyzed to deduce profiles of volume mixing ratio versus altitude for the four gases.

(C. P. Rinsland, 2576)



ATMOS spectra in the region of the  $802.7\text{ cm}^{-1}$  Q branch of  $\text{HO}_2\text{NO}_2$ . Shaded area in the bottom plot indicates absorption by  $\text{HO}_2\text{NO}_2$ .

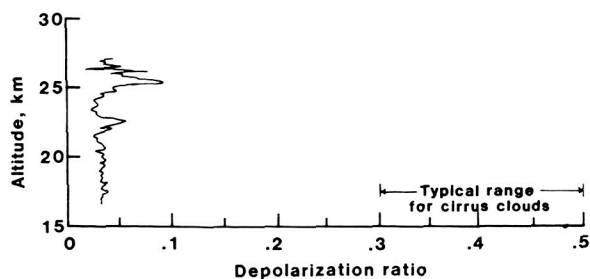
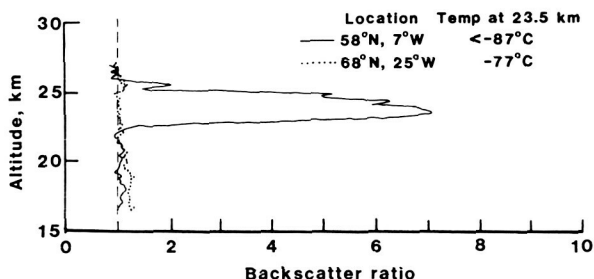
## Simultaneous Dual-Polarization Airborne Lidar Measurements of Polar Stratospheric Clouds

Polar stratospheric clouds (PSCs) form during polar winters in regions where the stratospheric temperature falls below a threshold temperature of  $-80^\circ\text{C}$ . These clouds may influence thermal radiation patterns as well as the budgets of aerosol and trace gases, such as water vapor and ozone. A PSC formation was probed during a January 1986 Arctic lidar survey mission, which was flown on the NASA Wallops P-3 aircraft. For the first time, cloud backscatter measurements were made simultaneously in polarization planes perpendicular and parallel to those of the transmitted laser beam. Formation of

the perpendicular-to-parallel (depolarization) ratio provides a semiquantitative indicator of the size and shape of the backscattering particles.

The 1986 PSC encounter occurred on January 18 in the Iceland/Scotland corridor. Radiosonde data obtained near the encounter area indicate minimum temperatures colder than  $-85^{\circ}\text{C}$  in the 22.5- to 26-km altitude range. The PSCs were observed in this same altitude range and exhibited a persistent three-layer vertical structure. The peak backscatter ratio (relative to that expected from purely molecular backscattering) was about 7; this ratio is in contrast to values near 1 observed throughout this altitude range northwest of the cold-temperature region. Depolarization ratios in the PSC formation were much smaller than values characteristic of cirrus clouds (0.3 to 0.5). These measurements indicate the likely presence of smaller, noncirrus-like particles throughout the bulk of the formation, with some variation in particle characteristics with altitude.

(L. R. Poole, 2065)



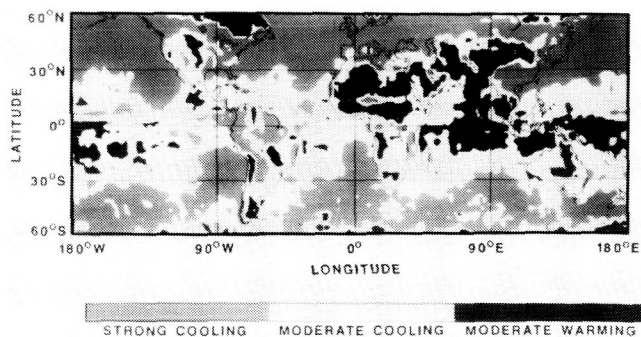
Profiles of backscatter ratio (top) and depolarization ratio (bottom) measured by airborne lidar on January 18, 1986.

## ERBE Measurements of Cloud Forcing

The ERBE (Earth Radiation Budget Experiment) has been measuring the three components of the Earth's radiation budget since late in 1984 when the Space Shuttle *Challenger* launched the ERBS (Earth Radiation Budget Satellite). These three components, incident and reflected solar fluxes (power incident on or leaving from the top of the atmosphere per unit area), and the flux emitted by the Earth and clouds provide the fundamental energy source of the atmospheric and oceanic circulation. Over the last decade, a scientific controversy has developed concerning the role of clouds in the radiation budget, particularly since the Earth's energy budget is being perturbed by the increase of carbon dioxide and other trace gases. Low clouds act to cool the Earth by reflecting sunlight; high clouds act to heat it by trapping the emitted energy. However, not enough is known about clouds for scientists to have confidence in their models of the Earth's climate.

As part of the ERBE data processing, clear skies are identified and treated separately from the rest of the data. By subtracting the radiative fluxes for clear skies from the fluxes that have been routinely sampled, it is possible to deduce the net effect of clouds. This is shown in the figure for the month of April, 1985. The darkest areas indicate where clouds are moderately warming; the intermediate shading indicates where clouds are cooling. Overall, it appears that clouds act to cool the Earth, particularly in cloudy areas off South America and Africa.

(B. R. Barkstrom, 2977)



Clouds cooling and heating the Earth, as observed by ERBS, April 1985.

## Springtime Antarctic Ozone Depletion Observed by SAGE II

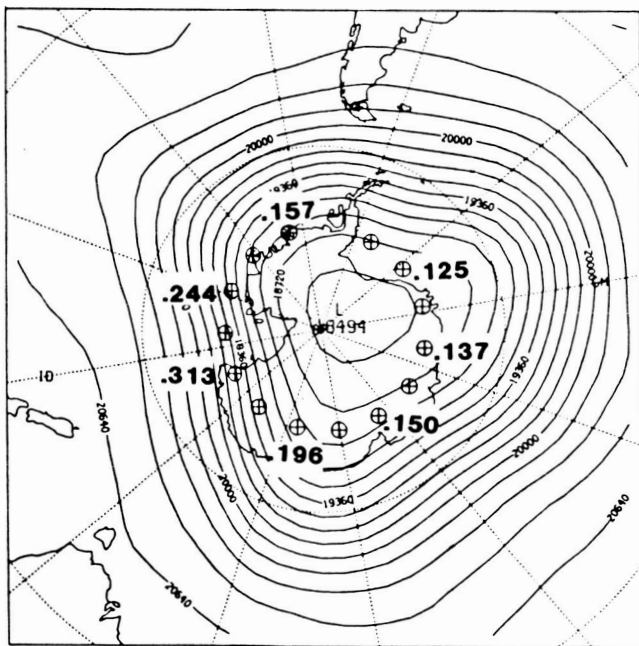
Stratospheric ozone, which shields the Earth's surface from the Sun's harmful UV (ultraviolet) radiation, has been reported by several researchers to have decreased some 40 percent in recent years in the springtime Antarctic region associated with the circumpolar vortex. Although the exact cause of this dramatic change is currently unknown, there is concern that man's activities play a significant role, primarily through the release of chlorofluorocarbons into the atmosphere.

The Stratospheric Aerosol and Gas Experiment II (SAGE II) is a seven-channel spectrometer developed by NASA Langley which infers the vertical distribution of stratospheric aerosols, ozone, nitrogen dioxide, and water vapor from the extinction of solar radiation measured during spacecraft sunset and sunrise. SAGE II was deployed by the Space Shuttle (mission 41-G) on October 5, 1984, on the Earth Radiation Budget Satellite. It has operated continuously since October 24, 1984, and has collected data over a latitude range from

80°S to 80°N. The orbital coverage of SAGE II is such that measurements are obtained within the vortex during October (the time of maximum ozone reduction). The figure shows the SAGE II measurement locations (circles with plus signs) for October 5, 1985, relative to the Antarctic region and the circumpolar vortex (the latter represented by the 50 mb geopotential height contours shown). The vortex is considered to be an isolated flow field. To the first approximation, air flows clockwise and follows the contour surfaces. Adjacent to every other measurement location is the total column sum of ozone expressed in cm-atm (0.001 cm-atm equals 1 Dobson unit) calculated from 100 mb upwards. For comparison purposes, pre-1973 total column sums would be approximately 0.250 cm-atm in the vortex where SAGE II now measures 0.125 cm-atm.

Prior to the analysis of the SAGE II measurements, it was believed that the ozone depletion occurred primarily over 16 to 24 km. However, the SAGE II satellite measurements show a significant decrease in ozone up to 50 km on this particular day and for most others that were investigated.

(M. P. McCormick, 2065)



*Total column amounts of ozone (cm-atm) adjacent to the SAGE II measurement locations relative to Antarctica and circumpolar vortex. The latter is represented by the 50-mb geopotential height contours shown. The contour interval is 160 m.*

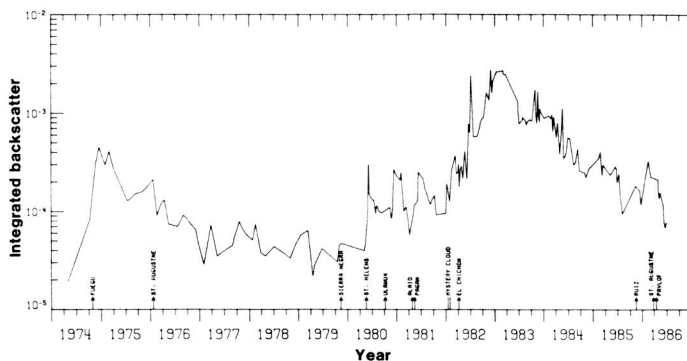
## Lidar Studies of Stratospheric Aerosols

A long-term data set on stratospheric aerosols is being produced using the 48-in. lidar system at NASA Langley Research Center. Routine observations of the stratosphere have been made since 1974 and represent the longest data set of its kind in the world. Stratospheric aerosols, with their relatively long resident times, are important because they may directly affect the Earth's climate by scattering and absorbing both solar radiation and upwelling thermal radiation.

This long-term data set, shown in the figure, indicates that the major contributor to stratospheric aerosol enhancements has been of volcanic origin. Plotted in the figure is the lidar backscatter from stratospheric aerosols integrated from the tropopause to 30 km, over the time period 1974 to 1986. A number of explosive volcanic eruptions, which are thought to have injected material in the stratosphere, are indicated at the time of their eruption. The integrated lidar backscatter is a measure of the relative column aerosol loading in the stratosphere and, by using optical models, can be converted to aerosol mass loading. The major perturbations to the stratospheric aerosols due to numerous volcanic eruptions are clearly evident. In particular, the effect

of the April 1982 eruption of the El Chichon volcano in Mexico, thought to have produced the largest perturbation in stratospheric aerosol loading in this century, can be compared to that of other eruptions. Also, the long "background" period from 1977 through 1979 is shown, as well as the decreases toward background conditions in October 1980, April 1981, December 1981, and the current trend. The most recent perturbation, March 1986, is thought to be associated with the November 1985 eruption of the Ruiz volcano in Colombia, South America.

(W. H. Fuller, Jr., 2065)



*Integrated lidar backscatter measurements from stratospheric aerosols by 48-in. lidar operating at 0.6943  $\mu\text{m}$  at NASA Langley (37.1°N, 76.3°W).*

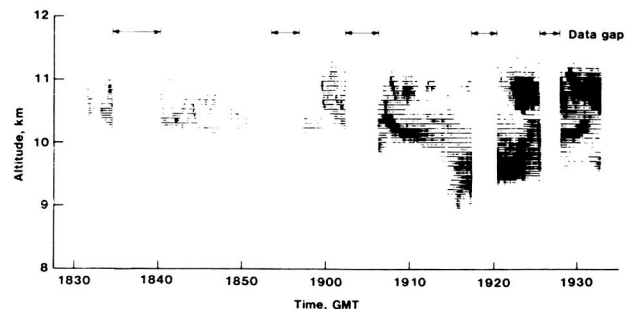
## Ground-Based Lidar Measurements of Cirrus Clouds for Project FIRE

Project FIRE (First International Satellite Cloud Climatology Project [ISCCP] Regional Experiment) is a collaborative research program involving NASA, other government agencies, and universities which is designed to validate and improve ISCCP data products and the cloud radiation and dynamics algorithms used in models of the atmospheric general circulation. A phase of project FIRE is dedicated to ground-based remote sensing of cirrus cloud systems, in coordination with satellite sensor overpasses, over an extended time period at various research stations, one of which is at

NASA Langley. Key elements in the ground-based remote sensing capability at the Langley site are the 14-in. and 48-in. multiwavelength lidar systems, which can provide high-resolution data in both time and space on the structure of cirrus clouds.

Measurements of cirrus clouds were made using the NASA Langley 14-in. ruby lidar system (wavelength = 694 nm) on May 6, 1986, in conjunction with the 1841 Greenwich mean time (GMT) (1341 e.d.t., eastern daylight time) overpass of the Advanced Very-High Resolution Radiometer (AVHRR) onboard the NOAA-9 Polar Orbiter satellite. The lidar data showed a cirrus formation in the 9- to 11-km-altitude range whose structure varied in a dramatic fashion over a temporal scale of minutes and a vertical scale of several hundred meters. In the densest regions of the cloud formation, lidar backscatter ratios relative to purely molecular backscattering were on the order of 100 or greater. The data clearly demonstrate the usefulness of lidar measurements in characterizing fine-scale structural variations within cirrus systems.

(L. R. Poole, 2065)



*Intensity-modulated record of backscatter ratio measured during cirrus cloud episode of May 6, 1986. Darkest areas represent backscatter ratios on the order of 100 or greater.*

## Improving Cloud Measurement From Space

The largest concern in cloud cover measurement from space is the accurate treatment of satellite fields



of view which are partially filled with clouds. The most rigorous solution to this difficulty is to examine clouds using much higher spatial resolution data than are available from current meteorological satellites. Landsat data have been used to achieve more than an order of magnitude increase in spatial resolution (57 m) over the highest resolution meteorological satellite instruments (1000 m).

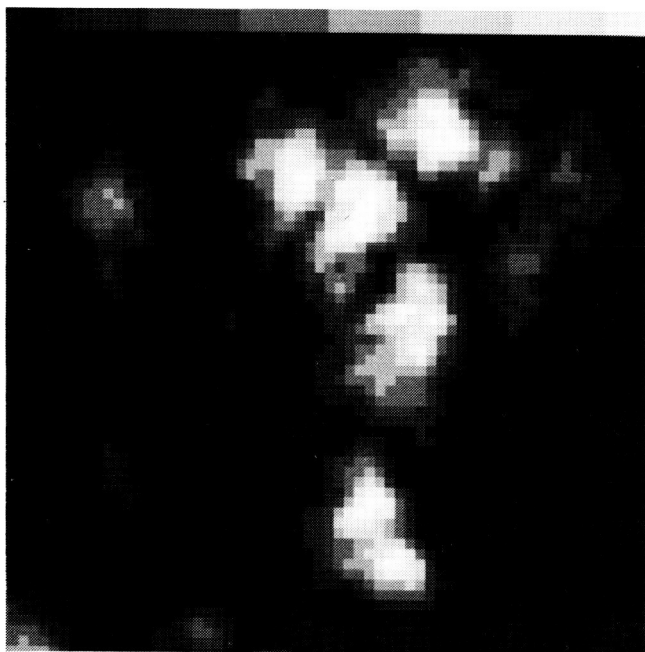
Cloud cover and the distribution of cloud sizes were determined for four Landsat views of fair-weather cumulus cloud fields. Examination of the high-resolution cloud data gave some unexpected results. First, the most common physical model of cloud elements is one in which clouds are portrayed by varying sized sheets of paper, with each sheet of reasonably uniform reflectance. This model was shown to be a poor representation for cumulus clouds which showed reflectance variations within a single cloud to be as large as or larger than variations between different clouds. These reflectance variations can be seen in the figure that shows the full-resolution Landsat data for a 3.6-km region of a cumulus cloud field over the western Atlantic on March 9, 1979. Reflectance varies from 0 percent (black) to 30 percent (white). Second, the cumulus clouds over the ocean did not exhibit the sharp increase in reflectance at cloud

edge that was found in the cumulus clouds over the land. Finally, the Landsat data were spatially averaged to simulate the coarser resolution meteorological satellite data of 1-km and 4-km resolution. The increase in cloud cover caused by spatial averaging was less than predicted by theory. Current theoretical cloud models appear to be oversimplified.

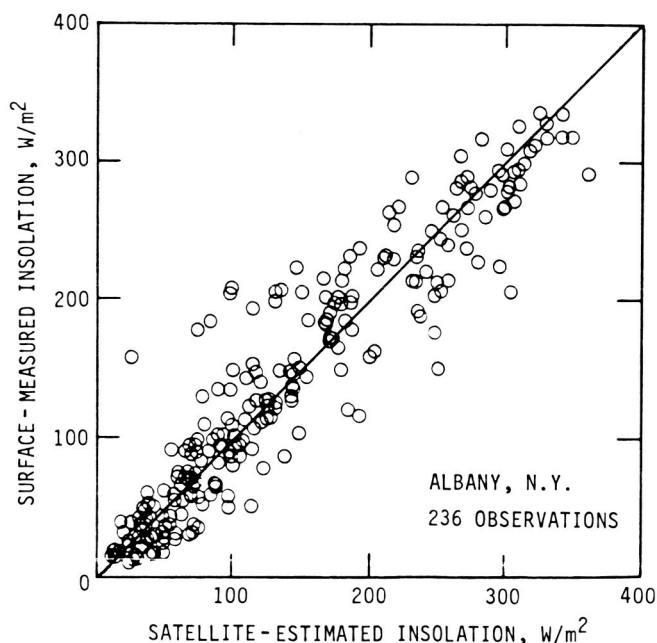
(B. A. Wielicki, 1977)

## Sun-Synchronous Satellite Estimates of Solar Radiation at Earth's Surface

Estimation techniques for determining by satellite the incoming solar radiation (insolation) at the Earth's surface have been in use for some time. Mostly, these techniques have used the data of geosynchronous satellites (GOES) which have the advantage of providing high-resolution data about every 30 or 60 min. These satellites, however, can view only a fraction of the Earth (generally  $60^\circ$  about the subsatellite point). Sun-synchronous satellites provide only two viewings, on the



Reflectance of cumulus clouds over the western Atlantic for a 3.6-km by 3.6-km region.



Comparison of corresponding estimated and measured daily insolation fluxes. Straight line shows location of perfect agreement between estimated and measured values.

average, over any given point each day but have the ability to cover the entire globe. As a result, it has been desirable to establish dependable, low-cost insolation estimation techniques using Sun-synchronous satellite data to obtain the full coverage needed for climate studies of the Earth.

A Sun-synchronous satellite technique has now been developed and tested at NASA Langley. The main purpose of this model is to determine insolation over large areas. The Earth's surface can be divided into a gridwork of such areas allowing the variation of regional insolation over the Earth to be studied and the total global insolation to be determined. Effects of clouds and atmospheric gases, such as water vapor, carbon dioxide, and ozone, are included in the model. Estimated insolation fluxes from the model and satellite data (NOAA TOVS [Tiros operational vertical sounder]) have been validated by comparisons with corresponding surface-measured fluxes over land sites. One such comparison is shown in the figure. Daily estimates can be made with about 15 percent root mean square (rms), and monthly averaged fluxes, which are the desired product, can be determined to about 5 percent rms error. (W. L. Darnell, 1977)

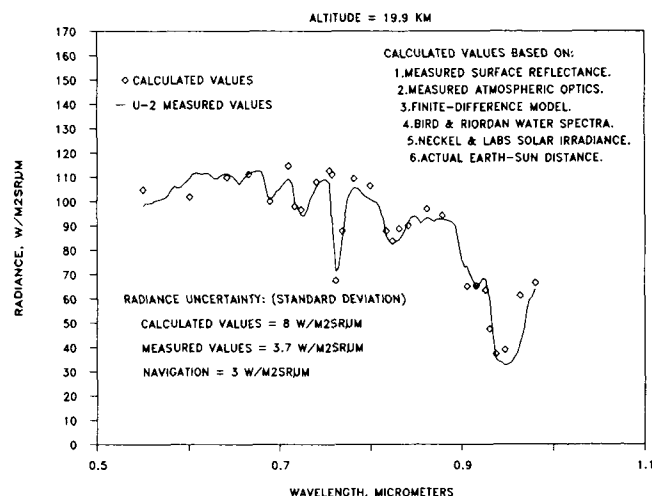
## Validation and Calibration Studies for Satellite Instruments

High-quality radiometric data from satellites are essential for climate, radiation budget, and cloud process studies. Satellite instruments, however, vary widely in quality of output data. Results range from the uncalibrated, narrowband measurements of the GOES (Geosynchronous Satellite) imaging system to the extensively calibrated, broadband measurements of the Earth Radiation Budget Experiment (ERBE).

A series of radiation experiments have been conducted for the Sonoran Desert near Yuma, Arizona, as part of the development of substitute calibration methods for systems such as GOES and as part of the validation studies for ERBE. During May 1985, experimental data were collected in conjunction with a U-2 high-altitude aircraft overflight, which included measurements from a NOAA high-resolution spectrometer. A major objective of the experiment was to test the utilization of detailed ground-based measurements for providing inputs to radiative transfer calculations of upward radiance at the top of the atmosphere. Comparison of calculated

values with the U-2 data is a very effective test of the radiative transfer technique because the NOAA spectrometer was precisely calibrated both before and after the flight. The figure shows excellent agreement between the calculated and U-2-measured values throughout the visible and near-infrared spectral range. These results have demonstrated the effectiveness of the radiative transfer approach.

(J. T. Suttles, 1977)



*Comparison of radiative transfer calculations and U-2 NOAA spectrometer measurements.*

## Detection of Stratospheric $\text{HNO}_3$ Response to Solar UV Variability

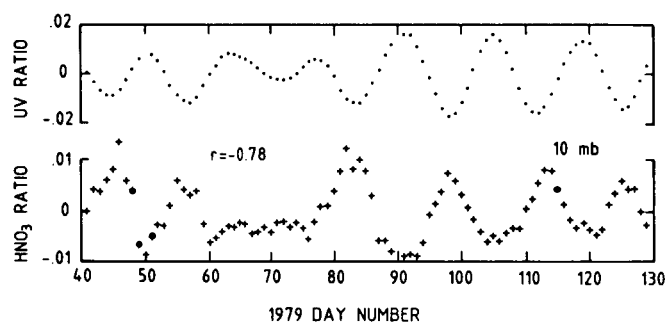
Variations in the solar ultraviolet (UV) irradiance with a period equal to or approximately one-half of the rotation period of the Sun (27 days) are currently observed by satellite monitoring. These variations have typical peak-to-peak amplitudes of  $\approx 3$  percent between 170 and 208 nm and  $< 1.5$  percent at longer wavelengths. Detection of the response of stratospheric species to solar UV variability is crucial for understanding the photochemical behavior of the middle atmosphere. Understanding the natural variations is also a prerequisite for isolating possible anthropogenic effects. The response of nitric acid in the middle atmosphere to



short-term solar UV variability has now been isolated. This is the first detection of such a response for a species other than ozone.

Analysis was performed on Nimbus 7 LIMS (Limb Infrared Monitor of the Stratosphere)  $\text{HNO}_3$  measurements using techniques to maximize precision for solar signal detection. Dynamical effects were minimized by removal of high latitude and winter data. Shown in the figure are fractional variations relative to a running mean of  $\text{HNO}_3$  mixing ratio and of 205-nm solar radiation for data averaged between  $\pm 40^\circ$  latitude at 10 mb. With increases in the UV flux,  $\text{HNO}_3$  is immediately photo-dissociated, and decreases in  $\text{HNO}_3$  are observed to occur. It was found that nitric acid was more than twice as sensitive as ozone to solar variability. Over the 11-year solar cycle, increased solar activity can result in increased conversion of  $\text{HNO}_3$  into active  $\text{NO}_x$ , which in turn can destroy and significantly affect the ozone balance.

(G. M. Keating, 2084)



*Relation between dayside nitric acid ratio  $[(\text{HNO}_3 - \overline{\text{HNO}_3})/\overline{\text{HNO}_3}]$  at 10 mbar (+) and 205-nm solar irradiance (UV) ratio  $[(I_{205} - \overline{I_{205}})/\overline{I_{205}}]$  (.) between days 40 and 130 of 1979. The correlation coefficient between the two parameters is  $r = -0.78$ .*

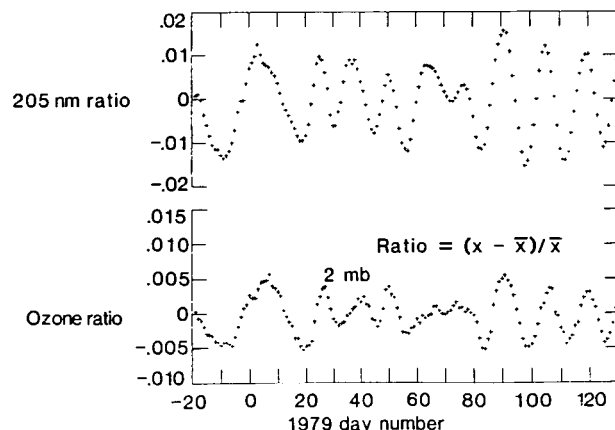
## Response of Stratospheric Ozone to Short-Term Solar UV Variability

Efforts toward detecting the response of ozone in the middle atmosphere to variations in solar ultraviolet (UV) radiation have been pursued for over 50 years with little success. Detection of such a relationship is

crucial for fully understanding the photochemical behavior of the middle atmosphere and for isolating possible anthropogenic effects. Analyzing high-precision Nimbus 7 LIMS (Limb Infrared Monitor of the Stratosphere) ozone measurements, the response of ozone to short-term solar UV variations associated with solar rotation has now been clearly detected in the middle atmosphere between the pressures of 10 and 0.2 mb. The definitive isolation of the small ozone variations associated with solar UV variability was accomplished only after removal of the larger changes of ozone related to temperature variations.

Using this approach, the correlation between detrended ozone and short-term 205-nm solar variation is found to be much greater than achieved in previous studies. Shown in the figure are fractional variations relative to a running mean of  $\text{O}_3$  mixing ratio of a 205-nm solar irradiance for data averaged between  $\pm 40^\circ$  latitude at 2 mb. With increases of 205 nm, irradiance-increased photodissociation of  $\text{O}_2$  occurs with subsequent  $\text{O}_3$  production so that increased  $\text{O}_3$  is observed. The response times are found to be rapid near 2 mb and slower deeper in the stratosphere as predicted. Determination of the amplitude of response provides better estimates of the  $\text{O}_3$  variability over the 11-year solar cycle.

(G. M. Keating, 2084)



*Response of  $\text{O}_3$  (LIMS) to short-term solar UV variability.*

## Nonlocal Thermodynamic Equilibrium Effects in Mesospheric Ozone

The Nimbus 7 Limb Infrared Monitor of the Stratosphere experiment measured radiances both day and night from ozone near  $9.6\ \mu\text{m}$ . The retrieval of ozone mixing ratio profiles was performed from those radiances assuming local thermodynamic equilibrium (LTE). Night and day ozone ratios for LTE conditions are shown in the figure as a function of pressure and altitude at the Equator, and they diverge from the photochemical model estimates between 0.5 and 0.05 mb.

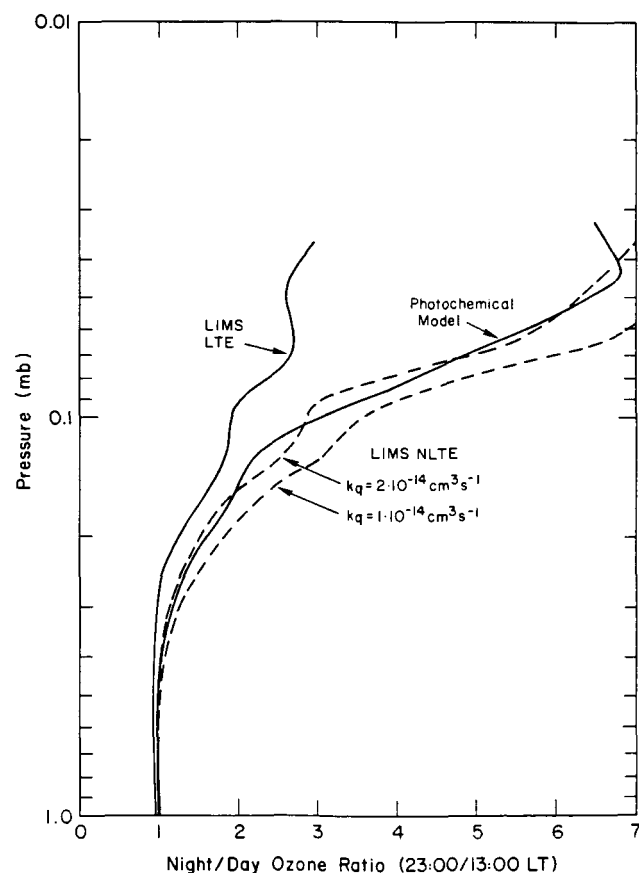
Laboratory kinetic studies suggest that an appreciable fraction of the ozone produced during daytime by recombination of atomic oxygen is vibrationally excited (i.e., in nonlocal thermodynamic equilibrium [NLTE]). Correction factors based on laboratory data were developed for ozone retrievals for a range of quenching factors  $k_q$ . Results are shown in the figure as dashed

curves. Note that the agreement with the theoretical night and day ratios has improved dramatically. There is also now general agreement with the ozone profiles from the Solar Mesospheric Explorer (SME) satellite. These findings are being incorporated into algorithms for retrieving ozone from future Limb emission experiments.

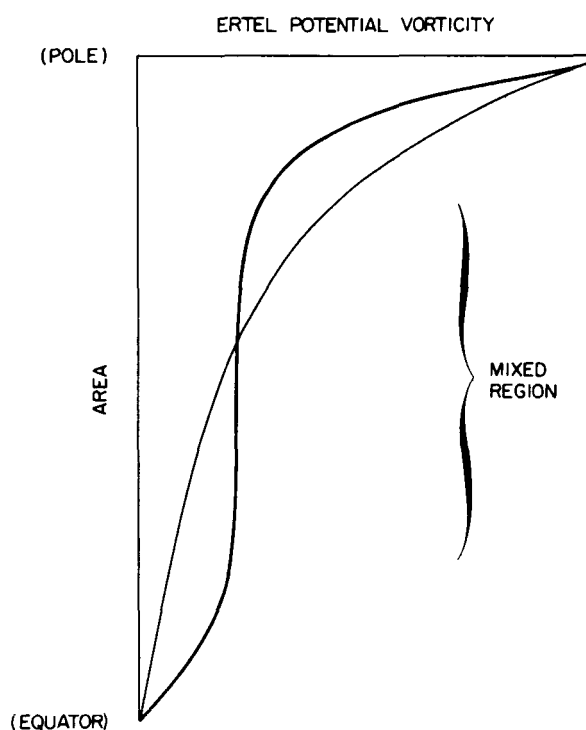
(E. E. Remsburg, 3306)

## Area Diagnostics of Seasonal Trends in Stratospheric Circulation

The wintertime Northern Hemisphere stratosphere is characterized by strong meridional transport and mixing. Attempts to quantify such effects have been improved by calculating the rate of change of area within contours of supposedly conserved atmospheric parameters. One such parameter is the Ertel potential vorticity (PV) calculated on a potential temperature surface.



Diurnal variation of ozone from one-dimensional model compared with LIMS data both before and after correction for NLTE effects.



Distribution of potential vorticity in middle stratosphere before (thin curve) and after (heavy curve) mixing by large-amplitude waves.

A schematic of the process is shown in the figure. Prior to periods of intense mixing, potential vorticity increases smoothly from Equator to Pole, consistent with a zonally symmetric circulation. After mixing, the mid-latitude PV gradient is weakened, and a pronounced PV gradient change occurs near the Pole. The regions of strong and weak PV gradients are representative of the main-vortex, surf-zone structure predicted by fluid dynamical theory of the stratosphere.

Trends in this PV structure have been examined each day for the winter of 1978 and 1979 using data derived from the Limb Infrared Monitor of the Stratosphere experiment. Regions and periods of irreversible mixing and diabatic effects are being studied with the aid of these area diagnostics. Correlations between PV and similar trends in the area of ozone and water vapor are excellent in the mid-stratosphere and verify these species as suitable tracers of stratospheric transport. (E. E. Remsberg, 3306)

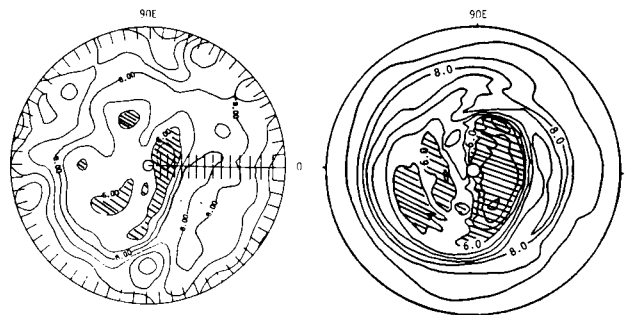
### Three-Dimensional Model Simulations of Ozone Transport During Sudden Stratospheric Warming

A three-dimensional (3-D) atmospheric model that incorporates comprehensive chemistry has been used to study dynamics and transport processes and to simulate the distribution of chemically active species in the stratosphere. The results illustrated are a portion of a long-term simulation of the seasonally varying behavior of important stratospheric trace constituents. The occurrence of a mid-winter stratospheric warming and the associated transport of ozone and other species are observed in the results. The simulated distributions of  $O_3$  and  $HNO_3$  compare well (as shown in the figures) with the satellite data obtained from the Limb Infrared Monitor of the Stratosphere experiment on Nimbus 7. The particular LIMS data shown in the figures are chosen because the circulation and thermal structure during the observed minor warming of January 1979 are quite similar to those of the model-simulated warming.

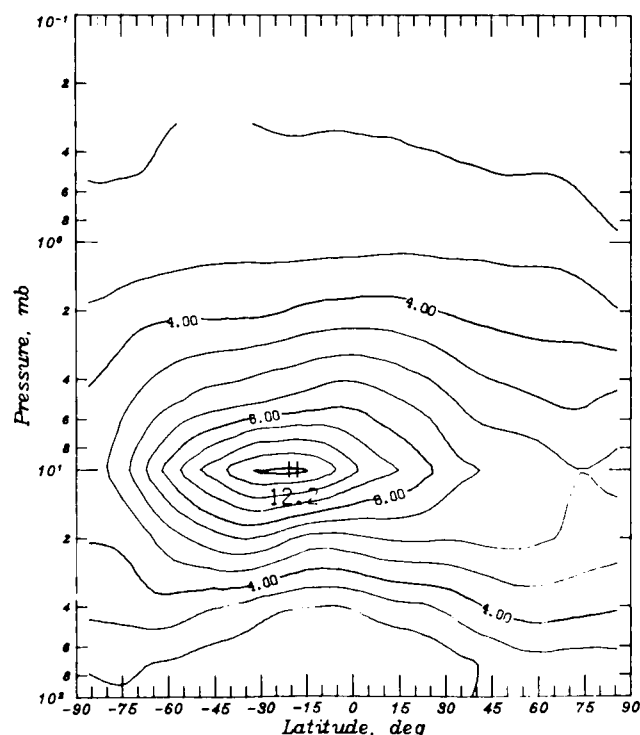
The model successfully simulates many aspects of the observed ozone distribution during the period of enhanced dynamical activity. Both simulated and observed ozone distributions display the characteristic signature of "wave-breaking" and irreversible mixing observed in isentropic potential vorticity distributions inferred from both LIMS data and Stratospheric Sounding Unit measurements. Also apparent are the incursions

or tongues of ozone-rich air parcels from lower latitudes into the polar cap region associated with the displaced polar vortex. The zonal mean ozone field obtained in the simulation is also depicted and compares favorably with similar representations of data and two-dimensional model results.

(W. L. Grose, 4788)



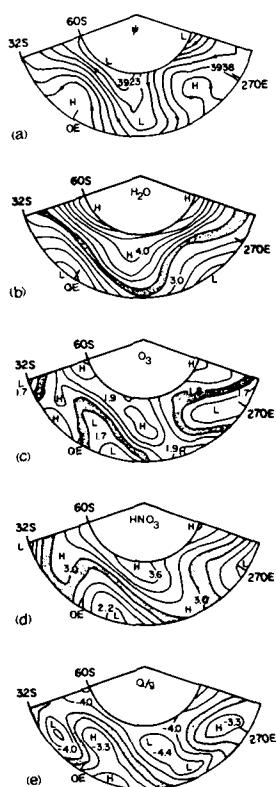
Ozone distribution in stratosphere in parts per million by volume (ppmv). Shown on left is NASA Langley 3-D model distribution of 10 millibars ( $\approx 32$  km) for Northern Hemisphere. Shown on right are LIMS ozone data at 10 mb for January 24, 1979. Shaded regions in polar plots indicate concentrations less than 6 ppmv.



Zonal mean ozone results computed from NASA Langley 3-D model.

## Transient Medium-Scale Wave Activity in Summer Stratosphere

Observations of medium-scale transient wave activity in the middle-latitude Southern Hemisphere summer stratosphere have been interpreted using the isentropic potential vorticity (IPV) distributions inferred from temperature data from the Nimbus 7 Limb Infrared Monitor of the Stratosphere (LIMS) instrument. Despite problems with errors in reference-level synoptic height information, the derived IPV distributions clearly exhibit dynamically coherent signatures of eddy mixing due to medium-scale wave disturbances in the lower middle stratosphere during early January 1979. The IPV distributions are shown to be strongly correlated with those of a contemporaneous set of isentropic maps of quasi-conservative tracers, such as ozone, nitric acid, and water vapor (as shown in the figure).



*LIMS isentropic analysis for region 32°S to 60°S and 255°E to 35°E on January 7, 1979. (a) 450K stream function (contour interval  $3 \times 10^2 \text{ m}^2 \text{ s}^{-2}$ ), (b) 470K  $\text{H}_2\text{O}$  concentration (0.2 ppmv), (c) 470K  $\text{O}_3$  concentration (0.05 ppmv), (d) 470K  $\text{HNO}_3$  concentration (0.2 ppbv), (e) 450K potential vorticity  $Q/g$  ( $0.2 \times 10^{-6} \text{ KPa}^{-1} \text{ s}^{-1}$ ).*

The results suggest that IPV maps inferred from satellite temperature data provide a useful diagnostic tool for studies of large-scale dynamics and transport in the extratropical stratosphere. Furthermore, the comparatively high vertical resolution of the LIMS data has enabled the vertical attenuation of Southern Hemisphere wave activity to be diagnosed in greater detail than could be achieved from nadir-viewing satellite information.

(W. L. Grose, 4788)

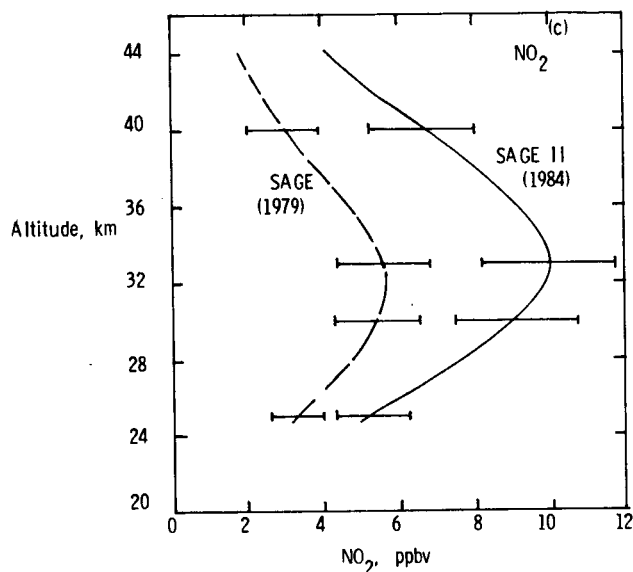
## Explanation for Antarctic "Ozone Hole"

Recently published satellite and Dobson measurements of total ozone in Antarctica in September and October have shown dramatic declines, beginning in the late 1970's, compared to long-term climatological averages. This phenomenon has been termed the "ozone hole" and has been suggested to be a precursor to severe and more widespread destruction of ozone by chlorofluoromethanes.

Photochemical calculations along trajectories in the meridional plane have been used to search for the cause of this dramatic springtime "ozone hole" in the Antarctic region. Results suggest that the minimum is principally due to catalytic destruction of ozone by high levels of total odd nitrogen. Calculations further suggest that these levels of odd nitrogen are transported within the polar vortex and during the polar night to the lower stratosphere from the mid-to-upper stratosphere and lower mesosphere. These odd nitrogen levels are thought to be related to the 11-year solar cycle and result from enhanced formation in the thermosphere and mesosphere during solar maximum conditions.

Analysis of satellite data (LIMS, SAGE, SME, and SAGE II) establishes significantly increased levels of stratospheric total odd nitrogen (60 percent) for the 1979 to 1984 time period, particularly at the mid-southern latitudes. This is illustrated in the figure by comparisons at 60°S to 65°S of SAGE and SAGE II  $\text{NO}_2$  measurements for late November 1979 and 1984, respectively. The persistent recurrence of the Antarctic ozone minima in the mid-1980's appears to be related to this growth of odd nitrogen. Chlorine species at double the present atmospheric levels are shown to have an insignificant effect on the formation of the "ozone hole" if only homogeneous processes are considered.

Heterogeneous chlorine reactions are found to have only a modest effect on the Antarctic ozone reductions.  
(L. B. Callis, 2985)



*Comparison of SAGE (1979) and SAGE II (1984) measurements of NO<sub>2</sub> for 60°S to 65°S during late November.*

## Improved Measurement Capability for Spectral Filter Characterization

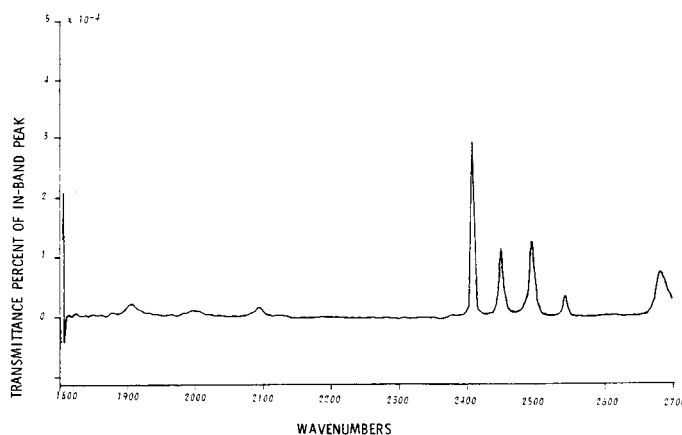
The Halogen Occultation Experiment (HALOE) is a solar occultation mission that will fly on the Upper Atmosphere Research Satellite to measure mixing ratio profiles of O<sub>3</sub>, HF, HCl, CH<sub>4</sub>, NO, H<sub>2</sub>O, and NO<sub>2</sub> in the stratosphere and lower mesosphere. The associated atmospheric pressure profile will be inferred from absorption measurements in a primary CO<sub>2</sub> band. The inversion of the HALOE data will be critically dependent on a detailed knowledge of the optical filters in the HALOE instrument.

In order to meet the stringent HALOE requirements, a filter characterization program was undertaken to measure the in-band transmission to a precision of 0.5 percent at three temperatures that covered the HALOE operating temperature range, the out-of-band

transmission to a precision greater than 0.001 percent of the peak in-band transmission over the spectral range 2 to 16  $\mu\text{m}$ , and the in-band reflection measurements to a precision of 1 or 2 percent. Special procedures were developed that involved (1) the use of different beam and source apertures and preamplifier gain settings to achieve a large dynamic range, (2) the averaging of 1,000 to 4,000 scans to achieve high signal-to-noise ratios, and (3) the use of special data collecting and data processing modes. The out-of-band transmission data of the HALOE flight filters showed leaks in all of the radiometer filters and the NO filter. The full set of eight correlation and radiometer filters has been measured to 0.0001 percent or greater precision level in order to quantify the leaks and to study the parameters that affect the transmission. The two parameters that greatly affect leaks are (1) the optical element in front of the filter, and (2) the angle between the filter face and the infrared (IR) beam axis.

The development of this capability has permitted the characterization of the HALOE filters to a level of precision which is believed to be greater than any previously attained. With this capability, it is now possible to characterize optical components of other instruments which are sensitive to transmission through out-of-band leaks.

(G. A. Harvey, 2576)



*Spectral leaks in the 4- $\mu\text{m}$  out-of-band region of HALOE H<sub>2</sub>O filter (in-band at 6.7  $\mu\text{m}$ ).*

---

# Structures Directorate

The Structures Directorate conducts basic research and develops technology in the areas of advanced aerospace materials and structures, structural loading and aeroelasticity, noise generation by aircraft propulsion systems and structures, and methodologies for interdisciplinary design and optimization. This technology development is directed toward reduction in both weight and cost of aircraft and space structures along with an increase in their reliability and service life. The technology developed also provides improved design capability through more accurate prediction of aerostructural loads, vibration, and noise.

The Materials Division conducts research on advanced materials and their application to aircraft and space structures. The division also develops novel polymeric, metallic, and carbon-carbon materials for these applications. The materials processing and fabrication sciences are developed, and the application of materials to specific flight and space structures is demonstrated. The division conducts research on thermal protection materials and hot structure systems for application to hypersonic and transatmospheric vehicles. The fatigue and fracture behavior of materials is studied in specialized laboratories to provide practical methods for insuring structural integrity. Specialized facilities are also used to study the behavior of materials under extreme conditions of high and low temperature, pressure or vacuum, and electron radiation.

The Structures and Dynamics Division conducts research on structures for advanced aircraft, space vehicles, and the space station. Analytical methods are developed for the prediction of static and dynamic stresses and strains in complex structures. Research is conducted on space structures to characterize and control dynamic response. Specialized facilities are used to study the dynamics of aircraft under simulated landing and crash conditions. The division develops new structural systems for aircraft and space structures and is also active in research and development of advanced computational methods for structural analysis and design.

The Loads and Aeroelasticity Division conducts research in aeroelasticity, aerothermal loads, high-temperature structures, unsteady aerodynamic loads, and aeroservoelasticity. Analytical methods are developed for calculating aeroelastic deformations and instabilities, for dynamic, vibratory, and thermal response of structures, and for the active control of aeroelastic and dynamic behavior of aircraft. Unique facilities are employed in experimental studies of unsteady

aerodynamics, aeroelastic behavior, and aerothermodynamic flows.

The Acoustics Division conducts research on the generation and propagation of aircraft noise and seeks to understand the relationships between unsteady aerodynamics, structural dynamics, and noise generation by the interaction of fluids with solid surfaces. This research is directed toward predicting and reducing the noise from helicopter rotors, conventional and advanced aircraft propellers, and turbofan engines. Research is conducted on the propagation of noise from its source through the atmosphere and through aircraft structures.

The Interdisciplinary Research Office develops methodologies for aircraft and spacecraft design which will provide a means of understanding and quantifying interactions among multiple engineering disciplines. The goal is to control and exploit these interactions for improved vehicle performance and increased efficiency of the design process. This research has focused on the development of algorithms and techniques for integrating strength and stiffness designs of large-aspect-ratio wing transport aircraft and of rotorcraft. The methodology has been developed for the optimization of space antenna dish shapes subjected to thermal loadings. Controls, structures, and structural dynamics have been integrated for use in the design of space station type structures.

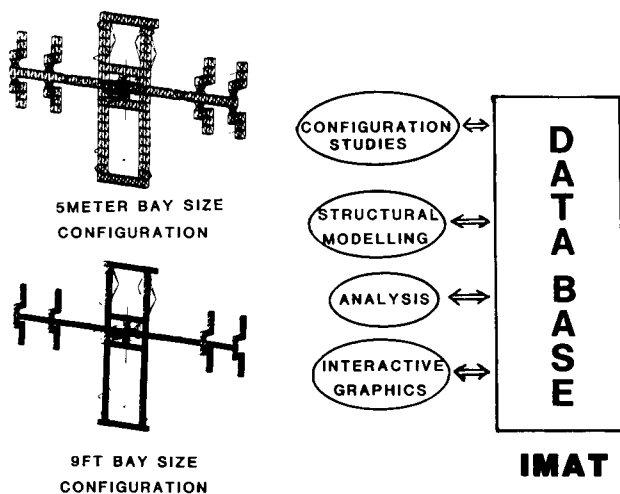
## Role of IMAT Study in Selection of Space Station Truss Bay Size

The Integrated Multidisciplinary Analysis Tool (IMAT), which integrates control, structures, and structural dynamics disciplines by using a common data base with an interactive file transfer executive system, is an operational, evolving computational capability developed by NASA Langley. With the relational information management (RIM) data base system as the key data storage and retrieval control capability, an interactive executive procedure has been designed to transfer and store input and output for several commercial general codes in the areas of computer-aided design, structural modeling, structural analysis, controls analysis, and graphical output. To aid in the Space Station truss-sizing activity, IMAT was used to design two growth versions of the dual-keel station with bay sizes of the cubic truss at 9 ft and 5 m as the only discriminator. Detailed finite-element models of the configurations

were computed, and the first 60 natural vibration frequencies were calculated.

Results showed that the natural frequencies of the 5-m-bay configuration exceeded the corresponding frequencies of the 9-ft-bay configuration by approximately 80 percent. Also, transient response studies showed that rotation of the solar dynamic system during a reboost maneuver was only about one-third as severe in the 5-m-bay configuration as in the more flexible 9-ft-bay configuration. Based in part on these results, the 5-m-bay size was selected as the reference configuration for the Level B Space Station design.

(P. A. Cooper, 3787)



#### Application of IMAT to Space Station.

### Use of Equivalent Plate Representation to Expedite Analysis of Aircraft Wing Box Structures

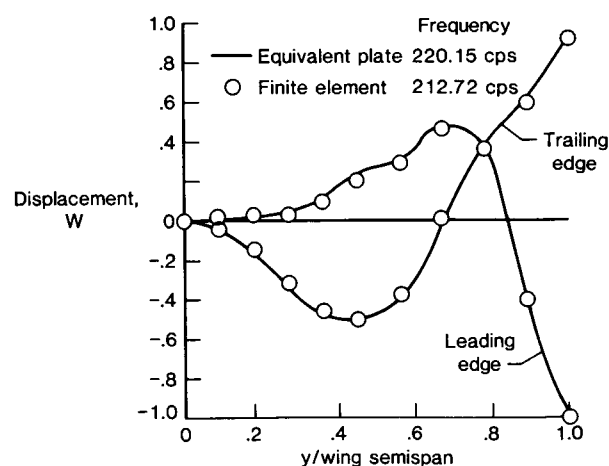
A new, equivalent plate analysis formulation, which has been developed at NASA Langley, has the capability to model aircraft wing structures with general planform geometry, such as cranked wing boxes. Such simplified plate models are often used for analysis during preliminary design but, in the past, have been limited to trapezoidal planforms. In the new method, the planform is defined by multiple planform segments. A Ritz

method of solution is used which has assumed-displacement functions defined in a global coordinate system and which automatically satisfies continuity requirements across common segment boundaries. Polynomials are specified by the analyst to define the wing depth and thickness of composite layers in the cover skins. The specification of model characteristics as continuous distributions in polynomial form requires only a small fraction of the volume of input data for a corresponding finite-element structural model in which both geometry and stiffness properties are specified at discrete locations.

Results from the equivalent plate analysis have been compared with corresponding results from a finite-element analysis program. Comparisons of these results indicate that good agreement, generally less than 5 percent difference, is obtained for both static displacements and vibration frequencies and mode shapes (as shown in the figure). The computation time required by the equivalent plate analysis to generate these results is a factor of 30 less than for a corresponding finite-element static analysis and a factor of 60 less than for a vibration analysis.

The continuous definition of displacement functions provides a direct method to interface this equivalent plate structural analysis procedure with aerodynamic programs for use in aeroelastic calculations. This interface has been applied to a full-potential supersonic aerodynamics program for use in interdisciplinary studies of an advanced fighter configuration.

(G. L. Giles, 2887)

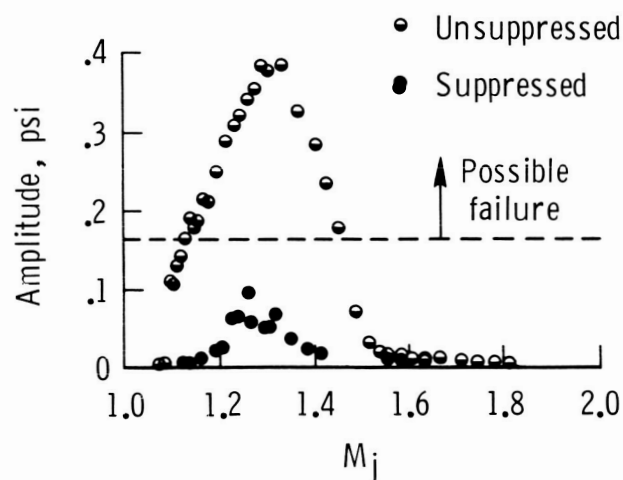


Sixth-vibration mode shape.

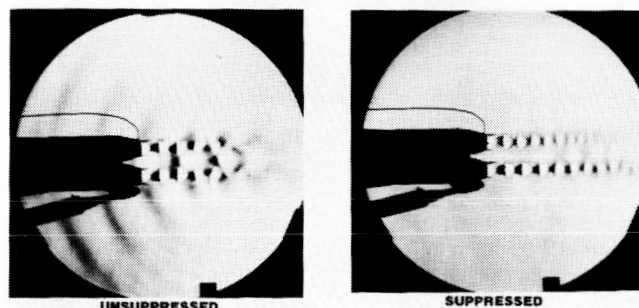
## Load Reduction Associated With Twin-Supersonic-Plume Resonance

Closely spaced supersonic engines are commonly utilized by the aircraft designer to improve performance. However, many of the aircraft that utilize this engine configuration have experienced fatigue failures in the internozzle region. In the present study, it has been conjectured that these fatigue failures are caused by strong coupling between the natural jet instabilities of each plume which lead to enormous growth rates and excessive near-field pressure levels.

To investigate this possibility, a 1/40-scale model was tested. A sensor was placed in the internozzle region to obtain fluctuating dynamic pressures. This sensor also served as a reference to obtain phase-averaged schlieren records. The optical records were used to identify the spatial plume structure associated with the large-amplitude pressure fluctuations. In addition, several passive methods of suppression were investigated to eliminate plume coupling by altering the stability characteristics of the individual plumes.



MAGNITUDE OF LOAD REDUCTION



Suppressed and unsuppressed pressure fluctuations.

The pressure data show that levels for many plume Mach numbers  $M_j$  are in a range in which possible sonic fatigue failures can be anticipated. A satisfactory reduction of these pressure levels can be achieved as is shown by the use of one suppression method in which thrust loss is expected to be minimal. The unsuppressed-version schlieren record shows that each plume is dominated by helical instabilities, and that these plumes are coupled together as they evolve downstream. Intense acoustic wave fronts can be observed propagating upstream on the inside and outside of each nozzle. The suppressed-version schlieren shows that the intense inner and outer pressure waves have been practically eliminated.

(J. M. Seiner, 3094)

## Sidewall Treatment for Aircraft Cabin Noise Control

The renewed interest in propeller-driven aircraft, due to their fuel efficiency, has caused the need to control their interior noise. One approach to control this interior noise is the use of sidewall acoustic treatments. These treatments are intended to reduce the noise transmitted through the structure and to provide absorption of sound within the cabin; however, not only is this treatment required to reduce the cabin noise but also it must have minimum weight and occupy a limited volume.

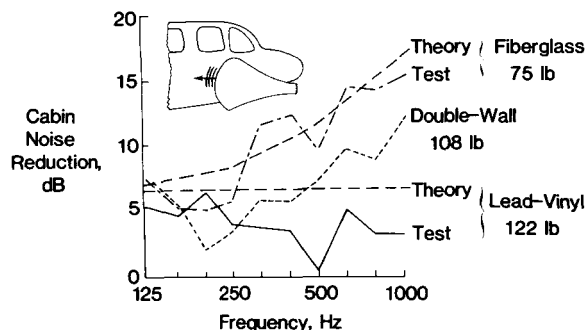
A production-type aircraft fuselage and horn noise source were used to test treatments that consisted of lead-vinyl attached to the skin, a flight-type double-wall installed by the fuselage manufacturer, and a 3-in. layer of high-density fiberglass. Absorbent fiberglass baffles surrounded the fuselage to reduce noise reflected from the test chamber walls. A horn was used to simulate the magnitude of the sound distribution of a propeller on the sidewall.

The three treatment configurations are shown to have similar values of noise reduction (the change in cabin noise between the bare and treated fuselage) at low frequencies and widely different values at high frequencies. The lead-vinyl provides the least noise reduction and is the heaviest of the tested configurations. The theoretical value of 6 dB assumes mass law transmission through the sidewall and confirms the measured trend. The double wall provides more noise reduction for less weight (except in one frequency band) than the lead-vinyl. The fiberglass provides the most noise reduction



for the least weight. The theoretical result includes both the transmission loss through the fiberglass and the increase of absorption in the cabin due to the fiberglass. The fiberglass absorption accounts for 7 to 8 dB of the noise reduction in all frequency bands and is, therefore, a significant noise control element not provided by the lead-vinyl or double-wall treatments.

(K. E. Heitman, 3561)



*Measured and predicted noise reduction for various acoustic sidewall treatments.*

## Low-Frequency Downwind Sound Propagation

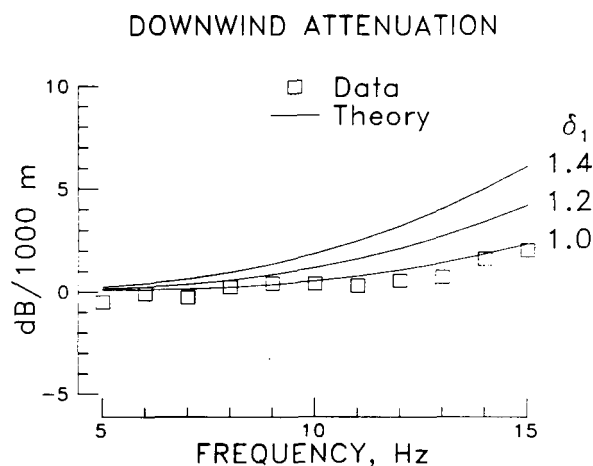
The amplitude of sound decreases with propagation distance due to air absorption and divergence (spreading out) of the sound field. Due to the smaller amount of air absorption at low frequencies, low-frequency sound propagates farther than high-frequency sound. In the absence of wind, low-frequency sound exhibits spherical divergence, which is characterized by a 6-dB decrease in level for every doubling of propagation distance. Downwind refractive effects channel the low-frequency sound and cause it to propagate over longer distances.

To investigate the propagation of low-frequency sound in wind, an experiment was conducted which used a two-bladed, 80-m-diameter wind turbine capable of generating 4.5 MW of electrical power as a sound source. The experiment included downwind measurements to distances of 20 km in winds up to 50 kn. The

measured data exhibited cylindrical divergence (a 3-dB decrease in level for every doubling of propagation distance).

A normal-mode formulation valid for low-frequency sound propagation in boundary layers over finite impedance boundaries was developed at NASA Langley. A comparison between measurement and normal mode theory is given in the figure. For the comparison, the effect of cylindrical divergence is removed from the wind turbine measured data. A residual attenuation is expressed in terms of dB/km, a quantity that has been predicted by the theory. The parameter  $\delta_1$  in the figure is the displacement thickness of the atmospheric boundary layer. Best agreement is achieved for a value of  $\delta_1$  of 1 m, whereas the measured displacement thickness was 1.2 m. Future work will compare upwind propagation data with normal-mode theory.

(W. L. Willshire, Jr., 4310)



*Comparison of data with normal mode theory.*

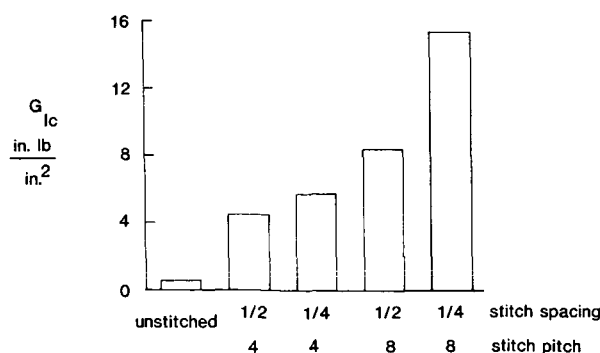
## Improved Interlaminar Fracture Toughness of Graphite/Epoxy Composites by Through-the-Thickness Stitching

Aircraft designers have not been able to utilize the full performance potential of composite materials due to their poor damage resistance and fracture toughness

properties. Therefore, a major research focus has been to develop composite materials with improved interlaminar toughness and damage resistance. Braiding, three-dimensional weaving, and through-the-thickness stitching offer the promise of improved damage tolerance, fracture toughness, and capability to withstand out-of-plane tension loads.

A quasi-isotropic T300/3501-6 graphite/epoxy composite was used to evaluate through-the-thickness stitching as a means to improve the interlaminar fracture toughness of composite materials. The composite was stitched through-the-thickness with a stitch spacing of either 0.25 in. or 0.50 in. and a stitch pitch of either 4 or 8 stitches per in. Kevlar yarn was used to stitch through the composite. The double-cantilever-beam interlaminar fracture toughness test was used to determine the Mode I critical-strain energy release rate ( $G_{Ic}$ ) of the stitched material. As the figure indicates, both stitch pitch and stitch spacing play an important role in improving the interlaminar fracture toughness of the composite. All of the stitched material had a higher interlaminar fracture toughness than unstitched T300/934 graphite/epoxy tape material. The stitched material with an 0.25-in. stitch spacing and a stitch pitch of 8 stitches per inch had a  $G_{Ic}$  30 times that of the unstitched tape composite. The increase in interlaminar fracture toughness was accompanied with only a 0.1- to 0.2-percent weight increase and a 20- to 25-percent reduction in tension and compression properties as compared to unstitched quasi-isotropic tape material. In stiffness-dominated composite material applications, the benefits of improved toughness may outweigh the sacrifice in the in-plane properties. Thus through-the-thickness stitching is a viable means to improve the interlaminar fracture toughness of composite materials.

(J. G. Funk, 4582)

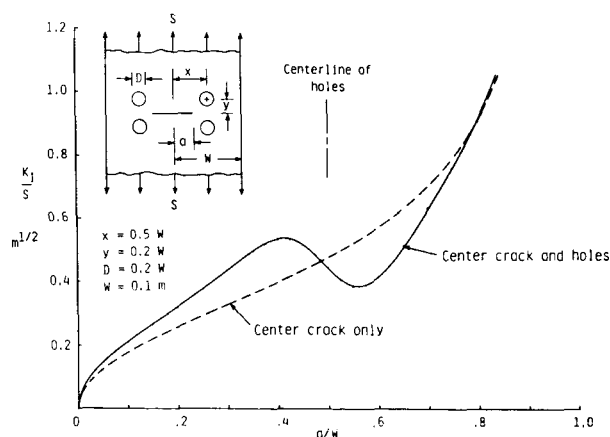


Effect of through-the-thickness stitching on  $G_{Ic}$  of graphite/epoxy composite.

## Method for Analyzing Complex Cracked Configurations to Minimize Modeling

In the field of fracture mechanics, stress-intensity factors are important parameters for predicting fracture strengths and fatigue lives. However, solutions for stress-intensity factors for complex, cracked, finite bodies are not readily available and are difficult to generate. A new, easier method called the boundary force method (BFM), which has been developed at NASA Langley, is computationally more efficient than conventional finite-element methods because only the internal and external boundaries of the region need to be modeled in the BFM as compared to the need to model the entire region in the finite-element method. Moreover, the stress-free conditions on the crack faces are satisfied exactly in the BFM (which eliminates the need for a concentration of elements in the crack-tip region as is used in finite-element modeling).

The accuracy of the method was established by comparing model results to exact solutions and was found to be within  $\pm 0.5$  percent of accepted solutions. The figure shows results for one of the complex configurations that was easily analyzed using the boundary force method. The four-hole cracked configuration was designed to simulate the effects of a stringer on an advancing crack. The mode I stress-intensity factor  $K_I$  is normalized with the applied stress  $S$  and plotted against the crack-length-to-width ratio. The case of a center crack without the holes (dashed curve) is also



Stress intensity factors for four-hole plate with central crack.

shown for comparison. The stress-intensity factor solutions for this configuration are not available in the literature and, therefore, will be a useful addition.

The boundary force method has been used to generate stress-intensity factor solutions to other common engineering configurations for which solutions have not been available. These configurations include an edge crack emanating from a semicircular, semielliptical, and v-shaped notch. The boundary force method has been found to yield very accurate solutions for complex crack configurations with minimal modeling effort.

(P. W. Tan, 3011)

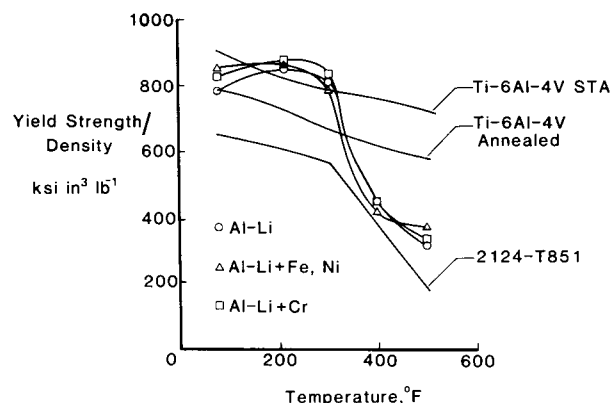
## Improved, Elevated Temperature Strengths Through Use of New Aluminum-Lithium Alloys

Numerous studies have shown that both ingot metallurgy and powder metallurgy processed aluminum-lithium (Al-Li) alloys not only have attractive combinations of low density and high modulus and strength but also retain reasonable ductilities. McDonnell-Douglas Research Laboratories, under contract to NASA Langley, have demonstrated that the rapid solidification rate (RSR) processed alloys of the base composition Al-3Cu-2Li-1Mg-0.2Zr (with additions of Fe, Ni, and Cr) have density-normalized strengths superior to all competitive titanium- and aluminum-based alloys for applications up to 300°F and 500°F, respectively. The improved density-normalized strengths result from a combination of low density due to Li additions, precipitation strengthening from additions of Cu, Li, and Mg, and strengthening by incoherent dispersoids formed with the additions of Fe, Ni, or Cr. These dispersoids cannot be sufficiently refined in ingot processing to significantly improve strength.

The figure shows variations in ratios of yield strength to density with 100-hour exposure at various temperatures for the RSR Al-Li alloys, 2124-T851, and Ti-6Al-4V in both annealed and solution treated and aged (STA) conditions. The data show that the RSR alloys can provide competitive or superior performance to the Ti-based alloys up to 300°F and are superior to 2124-T851 up to 500°F. The ratios of elastic modulus to density of the RSR alloys are approximately 20 percent greater than those of commercial 2XXX and 7XXX aluminum alloys, and ductilities of the baseline and Cr-containing alloys approach those of 2124-T851 at

300°F. The improved specific properties of the RSR Al-Li alloys at elevated temperatures indicate that these alloys are suitable substitutes for current titanium and aluminum alloys in applications that must withstand extended elevated-temperature exposure without loss in properties.

(M. S. Domack, 3372)



*Specific strength of aluminum-lithium alloys at room and elevated temperatures.*

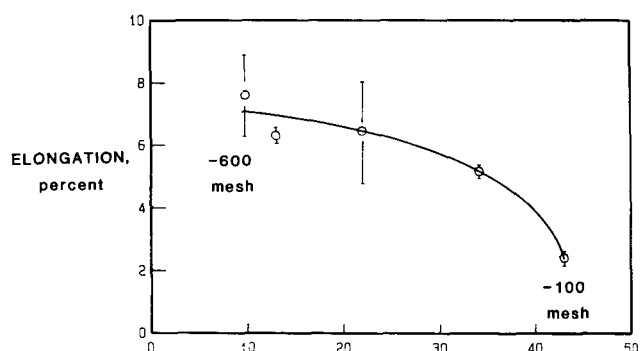
## Improvement of Aluminum Matrix Composite Properties Through Microstructural Refinement

Aluminum alloy matrix composites reinforced with silicon carbide whiskers are being developed for aerospace structural applications. These materials are usually stronger and stiffer than unreinforced alloys but have poor ductility and fracture toughness. Also, the true yield stress is only marginally increased over that of the unreinforced base alloy. One factor that is thought to contribute to these poor properties is a nonhomogeneous microstructure that results from nonuniform reinforcement distribution and creation of zones that are nearly void of whisker reinforcement (whisker-depleted zones). The condition is thought to be caused by practical limitations associated with initial aluminum powder particle-size distribution.

In order to assess the effects of inhomogeneous microstructure related to whisker-depleted zones, composite extrusions were prepared by blending equal

amounts of whisker (20 percent) with five aluminum powder batches that have particle-size distributions ranging from -100 mesh to -600 mesh. Composites with varying degrees of whisker distributions were produced. Mechanical property tests using 0.25-in. round tensile specimens that were prepared from 0.7-in.-diameter bar extrusions showed a marked effect of the whisker-depleted zones (resulting from use of different powder particle sizes) on measured properties. Systematic variation in both proportional limit (true-yield stress) and percent elongation (ductility) was observed to be related to whisker-depleted zones. The composite made with the finest powder had more uniform whisker distribution with much smaller whisker-depleted zones than those that were observed in composites fabricated with powder of large particle sizes. The composite processed with the finest powder particle size had tensile properties 25 percent to 50 percent greater than and elongation more than three times those of composites made with the coarsest powder.

(B. Sarkar, 4196)



Mean width (in  $\mu\text{m}$ ) of whisker-depleted zones.

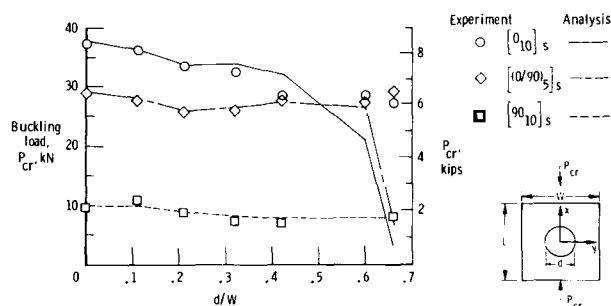
## Approximate Analysis for Buckling of Plates With Cutouts

During flight, structural members with cutouts often experience compressive loads; therefore, the ability of a compression member with a cutout to resist buckling is important in design. Understanding the buckling behavior of a rectangular laminated composite plate with a centrally located cutout provides valuable

insight into the behavior of more complicated structures. To permit in-depth parametric study of these structures, an economical approximate analysis was developed that converts the classical two-dimensional prebuckling and buckling problems to equivalent one-dimensional problems.

Results obtained from the approximate analysis were compared with finite-element analyses for isotropic plates and for three specially orthotropic plates with central circular cutouts of various sizes. In nearly all cases, the approximate analysis not only correctly predicted the buckling mode shapes but also predicted the buckling loads to within a few percent of the finite-element results. Experimental results for the specially orthotropic plates with hole-diameter-to-plate-width ratios  $d/W$ , which ranged from 0 to 0.7 (as shown in the figure), were also obtained. Comparison of analysis with experiment indicates that the approximate analysis predicts buckling loads to within 13 percent for most cutout sizes. Both the analytical and experimental results obtained in this study indicate that increasing the cutout size in a given plate does not always reduce the buckling load.

(M. P. Nemeth, 4052)



Experimental and approximate buckling loads for clamped specially orthotropic laminates.

## Computational Transonic Flutter Boundary Tracking Procedure Development

Flutter is frequently a limiting factor in the performance of aircraft in transonic flight. Because of this limitation, it is highly desirable to be able to accurately

and efficiently predict transonic flutter characteristics. Consequently, an automated tracking procedure, which uses a time-accurate unsteady aerodynamic code, was developed at NASA Langley for the efficient calculation of transonic flutter boundaries. A graphical description of the tracking procedure and a typical set of results are shown in the figure. The procedure makes use of a time-marching method along the boundary by taking steps in speed and Mach number. As shown in the upper half of the figure, the nondimensional flutter speed  $U_f$  is first predicted using calculations performed at points 1 to 3, and then is corrected by interpolation using calculations performed at point 4.

Transonic flutter boundary results for the NACA 64A010A airfoil at a mean angle of attack of  $1^\circ$  are shown in the lower half of the figure. The tracking procedure solution is virtually identical to the exact solution obtained using a conventional time-marching method. The tracking results were obtained in a single

computer job submission, and the use of this single submission reduces the elapsed analysis time for flutter boundary determination from 2 to 4 weeks to an overnight-turnaround time period. Furthermore, the computational costs were approximately cut in half.

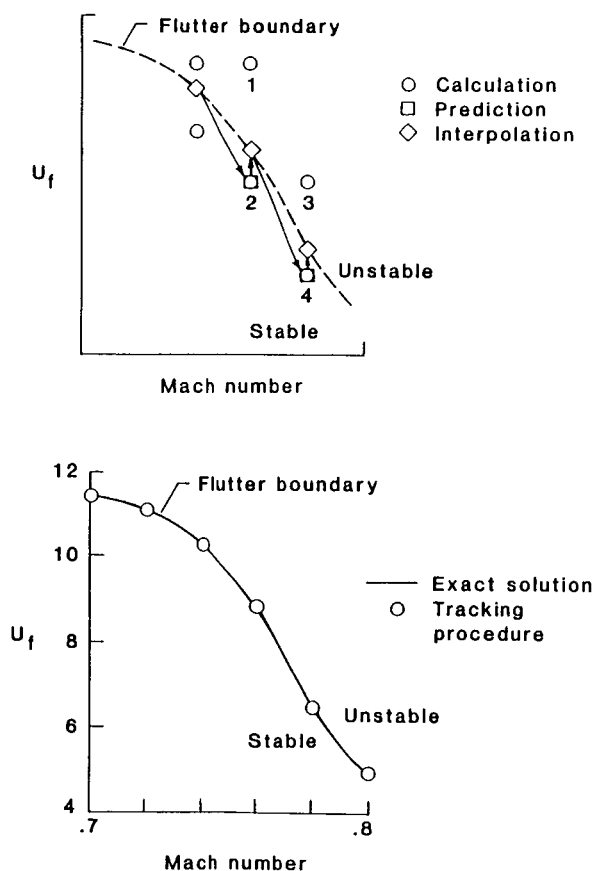
The tracking procedure was also extended to include static aeroelastic deformation and contains all of the essential features for practical three-dimensional analyses. The procedure has also been applied to determine flutter boundaries as a function of structural parameters and has been shown to be useful as a design tool.

(J. T. Batina, 4236)

## New Method for Approximating Unsteady Aerodynamics for Aeroservoelasticity Computations

The equations of motion for a flexible aircraft contain unsteady aerodynamic force terms which, when expressed in the Laplace domain, are transcendental functions. Aeroservoelasticity computations are often performed by first approximating the unsteady aerodynamic force terms with rational functions of the Laplace variable and then transforming to constant coefficient differential equations. Since the goodness of the approximation is generally proportional to the number of differential equations, there is a trade-off between the goodness of fit (see the approximation error in the top figure) and the reduction in the number of differential equations. A new method, which significantly reduces the number of differential equations when compared against other existing methods, has been developed for approximating unsteady aerodynamics.

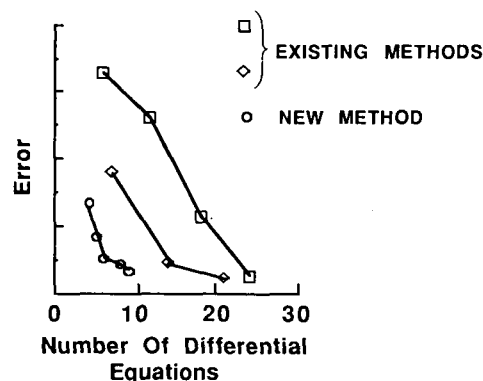
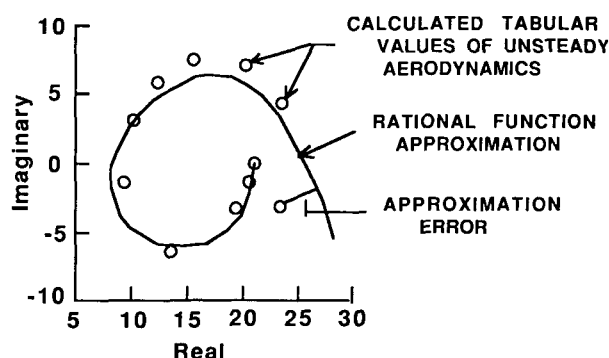
Existing methods employ a rational form of the approximation such that the number of differential equations necessary for approximating the unsteady aerodynamics is dependent on the number of structural modes in the equations of motion. Mordechai Karpel of Stanford University suggested a structure for the rational form such that the number of differential equations is independent of the number of structural modes. The new method, which was developed at NASA Langley, has extended and generalized Karpel's formulation. This new method and two existing methods have been included in a unified software system that allows easy selection of the method that best suits a particular application. Results presented in the figure show that the



Tracking procedure description and application.

new method decreases the number of differential equations by over 50 percent for the same approximate error, as compared to two existing methods. This significant reduction in the number of differential equations required to approximate the unsteady aerodynamics decreases computer time and cost for aeroservoelasticity analysis and design computations and allows larger problems to be analyzed.

(S. H. Tiffany, 1975)



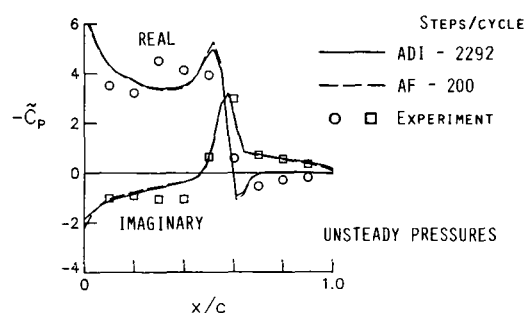
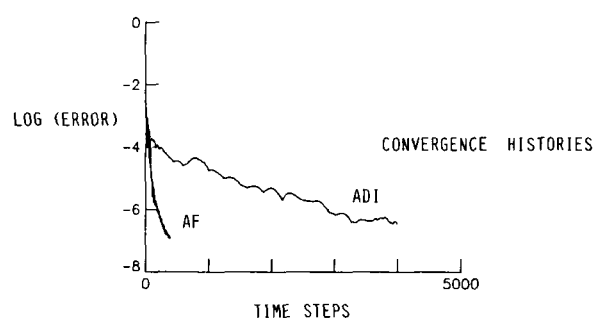
Results from applying new method.

## New Algorithm Development for Efficient Transonic Unsteady Aerodynamic Analyses

An approximate factorization (AF) algorithm was developed at NASA Langley for solution of the unsteady small-disturbance potential equation for transonic flow.

The new algorithm is very efficient for transonic unsteady aerodynamic and aeroelastic analyses when compared with the alternating-direction implicit (ADI) algorithm of the Air Force/Boeing XTRAN3S computer code. The figure shows results of applications of the AF algorithm to an F-5 fighter wing. The free-stream Mach number was 0.9 and the angle of attack was  $0^\circ$ . A comparison of convergence histories of the AF and ADI algorithms is shown in the upper part of the figure.

The AF algorithm provides a converged steady-state solution in one-tenth the number of time steps that the ADI algorithm requires. The AF algorithm gives similar improvements in computational expense for subsequent unsteady calculations required for aeroelastic analyses. A comparison of unsteady pressure coefficients per unit pitch angle  $\tilde{C}_p$ , versus fractional chord at the wing midsemispan  $x/c$ , is shown in the lower part of the figure. The calculations were performed for the rigid wing pitching harmonically with a reduced frequency of  $k = 0.14$ . The AF results were obtained in a fraction of the number of time steps per cycle that the ADI results require, and both sets of results compare well with the experimental data. Therefore, the new AF algorithm is accurate and efficient for transonic unsteady aerodynamic analyses.



Convergence histories and unsteady pressures.

The research was conducted as part of a larger effort directed toward developing computational methods of predicting unsteady flows with emphasis on the flutter critical transonic speed range. In addition, the algorithm has been demonstrated to be effective in the supersonic regimes (not shown). Work is continuing to further assess the accuracy and efficiency of the new AF algorithm.

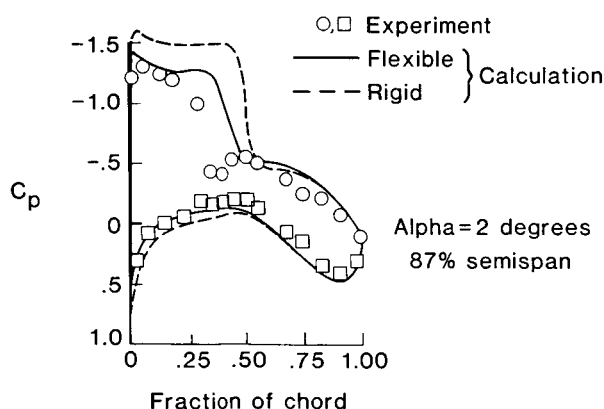
(J. T. Batina, 4236)

## Automated Transonic Aeroelasticity Analysis Program Development

A procedure developed at NASA Langley for non-linear transonic aeroelastic analysis of three-dimensional wings is based on the sequential and iterative use of a series of independent programs. For a fabricated wing shape, wing surface pressures are calculated using the FL022 aerodynamic program. A new wing shape resulting from the pressure loadings is then used in the next iteration. Three to six iterative loops are normally required to achieve convergence.

Running the individual programs, transferring files, and evaluating intermediate results for a converged solution were found to be extremely time-consuming tasks. Linking programs, automating file transfers, and adding logic to exit the iterative loop when the convergence criteria were met have resulted in significant savings in user time and computer resources.

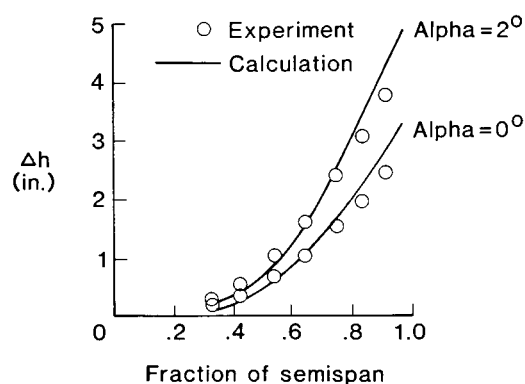
The automated procedure was used to provide results for comparison with experimentally measured data for a flexible transport-type wing tested in the Langley



Calculated and measured wing surface pressures.

Transonic Dynamics Tunnel. Computed pressure coefficients for a rigid and a flexible wing show the calculated aeroelastic effects. The calculated pressure coefficients for the flexible wing agree well with the measured data, although the computed location for the recompression shock is slightly farther aft when compared with measured data. Also shown are computed and measured wing vertical deflections that are also in close agreement.

(C. V. Eckstrom, 3834)



Calculated and measured wing vertical deflections.

## Identification of Unusual Instability Boundary for ARW-2 as Narrow Transonic Response Region

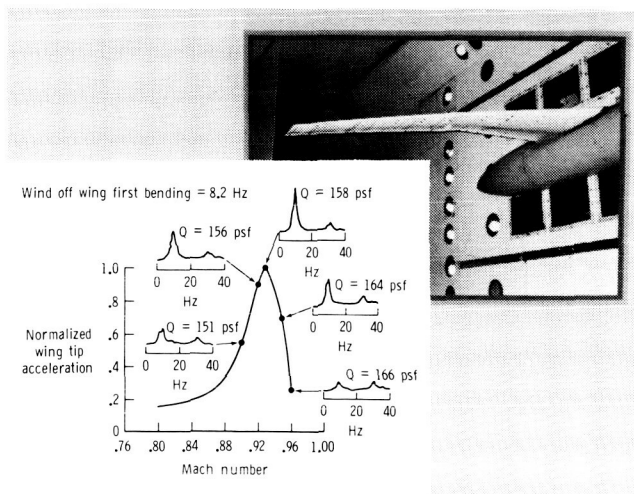
A test in the NASA Langley Transonic Dynamics Tunnel for measurement of steady and unsteady surface pressures on the Aeroelastic Research Wing ARW-2 revealed what appeared to be a wing-first-bending mode instability. The onset of this unusual instability occurred at a nearly constant Mach number ( $M$ ) of 0.90 for dynamic pressures from 50 to above 300 lb/ft<sup>2</sup>, which was well below the predicted classical flutter boundary.

An additional test to investigate the characteristics of this instability found no "hard flutter" conditions. With the wing at an angle-of-attack ( $\alpha$ ) of  $0^\circ$ , the previously identified instability boundary was penetrated at dynamic pressure levels near 80, 160, and 310 lb/ft<sup>2</sup>. Measurements indicated that the wing motion, which

increased with dynamic pressure, was comprised mainly of the wing-first-bending mode. Results shown are typical of the normalized wing tip motions measured. Wing tip motion rises rapidly at  $M=0.90$ , reaches a maximum near  $M=0.93$ , and decreases rapidly at  $M=0.95$ . Frequency response plots shown in the figure for several Mach numbers illustrate vividly the rapid rise in the wing-first-bending mode near 10 Hz over a narrow transonic Mach number range. The wind-off frequency for this mode was 8.2 Hz.

Tufts installed on the wing indicated visually large regions of flow separation near the trailing edge for both the upper and lower surfaces above  $M=0.90$ . Variations in wing angle of attack were made, but no consistent pattern of response was observed. The largest wing tip deflections of about 6-in. peak-to-peak were experienced at a dynamic pressure of 325 lb/ft<sup>2</sup>,  $M=0.92$ , and  $\alpha=1^\circ$  and resulted in the only use of the tunnel emergency stop system.

(M. C. Sandford, 2661)



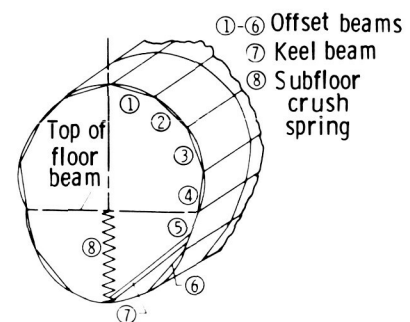
Test item and normalized wing tip response with Mach number.

## Structural Analysis of Jet Transport Controlled Impact Demonstration

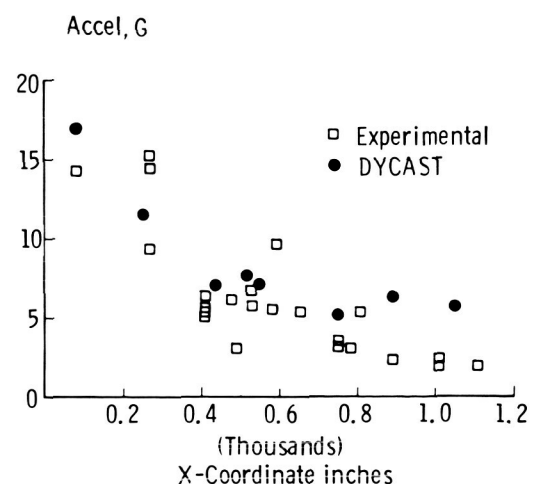
An extensive research and development program was initiated by the NASA Langley Impact Dynamics Branch and the FAA to quantitatively assess jet transport airplane crash dynamics using nonlinear dynamic finite-element computer codes. The FAA/NASA Controlled

Impact Demonstration (CID) of a remotely piloted Boeing 720 jet transport instrumented with over 350 crash sensors provided experimental data for the final modeling effort.

In cooperation with Boeing Commercial Airplane Company, a hybrid finite-element airplane crash model was developed with the nonlinear computer code DYCAST (Dynamic Crash Analysis of Structures, developed by Grumman under NASA Langley contract) to evaluate pre-CID impact scenarios and to simulate the actual CID test. Three transport fuselage section vertical drop tests performed at the Impact Dynamics Research Facility at NASA Langley at an impact velocity of 20 ft/s were modeled and analyzed using DYCAST to provide nonlinear subfloor crush springs for the hybrid CID model. Although a symmetric impact for CID



## PEAK VERTICAL FLOOR ACCELERATIONS



Comparisons of DYCAST-predicted peak vertical floor accelerations with CID experimental data.



was planned, the left-wing outboard engine impacted first with the airplane rolled and yawed 13 deg. Model predictions began at fuselage contact with the ground and continued for 0.15 sec. Initial conditions used in the analysis were 12 ft/s vertical sink rate at the center of gravity,  $-0.1$  rad/s pitch rate, and initial pitch of  $-2.5$  deg at fuselage impact. Yaw and roll conditions were not included. The figure shows a schematic of only the fuselage portion of the symmetric CID airplane model and comparisons of predicted vertical floor acceleration peaks with experimental peaks measured along the floor from nose ( $X=0$ ) to tail. Predictions of the acceleration levels from the model agree well with data from the CID experiment.

The building-block analysis approach of using results from detailed models of substructure to form hybrid elements for input to more complex structures (i.e., full airplane models) has been successfully used. Good agreement between the DYCAST model results and the CID experimental data demonstrates the validity of this approach as a useful method for assessing crash dynamics of large transport aircraft.

(E. L. Fasanella, 3796)

## FAA Test Data Comparisons Using NASA ANOPP Propeller Analysis System

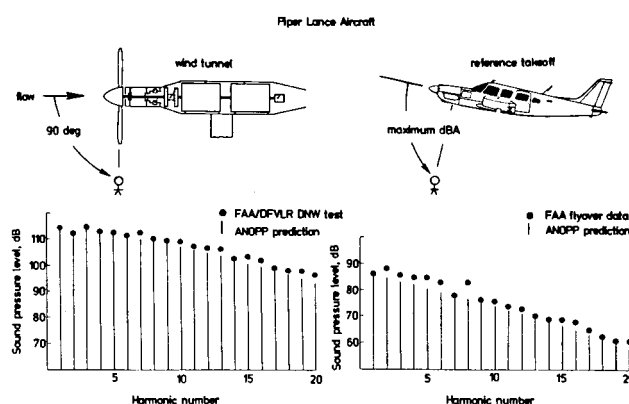
The NASA Aircraft Noise Prediction Program (ANOPP) Propeller Analysis System (PAS) is a set of computational modules for predicting the aerodynamics, performance, and noise of propellers. This system separates the flow field into an aerodynamic part and an acoustic part. Classical aerodynamic theory is used to find the surface pressures and frictional stresses on the blade surfaces, and acoustic theory based on Farassat's method is used to predict the noise.

The FAA, with assistance from NASA, recently compared data from wind tunnel and flyover tests with predictions from the ANOPP PAS. The wind tunnel tests were jointly conducted by the FAA and Deutsche Forschungs-und Versuchsanstalt fur Luft-und Raumfahrt (DFVLR) in the German/Dutch Wind Tunnel (DNW) on a full-scale Piper Lance propeller. Measurements of the radiated noise for various helical tip Mach numbers, power coefficients, advance ratios, and inflow angles were obtained as a function of directivity angle. The flyover tests were conducted by the FAA at the

Washington-Dulles International Airport. Far-field flyover noise measurements were made for 17 different takeoff and level flight conditions. Noise predictions were made using the PAS with only propeller geometry and operating conditions as input.

The figure shows example comparisons from both the wind tunnel and flyover data bases. The predictions agree with both sets for well past the tenth harmonic. Additionally, the predicted trends of the maximum A-weighted sound pressure level with helical Mach number, power coefficient, advance ratio, and inflow angle (not shown) agree well with measured trends. This resulted in the FAA proposing to the International Civil Aviation Organization (ICAO) that the ANOPP PAS be used to identify the major noise sources in certification flyover data and to establish trends for correction of data to reference conditions.

(R. A. Golub, 3842)



*Propeller noise prediction with ANOPP propeller analysis system.*

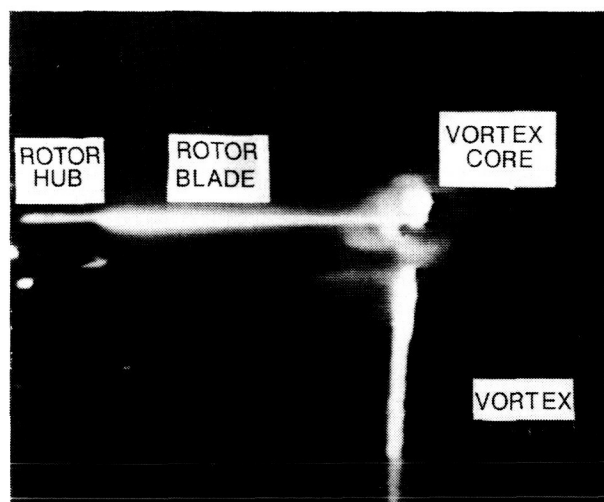
## Visualization of the Interaction Between Rotor Blades and Tip Vortices

The development of methods for visualizing the flow patterns around a rotor system during wind tunnel testing has been an important research area for many years because an understanding of the flow patterns is fundamental to the understanding of the aeroacoustics/aerodynamics of a rotor system. The introduction of smoke or high humidity into the flow has been used

successfully in hover tests. However, these methods have not been satisfactory in simulated forward flight. A promising system that employs a sheet laser in conjunction with smoke has been utilized to visualize tip vortices of a model rotor in forward flight. This system was developed by Boeing-Vertol, under contract to NASA Langley, as part of the NASA/American Helicopter Program. The system was used so that the physical separation between a vortex and an advancing blade could be measured and correlated with the acoustic signature.

The system utilizes smoke introduced upwind of the rotor by a probe positioned so that the smoke becomes entrapped in the tip vortex. A pulsed 1.6-J 30-ns ruby laser is then used to illuminate a very narrow (1.8-in.) "slice" through the vortex. Slices are taken every 5 in. over the area of interest so that the vortex position and the blade/vortex separation are determined as a function of blade azimuth. Since the ruby laser is of extremely short duration, it is necessary to use a parallel, lower intensity argon ion laser with a continuously sweeping beam to ensure proper location and alignment of the more powerful, short-duration system. Data are recorded by means of a 35-mm camera and a videotape system. The figure shows an example of this system applied to the visualization of a blade-vortex intersection during forward flight conditions in the Boeing-Vertol Wind Tunnel.

(O. Childress, Jr., 4302)



Laser photograph that shows blade-vortex intersection viewed from rear.

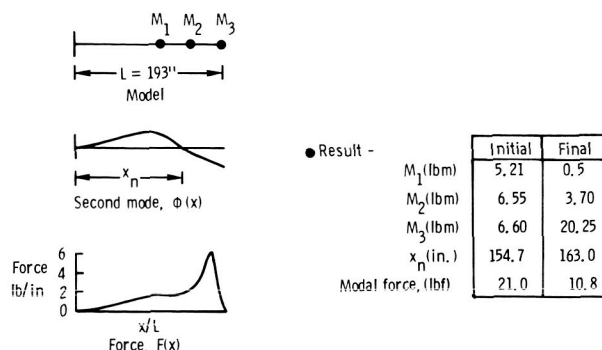
## Mathematical Method to Control Vibrations by Node Point Placement

In helicopter rotor blade and fuselage design, requirements concerning ride comfort, stability, fatigue life of structural components, and stable locations for equipment lead to design constraints on vibration levels. The concept of nodal point placement, which consists of modifying the mass distribution of a structure to place a node (a point of zero displacement) of a structural node shape at a desirable location, has been studied. A Langley-developed optimization procedure uses lumped masses on the structure as design variables to move the node to a preselected location while minimizing the total mass required to do so.

The procedure has been applied to a 193-in. cantilevered beam representation (shown in the figure) of a rotor blade. The objective is to locate the node  $x_n$  for the second mode (within 1.0 in. of the location  $x_o = 164$  in.) by using three lumped masses on the beam. This value for  $x_o$  is chosen because the resulting mode shape will be nearly orthogonal to the applied force and will give a very small generalized (modal) force for that mode and a resulting reduction in vibration response. The results of the optimization are shown in the table.

In the initial design, the node location was 8 in. to the left of the desired location. In the final design, the node is exactly 1 in. from the desired location as required. The mass is highly concentrated at the tip because tip mass is most effective in shifting the nodal point. Placement of the node point resulted in a significant reduction in generalized force (from 21.0 lb to 10.8 lb) and a corresponding decrease in vibration level.

(H. M. Adelman, 2887)



Example of nodal point location optimization for rotor blade.

## Euler Code for Blade-Vortex Interaction Noise

An Euler code has been developed at NASA Langley for calculation of the noise produced by the interaction of an incoming distributed vortex with a lifting Joukowski airfoil. The code first calculates the time-dependent flow produced by the interaction, including continuous satisfaction of the Kutta condition, and then integrates over the flow field to determine the sound production. This study of the intense "blade slap" source of helicopter noise is part of a continuing development of computational aeroacoustics techniques in which sound produced by the motion of fluids is calculated from first principles.

The figure illustrates typical flow and acoustical results of this study. On the left is a montage of contours of constant vorticity at various nondimensional times throughout the interaction. On close inspection, it can be seen that the vortex is first attracted vertically toward the airfoil and then repelled. This acceleration of the vortex, which is produced by the lift on the airfoil, is responsible for the noise radiation. On the right is the resulting acoustic pressure time history. Dimensions have been scaled to represent a helicopter with blade span and chord of 31 ft and 1 ft, respectively, a tip Mach number of 0.6, and a flight speed of 50 kn over an observer 200 ft below. The characteristic frequency (related to the interaction time) of noise radiation in this case is 436 Hz at a peak level of 103.7 dB, which is in agreement with expectations for this geometry.

The computer code developed in this study provides noise prediction for rotor blade-vortex interaction

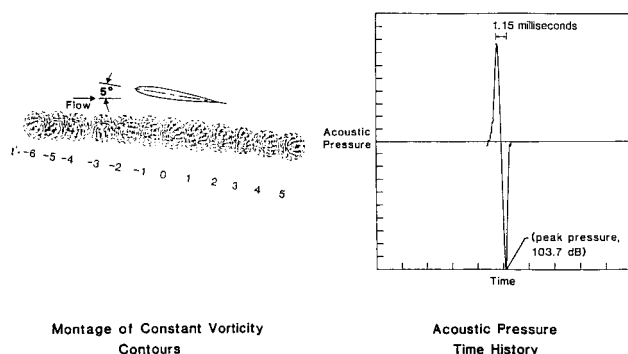
and is being utilized for direct comparison with experiment. In addition, parametric studies have led to the development of methods for reduction of this noise source.

(J. C. Hardin, 2645)

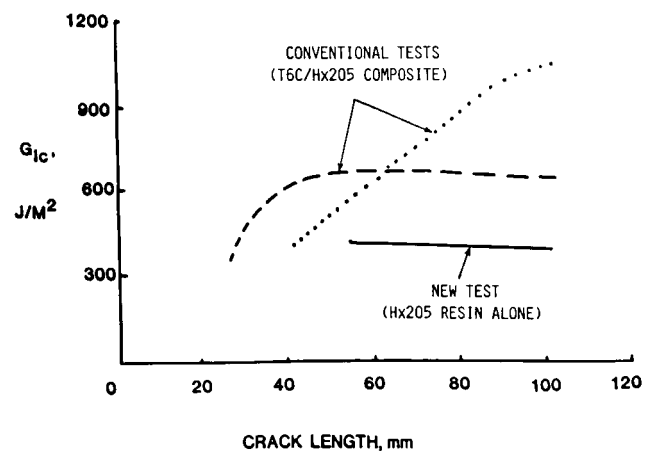
## Resin Use Amount in Test for Composite Matrix Toughness

To analytically model the fracture behavior of laminated composite materials, certain properties of the fibers and the matrix resin must be evaluated in tests. The conventional test to obtain one of those constituent properties (the opening mode fracture toughness of the matrix,  $G_{IC}$ ) is a delamination test of the composite material which couples the effects of both resin and matrix fibers. Tests on the composite material have been done because previous test methods for the bulk resin alone did not accurately represent the in situ behavior of the resin in composite material form. However, results from the composite material tests are difficult to interpret, specimen fabrication is expensive, and frequently, insufficient quantities of new resins are available to make composite material specimens.

A new, simple test for measuring resin fracture toughness has been evaluated at NASA Langley. This new test accounts for only the resin contribution and therefore gives a more accurate analysis of resin behavior. Experimental results that demonstrate the validity of the test are shown in the figure. Data are shown



Flow and noise for blade-vortex interaction.



Resin fracture toughness measurements from conventional and new test methods.

for two variations of the conventional test of a composite material (TC6 fibers in a Hexcel H205 matrix). In these tests, a thin (0.025-mm) Teflon insert was embedded in the composite to initiate a failure in the resin between layers of the fibers. In both of these tests, the  $G_{Ic}$  value increased with increasing crack length, apparently because intact fibers bridged across the crack in the resin. The minimum value of  $G_{Ic}$  in both tests was obtained just at the end of the Teflon insert where there was no fiber bridging. Results from the new test method are also shown in the figure. In the new test, a thin (0.025-mm) layer of resin was bonded between aluminum adherends, and fracture was initiated in the resin. The  $G_{Ic}$  results from this specimen are practically constant with crack length and, more importantly, are about equal to the minimum values from the composite tests. Since this new test provides a good measure of the in situ  $G_{Ic}$  value for the resin in a composite and requires use of only a small amount of resin, it should be very useful for screening new resins for potential applications in composites.

(W. S. Johnson, 2715)

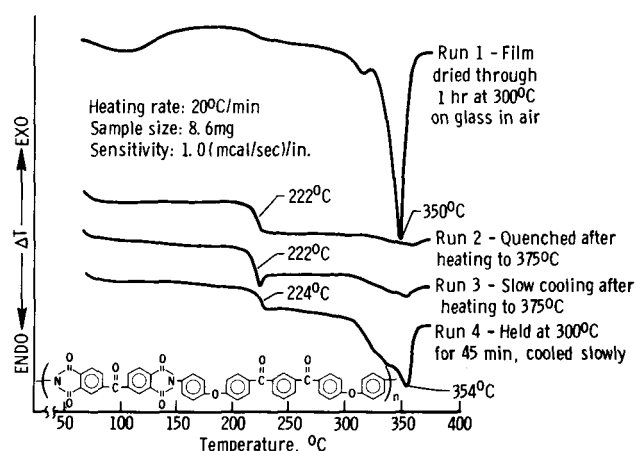
## High Mechanical Properties of Semicrystalline Polyimides

Polyimides were initially disclosed in the late 1950's and, since then, several polyimides have become commercially available. These materials, which are generally amorphous, are used as high-temperature adhesives, composite matrices, coatings, films, foams, and molding in the aerospace, automotive, electronics, and domestic household industries. The introduction of crystallinity into a polymer is an effective means of improving certain properties such as the solvent resistance and modulus. Crystallinity has been introduced into polyimides by using novel diamines that contain carbonyl and ether connecting groups between aromatic rings. These new diamines were polymerized with aromatic dianhydrides to yield novel semicrystalline polyimides.

As an example, the polyimide (the chemical structure in the figure) from the reaction of 3,3', 4,4'-benzophenonetetracarboxylic dianhydride and 1,3-bis-(4-aminophenoxy-4'-benzoyl)benzene exhibited a moderate degree of crystallinity, excellent solvent resistance, high modulus and high fracture toughness. A prominent glass transition ( $T_g$ ) and a crystalline melt ( $T_m$ ) are evident at 222°C and 350°C (see figure). An important

feature is that crystallinity can be thermally induced in this polymer (run 4). A transparent orange solvent-resistant film of this polymer has high mechanical properties with 25°C tensile strength of 21,600 psi, tensile modulus of 630,000 psi, elongation of 8.3 percent, and good retention of properties at temperatures to 232°C. Fracture toughness ( $G_{Ic}$ , critical strain energy release rate) of compression-molded samples at 25°C is extremely high with an average value of 37.8 in lb/in<sup>2</sup>. These initial results are very encouraging and indicate that similar approaches may be used with other polymer systems to enhance certain properties.

(P. M. Hergenrother, 3041)



Differential scanning calorimetric curves.

## Fatigue Performance of Toughened Matrices for Composites

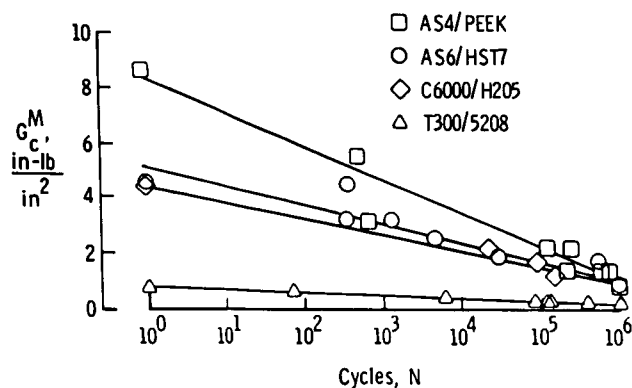
Graphite-reinforced composite materials often delaminate under repeated loading as a result of the interlaminar stresses that are created in the laminate. Recently, composite materials with toughened matrix resins have been developed to improve the inherent delamination resistance of the material. The fatigue performance of the new resins has been evaluated in a joint Army/NASA study.

The figure shows the number of load cycles required to form an edge delamination in the 0/90 interface

of (35/-35/0/90)<sub>s</sub> laminates as a function of the critical-strain energy release rate  $G_c^M$ , corresponding to the maximum cyclic strain applied. The cycles-to-delamination onset are presented as a function of  $G$  instead of the applied strain to obtain a generic representation of the material behavior that is independent of layup and ply thickness. Data are shown for four graphite-reinforced composites whose matrices have varying degrees of toughness. The matrix materials are (1) Narmco 5208, a 350°F brittle epoxy, (2) Hexcel H205, a 250°F epoxy, (3) Cyanamid HST7, a 350°F epoxy with a tough adhesive interleaf between each ply, and (4) ICI Polyetheretherketone (PEEK), a semicrystalline thermoplastic.

As the figure indicates, there is a large difference in the static interlaminar fracture toughness of these materials shown on the ordinate at  $N=1$ , but the cyclic strain energy release rate endurance limits at  $10^6$  cycles do not differ greatly. Therefore, structural behavior that depends primarily on the static interlaminar fracture toughness of the material, such as compression strength after impact, may be improved for a toughened matrix composite; however, structural performance in fatigue, such as the delamination around an open hole, may not be significantly improved.

(T. K. O'Brien, 2093)



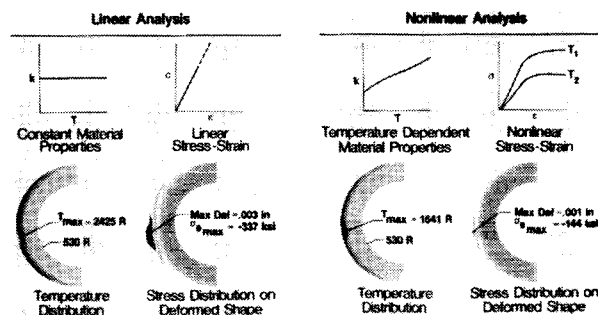
*Fatigue performance of composites with brittle and toughened matrices.*

## Integrated Fluid-Thermal-Structural Algorithm for Nonlinear Thermal and Stress-Strain Analysis

An integrated finite-element fluid-thermal-structural analysis capability that simultaneously solves for the aerothermal loads on a high-speed vehicle and the vehicle's thermal and structural response to those loads has been developed at NASA Langley. A Taylor-Galerkin algorithm, developed for the fluids analysis, has been applied to a linear thermal analysis (constant material thermal properties) and a linear stress/strain analysis (constant linear-elastic material stress-strain properties). The application of these linear analyses techniques to a cylindrical leading-edge model with an applied heating rate representative of Mach 7 flow with an incident shock is shown in the left figure. The predicted maximum surface temperature was 2425°R, and the maximum stress level was -337 ksi, exceeding the yield limit of the material.

The capability of the fluid algorithm to solve nonlinear equations was exploited by reformulating the nonlinear thermal and stress-strain equations into the form of the fluid equations. The results of the cylindrical leading-edge analysis considering temperature dependent material thermal properties and temperature dependent nonlinear stress-strain properties (illustrated by two temperature curves) are shown in the right figure. Now the predicted maximum surface temperature is 1641°R, and the maximum stress level is -144 ksi, within the operating range of the material. This reduced surface temperature reflects the ability of the new method to accurately represent the actual temperature-dependent properties of the material.

This method of solution avoids the usual extensive matrix manipulations that accompany conversion from



*Linear and nonlinear thermal-structural analysis.*

linear-to-nonlinear analysis and results in only minor computational costs. However, the improvement to the integrated fluid-thermal-structural analysis capability to accurately model complex interdisciplinary responses is significant.

(P. Dechaumphai, 3155)

## High-Strength Aluminum Alloys for Graphite-Reinforced Metal-Matrix Composites

Graphite-reinforced metal-matrix composites (MMC) represent the next generation of high-stiffness, low-thermal-expansion materials for structural applications on dimensionally critical spacecraft. These materials offer many advantages over resin matrix composites, such as higher electrical and thermal conductivity, better radiation resistance, and no outgassing. Currently, the 6061 aluminum alloy is one of the primary metals being considered as the matrix for MMC. However, composites made with this alloy exhibit large hysteresis during thermal cycling and residual dimension changes induced by thermal cycling. This behavior is unacceptable for the reliable performance in dimensionally critical spacecraft.

Combinations of commercial high-strength aluminum alloy matrices and postfabrication processes, developed at NASA Langley, have resulted in MMCs that do not exhibit residual thermal strain or strain hysteresis during thermal cycling. The thermal expansion

of a P100 graphite-fiber-reinforced 2024 aluminum alloy composite, as-fabricated and after processing and 1000 thermal cycles, is shown in the figure. Specimens were heated to the maximum temperature, cooled to the minimum temperature, and heated again to room temperature. The expansion of the as-fabricated composite is characterized by a large hysteresis and residual strain, also typical of the P100 Gr/6061 Al material. After post-fabrication processing, as well as after 1000 thermal cycles, the P100 Gr/2024 Al composite exhibits neither residual strain nor hysteresis. This behavior was also observed for similarly processed and cycled composites made with the 201 and 7075 aluminum alloys.

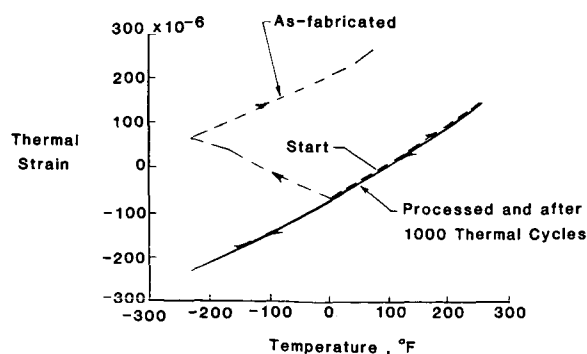
(S. S. Tompkins, 4558)

## Reusable High-Temperature Cryogenic Foam Insulation System

The development of reusable flight-weight cryogenic propellant containment structures has been one of the technological advances that has helped to realize the reduced operational costs inherent in fully reusable space launch vehicles. One of the key elements of reusable cryogenic tanks is a cryogenic insulation system that can reusablely endure relatively high thermal exposures during atmospheric entry to improve the external thermal protection system.

Under a contract to Lockheed-California Company, a series of material evaluation and processing experiments has been conducted to establish a viable manufacturing process for a reusable cryogenic foam insulation system. This foam insulation system has been developed and successfully demonstrated. The cryogenic foam system consists of two discrete layers of a 6.9 lb/ft<sup>3</sup> closed-cell polymethacrylimide foam (Rohacell 110 WF) adhesively bonded together. The foam block is wrapped with a precut and preformed cover made of the nonpermeable, high-temperature material, Kapton-aluminum-Kapton (KAK). The covered foam insulation blocks are then bonded to the cryogenic tank wall.

Several 2-in.-thick by 10-in.-square specimens, which were bonded to aluminum panels, have been fabricated to verify the manufacturing techniques and tested in a simulated service environment. One specimen has been successfully tested for 100 thermomechanical cycles that consisted of cooling the metal surface to -323°F, heating the outer surface of the foam insulation with 400°F air, and simultaneously applying a 15-kip



*Thermal expansion of P100/Gr/2024 Al as-fabricated and after processing and 1000 cycles between  $\pm 250^\circ\text{F}$ .*

tensile load in the aluminum panel. Another specimen was successfully subjected to 20 cycles in a similar environment but the metal surface was lowered to  $-423^{\circ}\text{F}$ . The test specimen showed no apparent damage or degradation of the cryogenic foam insulation system. (A. H. Taylor, 4142)

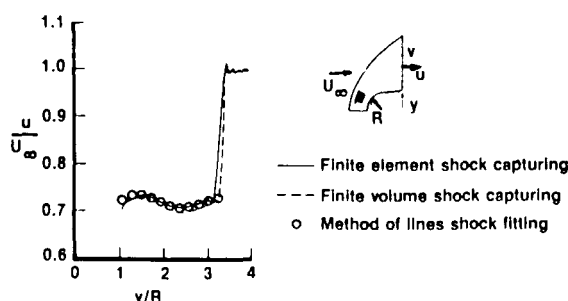
## Inviscid Finite-Element Flow Analysis Applied to Experimental Model

A two-dimensional inviscid finite-element code for high-speed flow has been developed at NASA Langley as an intermediate step in the development of a fully integrated fluid-thermal-structural analysis capability. The code is fully vectorized for efficient execution on the VPS 32 computer. To demonstrate and verify its capability to predict flow fields with complex geometries, the code has been applied to a wing-elevon cove experimental model tested at Mach 7 in the Langley 8-Foot High-Temperature Tunnel.

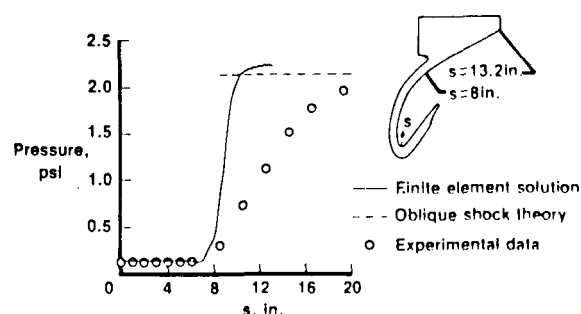
Analysis of the experimental configuration includes computations of the high-speed flow over both the blunt leading edge of the panel holder and the wing-elevon cove configuration. Although the cove configuration has strong viscous dominated flow regions, the inviscid analysis is valid in some regions and has been applied as a precursor to a viscous analysis to enhance understanding of the flow phenomena and validate the finite-element algorithm. Results of the blunt leading-edge analysis are compared to two other numerical methods: a finite-volume shock-capturing technique, and a method-of-lines shock-fitting technique shown in the first figure. The velocity profiles along the outflow plane of the blunt leading-edge model are in good agreement with the other two techniques.

Results of the cove analysis are compared with experimental data in the second figure. The predicted wall pressure distribution agrees with the experimental data inside the cove (where viscous effects are small) but not with the data at the entrance to the cove (where viscous effects dominate). In the outer flow region, the predicted pressures increase to a value slightly greater than that predicted by oblique shock theory because the flow expands slightly around the wing trailing edge. These results demonstrate the capability of the finite-element techniques to predict the flow field for complex configurations.

(K. S. Bey, 4441)



Blunt leading edge analysis



Wing-elevon cove analysis

L-85-11,997

*Comparison of finite-element solution with other numerical solutions and experimental data.*

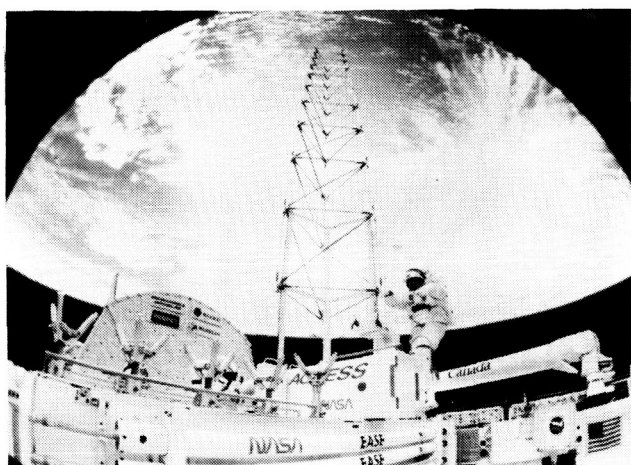
## ACCESS Flight Experiment Results

The Assembly Concept for Construction of Erectable Space Structure (ACCESS) was a NASA experiment launched November 26, 1985, on the Space Shuttle orbiter *Atlantis*. The experiment, designed to study assembly and handling of a space truss by astronauts in extravehicular activity (EVA), was divided into two parts: a baseline experiment and an expanded experiment. Each part was performed on separate EVA days of the flight. The baseline experiment used an assembly line method for space construction in which 93 tubular struts and 33 nodal joints were assembled into a 45-ft-long aluminum truss beam by two astronauts secured in fixed foot restraints located in the Shuttle cargo bay.

In the figure, the astronauts have just completed assembly of the truss beam, which is still attached to

the assembly fixture. The expanded experiment was used to study structural assembly, structural repair, flexible cable installation, and manual manipulation of the truss using only one astronaut in a mobile foot restraint. The manipulator foot restraint (MFR), attached to the end of the remote manipulator system (RMS) robot arm, was used for the expanded experiment. It was found that all assembly and postassembly tasks could be accomplished, and assembly times compared favorably with neutral buoyancy water tank ground simulation data.

(W. L. Heard, Jr., 2608)



L-86-2135

*Truss beam attached to assembly fixture.*

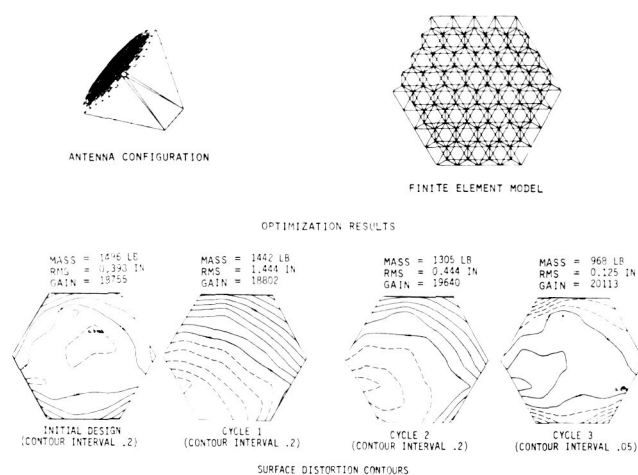
## Integrated Interdisciplinary Optimization Procedure for Large Space Antenna Design

Previous work in optimizing large space antenna structures generally concentrated on minimizing root mean square (rms) surface distortions, thereby indirectly maximizing electromagnetic (EM) antenna performance. The present work involves a direct approach to maximizing EM performance while minimizing mass. Integrating the thermal, structural, and EM analyses in the context of an optimization procedure is an effective design approach because the influence of each type of

response on the other is accounted for directly and automatically. A finite-element thermal analysis and structural deformation analysis program is combined with a NASA-Langley-developed electromagnetic radiation program and a standard optimization program. The system is used to perform a thermal analysis, transfer the temperatures to the structural model, and compute the deformed shape of the antenna reflector. The deformed shape in the EM analysis is used to determine performance parameters including peak gain, side lobe levels, beam width, pointing direction, and cross-polarization.

The procedure has been tested on a 55-m tetrahedral antenna reflector shown in the figure. A representative orbital position was chosen as the design point and a design was sought which minimized structural mass while attaining a peak gain of at least 19,000. The results of the optimization are shown in the lower part of the figure. Structural mass, rms surface distortion, and peak gain are shown for the initial design and for the first three design cycles. Design goals are essentially achieved at the third cycle. The contour plots show the evolution of surface distortion as the design is improved. Solid lines are displacements toward the feed, and dashed lines are displacements away from the feed. Initially, there is a deep valley in the reflector, but at the end of the third cycle, the distortion is much smaller, and the reflector shape is nearly a perfect paraboloid as required. The remaining distortion occurs near the outer edges, which are not as important to EM performance as the center because of feed taper.

(H. M. Adelman, 2887)

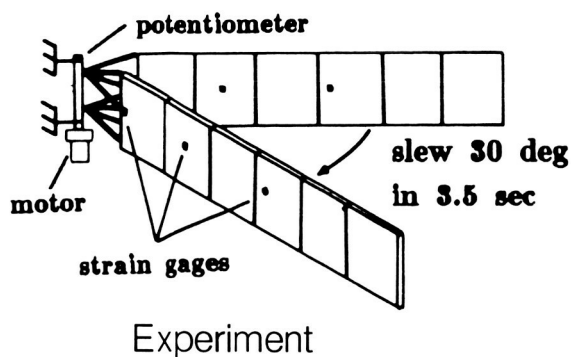
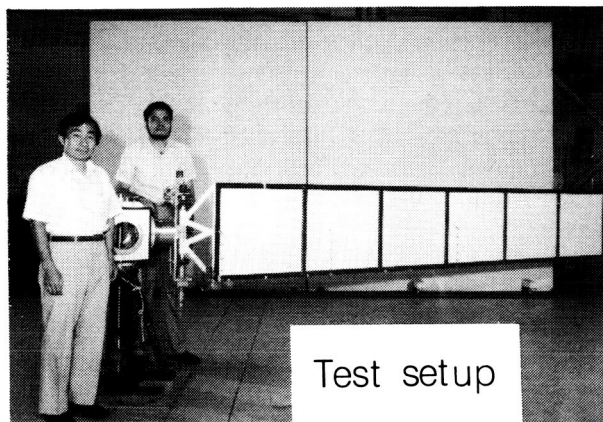


*Application of optimization procedure to space antenna design.*



## Effects of Atmosphere on Slewing Control of Flexible Structure

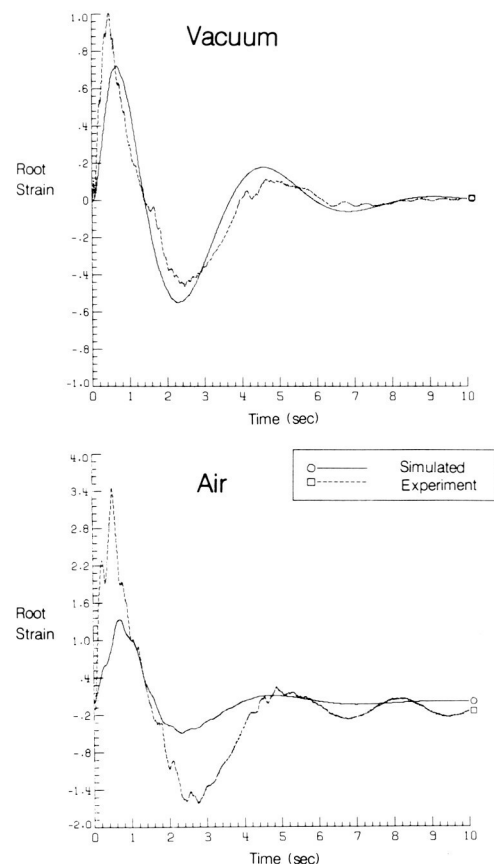
A 3.9-m-long flexible panel, which has a cross section of 0.64 m by 0.33 cm, has been used for laboratory experiments in air and vacuum to assess the effects of atmosphere on the slewing controller design. The first figure shows the test model, which is cantilevered in a vertical plane and rotated 30 deg in the horizontal plane by an electric gear motor. Transient response data are shown in the second figure for a controlled maneuver in air and vacuum, respectively. The solid lines represent simulated data, whereas the dashed lines represent experimental data. The predicted in vacuo first-C mode frequency and damping are within 5 percent of the measured values. Including air effects, the predicted frequencies are within 8 percent of the experimental values, but damping differed by almost 40 percent. Thus, although the curves show very similar trends, the damping discrepancy resulted in an underestimation of the peak strain values. The gear train backlash and deadband effects contribute significantly to the increase of the peak strain value when air opposes



*Slewing experiment setup.*

the slow maneuver. The discrepancy is also attributed to errors in modeling the drag forces.

A residual motion at the end of the maneuver was caused by circulating air currents in the laboratory. The magnitude of air damping effects depends on the controller design; the smoother the control command, the lower the effects of air. It is concluded that the effects of atmosphere can be systematically included in the equations for slewing maneuvers of a flexible panel to determine damping trends; however, improvement is still needed to determine absolute damping magnitudes. (J.-N. Juang, 2881)



*Slewing experiment results.*

## Vibration Testing and Analysis of Large Space Antenna

To achieve close surface tolerances with lightweight, deployable antennas, concepts are being developed which use tension cables for stiffening. New

methods for analyzing tension-stiffened structures must be verified by test data. In particular, vibration tests and analysis must be performed to assess the degree to which structural vibrations degrade the surface accuracy and antenna pointing stability. An advanced tension-stiffened concept, called the 15-m-diameter (approximately 50 ft) hoop/column antenna, was vibration tested in the Langley 55-Foot Vacuum Chamber. In parallel with the vibration tests, an analytical study was performed for comparison.

Modal vibration tests were performed by applying small vibratory forces to the structure and measuring the response. The 15-m antenna was tested in two ways: mounted on a tripod support system, as shown in the figure, and suspended in pendulum fashion. The vibratory response was found to be dominated by column-bending and hoop-rocking motion, which can adversely affect antenna pointing accuracy. However, because of the many structural joints in the hoop/column concept, the vibrations decay relatively rapidly. In addition, the reflective surface of gold-plated molybdenum wire mesh was found to have modal damping of approximately 10 percent of critical damping. This relatively high damping will help reduce the surface distortions that result from structural vibrations.

The original analytical model predicted frequencies 30 percent higher than those measured in the test. However, after the structural properties and effective joint stiffnesses in the analytical model were updated by static test data, predicted frequencies of the first four vibration modes were within 5 percent of the measured frequencies. Such agreement verifies that finite-element modeling can be used to predict the vibrations of large tension-

stiffened antennas. Because the original analytical model contained nearly 10,000 degrees of freedom, it could not be used efficiently to study design changes. Thus, advanced continuum modeling assumptions were applied to reduce the model to below 1000 degrees of freedom. The reduced model accurately predicts the vibration frequencies of interest and permits parametric design changes to be assessed economically.

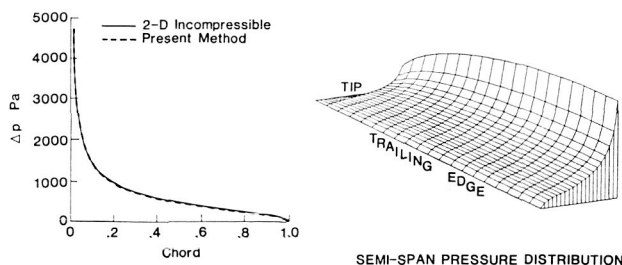
(W. K. Belvin, 2446)

## Lifting-Surface Theory Using Acoustic Approach

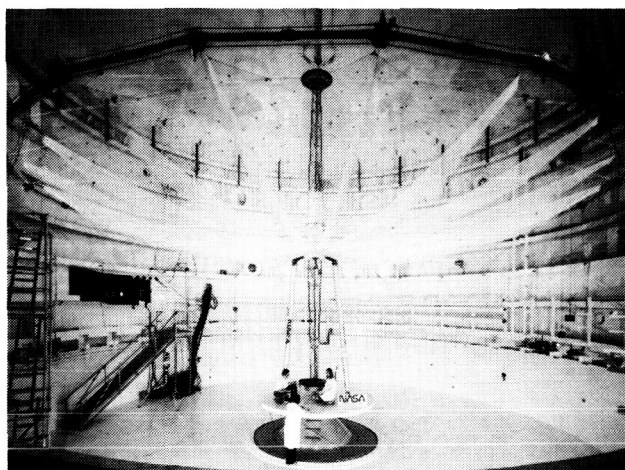
The prediction of surface pressure on high-speed propellers is required to calculate noise since most current noise prediction codes require the blade surface pressure as input. The objective of the present study is to develop an efficient code based on compressible linear aerodynamic theory which can give reasonably satisfactory surface pressure for propeller noise prediction.

An equation for predicting the acoustic pressure of rotating blades is integrated with respect to observer time to get the velocity potential at an arbitrary observer point in space in terms of pressure differential  $\Delta p$  across the blade surface. By taking the normal derivative of both sides of the resulting equation as the observer is moved on the surface, a linear singular integral equation in terms of the known local normal velocity of the surface and the unknown  $\Delta p$  is obtained. The blade surface pressure is then calculated by the Galerkin or collection method using the kernel function based on this integral equation.

The various singular integrals that appear in the kernel are integrated analytically in the singularity regions. In the special case of uniform rectilinear motion,



Surface pressure prediction using acoustic approach (rectangular wing,  $M = 0.2$ ,  $\alpha = 2.86^\circ$ , and AR of 10).



L-85-13,262

Vibration tests of 15-m hoop/column antenna.

the kernel function can be found analytically. The figure on the right shows the pressure distribution on a thin rectangular wing of aspect ratio 10 at an angle of attack  $\alpha$  of  $2.86^\circ$ . The forward Mach number  $M$  is 0.2. The chordwise pressure distribution at midspan station, which is also shown in the figure on the left, agrees very well with that from a two-dimensional incompressible computation. Future applications include unsteady surface pressure calculations for rotation blades. (F. Farassat, 2645)

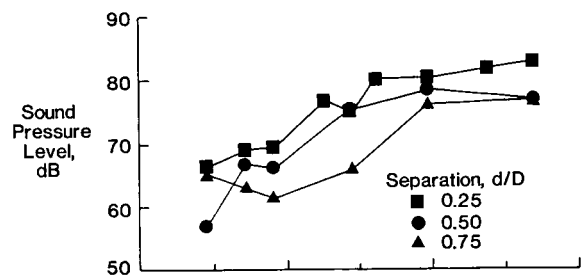
## Propeller-Induced Structureborne Noise

The interior noise of propeller aircraft contains airborne noise transmitted through the fuselage and structureborne noise resulting from both engine shaft vibration and the interaction of the propeller wake/vortices with the wing or other downstream aerodynamic surfaces. Because each of these noise components is highly correlated with the propeller shaft frequency, it has not been possible to independently study the controlling parameters of the structureborne noise in flight. Thus, very little is known about the potentially important contribution of the propeller wake/vortex interaction to the interior noise of the energy efficient advanced turboprop (ATP) airplane.

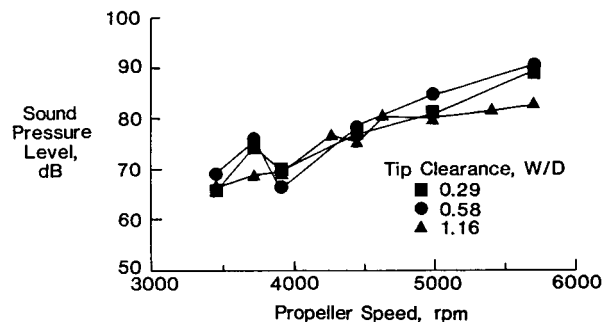
A laboratory model offers a means of isolating the noise sources so the controlling parameters and mechanisms of the wake/vortex interaction may be studied. A test apparatus that provides the necessary isolation has been built by Southwest Research Institute under a NASA contract. The separation or isolation of airborne and structureborne noise was accomplished by isolating the fuselage structure in a heavy concrete acoustic shield fitted with a wing acoustic seal and structurally isolating the propeller from the wing. Tests were conducted to study the influence of the propeller location relative to the wing on structureborne noise. In general, the data in the upper figure indicate as expected that the strength of the propeller-induced forces contributing to wing excitation and subsequent structureborne noise propagation falls off as the propeller-to-wing separation distance increases. The data in the lower figure, however, indicate that structureborne noise is independent of spanwise propeller placement for a range of propeller speeds.

(W. H. Mayes, 3561)

PROPELLER/WING SEPARATION



PROPELLER SPANWISE PLACEMENT



*Effect of propeller location on level of structureborne noise.*

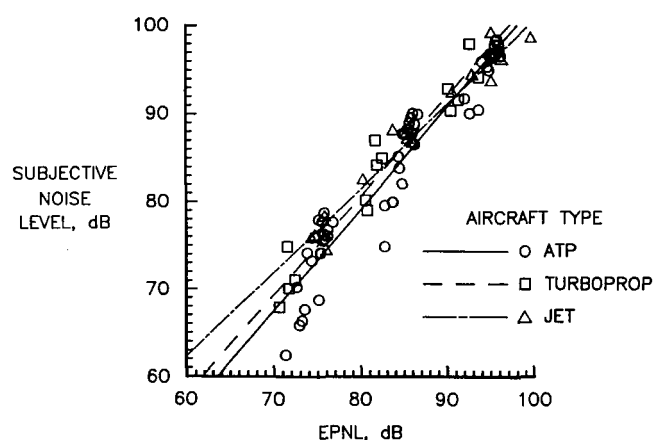
## Comparison of Advanced Turboprop and Conventional Aircraft Community Noise Annoyance

Advanced turboprop (ATP) aircraft will come into general usage only if their noise meets standards of community acceptability currently applied to conventional aircraft. The pure-tone harmonic content of ATP noise occurs at frequencies higher than those generated by conventional propeller aircraft but lower than those frequencies of conventional jet aircraft noise. An experiment was conducted to compare the annoyance of conventional turboprop and jet aircraft flyover noise with the annoyance of ATP aircraft flyover noise.

Eighteen realistic, time-varying simulations of ATP aircraft flyover noise in which the harmonic content

was systematically varied to represent the factorial combinations of six fundamental frequencies and three tone-to-broadband noise ratios were generated using the Aircraft Noise Synthesis System. The simulations were based on takeoff conditions and assumed a single-rotating-propeller tractor configuration with a thin, highly swept, twisted blade. Thirty-two subjects judged the annoyance of the 18 synthesized ATP takeoffs along with recordings of five conventional turboprop takeoffs and five conventional jet takeoffs. Each of the 28 noises was presented at three levels in a small anechoic chamber.

Analyses of the annoyance judgements from these subjects indicated that the advanced turboprops were not more annoying than the conventional turboprop and jets. In fact, as shown in the figure, the advanced turboprops were slightly less annoying than the conventional aircraft. Other results of the study indicated that the interaction of fundamental frequency with tone-to-broadband noise ratio had a significant effect on annoyance. Also, prediction ability was improved by the addition of duration corrections and corrections for tones above 500 Hz to the noise measurement procedures.  
(D. A. McCurdy, 3561)



*Comparison of annoyance responses using effective perceived noise level (EPNL).*

# Systems Engineering and Operations Directorate

The function of the Systems Engineering and Operations Directorate is to support ongoing aeronautical and space research at NASA Langley. This work force is divided into five divisions with specific support functions. The Systems Engineering Division is responsible for structural, mechanical, electrical, and aeronautical systems engineering functions required to provide research models and flight hardware for aerospace research, applications, and technology. The Facilities Engineering Division is responsible for engineering and design of aerospace research and development equipment and institutional facilities for aeronautical and space research, such as special handling equipment, model supports, and special test equipment. The Fabrication Division is responsible for developing and fabricating aeronautical and aerospace research hardware related to ground support equipment as well as research facilities test equipment. This division provides developmental manufacturing, technology and electronics technical support, including communications systems and instrumental hardware. The Operations Support Division is responsible for providing the technical, mechanical, electrical, and maintenance services for research and institutional facilities. This division operates laboratory equipment and wind tunnels and collects, records, and interprets test data. The Systems Safety, Quality, and Reliability Division has overall responsibility to insure the safety of operation of all aerospace and ground facilities as well as to insure that the aerospace hardware and ground research equipment meet all quality and reliability standards. This division also manages the environmental health program for the Center and inspects the construction of major modifications to the many unique research facilities. In addition to the five divisions, the Facilities Program Development Office is responsible to the directorate.

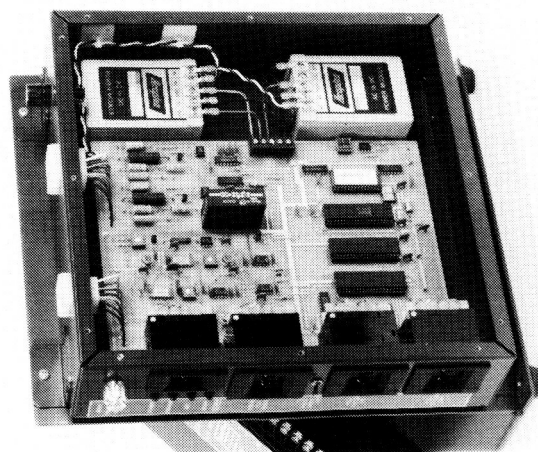
Because of the unique requirements of some of the aerospace research performed at the Center, both engineers and technicians are involved in applied research in solving engineering and fabrication problems. These problems relate to the support hardware and software necessary to provide the experimental systems requested by research. The following contributions represent typical engineering and fabrication research and technology development highlights in the Systems Engineering and Operations Directorate.

## Automatic Control for Particulate Pollution Reduction

A new voltage controller has been developed at NASA Langley to reduce particulate air pollution from combustion gases. Particulate matter is removed from combustion gases by passing the gases through an electrostatic precipitator. The operating voltage for the precipitator is normally adjusted according to the type and concentration of particulates in the combustion gases. The new microprocessor-based, independently intelligent, fully automatic controller (shown in the figure) maximizes precipitator efficiency by instantaneously and automatically adjusting the precipitator operating voltage according to the combustion gas composition. The controller proved to be the answer to efficient precipitator operation at the NASA Langley Refuse-Fired Steam-Generating Plant, and it is adaptable to any electrostatic precipitator. Two international suppliers of pollution control equipment have characterized the device as "a major technology breakthrough."

The application of this controller has been expanded from use in refuse-fired incinerators to include power plants and utilities, steel mills, pulp and paper mills, cement plants, and automobile industry incinerators. Utilization of this controller at industrial chronic-air-pollution trouble spots (for example, in Kentucky and Michigan) has assured compliance with EPA standards while saving millions of dollars in equipment and operating costs including thousands of man-hours of installation and maintenance time.

(D. F. Johnston, 2086)



L-86-6900

*Automatic adjusting voltage control for use in electrostatic precipitators.*



## Seeding System for In-Flight Flow Visualization of F-106B Leading-Edge Vortex Systems

A vapor screen technique has been developed and applied to the F-106B flight test aircraft to obtain qualitative and quantitative information about near-field vortex flows above the wings of high-performance fighter aircraft. Although a wide range of visualization methods suitable for use in wind tunnels exists, none has been developed to visualize the vortex structure in flight. The vapor screen technique is a logical way to determine vortex systems including core density. This technique requires that each of three basic components or systems (seeding, light sheet generation, and visual recording of events) must be available and integrated.

The seeding system generated a cloud of condensed propylene glycol particles at low flow rates into the airstream through nozzles that were generally located on the lower surface near the wing leading edge. The liquid propylene glycol was pumped from a 3-gal tank assembly to the vaporizer by means of an electrically driven variable-speed pump at a nominal rate of 2.8 gallons per hour. The vaporizer, which used 6 kW of electric heat to generate and maintain a preselectable constant temperature (up to 450°F), consisted of stainless-steel tubing embedded in a cast aluminum thermal mass. The propylene glycol vapor from the vaporizer flows to the nozzle through a flexible, electrically heated tube to minimize premature condensation of the vapor. A short length of uninsulated 0.5-in. (outside diameter) stainless-steel tubing was contoured to position the nozzle near the wing leading edge and terminated in one of six probe tip positions. The seeding system was controlled from the backseat station of the F-106B test aircraft. From this station, the thermal controllers for the propylene glycol vaporizer and the vapor-transfer-line heaters were maintained at proper limits, and the glycol feed pump, pumping rate, and the on/off switch were properly controlled.

(K. Davis, 4666)

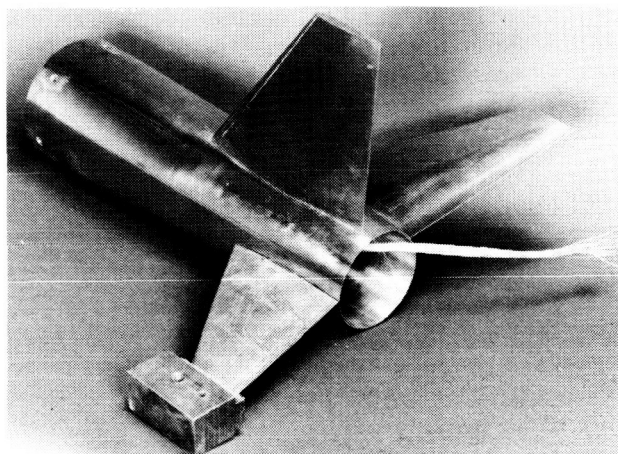
## Composite Wings for Cryogenic Wind Tunnel Models

An alternative method of fabricating pressure-instrumented wind tunnel model wings for high-Reynolds-number research in cryogenic facilities has been developed. The process provides high-quality continuous

surfaces and promises lower design and fabrication costs. This method utilizes a composite or metallic core for structural strength and stiffness. The core requires only rough contouring except at structural attachment points. After the core has been contoured, pressure tubing is attached to the core. The assembly is then wrapped with E-glass/epoxy. After curing, the element undergoes final contouring and orifice drilling.

This method has been used to fabricate stabilizers for the *Pathfinder I* National Transonic Facility (NTF) wind tunnel model. The horizontal stabilizers utilize a metal core to accommodate strength and stiffness requirements, whereas the vertical stabilizer utilizes an E-glass/epoxy laminate core. Each stabilizer has 32 static pressure taps and satisfies structural and surface quality requirements. The stabilizers will replace the original all-metal noninstrumented stabilizers in forthcoming NTF tests. The processes demonstrated by the fabrication of the stabilizers are applicable to most cryogenic wind tunnel model aerodynamic surfaces.

(G. Firth, 4666)



L-86-6799

*Composite stabilizer mated to Pathfinder I aft fuselage with original vertical and right horizontal stabilizers in place.*

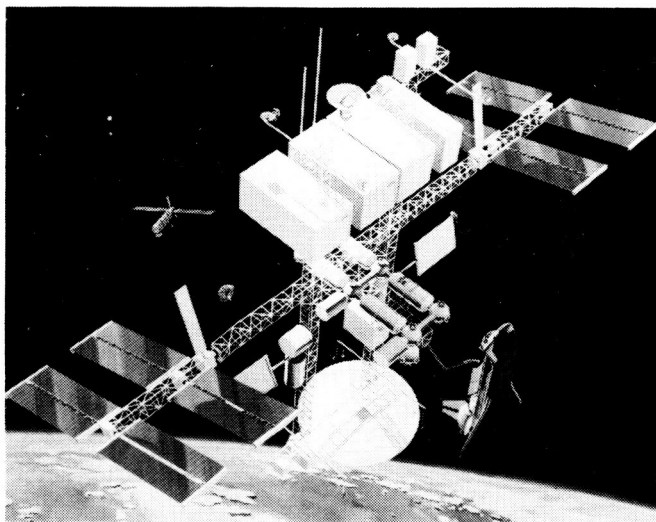
## Thermal Control of Tubular Composites in Space

The current baseline Space Station reference configuration consists of a truss network to which a gimbaled power system and pressurized modules are attached.

Because of light weight, high stiffness, and low coefficient of thermal expansion (CTE), as compared to more conventional aerospace metallic materials, a graphite/epoxy (Gr/Ep) composite material is being considered for truss tube construction. Microcracks that result from orbital thermal cycling can reduce by 35 percent the torsional stiffness of the tubes. In order to predict thermal stresses and conceptualize requirements of thermal control coatings to alleviate microcracking, thermal models have been developed of representative strut configurations with boundary conditions of typical and worst-case Space Station environments.

For the long, thin tubular structures likely to be used for the Space Station, radial conduction and longitudinal temperature changes were found to be negligible. Results from parametric steady-state thermal analyses indicate that circumferential temperature variations caused by the directional nature of fluxes in space can be minimized by treating the exterior tube surface with a low solar absorptance ( $\alpha=0.25$ ), low infrared emittance ( $\epsilon=0.25$ ) coating, with the ratio ( $\alpha/\epsilon$ ) equal to 1. A particularly promising concept to achieve these properties is the use of a high modulus Gr/Ep, which is oriented in the longitudinal direction and overlapped with thin chromic acid anodized aluminum foil. Transient analyses show that orbital temperature extremes can be reduced from 111°C to 22°C by using such a thermal control coating. This temperature reduction should significantly increase strut life.

(R. A. Foss, 4508)



*Space Station reference configuration.*

## Pultrusion Development for High-Performance Thermoplastic, Polyetherimide/Graphite Composite

Polyetherimide (PEI) is a high-performance thermoplastic that exhibits characteristics desirable in aerospace engineering materials. These characteristics, which include high heat resistance, stiffness, creep, impact and tensile strength, as well as the ability to be reformed and shaped by applying heat and pressure, place PEI high on the list of candidates for potential matrices in graphite-reinforced structures. Similar to other thermoplastics, PEI can be joined by welding techniques to further enhance its potential use. Prefabricated stock materials, which consist of continuous graphite and/or aramid fiber reinforcement systems that contain PEI as the matrix, could be further fabricated (similar to metals) into profiles such as hat sections, channels, Z-shaped stiffeners, and corrugated panels for use in primary and secondary structures. However, PEI is highly viscous at its melt temperature, and this results in poor fiber wetting in hot-melt applications.

A new approach to the hot-melt method has been initiated using a pultrusion technique. In using this method, the PEI is dissolved in methylene chloride, and its viscosity is adjusted to facilitate fiber wetting. The reinforcement fiber (graphite) is first pulled through the PEI/methylene chloride resin system for impregnation, then through a drying system, and subsequently through a heated die for shaping and polymerization. Unidirectional single-ply material and rectangular profiles have been produced by this technique, and further development, testing, and refinement of the process are ongoing.

(M. L. Wilson, 4615)

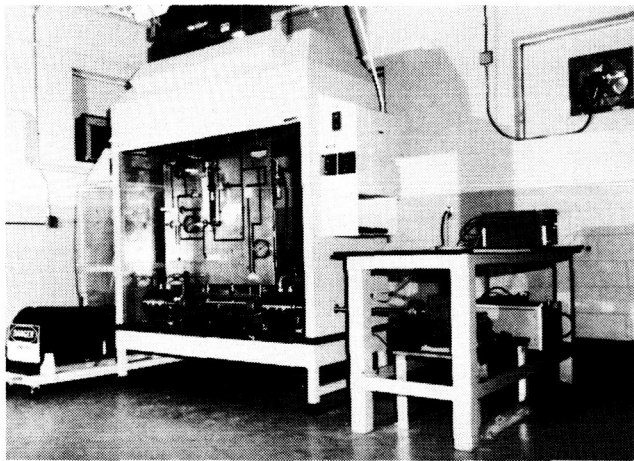
## Ammonia Flow Test Facility

The development of a multipass fluid coupling has been identified from Space Station studies as a primary technology requirement. A test facility has been required which can be used to test candidate coupling configurations under simulated coolant flow and orbital rotation rate conditions using anhydrous ammonia as the working fluid.

An ammonia flow test facility has been designed and built at NASA Langley which provides the range of flow and rotation rates required to simulate the Space

Station coolant system. The system was designed primarily to operate with liquid anhydrous ammonia, but other liquid coolants could be used. Flow rates from 0 to 2.65 gal/min may be selected. A motor/gear drive will provide rotation rates through a drive shaft of from 0.01 rpm to 1.00 rpm with an output torque of 5900 in-lb available over the entire range. The temperature of the fluid within the system may be controlled from -35°F to +90°F using a separate temperature-controlled liquid bath and a heat exchanger that are integral to the system. The facility is operational and has been used to evaluate a number of fluid transfer coupling configurations.

(O. H. Bradley, 4571)



L-86-1161

*Facility for testing Space Station rotary fluid coupling design concepts.*

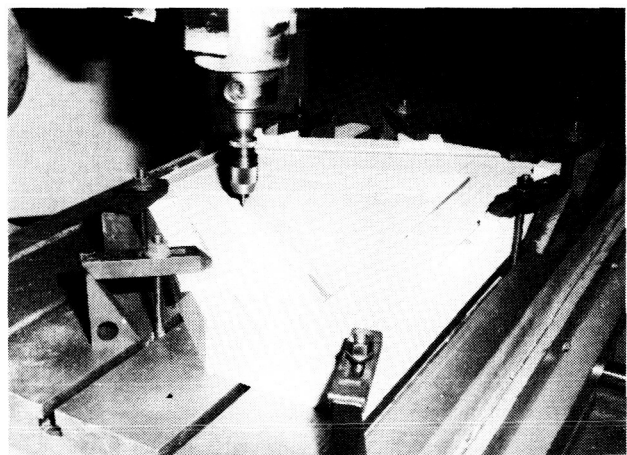
## Use of Closed-Cell Polyurethane Foam for Molds

Traditional methods of making molds for fiberglass-reinforced lay-ups have been refined at NASA Langley. The making of templates and patterns used to fabricate composite molds is a skill that has been developed over years of training and on-the-job experience. Although resulting molds are strong and long lasting, the vast majority of them are only used one time. In an era of lower budgets, declining manpower, and increased model complexity, other methods of fabricating these molds have been explored.

The introduction of numerically controlled milling machines at NASA Langley provided an opportunity to generate more accurate model parts and templates through the use of computer-assisted design/computer-assisted manufacturing (CAD/CAM). The advantages of the CAD/CAM system were extended further by directly machining the female molds. Many materials were tested for this application, and the closed-cell polyurethane foam proved to have an attractive balance in regard to machining qualities, ease of finishing, and service requirements. Material densities from 4 to 16 lb/ft<sup>3</sup> have been used depending on the requirements of the application. These molds are light in weight yet tough enough to be used several times. A thin coating of polyester resin provides an adequate surface for the molding operation. If the mold is to be used on an extended production basis, the parting surfaces can be given an extra thickness of resin to provide a more durable surface. Dowel pin holes are located in the parting surface to provide references to the geometry of the part (i.e., cut lines, reference lines, hinge points, and spar locations).

Utilization of this advanced technology has resulted in a 40- to 60-percent savings required to produce molds for complex model parts. It has also provided a reduction in the complexity of model alignment and assembly. Perhaps the most significant gain is the ability to mold the more complex geometry of current and future research models that have curved and twisted parting planes that are more easily used in the part fabrication process.

(J. S. Powell, 2651)



L-83-4,947

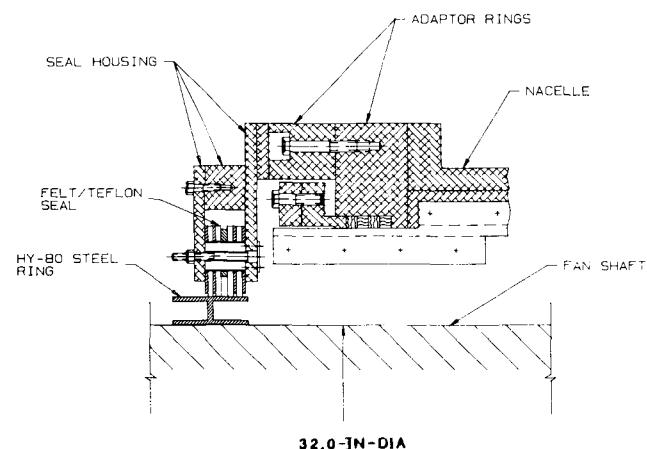
*Finishing cuts under way by computer-numerical-controlled milling machine on high-density polyurethane foam canard mold.*



## Gaseous Nitrogen Flow Blocker Seal for NTF Nacelle

During operation of the National Transonic Facility (NTF), problems were encountered due to thermal contraction within the tunnel. The heated upstream nacelle cavity, which houses inlet guide vane mechanisms, hydraulic lines, and instrumentation, cooled down rapidly to a below-limits condition at a tunnel stream temperature of approximately  $-220^{\circ}\text{F}$ . The probable cause of the nacelle cooldown was the increase in size of a shaft penetration shroud opening as the result of structural cooling. This increase, in turn, opened the way for excessive cryogenic nitrogen gas leakage along the shaft and into the nacelle. Previous attempts to prevent flow into the nacelle resulted in localized heating and excessive vibration of the shaft.

A felt/Teflon flow blocker seal, which rides directly on an HY-80 steel ring attached to the shaft, was installed to stop the nitrogen gas leakage along the shaft into the nacelle. The felt/Teflon seal was designed to minimize dynamic loads to the shaft and to accommodate the large relative movements (0.25-in. radial and 1.3-in. axial motions) between the nacelle and the shaft due to thermal and momentum loads during NTF operation. The felt/Teflon seal is free to move axially along the HY-80 ring as the nacelle moves. Oversized bolt sleeves allow the seal to float up to 0.50 in. radially, relative to the nacelle. The seal is counterbalanced to nullify rubbing loads due to the weight of the seal assembly. The HY-80 steel ring acts as a thermal barrier between the felt/Teflon riding surface and the shaft and reduces the local thermal load due to frictional heating.



NTF flow blocker seal assembly.

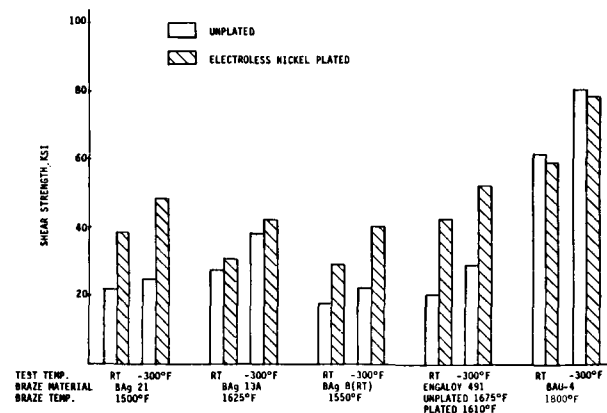
Test data confirm that the felt/Teflon flow blocker seal significantly reduces flow into the nacelle, and this reduction results in a warmer nacelle. The ability of the seal to float and travel axially along the HY-80 steel ring has resulted in a greatly improved dynamic performance of the tunnel drive shaft.

(R. J. Buehrle, 4571)

## Brazing Research Results

An extensive program to evaluate various braze alloys for use with 18 Ni 200 grade maraging steel has been conducted. The applications include the joining of wing structures and installation of a stainless-steel pressure tube in wings for highly loaded wind tunnel models to be tested in a cryogenic environment. Earlier work at NASA and in private industry raised concerns about using brazing in applications that required high-strength, high-quality braze joints exposed to cryogenic temperatures. In particular, problems were encountered with alloy selection, poor wetting characteristics, questionable strength, and braze temperature cycle effects on the parent material when exposed to high furnace temperatures ( $\geq 1650^{\circ}\text{F}$ ).

Various alloys have been tested at NASA Langley using specimens that simulated pressure tube installation and joining of wing structural members. A major breakthrough occurred when it was determined that the use of nickel plating on the parent material greatly enhanced the wetting and strength properties of the braze materials. In addition, a thermal management program has been developed to simulate brazing of the actual model



Shear strength properties for 18 Ni grade 200 maraging steel specimens.

and hardware to study changes in the microstructure of the 18 Ni 200 grade maraging steel. Such changes have the potential to significantly reduce the material toughness due to grain growth at high temperatures. It has been demonstrated that selected high-temperature braze alloys can be used without detrimental effects on the parent material, and, at the same time, can achieve acceptable strength characteristics. The shear strength data for various alloys that have been tested at room temperature and at -300°F for both plated and unplated specimens are summarized in the figure. Although this research has been aimed at application to a specific steel alloy, the results and procedures developed should also be applicable to the brazing of other steel alloys.

(J. F. Bradshaw, 4666)

## Composite Lightning Rods for Aircraft

The problem of protecting aircraft from electrostatic discharges and lightning strikes has stimulated a variety of protective measures including both passive and active dischargers. The problem becomes more severe as insulating composites replace more of the Faraday shields inherent in all-metal construction. Also, modern electronics and the practice of entrusting vital flight functions to computers create a need for protection from electrical charges that can induce disruptive currents in the electronic circuits. A composite, lightweight sacrificial tip with graphite was designed at NASA Langley especially to reduce lightning-strike damage to composite parts of aircraft and to dissipate the harmful electrical energy.

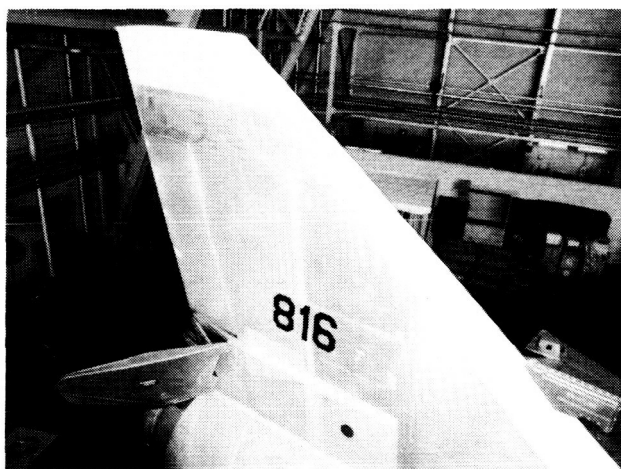
Extensive damage is often caused by lightning strikes on the relatively nonconductive composite structures now frequently used for the wings, tails, fuselage, or control surfaces on aircraft. This damage often takes the form of delamination and/or holes (complete burn-through) in the structural surfaces. When the sacrificial tip is installed in a position that protrudes from the aft surface of an aircraft part made of composite material, the energy from a lightning strike on the part is dissipated through the tip. These tips are inexpensive and sacrificial, but they may be usable for withstanding numerous lightning strikes.

The device consists basically of a slender composite rod fabricated from highly conductive unidirectional reinforcing fibers in a matrix material. These rods are strategically installed in the trailing edges of such aircraft parts as wings, tails, winglets, control surfaces, and the most rearward portion of the aft fuselage. The

rods fabricated thus far are made of unidirectional graphite fibers in an epoxy matrix, are 5/16 in. (0.8 cm) in diameter and 5.50 in. (14 cm) long, and are tapered from approximately the last inch (2.5 cm) to about 50 percent of the major diameter at the tip. This device has already been installed and used successfully on NASA Langley F-106 aircraft.

This invention is owned by NASA, and a patent application has been filed. Inquiries concerning nonexclusive or exclusive license for its commercial development should be addressed to the Patent Counsel, NASA Johnson Space Center.

(C. F. Bryan, Jr., 2651)



L-86-8308

*Graphite lightning stinger on F-106B vertical fin.*

## Telescope Door Release Device for HALOE Flight Instrument

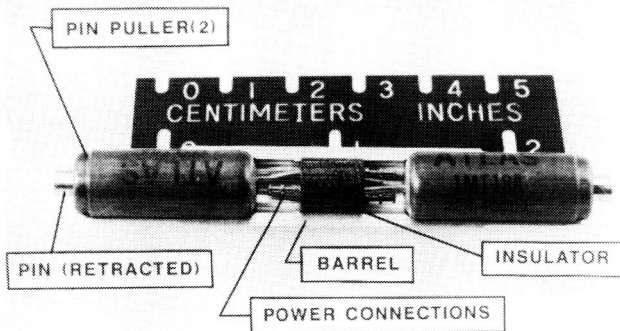
During the development of the HALOE (Halogen Occultation Experiment) instrument, a requirement was established for the in-orbit pin-withdrawal release of the telescope contamination protection door. The device utilized for this purpose had to be light in weight, provide feature-redundant operation, and yield low mechanical shock and contamination levels when activated in order to preclude damage to nearby critically aligned optical elements.

The NASA-Langley-developed device consists of two existing pyrotechnic pin pullers in a back-to-back configuration as shown in the figure. This assembly is

mounted within a housing that fixes the left pin; initiating either pin puller provides the necessary pin withdrawal in order to release the telescope door. These pin pullers feature 1.0-A no-fire and 4.50-A all-fire current characteristics and provide 20.0 lbf with a 0.30-in. stroke. This dual-pin-puller device features mechanical and electrical redundancy; has a total pin movement of 0.60 in., a weight of 0.09 lb (42 gm), and a volume of 0.47 in<sup>3</sup>; and is approximately 0.41-in. in diameter and 3.69 in. long.

The device has been subjected to a flight qualification program that consists of exposures to temperature extremes, random vibration, mechanical shock, long-term vacuum, and variations in firing current. During this program, action times, pyrotechnic shock, outgassing, and contamination features were characterized. The qualification status of this device is based on the successful firings of 13 pin pullers by the manufacturer for lot acceptance and the additional successful firings of 20 flight design packaged pin pullers for the qualification program.

(R. T. Sherrill, 4621)



*HALOE telescope door release device cutaway.*

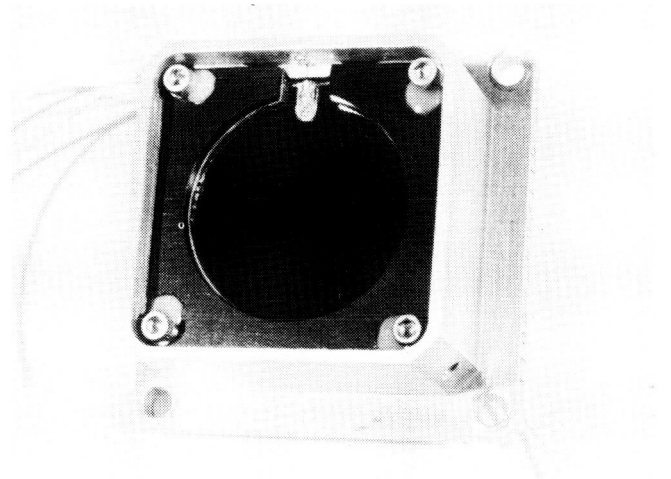
## Calibration of HALOE Broadband Sun Sensor

A novel technique has been used to calibrate the HALOE Sun sensor. Until development of this technique, no other calibration method has been acceptable. The HALOE instrument is an infrared sensor that uses solar occultation measurements to scan the Earth's

atmosphere and collect data to enhance the understanding of upper atmospheric chemistry. The solar scans are accomplished using a pointer/tracker system that consists of a biaxial gimbal (for azimuth and elevation rotation) and spectrally broadband and narrowband Sun sensors. The sensors are required to operate over a 1000:1 and 100:1 solar intensity range, respectively, and to provide pointing knowledge of 15 arc sec and 12 arc sec, respectively.

The calibration of these Sun sensors was performed on Mount Lemmon, near Tucson, Arizona. A NASA Langley plot technique was used for the narrowband sensor calibration. This plot technique is used extensively for other similar applications, but it is usually limited to the measurement of narrowband spectra. A modification to this technique, which extends the applicability to broadband solar spectra, was devised to accomplish the calibration for the broadband sensor. This modification of the NASA Langley plot technique involves integrating the output of a laboratory standard solar sensor across the spectrum of interest.

(A. S. Moore, 4621)



L-84-2793

*HALOE coarse Sun sensor.*

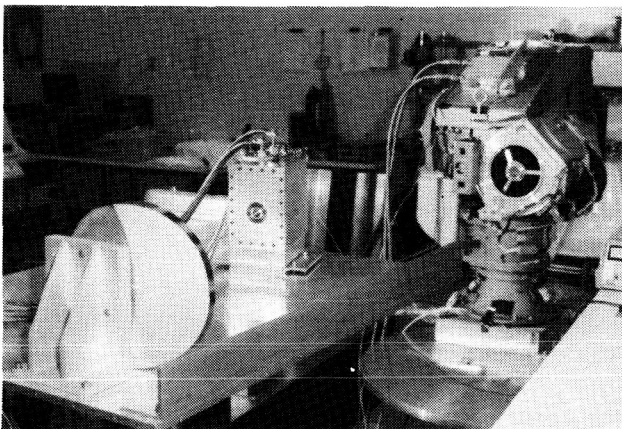
## HALOE Portable Radiation Stimulus Test Set

A small, portable infrared radiation source, whose output rays diverge at 32 arc min (equivalent to that of

the Sun's energy) has been developed for the HALOE instrument for the Upper Atmospheric Research Satellite (UARS). This output beam was required to fill the HALOE telescope input and stimulate the instrument detectors during environmental testing and subsequent field testing of the instrument. In addition, the radiation source had to be sealed in an enclosure that would not allow contamination of the HALOE instrument. A Portable Radiation Stimulus Test Set (PRSTS) was developed to satisfy these requirements.

The PRSTS consists of a 2000°C blackbody energy source aligned to optics that produce a 32 arc min, 10-in-diameter beam. A water-cooled enclosure has been designed for the blackbody which allows high-temperature operation of the unit in close proximity to the HALOE instrument during vacuum testing. The design utilizes Viton O-ring seals and Teflon compression sleeves to maintain case integrity.

The PRSTS has been used in HALOE instrument testing and has provided the required radiometric stimulation for all channels operating from 2.5 to 10  $\mu\text{m}$  and for the coarse and fine Sun sensors. It has demonstrated a stability of  $>0.1$  percent and has been tested in a thermal vacuum chamber at HALOE thermal test requirements. In addition, a 7-day-duration life test has been performed. After each of these usage periods, the blackbody source has been disassembled and inspected for degradation mechanisms. No significant degradation has been detected. The PRSTS will be the sole means of verifying and continuing HALOE instrument health during UARS observatory integration at the General Electric Company and during launch preparations at the NASA Kennedy Space Center.  
(W. W. Rohrbach, 3761)



L-86-6665

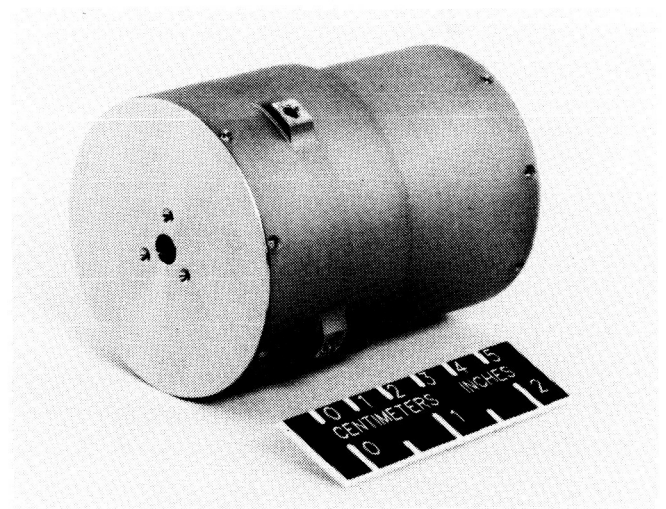
*Radiometric testing of the HALOE instrument using the PRSTS.*

## Miniature High-Stability High-Temperature Space-Rated Blackbody Radiance Source

An advanced conical-cavity-type blackbody radiance source has been developed at NASA Langley which meets the requirements of HALOE for UARS. This development effort was undertaken by NASA because a radiance source that meets all of HALOE's requirements is unavailable in the commercial market. This radiance source operates at  $1300\text{ K} \pm 1\text{ K}$  in space for 2 years, has a power consumption under 7.5 W, and fits within the 2.5- by 2.5- by 3.0-in. envelope allocated inside the HALOE instrument.

Fabrication techniques have been developed, and extensive performance, environmental, and life testing data have been acquired. The design involved the development of fabrication techniques to obtain very small close-tolerance parts from extremely difficult-to-machine materials. A space-rated ceramic core and unique low-thermal-conductivity ceramic-to-metal joint were also developed, tested, and incorporated in this design. The completed flight hardware has been performance and environmental tested.

(J. A. Jones, 4571)



L-86-6717

*1300 K blackbody radiance source.*

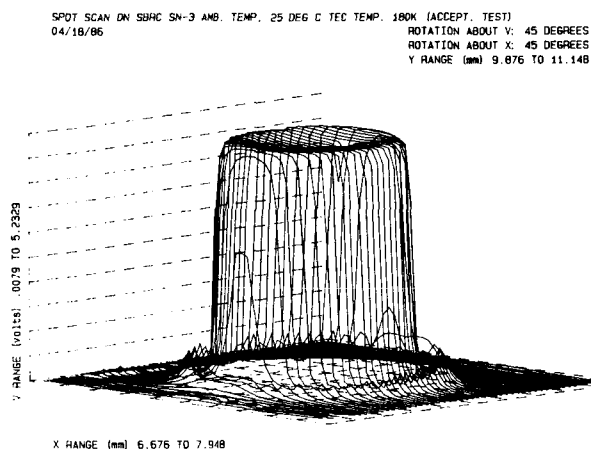
## HALOE Photovoltaic Detector Response Uniformity Mapping Program

A computerized method of accurately mapping photovoltaic detector response uniformity for the HALOE has been developed. This method is capable of verifying whether the HALOE performance specification is met. The HALOE gas correlation channel detectors are required to have the quantum efficiency of the central 80 percent of the detector's active area to be uniform to within  $\pm 5$  percent when measured with a probe beam that has a maximum full width, at half-power points, of  $50 \mu\text{m}$ . Extremely uniform response detectors are required to prevent output signal changes (which would be interpreted as an atmospheric gas density change) due to thermally induced beam movement over the face of the detector.

The HALOE instrument optics produce a  $350\text{-}\mu\text{m}$ -diameter focused beam at the detector surface. The detector active area is  $600 \mu\text{m}$  in diameter. Inverted Cassegrain telescope optics produce a probe beam spot that is  $25 \mu\text{m}$  in diameter. The probe beam spot is focused on the surface of the detector and automatically makes 10 scans across the edge of the active area at different vertical heights. The uniformity spot scan computer program steps the probe beam across the surface of the detector for a maximum of 51 steps along the  $x$  and  $y$  axes for a total of 2601 data points. Step size is  $24 \mu\text{m}$ , which gives a  $1\text{-}\mu\text{m}$  spot overlap in the travel direction. The number of steps can be reduced as desired to provide more rapid maps. A complete scan, at maximum resolution, can be completed in about 2.5 hr. The uniformity spot scan data can be output on either a printer in tabular

form (including averages for the center 60 percent and 80 percent of the active area) or on a plotter in two- or three-dimensional plots.

(C. A. Hardesty, 3761)



*Three-dimensional uniformity spot scan profile.*



# Technology Utilization Program

One of NASA's Congressionally mandated responsibilities is to promote economic and productivity benefits to the nation by facilitating the transfer of aerospace-generated technology to the public domain. NASA's means of meeting this objective is its Technology Utilization Program, which provides a link between the developers of aerospace technology and those in either the public or private sectors who might be able to employ the technology productively.

One important facet of NASA's Technology Utilization Program is its applications engineering projects, which involve the use of NASA expertise to redesign and/or re-engineer existing aerospace technology to solve problems encountered by federal agencies or other public-sector institutions. Applications engineering projects originate in various ways. Some stem from requests for NASA assistance from other government agencies, and some are generated by NASA engineers or scientists who perceive possible solutions to public-sector problems through the adaptation of NASA technology. In addition, NASA employs a multidisciplinary applications team that contacts public-sector agencies, medical and public-health institutions, and professional organizations to uncover significant problems in fields such as health care, public safety, transportation, and industrial processes which might be amenable to solution by the application of NASA technology. The projects reported on here are typical of the applications engineering efforts conducted at NASA Langley in support of the Technology Utilization Program.

## Water Quality Monitoring System

A van-portable water quality monitoring system has been developed and evaluated. The system provides in situ sampling and determination of the elemental constituents in water and toxic wastes. Developed under NASA Langley management through a NASA/EPA (Environmental Protection Agency) cooperative project arrangement, this monitoring system represents a modification and outgrowth of the portable element analyzer developed for geological exploration under Technology Utilization auspices. Both systems trace their lineage to the X-ray fluorescence spectrometer package used to

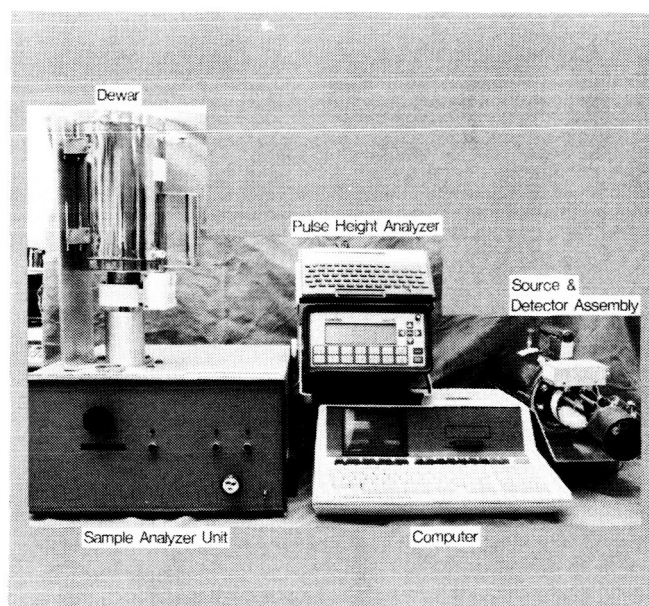
determine the inorganic constituents in Martian surface samples for the Viking missions to Mars in 1976.

The system, designed to accommodate EPA's objectives, is self-contained and readily transportable by van to a source of ground water (e.g., lake, stream, estuary, or industrial effluent discharge channel) to sample and perform analyses on site to determine the chemical constituents of the sample. Of particular interest are the high-priority toxic metals such as As, Hg, Pb, Cd, and Cr. Over 30 elements can be detected in the range of 10 ppm (parts per million) or less.

The system (shown in the figure) is powered by rechargeable batteries and includes: (1) a 1000-channel pulse height analyzer, spectrum display, and computer interface; (2) a sensor head containing a high-resolution cryogenic Si(Li) solid-state X-ray detector and ruggedized portable X-ray tube powered by an auxiliary battery pack; (3) a data processor unit including a computer, liquid crystal display, printer, and mass storage; and (4) a sample handling equipment module.

Field tests at two sites and delivery of the system to the EPA are scheduled for late 1986.

(W. Kelliher, 3068)



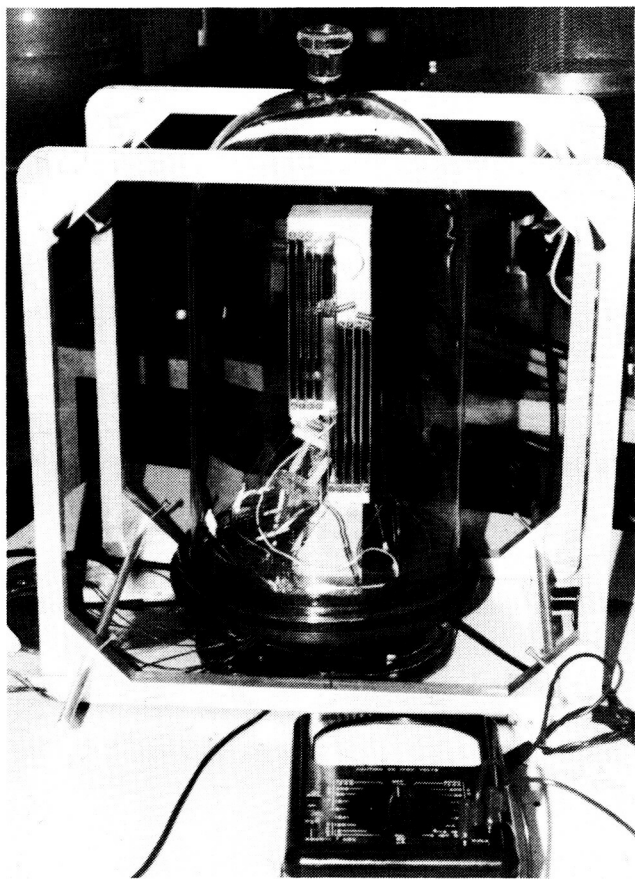
L-84-8946

*Van-portable water quality monitoring system.*

## Low-Energy Electron Magnetometer

In response to an expressed need for on-line, noninvasive, real-time monitoring of electric motors and rotating machinery in engineering laboratories, a fast, sensitive low-energy electron magnetometer (LEEM) has been developed for detecting magnetic transients associated with electrical faults. The instrument was conceived and designed at NASA Langley; development and testing were accomplished under contract to the University of Southern Mississippi.

The instrument also has applications for precisely locating underground electrical faults and for monitoring electric utility substation circuitry in the general areas of electric power transmission and distribution systems. Corona in high-voltage transformer lines and transformers can also be detected by the magnetometer. In fact, magnetic signature analysis techniques can provide a new form of sensitive nondestructive testing capability in the laboratory as well as in field applications.



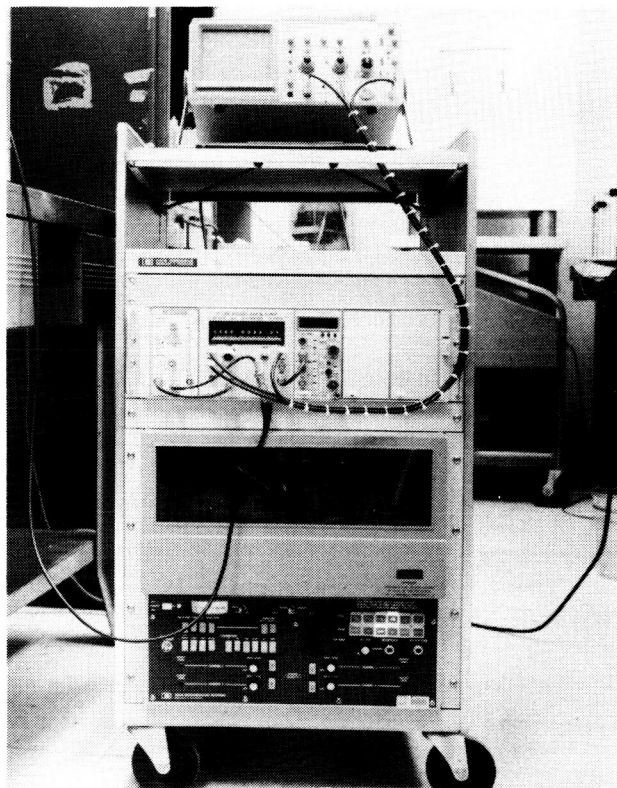
*Experimental setup showing various components of low-energy electron magnetometer.*

The device consists of a commercially available electron gun and two 30° second-order focusing parallel plate electrostatic analyzers. The first analyzer acts as a monochromator located in the field-free space. The second analyzer, located in the test field region, acts as the detector for electrons deflected by the test field. Any fluctuations in the test field will be reflected in the electron signal at the detector located at the exit end of the second analyzer. The system resolution is at least 1 part in  $10^3$ .

(J. J. Singh, 3907)

## Intracranial Pressure Dynamics

A new instrument has been developed to aid in determining important parameters associated with intracranial pressure dynamics. This instrument incorporates NASA-Langley-developed pulsed phase-locked-loop technology, which is based on a phase-sensitive detection principle. As an ultrasonic tone burst is sent through the skull and received, the frequency of the transmitted



L-86-3009

*Rack showing equipment used in monitoring intracranial dynamic parameters.*

wave is adjusted until the received wave is in quadrature with the transmitted wave. Any change in the ultrasonic transmission properties of the intracranial tissue results in frequency changes that can be measured and recorded. This information can be used to determine, without using invasive techniques, important mechanical properties of the cranial system, including the brain.

Using a nonlinear mechanical model simulating brain tissue, the instrument has enabled the measurement of the pressure-volume index (PVI), in vivo, in cats. (The PVI is a parameter that is useful in determining prognosis and treatment of brain trauma.) The agreement between the currently used PVI measurement (invasive) technique and the ultrasonic (noninvasive) technique is within 2 percent. This is well within the precision needed for clinical diagnostic purposes. The ultrasonic technique also yields other information related to such variables as intracranial pressure and blood flow in the brain.

Currently, clinical studies are under way at the Medical College of Virginia, Richmond, VA, under the direction of Anthony Marmarou, to determine significant physiological parameters from data obtained using this NASA-Langley-developed instrument.

(W. T. Yost, 3036)



# Standard Bibliographic Page

|  |  |  |   |  |  |
|--|--|--|---|--|--|
| 1. Report No.<br><b>NASA TM-89037</b>  |  | 2. Government Accession No.                                |   | 3. Recipient's Catalog No.   |  |
| 4. Title and Subtitle<br><b>Research and Technology 1986<br/>Annual Report of the Langley Research Center</b>  |  |  |   | 5. Report Date<br><b>December 1986</b>                               |  |
|  |  |  |   | 6. Performing Organization Code                                      |  |
| 7. Author(s)   |  |  |   | 8. Performing Organization Report No.                                |  |
| 9. Performing Organization Name and Address<br><b>NASA Langley Research Center<br/>Hampton, VA 23665</b>   |  |  |   | 10. Work Unit No.  |  |
|  |  |  |   | 11. Contract or Grant No.  |  |
| 12. Sponsoring Agency Name and Address<br><b>National Aeronautics and Space Administration<br/>Washington, DC 20546</b>  |  |  |   | 13. Type of Report and Period Covered<br><b>Technical Memorandum</b> |  |
|  |  |  |   | 14. Sponsoring Agency Code   |  |
| 15. Supplementary Notes  |  |  |   |  |  |
| 16. Abstract<br><br><p>The mission of the NASA Langley Research Center is to increase the knowledge and capability of the United States in a full range of aeronautics disciplines and in selected space disciplines. This mission will be accomplished by: performing innovative research relevant to national needs and Agency goals; transferring technology to users in a timely manner; and providing development support to other United States Government agencies, industry, and other NASA centers. This report contains highlights of the major accomplishments and applications that have been made during the past year. The highlights illustrate both the broad range of the research and technology activities at the NASA Langley Research Center and the contributions of this work toward maintaining United States leadership in aeronautics and space research. For further information about the report, contact Jerry C. South, Chief Scientist, Mail Stop 103, NASA Langley Research Center, Hampton, Virginia 23665, (804) 865-3316.</p> |  |  |   |  |  |
| 17. Key Words (Suggested by Authors(s))<br><br><b>Research and technology</b>  |  |  | 18. Distribution Statement<br><br><b>Unclassified — Unlimited</b><br><br><b>Subject Category 99</b> |  |  |
| 19. Security Classif.(of this report)<br><b>Unclassified</b>   |  | 20. Security Classif.(of this page)<br><b>Unclassified</b> |   | 21. No. of Pages<br><b>113</b>                                       |  |
|  |  |  |   | 22. Price<br><b>A06</b>  |  |